SPECTROSCOPIC ANALYSIS OF γ DORADUS VARIABLE STARS

AARON GREENWOOD

A thesis submitted in partial fulfilment of the requirements for the degree of Master of Science in Astronomy at the University of Canterbury

February 2014

UC
UNIVERSITY OF CANTERBURY
Te Whare Wānanga o Waitaha
CHRISTCHURCH NEW ZEALAND

It's just flashes that we own
it's little snapshots
made of breath and of bone
and out on the darkling plain, alone
they light up the sky

— Jeffrey Foucault

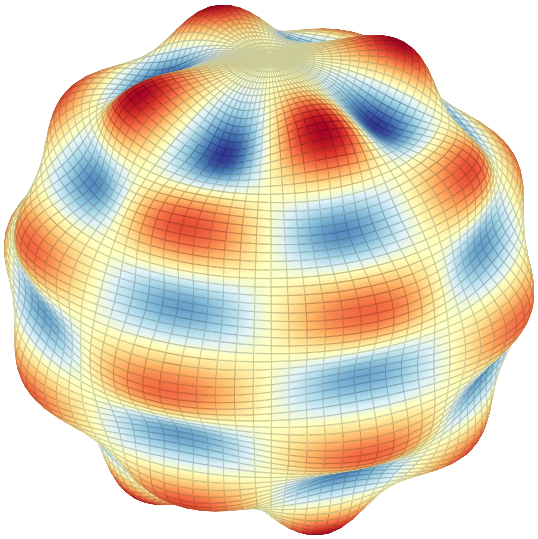

ABSTRACT

In this thesis, three γ Doradus-type stars are analysed: HD139095, HD153580, and HD197541. Long-term observation campaigns have been conducted on each star, with over 300 spectra of each star being gathered for analysis using the HERCULES spectrograph at Mount John University Observatory. For each star, cross-correlation techniques were used to obtain representative line profiles for each spectrum. The analysis of these line profiles has resulted in frequency and pulsation mode identifications for these three stars. Abundance analysis has also been performed on HD139095 and HD197541, and their fundamental parameters are confirmed as being consistent with the γ Doradus class of stars. HD153580 and HD197541, previously only candidates for the class, can now be classified as bona fide γ Doradus type stars.

The frequencies and modes identified in this thesis will be very useful in constraining future theoretical models, allowing us to better understand and model the interiors of γ Doradus stars.

DECLARATION

I declare that all work presented in this Master's thesis my own, unless otherwise indicated or cited.

I acknowledge the contributions of Duncan Wright, Emily Brunsden, and Jovan Skuljan for their parts in writing the MATLAB scripts for data reduction and processing. I also acknowledge the help of Emily Brunsden and Matt Davie, as well as my supervisors, in teaching me their analysis methods during my undergraduate studies. Any other pieces of scientific software used in this thesis have been acknowledged and cited as appropriate.

I also gratefully acknowledge the help of my supervisors, Associate Professor Karen Pollard and Professor Peter Cottrell, for their ideas, advice, and proof-reading of this thesis.

Aaron Greenwood
Christchurch, February 2014

CONTENTS

LIST OF FIGURES

LIST OF TABLES

GLOSSARY

ARES ARES (Automatic Routine for line Equivalent widths in stellar Spectra) is a C++ routine to automatically compute the equivalent widths of the stellar spectral lines stipulated by an included linelist (Sousa et al., 2007), available from `http://www.astro.up.pt/~sousasag/ares/`. 32, 33, 132

ATLAS9 ATLAS9, written by Robert L. Kurucz, is an LTE code for generating stellar model atmospheres (Kurucz, 1993). The FORTRAN77 code has been ported to Linux (Sbordone et al., 2004). 29, 34

FITS Flexible Image Transport System (Wells et al., 1981), the de facto standard for astronomical images. Combines uncompressed raw image data with text headers detailing information such as observation date, time and location, and information specific to the telescope and instruments used. 27, 28

FPF The Fourier Parameter Fit (FPF) method, employed by FAMIAS, is a new technique that uses the Fourier parameters to identify stellar pulsation modes (Zima, 2006; Zima et al., 2006). 39, 69

FUNDPAR FUNDPAR is a package that integrates with MOOG and ATLAS9 to perform an iterative least-squares abundance analysis on a set of measured equivalent widths (Saffe, 2011). 34, 81, 82, 108, 132, 133, 157

HERCULES The High Efficiency and Resolution Canterbury University Large Échelle Spectrograph is a fibre-fed échelle spectrograph operated at Mount John University Observatory, and attached to the 1 m McLellan telescope (Hearnshaw et al., 2002). 25, 29, 44, 105, 106, 139–141

HIPPARCOS — The High Precision Parallax Collecting Satellite was launched by the European Space Agency in 1989, and operated for 3.5 years. The mission goal of collecting precise astrometry of stars produced a useful by-product: a large catalogue of epoch photometry. 12, 22, 27, 35, 43, 44, 52, 68–70, 76, 79, 82, 84, 91, 105, 110, 117

IACC — Inclination Angles of Complete Cancellation. 9, 76

IALC — Inclination Angles of Least Cancellation. 9

LTE — LTE is the assumption of local thermodynamic equilibrium. 34

MATLAB — MATLAB (matrix laboratory) is a programming language developed by MathWorks in Natick, Massachusetts. It specializes in providing a fast, high-level numerical programming environment and contains a large library of built-in functions. Release version R2012b was used. 9, 27, 29, 30, 122, 134

MJUO — Mount John University Observatory (MJUO) houses the HERCULES spectrograph, which is linked by optical fibre to the 1 m McLellan telescope. MJUO is situated at an altitude of 1029 m, at 170° 27.9′ E, 43° 59.2′ S. 19, 25–27, 43, 44, 52, 54, 65, 77, 79, 80, 82, 83, 105, 106, 122, 134, 135, 137, 139

MOOG — MOOG is an LTE line analysis and spectrum synthesis package, developed by Chris Sneden (Sneden, 1973) and available from `http://www.as.utexas.edu/~chris/moog.html`. 34

MUSICIAN — The Marsden-funded project group led by Dr Karen Pollard at the University of Canterbury: Mapping and Understanding Stellar Interiors through a Coordinated International Asteroseismology Network. 26, 135

SME — Spectroscopy Made Easy (Valenti and Piskunov, 1996), a spectrum synthesis program used for determining fundamental stellar parameters. 34, 81, 82, 104, 108, 120, 132–134

SPECTRE	SPECTRE is an interactive spectrum analysis code (Fitzpatrick and Sneden, 1987), available from http://www.as.utexas.edu/~chris/spectre.html. 32, 33, 81, 108, 157
VALD	The Vienna Atomic Line Database (Kupka et al., 2000). 34, 81
ZAMS	Zero-age main sequence. 20
Moment Method	The moment method uses the moments of the line profile to identify pulsation modes (Aerts, 1996; Balona, 1986; Briquet and Aerts, 2003). 35, 39, 40
Synspec	A spectrum synthesis program (Zboril, 1996). 29

1

INTRODUCTION

In order to fully understand the structure and evolution of stars, we must find ways to determine the processes that are happening deep below the opaque photosphere. The impenetrable core of the star, converting mass to energy through nuclear fusion, is what drives the structure and evolution of a star. The technique of asteroseismology[1] can be used to peek into the interior of a star, and infer what processes are occurring deeper in its core, by observing the physically pulsating surface of the star. By conducting intensive spectroscopic analyses, we can determine or constrain parameters such as stellar inclination and rotation speed, mass, radius, metallicity, effective temperature, surface gravity, and most importantly the frequencies and modes of a star's pulsations.

1.1 A BRIEF HISTORY

In 1920, Sir Arthur Eddington published his proposal that the energy of the Sun was produced not by gravitational contraction (a theory he derided as an 'unburied corpse'), but some as-yet unknown process drawing energy from mass itself:

> *A star is drawing on some vast reservoir of energy by means unknown to us. This reservoir can scarcely be other than the sub-atomic energy which, it is known, exists abundantly in all matter; we sometimes dream that man will one day learn how to release it and use it for his service. The store is well-nigh inexhaustible, if only it could be tapped. There is sufficient in the Sun to maintain its output of heat for 15 billion years.*
>
> — Sir Arthur Eddington (1920)

Indeed, Eddington concluded that the conversion of hydrogen into helium is the probable power source for our Sun. This was spurred by recent advancements in mass spectrometry by F. W. Aston, who also in 1920 had measured the difference in mass between hydrogen and helium (Aston, 1920). It is amazing just how far we have come,

1 I refer the reader to Gough (1996), who provides an interesting discussion about the etymology of the term 'asteroseismology', and why it isn't called astroseismology.

in scarcely more than a human lifetime, since this seminal moment in stellar physics. Yet it is also simultaneously daunting how much we do not know. For although we know in broad strokes the processes that drive the formation, evolution, and destruction of stars, the peculiar details which make every object unique are scarcely even postulated. Asteroseismology allows us to probe deep into the core of a star and to reveal the secretive mechanisms that make each star different. We do this by using physical pulsations on the surface of the star to infer its interior structure.

As you trace up the main sequence of stars on a Hertzsprung-Russell (HR) diagram, and up to the giant branches, the rough description is that you will encounter different thresholds of stellar properties which produce sets of boundary conditions throughout the diagram. Stellar variability characteristics are intrinsic to these regions. These are the so-called instability strips, and Figure 1.1 illustrates these regions. Thus it is an inevitable conclusion, and a triumph of stellar structure theory, that a star's manner of pulsation may be predicted by observing its fundamental parameters.

It is the marriage of these two areas, the theoretical models and observed pulsations, that is a necessary goal in order to progress asteroseismology as a unified science. It is, however, a difficult and resource-intensive task to identify the nature of these pulsations, because a large set of high-resolution spectroscopic data is required for an optimal analysis. This has resulted in a comparative lack of observational data, significantly hampering the testing of theoretical models which are still governed largely by approximations and parameterized descriptions of poorly understood physics. Further observational data allows more precise constraints to be applied to the theoretical models.

1.2 STELLAR PULSATIONS

1.2.1 *The cause of stellar pulsations*

Stellar pulsations are caused by a periodic forcing coming from within the star, that subsequently distorts its outer layers and produces an observable, periodic variability. Figure 1.2 shows the most recent theoretical γ Doradus instability strip by Dupret et al. (2004), produced using a time-dependent treatment of convection. An earlier instability strip by Warner et al. (2003) is not as refined as Dupret et al.. The simpler "frozen convection" model of Warner et al. is not valid throughout much of the convective envelope (Dupret et al., 2004). Figure 1.3 shows this simpler model, which does have the added bonus of a δ Scuti instability strip, showing (roughly) the overlap between the instability strips of each class. With this information we can say that many γ Doradus stars have been observed inside the theoretical δ Scuti instability strip.

Instability strips such as these show particular regions of the HR diagram where specific conditions are commonly met that excite instability within the star. The inner workings that drive the pulsations are called *driving mechanisms*. These mechanisms

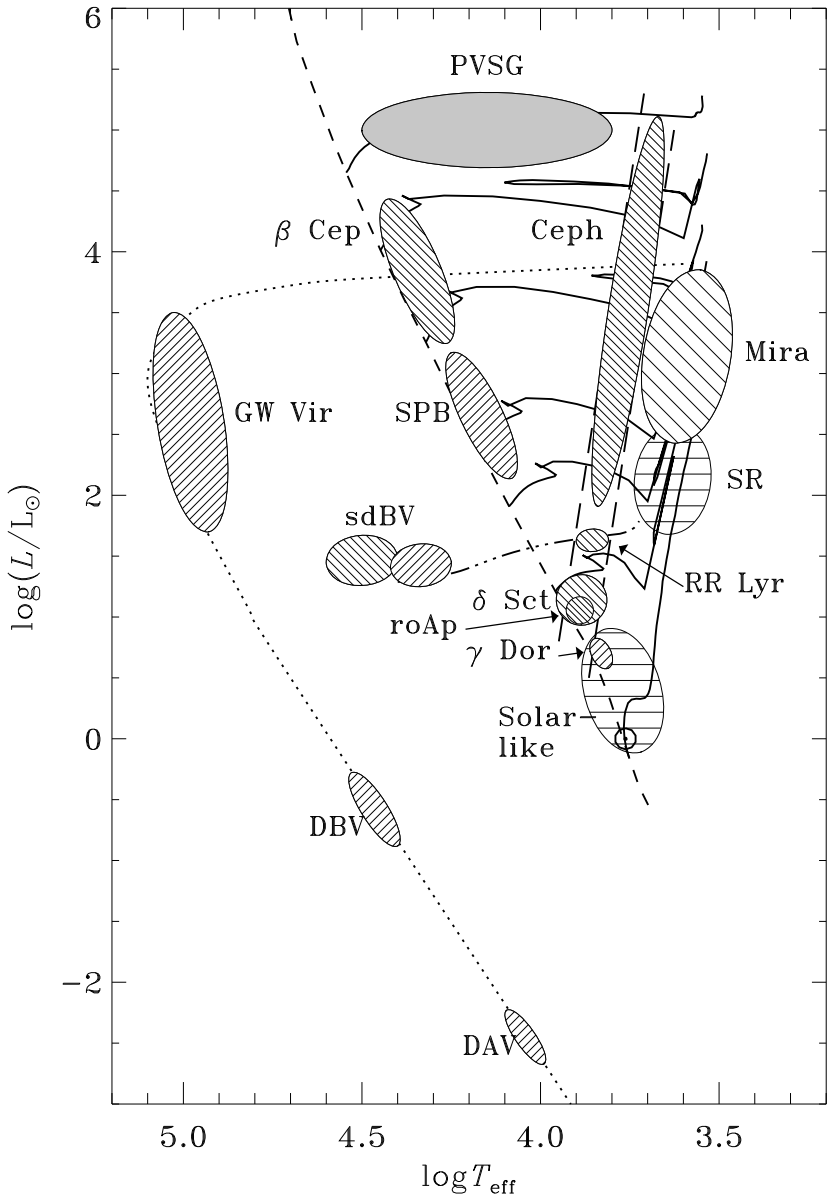

FIGURE 1.1: A Hertzsprung-Russell diagram showing the many known classes of variable stars. Diagram reproduced from Aerts et al. (2010).

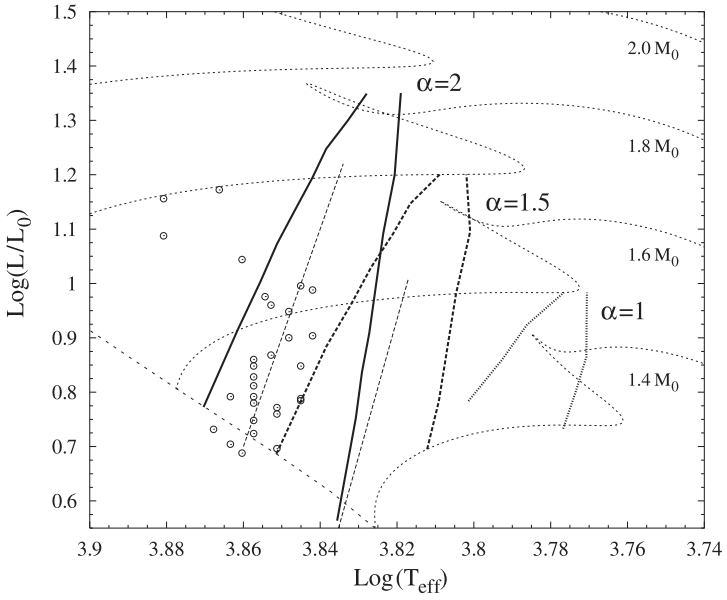

FIGURE 1.2: A theoretical γ Doradus instability strip, with time-dependent convection treatment and reproduced from Dupret et al. (2004). The strips are computed for three different values of the mixing length parameter, α, for $\ell = 1$ modes. The thin dashed lines represent the frozen-convection results from Warner et al. (2003), and the $\odot$ symbols are bona fide γ Doradus stars.

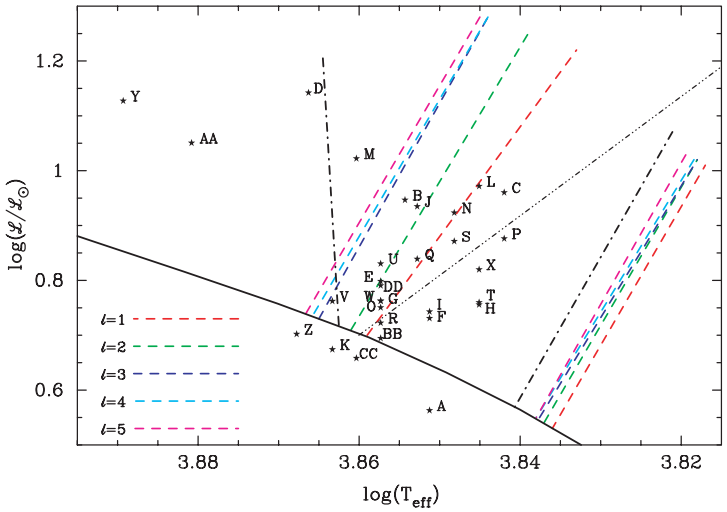

FIGURE 1.3: A theoretical γ Doradus instability strip, with frozen convection treatment and reproduced from Warner et al. (2003). Varied values of ℓ are plotted in different colours (dashed lines), while the main sequence is a solid black line and the theoretical red edge of the δ Scuti instability strip is the triple-dot-dashed line. The observational γ Doradus instability strip is the dot-dashed line.

actively drive the pulsations: without sustained and periodic forcing, any temporary distortions will be quickly damped. These can often be thought of as heat-engine mechanisms, as Eddington first postulated in 1917. Most pulsating variable stars, including Cepheids, RR Lyrae stars, δ Scuti stars, and β Cep stars are driven by a mechanism called the opacity mechanism, or κ-mechanism (Aerts et al., 2010, described in Section 1.5.3). The γ Doradus stars analysed in this thesis also pulsate via a flux-blocking mechanism; however, they pulsate due to convective flux blocking rather than opacity variations (Guzik et al., 2000).

There are two fundamental manners in which a star may pulsate. These are the radial and non-radial pulsations. The simplest definition to distinguish the two is that radial pulsations are spherically symmetric – the entire photosphere of the star pulsates inwards and outwards. Non-radial pulsations are no longer spherically symmetric, as there are nodal and anti-nodal lines on the stellar surface.

1.2.2 *Radial pulsations*

The modes of spherically symmetric radial pulsations are classified by only one number, the radial order n. This describes the number of spherically symmetric and concentric nodal shells that are present within the star. The fundamental mode thus has $n = 0$, the first overtone has $n = 1$, and so on. The classic example of radial pulsators is the Cepheid variables, but RR Lyrae and δ Scuti stars can also show radial pulsations. As these stars swell and contract in radius, their luminosity fluctuates and causes a periodic photometric variability. The Cepheid variables often pulsate in the fundamental radial mode, which means that there *is not* a concentric nodal shell within the star (Aerts et al., 2010). It is this which links their pulsation periods to their intrinsic brightness, making Cepheid variables excellent beacons on the cosmic distance ladder.

The relatively simple manner of these Cepheid pulsations, plus their luminous nature, means that they are a well-understood class of stars. Their key usefulness in asteroseismology lies in the presence of double-mode Cepheids: stars that pulsate in both the fundamental and first overtone radial modes (see, for example, Antonello and Mantegazza, 1984). The ratio between the periods of these two modes (which differs from the usual 1:2 or 1:3 from, say, a string or an open pipe respectively) is 0.71 (Aerts et al., 2010). This high ratio is caused by a gradient of the speed of sound within the star: just by observing two pulsation periods, we can infer the internal structure of a star!

1.2.3 *Non-radial pulsations*

Non-radial pulsations are classified by three numbers: n, ℓ, and m. The radial order n is the same as above, but we now have the addition of the degree ℓ and azimuthal order m. The degree ℓ is the total number of nodes present on the surface of the star,

and the azimuthal order m is the number of these nodes which intersect with the poles of the rotation axis. Strictly speaking, radial pulsations are also defined with the ℓ and m numbers, but with $\ell = 0$ and $m = 0$. Non-radial pulsations have $\ell \geq 1$.

There are three main types of non-radial pulsation modes: p-modes, g-modes, and f-modes. These types of variability can be summarized as follows:

- p-modes, or pressure modes, have pressure as their restoring force. These are waves that vibrate in the direction of propagation.
- g-modes, or gravity modes, have buoyancy as their restoring force. Their displacement is mostly perpendicular to the direction of propagation.
- f-modes are akin to waves on a beach or in the atmosphere of Earth: they are surface waves that travel across the star, like surface g-modes.

The presence of these non-radial pulsation modes allows us to probe the interior conditions of the star. However, our knowledge of the interior is still limited by our ability to model how and why particular modes of pulsation are excited. The identification of pulsation modes and frequencies can help to refine models of the stellar interior. Figure 1.4 shows the different regions in which these modes theoretically propagate in a polytropic star: it can be clearly seen that the g-modes propagate deeper into the star, and at lower frequencies, than the p-modes. In the case of g-modes, we can gain valuable information about the conditions of the star around the boundary between the convective envelope and radiative zone, where these modes are excited, and as deep as the boundary with the convective core. With this information, we can describe the parameters that determine the nature and evolution of the stellar core.

1.2.4 *The geometry of non-radial pulsations*

In asteroseismology it is important to have a well-defined system of coordinates in which to operate. Our observations are sensitive to the orientation and rotation rate of the star, and the pulsation modes we observe are typically defined in spherical coordinates. Figure 1.5 introduces the basic geometry of the situation. Because we often do not know the inclination of the star precisely, its rotation rate is often expressed as $v \sin i$ – that is, its true rotational velocity multiplied by the sine of the (unknown) inclination.

We model non-radial pulsations as spherical harmonics that distort the stellar photosphere, so to understand what this nomenclature means it is necessary to briefly describe the underlying mathematics. Following Aerts et al. (2010) and Zima (2008b), the mathematical basis upon which stellar pulsations are modelled is introduced. First, we begin by defining the Legendre functions

$$P_\ell^m(x) = (-1)^m \left(1 - x^2\right)^{m/2} \frac{d^m}{dx^m} P_\ell(x), \tag{1.1}$$

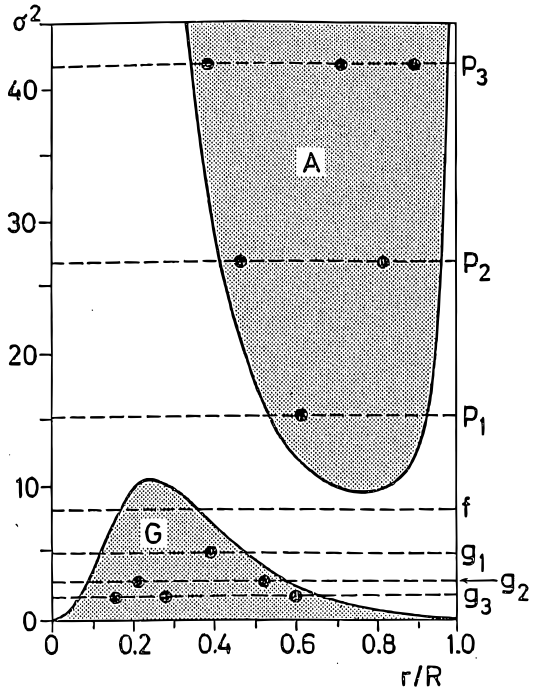

FIGURE 1.4: A propagation diagram for pulsations of order $n = 3$ and degree $\ell = 2$ in a polytropic star. The square of the frequency σ is plotted against the radial distance from the stellar centre and propagation of p-modes is possible in the A (acoustic) region, while propagation of g-modes is possible in the G (gravity) region. Figure reproduced from Kippenhahn et al. (2013).

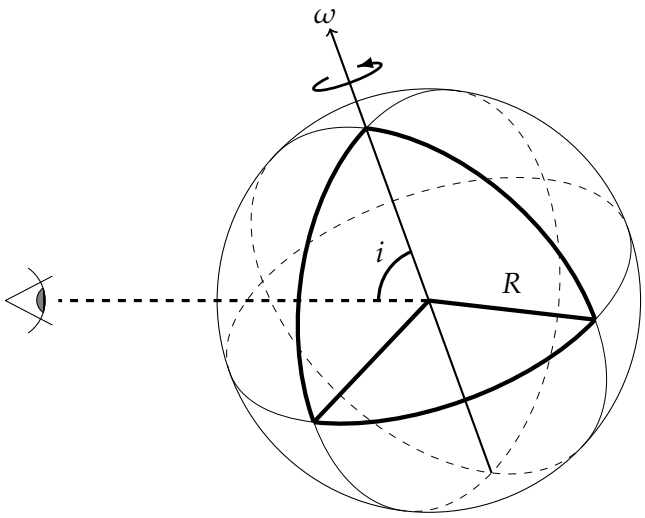

FIGURE 1.5: A star of radius R is rotating about its axis at an angular speed of ω. The star in question is invariably tilted in some way towards the viewer. Its inclination, i, is defined as the angle between the star's rotation axis and the viewer's line of sight. The lines across the surface also indicate the nodal lines of an $\ell = 2,\ m = 1$ pulsation mode (see Section 1.2.4).

where $P_\ell(x)$ is a Legendre polynomial of degree ℓ:

$$P_\ell(x) = \frac{1}{2^\ell \ell!} \left(\frac{d^\ell}{dx^\ell} \left(x^2 - 1 \right)^\ell \right) \tag{1.2}$$

which is valid for $m > 0$.[2] The spherical harmonics are defined as

$$Y_\ell^m = N_\ell^m P_\ell^{|m|} \exp^{im\phi} \cos\theta \tag{1.3}$$

where

$$N_\ell^m = (-1)^{\frac{m+|m|}{2}} \sqrt{\frac{2\ell+1}{4\pi} \frac{(\ell - |m|)!}{(\ell + |m|)!}} \tag{1.4}$$

is a normalization constant as defined in the non-radial pulsation mode-identification software, FAMIAS, by Zima (2008b).[3] The computational analyses in this thesis assume the specific case where the polar and symmetry axes of the spherical harmonic coordinate system are aligned with the rotation axis of the star. The physical interpretation of these spherical harmonics is that the degree ℓ denotes the number of observed nodal

2 In the case of $m = 0$, we have the simpler Legendre polynomials $P_\ell^0(x) = P_\ell(x)$.

3 Note that a positive m denotes a prograde mode propagating in the direction of rotation, and a negative m denotes a retrograde mode.

lines. The azimuthal order m is the number of nodes that intersect with the axis of symmetry: in our observations, these are the poles of the rotation axis. The radial order n is the number of radial nodes that exist within the star.

To summarize, the Legendre polynomials are mapped to the stellar surface in the form of spherical harmonics. The form of these harmonics, and thus the stellar pulsations themselves, is largely determined by the degree and azimuthal order of the mode. Notably, the effects of rotation (in particular that from the Coriolis force, as described by Bouabid et al., 2013) must also be subsequently accounted for.

Aerts et al. (2010) also define the Inclination Angles of Complete Cancellation (IACC), which describe situations where there is a first-order (linear) cancellation of the effects of pulsation in the line profile, due to the geometric effects of observing at particular inclinations. For example, a $(\ell, m) = (2, -1)$ mode has IACC at $0°$ and $90°$, and Inclination Angles of Least Cancellation (IALC) at $45°$ (where there is the least cancellation). These cancellation angles apply to the *monochromatic* visual magnitude, as having resolution of each spectral line in radial velocity space reduces the impact of these effects. However, pulsations in the second (variance) and third (skewness) moments may still be visible in analyses using the 'moment method' (Aerts et al., 1992). Table B.1 in Aerts et al. (2010) provides a list of IACC and the corresponding IALC for a selection of modes in a non-rotating (or slowly rotating) star.

Figure 1.6 shows a selection of pulsation modes at an inclination angle of $60°$, computed using MATLAB's built-in implementation of spherical surface harmonics. Owing to observational factors, such as a limited spectral resolution, it is not likely that modes of higher degrees than $l = 4$ will be successfully identified. The effect of high-degree oscillations is that they become progressively more confined to the equator when m approaches ℓ.[4] Figure 1.7 illustrates this effect. The graphic inside the front cover of this thesis illustrates an $(\ell, m) = (10, 4)$ mode, with the addition of grid lines, so as to better see the distortions.

1.2.5 *Rotation*

Rotational effects become apparent when the pulsations occur on a timescale that is significant in comparison to the rotation period of the star. Current spectroscopic analysis methods are lacking in terms of modelling rotation, especially for γ Doradus stars given the proximity of their pulsation frequencies to their rotation frequencies. For example, an effect called frequency splitting (or rotational splitting) can occur (Cowling and Newing, 1949), where rotation may cause an increase in the number of observed frequencies. The Coriolis force may cause a single frequency to be split into a multiplet of $2\ell + 1$ frequencies. However, depending on how each of the split components is excited, they will not all be visible at the same amplitude. Measuring rotationally-split

4 See Aerts et al. (2010) and references therein for the mathematical details. Note that this effect is independent of the equatorial waveguide effects discussed in 1.2.5.

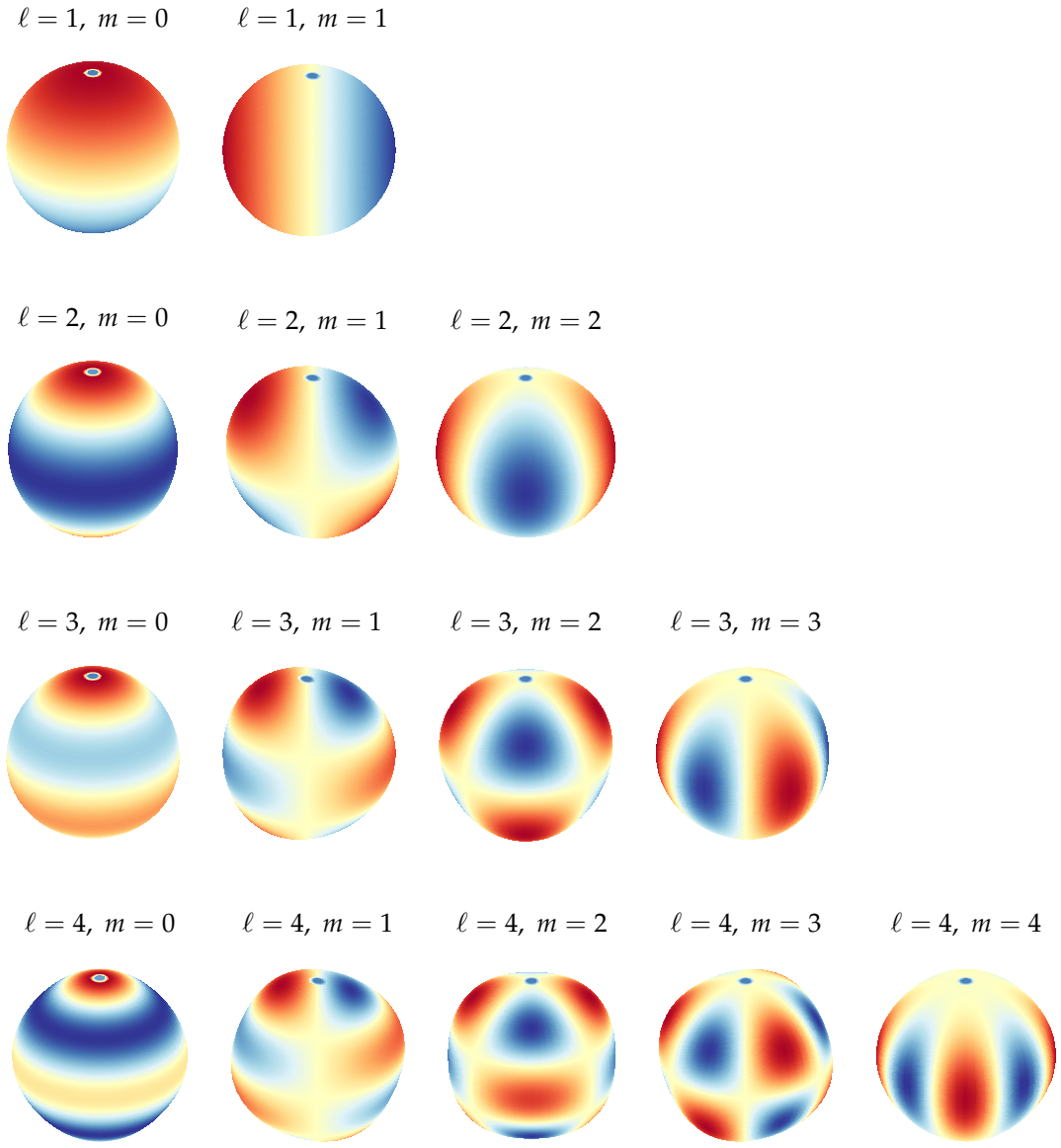

FIGURE 1.6: A grid of pulsation modes at an inclination angle of $i = 60°$, from $\ell = 1, m = 0$ to $\ell = 4, m = 4$. The poles are painted on the surface as a dark blue circle, and the pulsation amplitudes are subtly enhanced so as to visibly distort the surface. In these diagrams, no additional effects (such as the effects of rotation) have been computed. It is a simple mapping of the spherical harmonics to a visible surface.

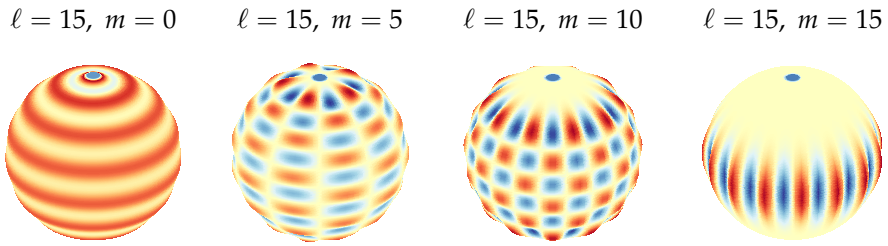

FIGURE 1.7: Pulsation modes at an inclination angle of $i = 60°$ are progressively confined to the equator as m approaches ℓ. By comparison with Figure 1.6, it is visible how the effect also becomes more pronounced at higher degrees (ℓ) of pulsation.

frequencies allows us to obtain the rotation rate of a star, and the subsequent measurement of overtones can tell us the interior rotation rate (Aerts et al., 2010). It is possible that spaced-based photometry is precise enough to detect frequency splitting in γ Doradus stars. Current efforts give some tentative results (Chapellier et al., 2012), but it is still difficult to be certain about the identification of split frequencies. When dealing with a high density of frequencies, it becomes very difficult to distinguish between an array of harmonics, aliases, split frequencies, and frequency combinations.

Rotational splitting is not the only significant implication of rotation. Perhaps practical implementations of new theory (see, for example, Bouabid et al., 2013) will shed some light on the hybrid phenomenon (this is where the short-period, p-mode pulsations of δ Scuti-type stars could occur simultaneously with the longer-period, g-mode pulsations of γ Doradus-type stars). In particular, it will be interesting to see if models of rotational splitting can identify frequencies in the δ Scuti range of $\sim 5 - 15$ d^{-1} as γ Doradus-like g-modes that have been rotationally modified.

Coriolis forces and centrifugal distortion can also break the symmetry of pulsations (Reese et al., 2006), which effectively mean that a single spherical harmonic can no longer truly describe the observed pulsations. Such perturbations are still not used in current methods of spectroscopic mode identification.

An additional effect of rotation is that any mode other than a prograde sectoral mode (that is, any mode *other than* when $m = \ell$) can be suppressed photometrically when confined to an equatorial waveguide owing to rotation (Townsend, 2003a).[5] Following Townsend, we define a spin parameter

$$\nu \equiv 2\Omega/\omega, \tag{1.5}$$

where $\omega \equiv \sigma - m\Omega$. Ω is the angular rotation frequency of the star, ω is the co-rotating pulsation frequency, σ is the observed pulsation frequency, and m is the azimuthal order *according to the sign convention of this thesis*. For $\nu \gtrsim 1$, the amplitude of all modes

5 Once again, it is important to note that the notation of prograde and retrograde modes is not always consistent between papers. In this thesis, a prograde mode has $m > 0$ while retrograde is $m < 0$. Townsend (2003a) uses the opposite convention.

except prograde sectoral modes rapidly decreases as ν rises, particularly at higher inclinations (Townsend, 2003a). This is due to the progressive confinement of the pulsations to an equatorial waveguide, as detailed by Townsend (2003b). Retrograde modes are particularly vulnerable to this effect.

The consequence of this equatorial waveguide is that a rapidly rotating star may have to be viewed from a particular range of inclinations for the frequencies to be visible in single-colour photometry, as shown in Figures 1.8 and 1.9. As such, the HIPPARCOS data cannot be relied upon to detect all pulsation frequencies, even given an adequate number of good quality data points.

The slowly pulsating B (SPB) models considered by Townsend (2003a) are used in Figures 1.8 and 1.9. In these figures, the dependence of the star's inclination and rotation rate on its observable photometric frequencies is clearly seen. For all but the prograde sectoral mode, rotation rapidly suppresses variations at greater latitudes. Although Townsend considered a different spectral type of star, the same effects should be observable for the cooler and less massive γ Doradus stars which show similar g-mode pulsations.

Another important property to consider is the k-value, the ratio of the horizontal to vertical pulsation amplitudes, defined by Zima (2008b) as

$$k = \frac{a_h}{a_s} = \frac{GM}{\omega^2 R^3}, \tag{1.6}$$

where a_h and a_s are the horizontal and vertical pulsation amplitudes respectively, G is the gravitational constant, and M and R are the stellar mass and radius. The formalism in FAMIAS that models the pulsations is generally only reliable where the ratio between the stellar rotation frequency Ω and the observed angular pulsation frequency ω meets the criterion $\Omega/\omega < 0.5$, but may provide a good approximation for $\Omega/\omega < 1$ (Schrijvers et al., 1997).

This k-value is an approximation as it has been derived without rotation. The consequence of this is that a high k-value lowers the observed frequency of pulsation and thus increases the Ω/ω ratio. It is an unavoidable limitation of γ Doradus stars that their pulsation periods are around same order of magnitude as their rotation periods, thus this ratio must be kept in consideration until more sophisticated models are developed.

T_{eff}	$\log g$	M	R	Z
15,300 K	4.07	4.7 $M_\odot$	3.31 $R_\odot$	0.02

TABLE 1.1: The T_{eff}, $\log g$, mass, radius, and metallicity Z of the slowly pulsating B star (SPB) model used by Townsend (2003a).

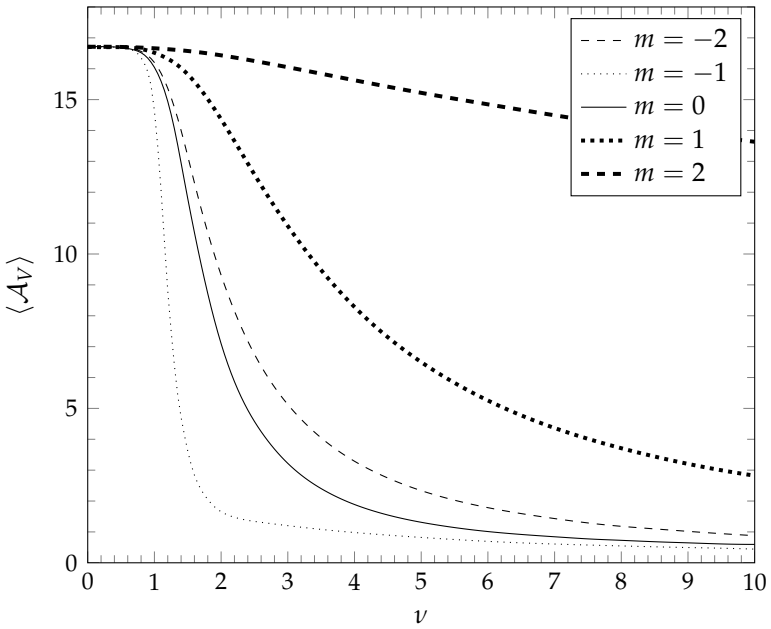

FIGURE 1.8: Variations in the rms semi-amplitude in the V-band for the $\ell = 2$, $m = -2 \ldots 2$ modes against the spin parameter ν, using the SPB model in Table 1.1. The figure data have been reproduced from Townsend (2003a). The sign of the azimuthal order m uses the convention of this thesis.

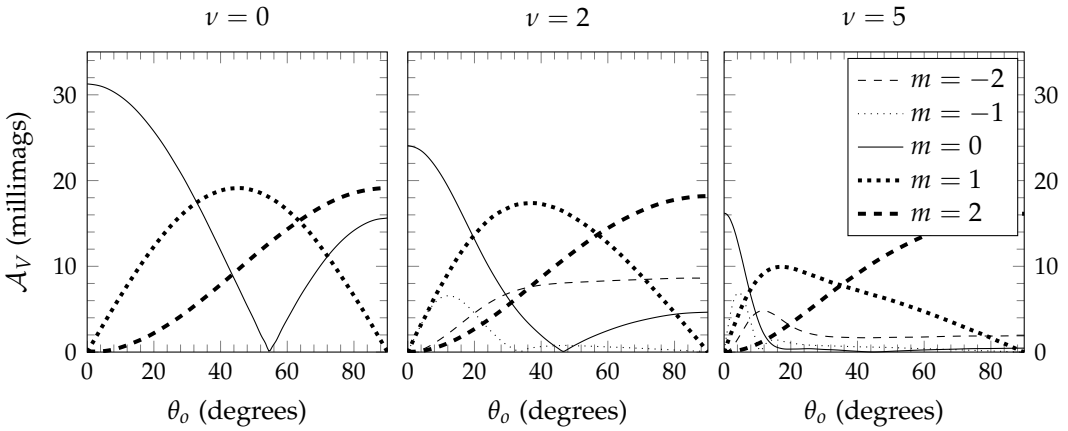

FIGURE 1.9: The θ_o dependence of the semi-amplitude in the V-band, of the same modes as Figure 1.8 and plotted for three different values of the spin parameter ν (Equation 1.5). θ_o is the latitude of the star with respect to its equator. The figure data have been reproduced from Townsend (2003a). The sign of the azimuthal order m uses the convention of this thesis.

1.3 SPECTRAL LINE BROADENING

The broadening of spectral lines is a mixed blessing when it comes to asteroseismology. Since only an exceptional few stars have been directly imaged with a measurable spatial resolution, we are effectively limited to the study of photometric and spectroscopic data to analyse stars other than our own Sun. No matter which star or what analysis methods are chosen, there are always observational factors to consider.

For example, thermal motions produce a Doppler broadening that is well characterized by the effective temperature of the photosphere. However, in stronger lines, pressure broadening becomes significant (Gray, 1988). Thus it is important to remove the strongest absorption lines from our analyses.

1.3.1 *Rotational broadening*

In order effectively to analyse pulsations from spectroscopic data, we must have a rotationally broadened line profile. If rotational broadening dominates the width of the spectral lines, then we can imagine that an integrated strip across the stellar surface (representing an infinitesimally quantized radial velocity) will produce a specific Doppler shift. By integrating these strips across the surface of the limb-darkened stellar disk, the result is a profile that describes the rotational contribution to spectral line broadening. Current analysis methods assume that rotational broadening is the *dominant* line broadening mechanism.

1.3.2 *Microturbulence*

Microturbulence is something of a 'fudge factor', having the property that it describes motions in the stellar photosphere that are smaller than the mean free path of a photon. Its relatively small amplitude (a typical assumption is 2 km s^{-1}) means it is difficult to determine the shape of the microturbulence profile: the classic assumption is that it has an isotropic Gaussian form in non-solar analyses (Gray, 2005). Microturbulent broadening alters the width and depth of an absorption line, but in an unsaturated line, the equivalent width is conserved.

1.3.3 *Macroturbulence*

The properties of macroturbulent broadening are somewhat better characterized than microturbulent broadening, as it is often of measurable amplitude in hotter stars which means that we can observe its shape. Macroturbulence describes motions in the photosphere that are *larger* than the mean free path of a photon (in contrast to microturbulence). The distribution of convective cells in the photosphere is what causes this

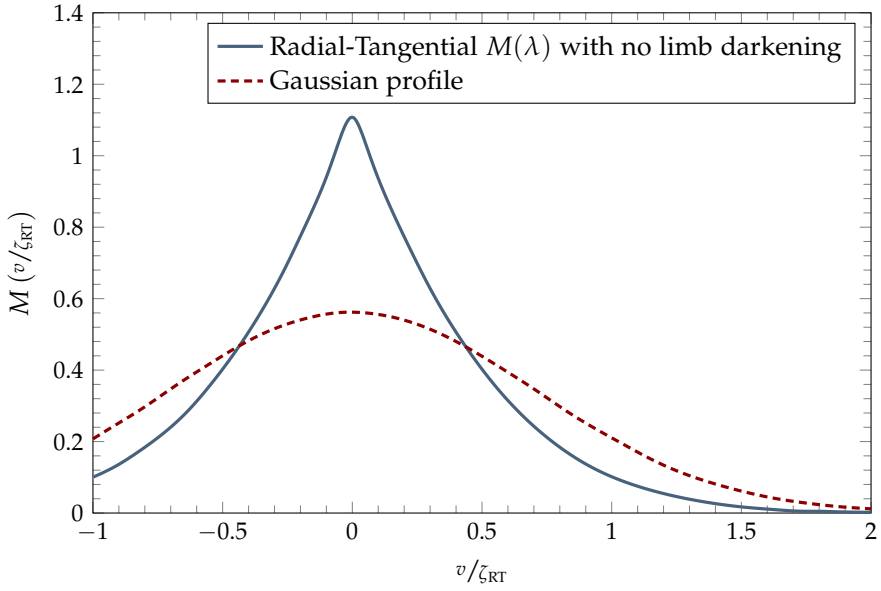

FIGURE 1.10: The cusp-shaped Dopper shift distribution produced by radial-tangential macroturbulence, in comparison with a Gaussian distribution. Figure data are from Gray (2005).

broadening: it is of a similar manner to thermal broadening, except we are now considering a group of convective cells as a singular entity.

The commonly accepted model for macroturbulence is the radial-tangential model (Gray, 1975, 1988). This is an anisotropic model that parametrizes the turbulent motions into radial and tangential components. The shape of the distribution, as seen in Figure 1.10, is that of a cusp with the peak centred in the middle of the stellar disk.

Following the methods set out in Gray (2005), the Doppler-shift distribution for the radial-tangential macroturbulence is given by

$$\begin{aligned}\Theta(\Delta\lambda) &= A_R\Theta_R(\Delta\lambda) + A_T\Theta_T(\Delta\lambda) \\ &= \frac{A_R}{\pi^{1/2}\zeta_R\cos\theta}e^{-(\Delta\lambda/\zeta_R\cos\theta)^2} + \frac{A_T}{\pi^{1/2}\zeta_T\sin\theta}e^{-(\Delta\lambda\zeta_T\sin\theta)^2},\end{aligned} \tag{1.7}$$

where

$\Theta(\Delta\lambda)$	is the Doppler-shift distribution
A_R	is the rest radial motion
A_T	is the rest tangential motion
ζ_R	is the radial macro-broadening parameter
θ	is the angle from the stellar disk centre
$\Delta\lambda$	is the wavelength distribution $\Delta\lambda = \frac{\lambda v}{c}\cos\theta$

This gives us the spectrum

$$\mathcal{F}_v = 2\pi A_R \int_0^{\pi/2} \Theta_R(\Delta\lambda) * I_v \sin\theta\cos\theta \mathrm{d}\theta + 2\pi A_T \int_0^{\pi/2} \Theta_T(\Delta\lambda) * I_v \sin\theta\cos\theta \mathrm{d}\theta \tag{1.8}$$

The reason why macroturbulence is detailed here to an unusual degree is that there is currently speculation that stellar pulsations are the physical cause of macroturbulence in hot stars (Simón-Díaz et al., 2010). Thus, there is no clear reason why it cannot also be a valid explanation for the relatively large macroturbulence values of $v_{\mathrm{mac}} \approx 15$ km s^{-1} observed in this thesis for HD139095 and HD197541. It is not entirely clear what a 'normal' macroturbulence value is for a star at around 7000 K. The most comprehensive survey of macroturbulence, by Valenti and Fischer (2005), unfortunately does not extend past $T_{\mathrm{eff}} \approx 6300$ K. A reasonable extrapolation from this survey could suspect $v_{\mathrm{mac}} \approx 13$ km s^{-1} to be an approximate *upper limit to the mean* macroturbulence of stars with $T_{\mathrm{eff}} \approx 7000$ K. This is an interesting question that needs much more work. What are typical macroturbulence values for stars located within the γ Doradus instability strip – including *all* stars, not just known pulsators? Do all stars in that strip exhibit similar macroturbulence values and compliant line profile variations? If this is true, the next question is why would the line profile variations of only *some* stars be periodic?

1.3.4 *Granulation*

The surface of a star is always turbulent, with rising granules of material and falling lanes in between. The rising granules are more luminous, and blueshifted. The infalling matter is redshifted and less luminous. The combination of these two effects can often cause asymmetries in the line profile, where the red wing of the line profile is less luminous than the blue wing (Gray, 1988).

1.4 METHODS OF ASTEROSEISMOLOGY

With the knowledge that we can model stellar pulsations as spherical harmonics applied to a rotating star, we can describe the basic methods of pulsational mode identification.

1.4.1 *Photometric mode identification*

Multicolour photometry is capable of determining the ℓ value of a pulsation mode. The photometric methods model the amplitude and phase differences between the available photometric passbands (see, for example, Garrido, 2000), and a photometric

implementation is available in FAMIAS (Zima, 2008b). No multicolour photometry data are available for the stars analysed in this thesis, so these methods are not covered in detail.

1.4.2 *Spectroscopic mode identification*

A non-radial pulsation at a particular frequency will introduce systematic distortions across the surface of the star. Figure 1.11 shows the general shape of these variations for all modes where $0 \leq \ell \leq 3$, and how these variations manifest themselves across the line profile of each spectral line. These variations result because the luminosity across the surface of a pulsating star is not uniform: the *localized* luminosity increases for outwards pulsations, and decreases for inwards pulsations. The cumulative localized variations usually also combine to create photometric variations, but they also produce periodic distortions at particular radial velocity values across the line profile.

The general shape of the observed line profile variations becomes a function of the ℓ and m values of each mode, as well as the star's inclination. These variations across the line profile form the basis of our spectroscopic analyses. By performing Fourier analysis on a series of observations, we can find frequencies of pulsations that occur in the spectroscopic line profiles. Computational methods within the FAMIAS software (Zima, 2008a) are then used to search a wide parameter space and converge on the best-fit parameters for each observed frequency.

Thus, the ability of FAMIAS to model theoretical line profile variations forms the main constraint on the accuracy of our results. If FAMIAS cannot accurately model the observed variations, then it will not converge to as low a χ^2 value for the final solution, or may not correctly identify the ℓ and m values of the mode. Thus, FAMIAS results should always be treated with caution, especially with these γ Doradus-like frequencies that are prone to distortion due to the effects of rotation. The operation of FAMIAS is further detailed in Section 2.5.5.

1.5 ASTEROSEISMOLOGY OF GAMMA DORADUS STARS

Stars showing γ Doradus-like pulsations are very interesting and unique targets for asteroseismic investivation. Easier targets, such as Cepheids, are well-studied, and methods of pulsation analysis have revealed fruitful results about the masses of Cepheid stars. For example, analysis of Cepheid overtones has refined the period-luminosity relation (Feast and Catchpole, 1997; Sandage and Tammann, 1969), and we are even progressing towards three-dimensional hydrodynamical simulations of Cepheids (Félix et al., 2013). Revealing the interior of stars through the determination of properties such as convection, opacity, rotation, and ionization is not the only use of asteroseismology: it also has profound impacts on stellar evolution. For example, using asteroseismology to constrain the masses of the outer hydrogen and helium layers in white

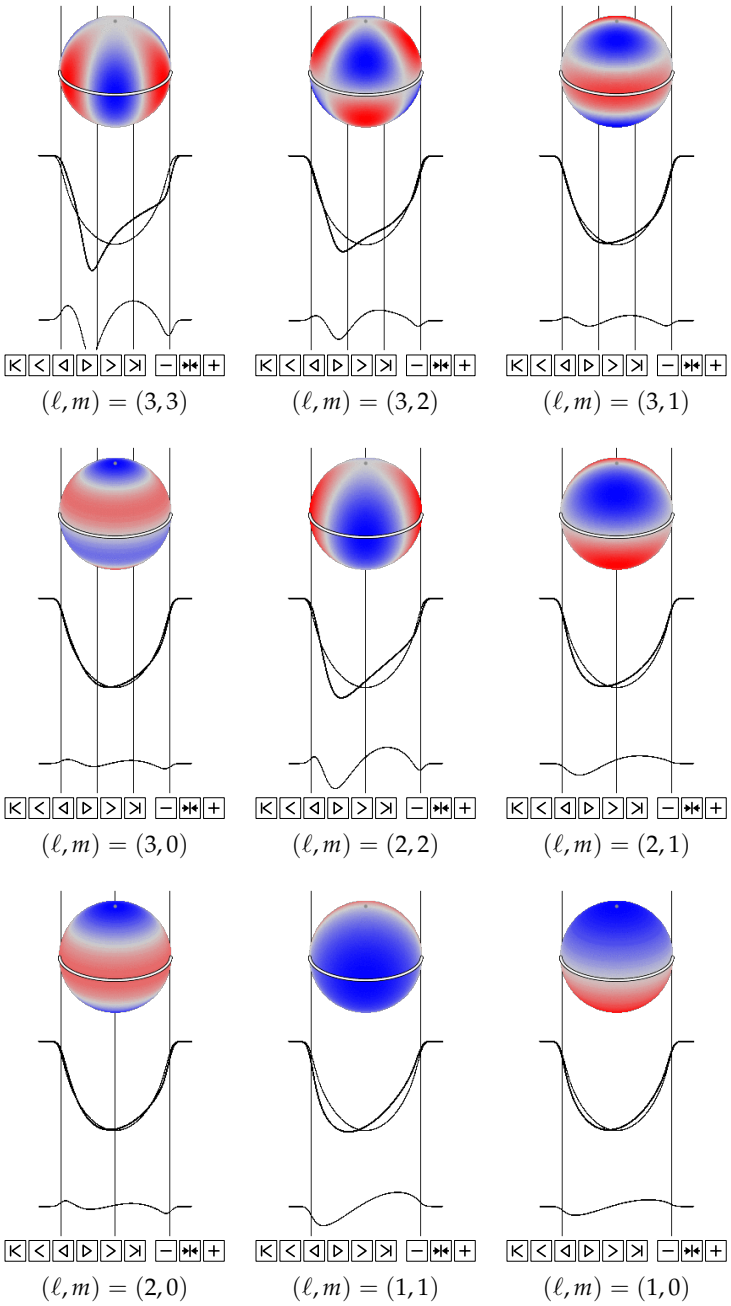

FIGURE 1.11: Models of pulsation modes courtesy of John Telting (http://staff.not.iac.es/~jht/science/nrpform/). The top panel shows the spherical harmonics mapped to the surface, the middle panel shows the distorted line profile in comparison to the at-rest Gaussian profile, and the lower panel shows the deviation from the at-rest profile. The same velocity amplitude is applied to each mode selection. In the electronic version of this thesis, the subfigures are animations playable in Adobe Acrobat Reader.

dwarf stars has allowed us to constrain the evolutionary theory of post-AGB stars (Jeffery, 2008).

The γ Doradus stars are interesting because the high-order g-modes they pulsate with propagate deep into the star, allowing us to probe large regions of their interior. Their position on the HR diagram – slightly hotter and more massive than our own Sun – gives them a similar overall structure to the Sun. Their outer convective envelopes are somewhat smaller, but they also have a convective core. In between the two inner and outer convective zones is the radiative zone, where the g-modes propagate. γ Doradus stars are in a unique position on the HR diagram, in the sense that there are no other stars of similar spectral types that show such deeply propagating pulsations. Thus it will be a very useful result of the emerging area of γ Doradus asteroseismology eventually to be able to accurately determine their internal conditions, such as the sizes of their convection zones and their internal rotation rates.

There are also observational reasons (and constraints) for choosing γ Doradus stars. One advantage is that their relatively long pulsation periods allow good spectroscopic investigations to be done. Since photometric mode identification can only discriminate the degree ℓ of a mode, and not the azimuthal order m, spectroscopic mode identifications allow a more complete study of the stellar interior. We are constrained to using only very bright stars for short-period targets such as δ Scuti stars, or else there is simply not enough time to get a good signal-to-noise spectrum before temporal blurring becomes too great. We can expose γ Doradus stars at Mount John University Observatory (MJUO) for 20 to 30 minutes, and the resultant exposure time is usually between about 1% and 4% of the pulsation period: an adequate temporal resolution.

The most significant observational constraint is also tied to these long periods: it is almost impossible to continuously observe a γ Doradus star through several pulsation phases from ground-based observatories. For this, excellent multi-site coverage and a good deal of luck with the weather are needed. As a result, aliasing is almost always a concern, and the data collection process is slow. Usually at least 300 spectra will be needed for a good analysis, and ideally more than 500. Considering how few high-resolution spectrographs there are in the world, combined with the huge demands on resources, it is easy to see why spectroscopic data of these stars are still lacking.

1.5.1 *The γ Doradus class*

The γ Doradus class is a relatively new class of variable stars, first defined in 1993 (Krisciunas, 1993). Two recent reviews (Kaye, 2007; Pollard, 2009) summarize our current knowledge of these stars, and describe the current and future observational and theoretical challenges that must be overcome. The prototypical member, γ Doradus (or HD27290), was observed to show photometric variations indicative of high radial order, low-degree, g-mode non-radial pulsations (Balona et al., 1994). γ Doradus pulsations are characterized by periods between 0.4 days and 3 days, with photometric

amplitudes up to 0.1 mag and spectroscopic radial velocity amplitudes up to several km s^{-1} (Guzik et al., 2000). They are late-A and early-F type, g-mode pulsators. The incidence rate of variability from photometric survey data suggests that up to about 22% of A7 to F5 type stars could exhibit γ Doradus-like pulsations (Henry et al., 2011).

1.5.2 *Fundamental parameters*

These stars are somewhat hotter than the Sun, and generally occupy a temperature range between 7200 K and 7700 K on the zero-age main sequence (ZAMS), and 6900 K to 7500 K one magnitude above the ZAMS (Handler, 1999). Typical masses are around 1.6 $M_\odot$ (Kaye et al., 1999). However, theoretical models by Warner et al. (2003) place a lower mass limit of 1.4 $M_\odot$ for a ZAMS model, to $\sim$ 1.9 $M_\odot$ for more evolved main-sequence models. Models that allow γ Doradus-like pulsations have been computed in pre-main sequence stars with masses up to 2.5 $M_\odot$ (Bouabid et al., 2010). Radii are only loosely constrained, though are usually between 1.4 $R_\odot$ and 2.4 $R_\odot$ (Kaye et al., 1999).

γ Doradus pulsations have been observed in both dwarf (V) and subgiant (IV) luminosity class stars (Henry et al., 2011). Figure 1.12 shows the distribution of $T_{\rm eff}$, $\log g$, $v \sin i$, and [M/H] from a spectroscopic analysis of Kepler-identified targets (Tkachenko et al., 2013). From this survey, it can be seen that γ Doradus stars are observable with $v \sin i$ values of tens or hundreds of km s^{-1}, tend to have $\log g \approx 4$, and are slightly metal poor. The more extreme values of $\log g$ ($\gtrapprox$ 4.5 or $\lessapprox$ 3.6) in Figure 1.12 are, with the exception of $\log g \approx 3.15$ and according to the polynomial relationships in Torres et al. (2010), generally consistent with the likely range of masses of γ Doradus stars. The $\log g$ variations do indicate significant variations in radii, between around 1.1 $R_\odot$ and 4.1 $R_\odot$.

1.5.3 *Excitation mechanism*

The most common driving mechanism for pulsating stars is the κ-mechanism, which is driven and self-perpetuated by opacity variations. In this mechanism, a particular radial layer(s) in the star gains heat on compression, while other layers lose heat and damp the pulsation (Aerts et al., 2010). This process functions as a heat engine. If on atmospheric compression there is a localized increase in opacity, the release of flux from the stellar interior is withheld. Layers of hydrogen and/or helium in a star's convection zone do just this, and when they are compressed and the opacity increases, the resultant build-up of heat and pressure forces the star's radius to increase. The increase in temperature and pressure ionizes the gas, which *reduces* its opacity. The build-up is relieved and the gas cools, so the star contracts and the gas recombines. The recombination increases opacity once again, therefore renewing the cycle.

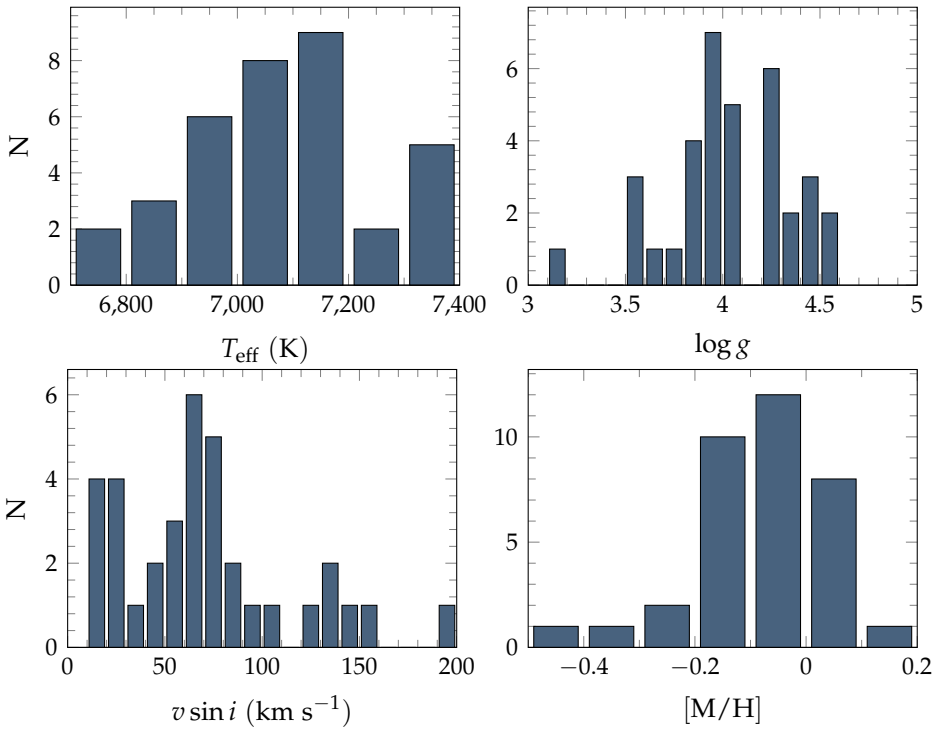

FIGURE 1.12: Fundamental parameter determinations (from spectroscopic methods) for 35 γ Doradus stars. Figure data are from Tkachenko et al. (2013).

The excitation mechanism of the γ Doradus class of stars varies slightly from this. Dupret et al. (2005) have used Time Dependent Convection models to confirm earlier proposals (Guzik et al., 2000) that a convective flux blocking mechanism (Pesnell, 1987) is the excitation mechanism of the pulsations. Convective flux blocking can be thought of as a variation of the classical opacity or κ-mechanism that drives stars such as the Cepheid and δ Scuti variables. The internal structure of γ Doradus stars is such that, because of their moderate masses, there exists a radiative zone in-between a convective core and a convective envelope. The pulsations in γ Doradus stars are driven from the base of this convection envelope (Guzik et al., 2000). Here, there is a very rapid transition between the interior radiative zone and the outer convection envelope (Pesnell, 1987). If fluctuations in the convective luminosity remain relatively unresponsive to periodic variations in radiative luminosity, there is a periodic blockage of radiative flux which drives the stellar pulsations. This is the driving mechanism for the g-modes observed in γ Doradus stars (Dupret et al., 2007; Guzik et al., 2000).

These g-modes propagate in the interior radiative zone, between the inner and outer convective zones. Thus, they are affected by the conditions at the boundaries between the radiative zone and the two convective zones.

1.5.4 *Current status*

There is currently a reasonably large amount of observational activity surrounding γ Doradus stars. The HIPPARCOS, CoRoT, MOST, and Kepler space-based telescopes have each proven valuable in the analysis of γ Doradus stars, by contributing multitudinous photometric data. HIPPARCOS data are generally not comprehensive enough to perform reliable identification of many frequencies, but it is still useful for finding candidates for further analysis – for example, Henry et al. (2011) used the HIPPARCOS photometry to select targets for performing ground-based photometry on selected candidates, confirming a further 15 γ Doradus stars. As of Henry et al. (2011), there were 86 confirmed γ Doradus stars.

The possible relationships (Handler and Shobbrook, 2002) between the g-mode γ Doradus pulsators and p-mode δ Scuti pulsators are still debated – the existence or prevalence of hybrid stars (those that exhibit both g-modes and p-modes) is not certain. δ Scuti stars show high-frequencu (about 4 d^{-1} to 80 d^{-1}) p-modes that are excited by the κ-mechanism, and their instability strip overlaps with the γ Doradus instability strip (see Figures 1.1 and 1.2). The possibility of hybrid stars is asteroseismically interesting, as the observation of p-modes allows us to probe the outer layers of a star. In combination with the deeper g-modes, we could gain more complete and accurate information on the stellar interior.

Many *candidate* hybrid stars have been discovered as a result of Kepler (Tkachenko et al., 2013), CoRoT (Hareter, 2012; Hareter et al., 2010), and MOST (King et al., 2006) satellite photometry. There is no theoretical reason why a hybrid star cannot exist

(Dupret et al., 2005) – they are even predicted (Bouabid et al., 2009). There are, however, a number of existing concerns about the current candidate hybrids. For example, hybrids found by Kepler do not appear to be well constrained to within the region of overlap between the δ Scuti and γ Doradus instability strips. These and other concerns are discussed and summarized by Brunsden (2013). In spite of the uncertain status of hybrid stars, the large number of space-based photometric results ensures that there is a good database of frequency data emerging for γ Doradus stars.

It should also be possible to use both space-based multicolour photometry and spectroscopic line profiles simultaneously during mode identification, as similar work for B-type stars has already been done (Daszyńska-Daszkiewicz et al., 2005).

Further goals in the field of observational asteroseismology of γ Doradus stars are simply to increase the quality and quantity of available data, particularly in the form of spectroscopic mode identifications. These data may then be used to inform and constrain theoretical models to help us better understand the interior structure and excitation mechanisms of these stars.

1.6 THESIS FORMAT AND GOALS

The primary goal of this thesis is to provide further spectroscopic mode identification data for three γ Doradus stars, HD139095, HD153580, and HD197541. A secondary goal (and future necessity) is accurately to estimate fundamental stellar parameters such as mass, radius, temperature, metallicity, and surface gravity.

The next chapter, Chapter 2, introduces the methods of data gathering and processing. The steps of obtaining and reducing spectra are explained, as well as methods of abundance analysis, frequency analysis, and mode identification. Chapters 3 to 5 contain the analysis of the individual stars HD153580, HD139095, and HD197541 respectively. Chapter 3 is the most comprehensive, and enters into some detail about the methods and limitations of analysis. The latter two chapters are slightly briefer in this regard, as the general methodology of analysis is similar where not otherwise mentioned.

Finally, Chapter 6 summarizes the thesis results and provides some thoughts for directions that future research could take.

2

OBSERVATIONS AND METHODS OF DATA PROCESSING

2.1 MOUNT JOHN UNIVERSITY OBSERVATORY

MJUO is the University of Canterbury's observatory, situated near the township of Tekapo in the South Island of New Zealand (see Figure 2.1). The observatory is situated at an elevation of 1029 m, at 170° 27.9′ E 43° 59.2′ S. Spectroscopic data have been gathered using the HERCULES spectrograph attached to the 1 m McLellan telescope. HERCULES is a fibre-fed échelle spectrograph, offering high efficiencies of between 10% and 15% at a typical seeing of 3″ (Barnes, 2004). The spectrograph has a resolving power of 41,000 when attached to the 100 μm diameter fibre (Hearnshaw et al., 2002). This fibre, used in the observations for this thesis, has an acceptance angle of 4.2″ (Hearnshaw, 2009). Such an angle allows for a good light throughput even in relatively poor seeing.

In early 2007, the spectrograph's CCD detector was upgraded to a Fairchild 486 model detector, with 4096 by 4096 pixels of 15 μm size and cooled to around $-100°C$. The new, larger CCD allows for observations over a wavelength range of 380 nm to 880 nm to be captured in a single exposure of a single chip (Hearnshaw et al., 2002). An Astrovid StellaCam provides continuous autoguiding. HERCULES is located in a well-insulated and temperature controlled room, at 20.0 ± 0.1 °C (Hearnshaw, 2009), in an evacuated tank at a pressure of around 3 mm Hg (0.004 atm). Thus the spectrograph is extremely stable.

FIGURE 2.1: The view looking north from the Observatory site at Mount John.

2.1.1 *Spectroscopic techniques and observations*

Data from MJUO in this thesis have been collected between 2009 and 2013, during the tenure of the MUSICIAN project. Many spectra were taken by other observers: much credit goes to Pam Kilmartin, Florian Maisonneuve, Emily Brunsden, and Matt Davie. Three candidate or bona fide γ Doradus stars were analysed from a large number of MJUO spectra, and chosen because they all showed line profile variations that were good for analysis. HD153580 and HD139095 each had over 300 existing spectra yet were not yet studied in detail. HD197541 was also chosen owing to its strong line profile variations, moderately low $v \sin i$, and relatively non-blended spectral lines. Most of the spectra for the analysis of HD197541 were taken during the course of the thesis. The dates of observations[1] of the three stars analysed, HD153580, HD139095, and HD197541, are detailed in Table 2.1 and Figure 2.2.

Exposure times used were dependent on the current seeing conditions and magnitude of the star, but usually were 20 minutes (though occasionally 30 minutes) for

1 One observation of HD197541 by Karen Pollard in November 2007 has been omitted from the date ranges in Table 2.1 and Figure 2.2, to avoid misrepresenting the effective temporal range of observations.

TABLE 2.1: The date ranges of the MJUO observations for the three stars analysed in this thesis.

Star	m_V	Typical exp. time	No. of spectra	Date range	JD range (JD − 2 450 000)	Observers [a]
HD139095	7.91	30 min	348	Feb 2009 – Feb 2013	54876 – 56170	EJB, FM, MWD, PMK
HD153580	5.28	20 min	333	Jun 2009 – Aug 2012	55002 – 56170	MWD, PMK
HD197541	6.78	20 min	312	Jun 2009 – Oct 2012	54999 – 56578	AJG, PMK

[a] The observers were: Aaron Greenwood (AJG), Emily Brunsden (EJB), Florian Maisonneuve (FM), Matt Davie (MWD), and Pam Kilmartin (PMK).

HD153580 ($m_V = 5.28$) and HD197541 ($m_V = 6.78$), and 30 minutes for HD139095 ($m_V = 7.91$). About every hour during observing a thorium-argon lamp spectrum was taken for wavelength calibration. Either at the beginning or end of a night, flat field images with a white tungsten lamp were taken. The flat field images were exposed for 1 second, and the thorium-argon images for several seconds. A useful guide is to expose the flat fields such that the 16-bit depth of the CCD is around two thirds saturated, and to expose the thorium-argon images so that the photomultiplier tube reads between 3 and 4 million counts. The brightness of the thorium-argon lamp depends on both the input current (set each night with an analogue dial), and on the lamp in place at that particular time (which must be replaced from time to time). Therefore, using the photomultiplier tube gives the best reliability for obtaining a reasonably consistent exposure. Figures A.1 and A.2 show examples of the raw spectrum images obtained.

At some stage during the night, a few high signal-to-noise spectra of a radial velocity standard star were obtained (β Lep and β Oph were the desirable targets, depending on the time of year). These radial velocity calibration spectra were not used, but were taken in case some wavelength calibration issues or radial velocity anomalies arose.

2.2 HIPPARCOS PHOTOMETRY

The HIPPARCOS satellite produced a large catalogue of astrometric and single-channel photometric data (Perryman et al., 1997). Although the single-channel nature of the data precludes any asteroseismic mode identification, the data are still a useful tool for frequency identification. HIPPARCOS photometry data from HD139095, HD153580, and HD197541 are therefore used in tandem with analysis of the spectroscopic data in order to detect and assess the significance of pulsation frequencies.

2.3 THE SPECTROSCOPIC DATA REDUCTION PROCESS

This thesis makes use of both the MATLAB data reduction pipeline, written by Dr. Duncan Wright, for all data gathered at MJUO, and the data processing codes written by Wright and Dr. Emily Brunsden. Although the reduction algorithms remain unchanged (in practice) with regards to their mathematical function, the code's usability and resistance to errors has been improved by the author. In particular, the changes now allow for the reduction to draw data directly from the servers without having manually to collate the relevant nights of data, as well as improved handling of the thorium-argon and flat field images that includes checks to query any anomalous images. MATLAB remained the programming language of choice for all analyses, except where non-original code was used.

2.3.1 *Configuration*

The MATLAB data reduction process is controlled by a script called `config.m`. This script contains all of the user-configurable options of the reduction routine and writes these options to a temporary directory where they are later read as required by subsequent functions.

MJUO data is archived on the Department of Physics and Astronomy servers at the University of Canterbury. A catalogue of all the spectra obtained is created and sorted by object. Because object names are entered manually into the FITS headers, a functionality exists to account for the slight spelling and syntax variations between the object names that each observer may use – for example, the duplicates 'bet_oph' and 'Bet Oph' will be automatically resolved. The script `config.m` uses the secure network file transfer protocol `sshfs` to access FITS files on the remote disk as they are requested, which makes this code reasonably portable. A check is also done to ensure that the barycentric correction module, the C code `barycorr_HRSP` from the Hercules Reduction Software Package (Skuljan, 2004), has been compiled and runs correctly on the current machine.

Now that the location of each spectrum file of a star is known, the script then proceeds to reduce the data on a 'run-by-run' basis. In some earlier observing runs (during 2011 or earlier), sufficient numbers of flat field frames were not taken on a nightly basis. This has necessitated combining the flat field frames from several nights together for use in reducing the stellar images of that respective time period. In later observations (from May 2011 onwards), sufficient numbers of flat field frames (usually ten) have been taken nightly, such that for recent observations an observing 'run' may consist of only a single night. In the case where multi-day runs are required, it is currently necessary to manually compile an index of the dates to use for each 'run'. In the framework of the reduction code, the definition of a run is the date(s) across which the flat field frames are combined.

2.3.2 *Flat field processing*

During the processing of each run, the first step is to reduce the flat field images using the script `flat_processing.m`. The flat field images are summed together, whilst running a statistical comparison that makes sure there are no significant differences between the images. The first 1000 rows of the CCD, at the blue end of the chip, are too noisy to be useful and are removed once the FITS data are read into memory. The result is a summed flat field image. By using the flat field image as a guide, the remaining spectral orders are traced, which provides a reference axis for locating each order on stellar and thorium-argon images. Although flat field exposure times are in most cases only 1 second, cosmic rays are still possible so cosmic ray removal is performed. The

other function of the flat field images is to correct for the intensity response of the CCD, which is non-uniform along both axes.

The output of the flat field processing stage is that for each night, a reference structure is obtained which tracks the location of each spectral order on the CCD. Also given are the corresponding flat-field intensity values at each pixel, which are later used to normalize against the non-uniform response of the CCD.

2.3.3 *Thorium-argon processing*

Next, the thorium-argon arc lamp images taken before and after each stellar spectrum are processed using the script `processing_all_ThArs.m`. Once again a statistical check is carried out to ensure that there are no significant pixel-to-pixel deviations between the images. Some images are affected by readout problems or user errors that could result in a poor wavelength calibration, so these images can be rejected at this stage. The arc lines on each of these images are located using a pre-existing calibration matrix as a starting point. If too few arc lines are identified the user is queried to ensure that the initial calibration matrix was a good approximation. If the HERCULES vacuum chamber has been opened or evacuated since the last calibration matrix was created, this can cause some shifts in the orders on the CCD and thus a new calibration must be performed and saved. The new calibration is applied to any subsequent observations, from then until the time of the next calibration.

By tracing the thorium-argon orders along the axes defined by the flat fields and using the locations of the spectral lines used for wavelength calibration, a full set of wavelength-calibrated axes is obtained along which the stellar orders can be traced.

2.3.4 *Stellar image processing*

Using the script called `processing_all_stellar_images.m`, the spectral orders of each wavelength-calibrated stellar image are then extracted. Cosmic ray removal is performed and the intensity data along each order are then saved as MATLAB matrices for later use in the data processing stages. The main control script, `config.m`, also provides the option to write these data to plain text (ASCII) files, which can then be distributed to others who wish to obtain wavelength-calibrated data in an accessible format.

2.3.5 *Processing the wavelength-calibrated stellar spectra*

Once the individual spectral orders have been reduced to wavelength-calibrated arrays, there still remains the task of merging the spectral orders and continuum fitting the data. The scripts for these processes were co-written by Duncan Wright and Emily

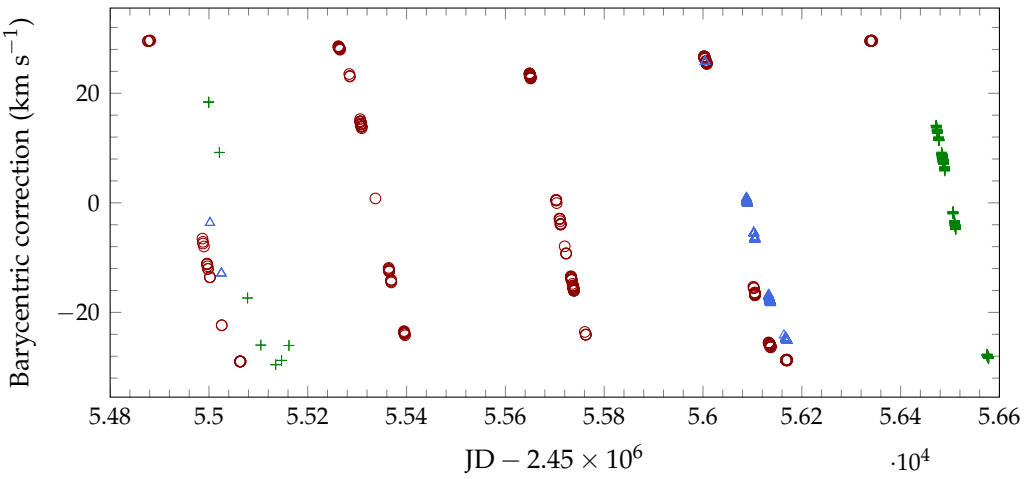

FIGURE 2.2: Julian dates and barycentric correction values for HD139095 (circles), HD153580 (triangles), and HD197541 (plusses).

Brunsden (Brunsden, 2013; Wright, 2008), with some subsequent usability enhancements carried out during this thesis. Individual subroutines are called by the controller script, `Begin_processing.m`. The first step is to merge the orders of each observation onto a common wavelength scale. Barycentric correction is performed at this stage, using the barycentric correction values computed during reduction by `barycorr_HRSP` (Skuljan, 2004). Figure 2.2 shows the annual cycle of the barycentric correction values for the three targets observed and analysed in this thesis.

Order-to-order differences are then removed, and the wavelength axes of each order are corrected for the radial velocity shift of the star. If no radial velocity shift is available in the literature, the location of the centroid of the cross-correlated line profiles with a radial velocity of 0 km s^{-1} gives a good estimate. Next, a manual continuum fitting process is carried out by comparing the observed mean spectrum with a synthetic spectrum generated by the program Synspec. Synspec is a FORTRAN code that is used to calculate a synthetic spectrum from an ATLAS9 model atmosphere and given temperature, metallicity, and surface gravity (Hubeny and Lanz, 2011; Zboril, 1996). A spline interpolation is carried out between manually-defined continuum points on the observed spectrum, to produce a smooth function. Each stellar spectrum is then divided by the continuum fitting function, which normalizes the mean stellar spectrum in order to match it as closely as possible to the synthetic spectrum. Figure 2.4 shows the pre- and post-continuum-fitted mean stellar spectrum, along with the manually defined continuum function and the synthetic spectrum. A final cosmic ray removal process is carried out, then the orders are merged to produce the final wavelength-calibrated and normalized stellar spectra. Figure 2.3 shows the mean spectrum of HD139095 once the hydrogen and telluric regions have been removed.

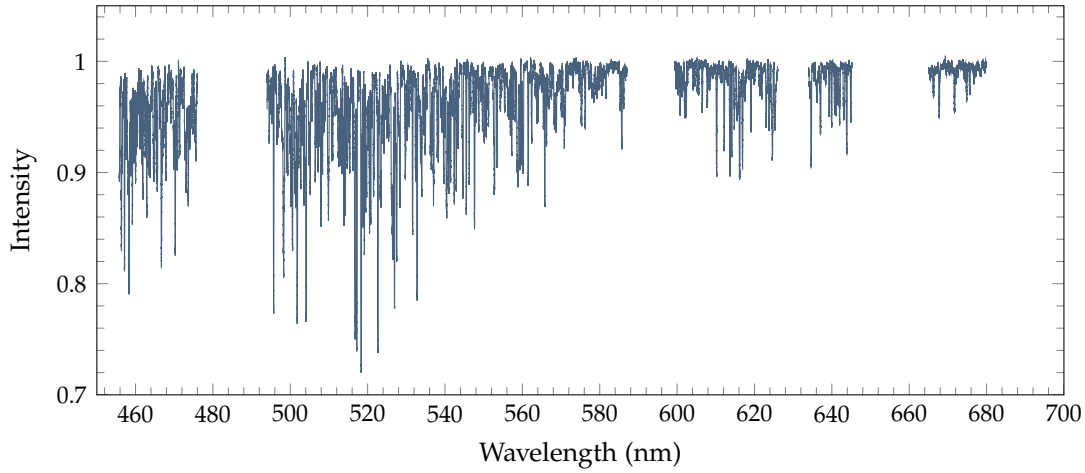

FIGURE 2.3: The mean spectrum of HD139095, with the hydrogen and telluric regions removed.

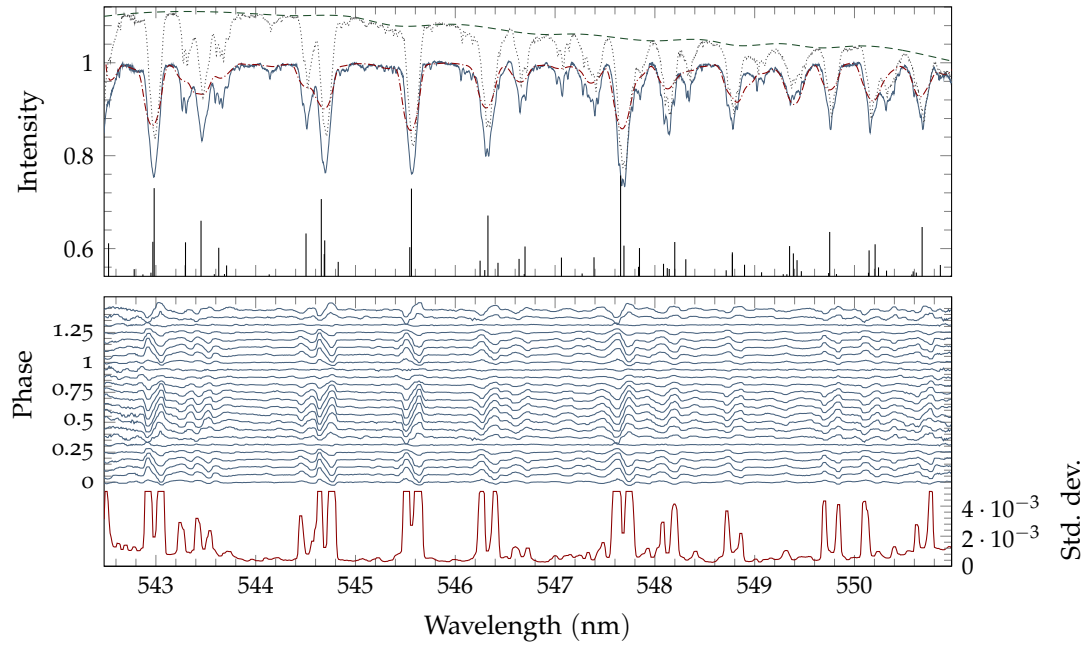

FIGURE 2.4: Spectral order 104 of HD153580, showing various features of the data reduction process. In order from top to bottom, the data in the upper axis are: the continuum-fitting function (dashed), mean stellar spectrum before continuum fitting (dotted), synthetic spectrum (dash-dotted), continuum fitted mean stellar spectrum (solid), and the cross-correlation delta functions (vertical solid lines, arbitrarily scaled onto the intensity axis). In the lower axis, deviations from the mean stellar spectum are shown phased and binned to $f_1 = 0.6589\ \mathrm{d}^{-1}$ (with noise reduction applied), while below is plotted the standard deviation from the mean stellar spectrum. The amplitudes of the standard deviations are artificially capped to keep the figure compact.

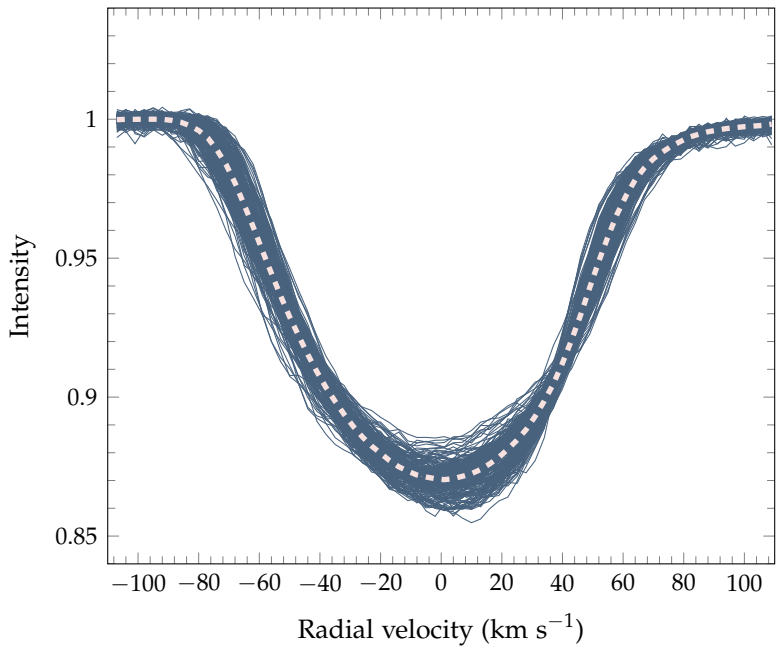

FIGURE 2.5: Cross-correlated radial velocity line profiles of HD139095, along with the mean line profile (dashed, bold line).

The final step is to produce cross-correlated line profiles. By cross-correlating many spectral lines, there is a substantial increase in the signal-to-noise ratio (in comparison to analysing a single line), while periodic line profile variations are preserved under the assumption that all cross-correlated lines are congruously distorted. The cross-correlation process uses the δ-function method developed by Wright (2008). A template of δ-functions is created from a spectral line list, with an equivalent width cut-off to remove weak lines with (non rotationally-broadened) equivalent widths less than 0.5 m (0.05 pm); leaving approximately 1500 lines. The δ-functions of each spectral line are scaled to their equivalent widths.

The δ-functions are rotationally broadened by the star's $v \sin i$, using the rotational broadening function of Gray (2005). A least-squares fitting analysis between the broadened delta functions and the mean stellar spectrum is performed in order to fine tune the amplitudes of each δ-function. Using the MATLAB function `xcorr`, the δ-function template is cross-correlated with the spectral lines in each stellar spectrum. After cross-correlation, the resultant cross-correlated profiles are interpolated onto a common radial velocity axis. This produces a cross-correlated representative line profile for each observation, such as in Figure 2.5.

2.4 ABUNDANCE ANALYSIS

Better defining the fundamental parameters of these stars is an important step before the integration of mode identifications with theoretical models. An abundance analysis was carried out on two of the three γ Doradus stars in this thesis, HD139095 and HD197541. Since the spectrum of HD153580 is contaminated by a dimmer companion star, the two components need to be deconvolved prior to an abundance analysis. For this reason, an abundance analysis of HD153580 was not carried out. Two methods of abundance analysis were tested; the well-proven equivalent width method, and a spectrum synthesis method.

2.4.1 *Abundance analysis by equivalent widths*

One well-proven and standard method of performing abundance analysis is to measure the equivalent widths of metallic spectral lines and then use these in combination with model atmospheres to derive stellar parameters and photospheric abundances. Here, two different approaches were used, both using a line list compiled by Davie (2013). The first method used the code ARES (Sousa et al., 2007), an automatic equivalent width-fitting routine written in C. The second method of equivalent width measurement was to use SPECTRE (Fitzpatrick and Sneden, 1987), a manual process of fitting Gaussians to each spectral line. This latter method proved more reliable, chiefly because the manual process allowed strongly blended, weak, or noisy lines to be heuristically removed.

The traditional equivalent width method was tried on HD139095 under the premise that a $v \sin i$ of around 60 km s^{-1} was not too great for this method to work satisfactorily. HD197541 provides a higher signal-to-noise spectrum with narrower spectral lines, making equivalent width measurements easier. However, Bruntt et al. (2008) report that (using their own spectrum synthesis code, VWA) their spectral synthesis methods for abundance analysis are unable to constrain $T_{\rm eff}$, $\log g$, and $v_{\rm mic}$ simultaneously for stars with $v \sin i > 50$ km s^{-1}. Thus, caution is still necessary here as the same limitations may well apply to the equivalent width method.

The advantage of the ARES code is that it is fully automatic. However, with the relatively noisy spectra of HD139095, the results were found to be unreliable. The program was run in two different ways. It was run on each stellar spectrum in turn and then on a mean spectrum. This produced relatively poor results for HD139095 in each case: some lines were poorly detected and the overall results did not correlate well with manual measurements. Figure 2.6 shows how the ARES per-spectrum equivalent width results are significantly lower than the ARES results from a mean spectrum. Even though ARES incorporates noise smoothing, it mistakes noise elements in the spectrum for spectral lines. The mean spectrum ARES results also correlate poorly with the manually-measured SPECTRE equivalent widths. Clearly, manually measuring the

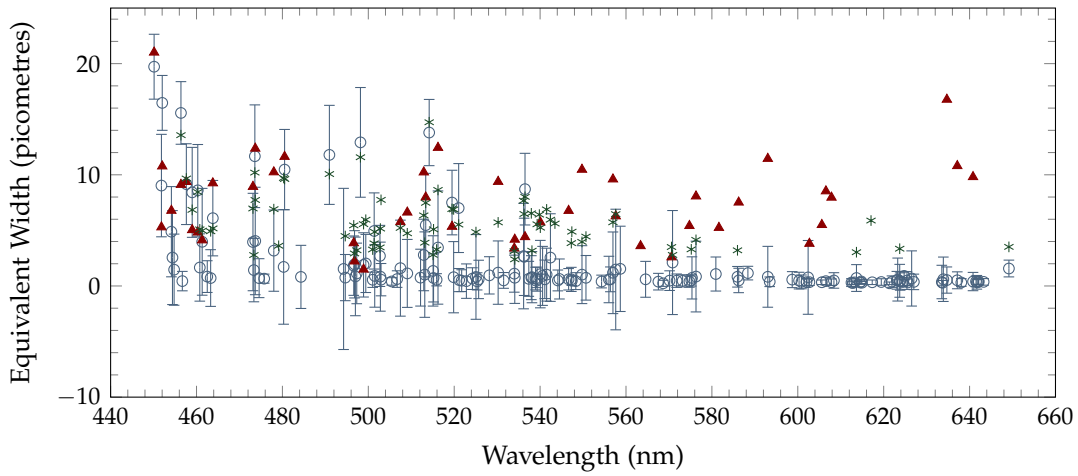

FIGURE 2.6: The equivalent width measurements of Fe I and Fe II lines for HD139095: the blue circles are the automatic per-spectrum ARES results with standard deviation error bars, the red triangles are the manual results from SPECTRE, and the green asterisks are a mean-spectrum result from ARES.

equivalent widths is the more reliable method. Manual equivalent width measurements from SPECTRE are used in the results of this thesis.

Abundance analysis was performed in an iterative, least-squares manner. The code FUNDPAR (Saffe, 2011) was used for this purpose, which acts as a driver for MOOG (Sneden, 1973) and the Linux port[2] of R. L. Kurucz's ATLAS9 code (Sbordone et al., 2004). FUNDPAR uses the line list along with the measured equivalent widths to perform a least-squares, iterative process to converge to solutions for $T_{\rm eff}$, $\log g$, and [Fe/H]. Model atmospheres are computed on demand using ATLAS9 and fed into MOOG to remove the correlations between the excitation potential and reduced equivalent width using LTE line analysis. It is important at this stage to ensure that there is no correlation between the excitation potential and reduced equivalent width, or it becomes impossible to converge to a solution. To converge to a good result, only solutions for the Fe I lines were included in the χ^2 parameters. This may be done by modifying the weight factors in the `fundpar.par` parameter file. The significant levels of line blending mean that far too few Fe II lines could be found.

2 The code for the Linux port of ATLAS9 was obtained from `http://spectra.astro.uni.wroc.pl/code.php`. Note that on line 514 of `atlas9mem_newodf.for`, the variable `itration` should be changed to `iteration`, or ATLAS9 will become stuck in an infinite loop if it cannot converge sufficiently. The ODF and Kappa Rosseland coefficients were obtained from `http://wwwuser.oat.ts.astro.it/castelli/` (Castelli and Kurucz, 2004).

2.4.2 *Abundance analysis by spectral synthesis*

The method of performing abundance analysis by LTE spectrum synthesis promises the possibility of greater reliability for faster rotators since line blending is of much less concern. Additionally, in the case of HD197541, it was found that a significant level of macroturbulence may explain the observed shape of the line profiles, which are abnormally deep with respect to the literature $v \sin i$ value.

The spectral synthesis method of abundance analysis uses the program Spectroscopy Made Easy (SME) (Valenti and Piskunov, 1996). SME calculates a synthetic spectrum for the star from a comprehensive VALD spectral line list (Kupka et al., 2000) and can account for different abundances in individual elements, microturbulence, macroturbulence, and the instrumental profile – the parameter space is fully customizable and is not limited to solving for temperature, gravity, and metallicity. For spectral synthesis, SME uses precomputed ATLAS9 model atmosphere grids. In practice the disadvantages of interpolating the atmospheric grids compared to generating them from the ATLAS9 source (such as FUNDPAR does) are negligible. Valenti and Piskunov (1996) report that their bicubic spline interpolation between $T_{\rm eff}$, $\log g$, and [Fe/H] achieves a fractional precision of 10^{-4}. Since over 90 per cent of SME compute time is spent in spectrum synthesis (Valenti and Fischer, 2005), its use of atmospheric interpolation is a good approximation that provides a useful speed boost.

2.5 LINE PROFILE VARIABILITY ANALYSIS

2.5.1 *Frequency identification*

The first challenge is to identify the pulsation frequencies of the stars: their identification is often complicated by the presence of aliasing. Two programs, SIGSPEC (Reegen, 2011) and FAMIAS (Zima, 2008a), are used in tandem to identify the most likely frequencies of pulsation. The analysis is performed on the set of cross-correlated radial velocity line profiles obtained for each star.

SIGSPEC is used to perform a temporal analysis of each pixel of the stellar line profile by computing Lomb-Scargle periodograms. Compared to FAMIAS, it is more sophisticated in its frequency identification methods as it contains some algorithms to reduce the number of false detections. When combining the temporal analysis results across the pixels of the line profile, SIGSPEC is regarded as having superior frequency detection to FAMIAS due to its false-alarm probability algorithm.

FAMIAS, on the other hand, can produce a straightforward Lomb-Scargle periodogram that is the mean result of each individual pixel across the line profile. The highest-peak frequency is then removed through pre-whitening and the periodogram is computed again on the residuals (see Figure 2.7). Although relatively quick, this method is more prone to detecting false frequencies. FAMIAS can also use the Moment Method (Aerts,

1996; Balona, 1986; Briquet and Aerts, 2003) to find frequencies in the various moments of the line profile (the equivalent width, radial velocity, variance, and skewness moments).

Both SIGSPEC and FAMIAS can be used to do a Fourier periodogram analysis of the one-dimensional HIPPARCOS datasets. Although the HIPPARCOS data suffer from a relatively low number of data points, the long timebase and comparatively even sampling can add additional credence to any frequencies that are detected, both photometrically as well as spectroscopically.

2.5.2 SIGSPEC *frequency determination*

SIGSPEC uses a quantity called spectral significance to refine frequency determinations. Instead of the simple step-by-step frequency pre-whitening routine followed when using FAMIAS, SIGSPEC will examine several stages of pre-whitening simultaneously in an attempt to remove alias frequencies. It calculates the spectral significance (sig) of an amplitude A (at a particular frequency) as:

$$\mathrm{sig}(A) = -\log_{10}[\Phi_{\mathrm{FA}}(A)] \tag{2.1}$$

where Φ_{FA} is the so-called False-Alarm Probability, which is the probability that a frequency peak could have been generated by white noise. Thus, a significance of 4 means that the false-alarm probability is 10^{-4}. Kallinger et al. (2008) find that an error upper limit of

$$\sigma(f) = \frac{1}{T\sqrt{\mathrm{sig}}}, \tag{2.2}$$

from an observation time base T, satisfies all but 13 out of ∼50,000 numerically determined frequency errors in a synthetic trial. In the case where a *second* frequency peak is present within around $3T^{-1}$, and sig > 16, the upper limit becomes $\sigma(f) = 1/(4T)$. By using SIGSPEC to analyse each pixel of the line profile to produce a cumulative frequency analysis, we can use those results in combination with an error estimate to assess the likelihood that each frequency is significant. Normally a significance level of 4 would provide an excellent level of certainty, but SIGSPEC's significance results must be treated with caution as noise and observational errors mean that greater significance levels are required in practice.

Due to the relatively long timebase of observations, and the uneven sampling, the influence of T becomes a significant factor. However, it is not reasonable to expect that a few outlier observations which notably expand the timebase T will correspondingly decrease the frequency error. It is thus proposed that a better (at the risk of error overestimation) timebase calculation will ignore any large gaps such as those of several weeks or months between observing runs, and instead only count the nights during which observations were taken towards the timebase T.

2.5.3 FAMIAS *frequency determination*

Frequency determination in FAMIAS simply follows selection of the highest peak of the Lomb-Scargle periodogram. Pre-whitening routines remove each successive peak frequency, and the periodogram is computed again on the residuals. A mean Fourier periodogram is produced from the individual periodograms of each pixel across the line profile. Taking the mean periodogram gives a good assurance that significant peaks are not simply the chance result of white noise. Figure 2.7 shows this process. However, since there are no measures in place to detect alias frequencies, their possible presence must be carefully considered when selecting frequencies using this method.[3]

An estimate for the frequency errors from FAMIAS results can be drawn from Montgomery and Odonoghue (1999), who propose that

$$\sigma(f) = \sqrt{\frac{6}{N}} \frac{1}{\pi T} \frac{\sigma(m)}{A}, \tag{2.3}$$

where N is the number of observations, $\sigma(m)$ is the rms deviation of the noise, and A is the amplitude. This returns $\sigma(f)$ as a one standard deviation uncertainty. Again, the limitations on the timebase T here are the same as that for the uncertainty relation for SIGSPEC frequencies.

2.5.4 *Frequency selection*

To be selected as a reliable pulsation, a frequency should have been identified in the pixel-by-pixel methods using both SIGSPEC and FAMIAS. FAMIAS computes a least-squares fit to the data of a sum of the sinusoids of the chosen frequencies. This is done either pixel-by-pixel across the line profile or for the line moments. The fitting formula (Zima, 2008b) is

$$y_i = Z + \sum_i A_i \sin\left[2\pi \left(F_i t + \phi_i\right)\right]. \tag{2.4}$$

where Z is the zero point,[4] and A_i, F_i, and ϕ_i are the amplitude, frequency, and phase of the i^{th} fitted frequency. A Levenberg-Marquardt least-squares algorithm optimizes the amplitude and phase of the fitted frequencies. For a one-dimensional data set (i.e. using the moment method), the frequency itself can also be optimized. It is these optimized values that are also used to pre-whiten data sets during the frequency selection stage.

3 In presenting these periodograms on paper, the number of data points has been significantly reduced in order to optimize file size and PDF viewer performance. There is some loss of density and fine detail; however, any significant peaks are preserved. The physical scale of the y-axis across sub-plots is always conserved, which aids visual comparison (that is, if the gap between 0 and 0.5 is 1 cm, it remains 1 cm in each sub-plot of the figure).

4 The zero-point line profile is the 'at rest' mean line profile – that is, it is the shape of the line profile in the absence of any *phase-dependent* effects of the pulsations. Note that pulsational broadening is still applied.

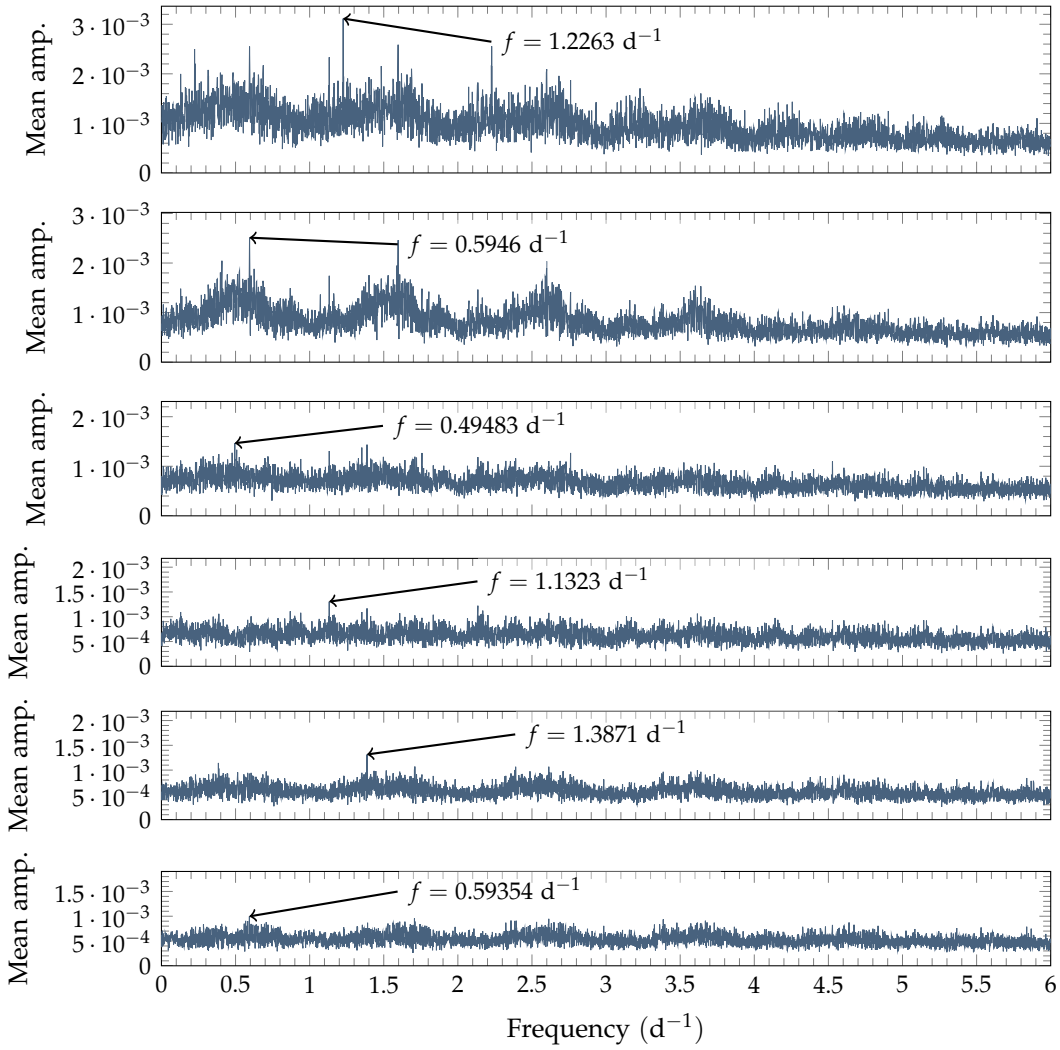

FIGURE 2.7: The pixel-by-pixel mean Fourier periodograms for HD139095 from FAMIAS, illustrating the progressive removal of the highest detected frequency peaks.

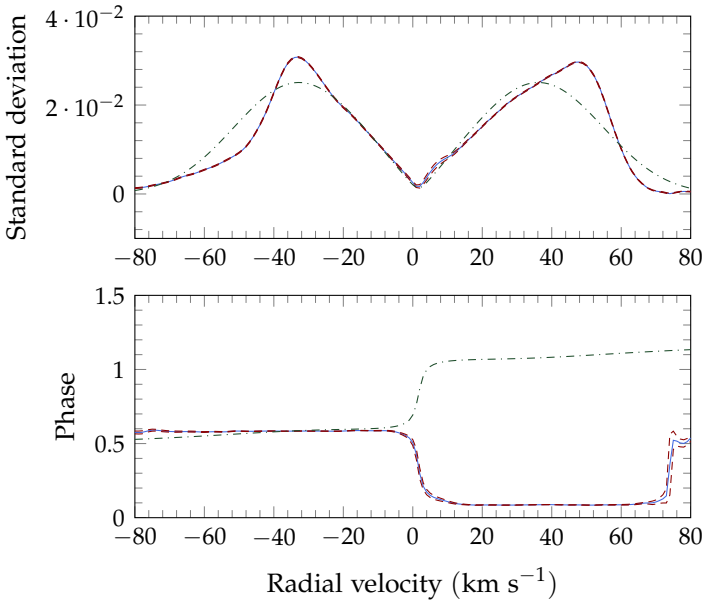

FIGURE 2.8: The least-squares fit at frequency $f_1 = 0.6589$ d^{-1} for HD153580. The solid lines indicate the amplitude and phase fits, while the dashed lines indicate uncertainties. The dash-dotted line is a $(\ell, m) = (2, -1)$ fit to the profiles.

The combination of all likely frequencies should remove the majority of observed variations in the line profile – that is, the least-squares fits (across the line profile) of the selected frequency set should adequately predict the shape of the overall line profile at any point in time. The frequencies should also be independent of one another: as each frequency is added to, or removed from, the least-squares fit, the shapes of the standard deviation and phase fits for each frequency should not significantly change. If adding a frequency causes another to disappear, then one is most likely to be an alias. Figure 2.8 shows the general form of the amplitude and phase fits across the line profile. Sometimes, as seen in this figure, the modelled phase transitions can deviate in the opposite direction to the observations. The difference between phase transitions of -0.5π and $+0.5\pi$ is merely a mathematical quirk, and is of no real significance.

Thus a criterion can be developed to describe how much of the observed line profile variations are cumulatively explained by a series of proposed frequencies. If the prior criteria are satisfied and a significant portion of the line profile variations is explained by the cumulative least-squares fits of the chosen frequencies, then they can be determined as reliable pulsation frequencies.

2.5.5 *Mode identification*

Mode identification was carried out using the Fourier Parameter Fit (FPF) method in FAMIAS (Zima, 2006). Wright (2008) determined that for $v \sin i \gtrsim 30$ km s^{-1}, the FPF method is superior to the Moment Method for mode identification. However, the lesser computational cost of the Moment Method means that it can still be a useful tool to constrain the degree ℓ of a mode. FAMIAS has been specifically written to analyse p-mode non-radial pulsations and, when used carefully, it is appropriate for the analysis of γ Doradus stars (Brunsden, 2013), which pulsate with g-modes.

The FPF method

The Fourier Parameter Fit (FPF) method in FAMIAS builds upon the pixel-by-pixel method by Mantegazza (2000). The method relies upon the fact that for a given pulsation mode, each pixel across the line profile should vary in flux with the same period. It computes synthetic line profiles for a variety of pulsation modes and stellar parameters, and uses a genetic algorithm to search the parameter space until the best-fit parameters are found, as determined by minimizing the χ^2 of each fit. The χ^2 values reported by FAMIAS are *reduced* χ^2, that is, the χ^2 has been divided by the estimated number of free parameters. Although a statistically significant result is usually where $\chi^2 \approx 1$, in practice the χ^2 values are usually much higher because of the imperfect fitting of the amplitude and phase.

The Moment Method

The Moment Method can be interpreted as the time-series analysis of a single property of the line profile such as the equivalent width: it produces a one-dimensional dataset. It relies on the fact that a line profile could be fully reconstructed from an infinite series of moments and the first few moments provide an excellent approximation of the line profile while each moment retains a strong signal-to-noise ratio. It has proven to be best in identifying low-degree modes ($l \leq 4$) of relatively slow rotators where $v \sin i \leq 50$ km s^{-1} (Aerts et al., 2010). Following Aerts et al., a line profile $p \equiv (f * g)(v)$ is the convolution between an intrinsic profile $g(v)$ and the flux profile from the observer's point of view, $f(v)$. Given these, the nth moment of the line profile is

$$\langle v^n \rangle_{f*g} \equiv \frac{\int_{-\infty}^{\infty} v^j p(v)\, \mathrm{d}v}{\int_{-\infty}^{\infty} p(v)\, \mathrm{d}v} = \frac{\int_{-\infty}^{\infty} v^j (f * g)(v)\, \mathrm{d}v}{\int_{-\infty}^{\infty} (f * g)(v)\, \mathrm{d}v} \tag{2.5}$$

where v is the *total* (pulsation plus rotation) velocity field in the line of sight (Aerts et al., 2010). The first three moments represent specific properties of the line profile. The zeroth moment, $\langle v^0 \rangle$, is the equivalent width of the line profile. The first moment $\langle v^1 \rangle$ is the centroid of the line profile, such that it can measure any radial velocity

variations of the centroid. The second moment $\langle v^2 \rangle$ is the width of the line profile, and the third moment $\langle v^3 \rangle$ measures the skewness. FAMIAS can also compute the 4^{th}, 5^{th}, and 6^{th} moments: for line profiles that remain relatively Gaussian, these moments become combinations of the first moments. Typically only the first, second, and third moments provide useful information for mode identification and the signal of the higher moments can be buried in noise (Aerts, 1996; Aerts et al., 1992). For these reasons, the higher moments are not analysed.

Limitations

The current mode identification techniques in FAMIAS are not without their limitations. The rotational effects that are modelled are limited to first-order Coriolis terms, which may be insufficient for the mode identification of rapidly rotating stars. The addition of the Coriolis correction results in one spherical and two toroidal terms being used to describe the amplitude displacement field across the stellar surface. These terms, described in Zima (2008b), have been derived from Martens and Smeyers (1982), Aerts and Waelkens (1993), and Schrijvers et al. (1997). The fact that pulsation periods are often similar to the rotation period of the star introduces further complications: Section1.2.5 outlines some of the effects and imposed limitations of rotation.

Mode identification

To begin mode identification in FAMIAS, a set of *fixed* stellar parameters is required: T_{eff}, $\log g$, [Fe/H] and the central wavelength. The central wavelength determines the limb darkening coefficients which can slightly affect $v \sin i$ and the intrinsic width of the line profile (Zima, 2008b). Limb darkening is generally negligible for mode identification, so when using cross-correlated line profiles we use the mean wavelength of the cross-correlated range. A zero-point fit is then computed, which determines the $v \sin i$, equivalent width, intrinsic width, and velocity offset of the zero-point line profile. This is a very fast computation which reduces the parameter space by predetermining and fixing the factors that shape the line profile. Figure 2.9 shows an example of the computed zero-point fit.

The final, and by far the most time consuming step, is to proceed with identifying the pulsation modes that correspond to the previously determined frequencies. Further free parameters introduced are radius, mass, inclination, the degree ℓ, and azimuthal order m of each mode. The resolution of the computations is determined by the 'No. of segments' parameter, which describes how many segments the surface area of the star is broken up into for modelling. Computation time scales linearly with this, and is usually set at around 5,000 for a balance between speed and accuracy. The number of models per iteration and the convergence speed are also adjusted in accordance with the size of the parameter space. The fitting proceeds by computing the standard deviation and phase profiles for an assortment of models within the parame-

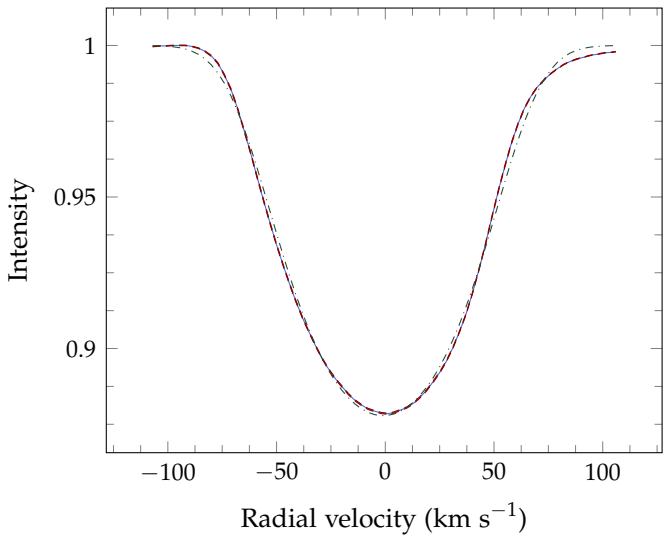

FIGURE 2.9: A zero-point fit to the mean line profile of HD139095. The solid lines indicate mean line profile, with dashed uncertainty (which is materially equal to the mean). The dash-dotted line is the zero-point fit to the profile.

ter space and gradually converging to a best-fit solution. Having fitted the line profile previously, this is excluded from the final mode identification process to speed up the analysis and prevent it from affecting the χ^2 values. Figure 2.8 shows an example of a best-fitted pulsation mode.

Careful consideration of a model's physicality is needed during the identification process. For example, inclination values that place the star within the Keplerian breakup limit are unphysical. FAMIAS is also capable of fitting a prograde pulsation mode with a period longer than the rotational period of the star, which is physically impossible (by definition, such a mode would be retrograde). In Section 1.2.5, some further constraints and consequences of rotation were discussed.

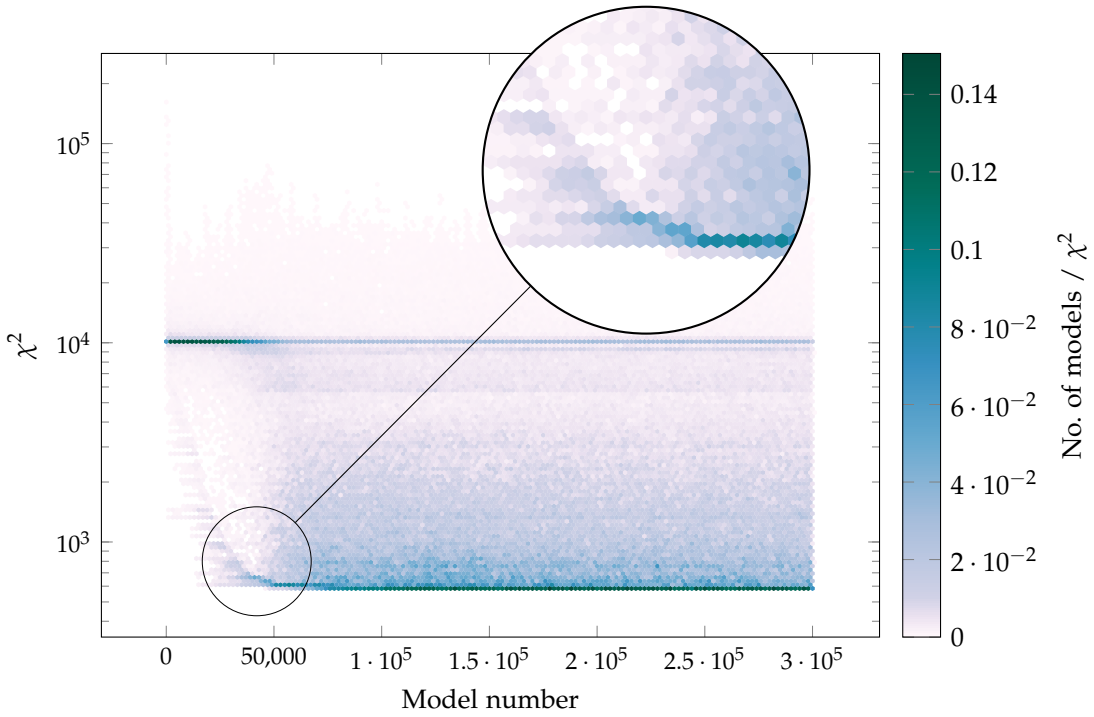

FIGURE 2.10: A hexagonally-binned histogram showing the convergence of 3×10^5 models of HD153580 and showing a clear and rapid convergence to a small range of χ^2 values. The parameter space continues to be explored as a large number of models are run. The intensity map indicates the number of FAMIAS models computed that landed in each hexagonal bin. The colourmap intensity of each hexagon has been normalized by the χ^2 value at each (x, y) co-ordinate to negate the effects of the logarithmic scale on binning.

3

HD153580

HD153580 (otherwise known as HR6314, ϵ^2 Arae, or HIP83431), is a moderately bright, candidate (Baade and Kjeldsen, 1997) γ Doradus star in the constellation Ara, at the coordinates 17 h 03 m 08.71 s, -53° 14′ 13.3″ (J2000 epoch, van Leeuwen, 2007). HIPPARCOS data places the star at a distance of 27.2 ± 0.5 pc from the Sun (van Leeuwen, 2007).

As early as 1972, HD153580 has been observed in uvby photometry (Stokes, 1972), but no periodic photometric variability has been reported from either ground-based (Twarog and Anthony-Twarog, 1995) or HIPPARCOS photometry (Perryman et al., 1997). Line profile variations have previously been observed by Baade and Kjeldsen (1997), who report the appearance of γ Doradus-like line profile variations due to pulsation modes with high azimuthal orders, where $8 \leq m \leq 14$. Not enough spectra to perform frequency and mode identification were collected, but the authors did suggest the candidature of HD153580 for the newly-defined γ Doradus class of variables. Since the star's variability has not been observed in photometry and no high-resolution, long-term spectroscopic campaigns have been conducted, HD153580 has not previously been confirmed as a bona fide γ Doradus variable.

HIPPARCOS data confirms that HD153580 is a double star, with a companion at an angular separation of 0.58″ (Tokovinin et al., 2010) and visual magnitude $m_V = 8.65$ (Worley and Douglass, 1997).[1] The spectral type of the companion is not known, and there are no observations that suggest or determine that the two stars are gravitationally related (either in this work, or in prior literature). Nevertheless, because of the small angular separation and the atmospheric seeing at MJUO, there is an unavoidable spectral contamination from the dimmer star. Disentangling the spectra is beyond the scope of this thesis, which precludes any spectroscopic abundance analysis.

This spectral contamination was also observed by Baade and Kjeldsen (1997), who suggested that it is the result of a cooler companion star. HD153580 also has a common proper motion white dwarf companion, WDS J17031-5314C, at a separation of 113.50″ and visual magnitude $m_V = 13.48$ (Worley and Douglass, 1997). The white dwarf

1 HD153580, in the Washington Double Star (WDS) Catalog (Worley and Douglass, 1997), is WDS J17031-5314Aa and hereinafter referred to as the 'primary' star. WDS J17031-5314Ab, the dimmer companion, is hereafter referred to as the 'secondary' star. The WDS catalog lists the star as "duplicity doubtful".

companion is far too dim and well-separated to have an effect on observations of HD153580, and there is no evidence of gravitational interaction between the white dwarf and HD153580.

The relatively cool temperature of HD153580 of around $T_{\rm eff} = 6400$ K (see Table 3.1) places it outside of both the γ Doradus and δ Scuti theoretical instability strips (Warner et al., 2003). At a B − V magnitude of 0.48 (Hoffleit and Warren, 1995) and absolute magnitude $M_V = 3.34$ (Ammler-von Eiff and Reiners, 2012), HD153580 is notably cooler than other stars that show γ Doradus-like pulsations, as well as being dimmer than most (but not all) others (Henry et al., 2011). Table 3.1 presents a summary of the observed properties of HD153580 reported in the literature. Of note is that HD153580 is a moderate rotator ($v \sin i = 45.4$ km s^{-1}) and slightly metal-rich in comparison to solar abundances. Isochrone estimates put its age at about 2 Gyr.

3.1 OBSERVATIONS

The primary data set for this analysis is 342 spectra taken at MJUO by Matt Davie and Pam Kilmartin, mostly between 9 June 2012 and 31 August 2012 (Figure 2.2 shows the Julian date of each observation). Usual exposure times were 20 minutes, using the 100 μm fibre. Discarding some particularly noisy spectra, the data set was reduced to 333 spectra. A set of HIPPARCOS epoch photometry augments this dataset (Perryman et al., 1997), consisting of 77 data points (after the removal of data points marked as unreliable). HERCULES spectral orders 84 to 124, encompassing a wavelength range of 460.7 nm to 671.9 nm, have been used for cross-correlation. The usefulness of orders outside this range is limited, as the data become noisy and are more contaminated by strong hydrogen lines and regions containing telluric lines.

3.2 ASYMMETRIES AND DISTORTIONS DUE TO BINARITY

HD153580 is a double star, which does necessitate some special treatment in the analysis of its line profiles. Figure 3.1 shows the raw cross-correlated representative line profiles, where the influence of the secondary star is clearly seen as a sharp dip at the bottom of the line profile. Figure 3.2 confirms that the influence of the dimmer companion is more prominent at longer wavelengths, indicating that the companion is indeed cooler than HD153580 (as suggested by Baade and Kjeldsen, 1997).

Before proceeding with frequency analysis and mode identification, the primary goal is to mitigate the effects of the secondary star. It is not feasible to disentangle the spectra, given that the secondary star is of an unknown spectral type and possibly a pulsator. Therefore it is an effective and simple method to remove a constant function from each cross-correlated line profile, which preserves *all* pulsational information and

TABLE 3.1: A summary of properties of HD153580 from the literature.

m_V	$T_{\rm eff}$ (K)	SpT	$\log g$ (cm s^{-2})	$v \sin i$ (km s^{-1})	[Fe/H]	[α/Fe]	$\mu_{\rm turb}$ (km s^{-1})	$v_{\rm r}$ (km s^{-1})	Distance (pc)	Age (Gyr)	Mass ($M_\odot$)	Reference
...	6324	...	...	45.4[a]	...	...	...	...	...	...	...	Ammler-von Eiff and Reiners (2012)
...	6510	...	4.14	...	0.23	0.09	...	4.9	...	2[d]	1.41[d]	Casagrande et al. (2011)
...	6516	...	4.31	45.4	...	...	...	...	...	...	...	Schröder et al. (2009)
5.280	6380	...	...	...	0.15	...	...	...	27	1.9[d]	...	Holmberg et al. (2009)
...	6501	F5 V[b]	4.07	...	0.11	...	2.1	...	...	...	...	Gray et al. (2006)
5.27	...	...	...	...	...	...	...	6.0[c]	...	...	...	Gontcharov (2006)

[a] $\sigma = 2.3$
[b] with abundance modifier Fe + 0.5
[c] $\sigma = 1.5$
[d] Padova isochrone derivation

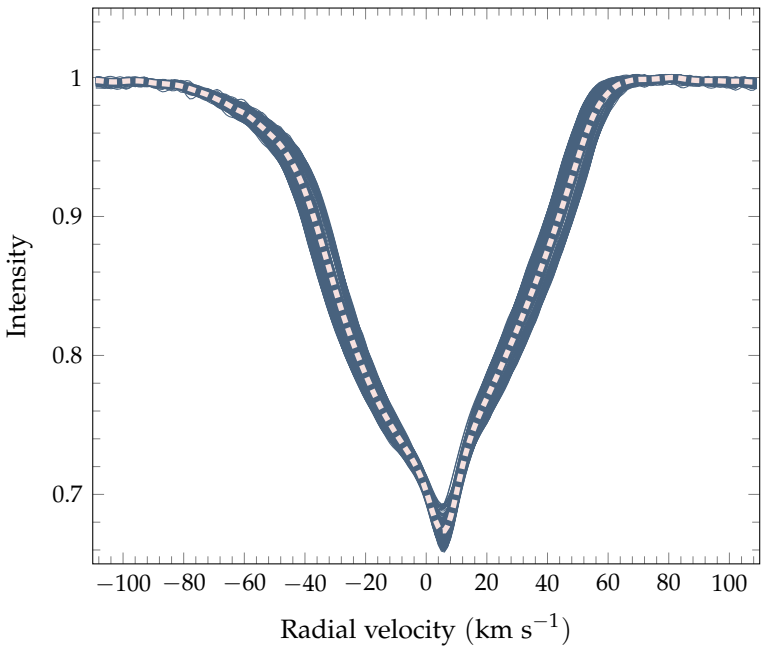

FIGURE 3.1: Cross-correlated representative line profiles of HD153580, showing the effects of the secondary star. The dashed line plotted over the individual line profiles shows the mean line profile.

avoids the pitfalls of disentanglement by spectral synthesis. The fact that the spectral lines of the secondary component have a significantly smaller equivalent width than the primary is very useful here. It is important to begin this knowing a reasonably accurate radial velocity value of HD153580, and the most recent radial velocity determination of 4.9 km s^{-1} (Casagrande et al., 2011) from the literature has been used. The wavelength axis of the HD153580 spectra has been corrected by this radial velocity during the reduction process (and prior to cross-correlation).

3.2.1 *Normalizing the line profiles*

Because FAMIAS (the program used for line profile fitting and mode identification) can only synthesize sets of Gaussian zero-point line profiles (that may be subsequently broadened by pulsational broadening), it is typically much more difficult to fit modes to stars with abnormally shaped line profiles because the mean line profile fit is relatively poor, with a significantly large χ^2 factor (thus affecting its ability to converge to an appropriate solution). In this case, the secondary star in the HD153580 spectra contaminates the line profiles of the star we are interested in. In order to effectively remove the effects of a secondary star on the mean line profile shape, while preserving the shape of the variations in the line profile, a scaling function was introduced.

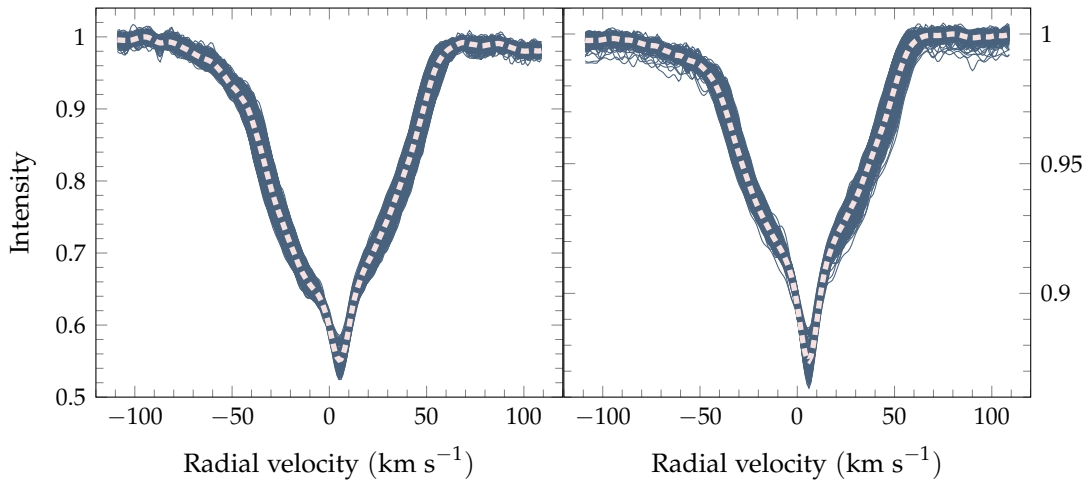

FIGURE 3.2: Cross-correlated representative line profiles of HD153580. The dashed line plotted over the individual line profiles shows the mean line profile. The line profiles have been cross-correlated across two restricted sets of wavelengths: from 460.7 nm to 495.0 nm (left), and from 609.6 nm to 671.9 nm (right). The secondary component has a significantly greater effect at the red end of the spectrum, indicating that it is a cooler star.

Scaling each individual line profile by this constant function results in the mean of the scaled line profiles having a Gaussian form: any asymmetries in the mean line profile are also corrected for.

The correction of these asymmetries is non-physical. However, because FAMIAS does not generally compute asymmetrical mean line profiles, there is little consequence in doing this. Asymmetries in the mean line profile are thus excluded from the analysis, but any frequency-dependent asymmetries due to individual pulsations will remain, since the same correction function has been applied to each observed line profile.

It is necessary to introduce a multiplicative (rather than additive) correction, because features superimposed on each other at overlapping wavelengths have a multiplicative effect on the intensity axis values. The correction has the following mathematical form. First, let

$$M = \frac{\sum_{n=1}^{k} O_n}{k}, \tag{3.1}$$

giving a mean line profile M from k individual observed line profiles O. Using FAMIAS, a synthetic line profile S of a best-fitting equivalent width, $v \sin i$, and intrinsic width is calculated. We assume that the vector S is a good representation of the true, distortion-free line profile of the star. Then, the scaling factor F is given by

$$F = 1 - M + S. \tag{3.2}$$

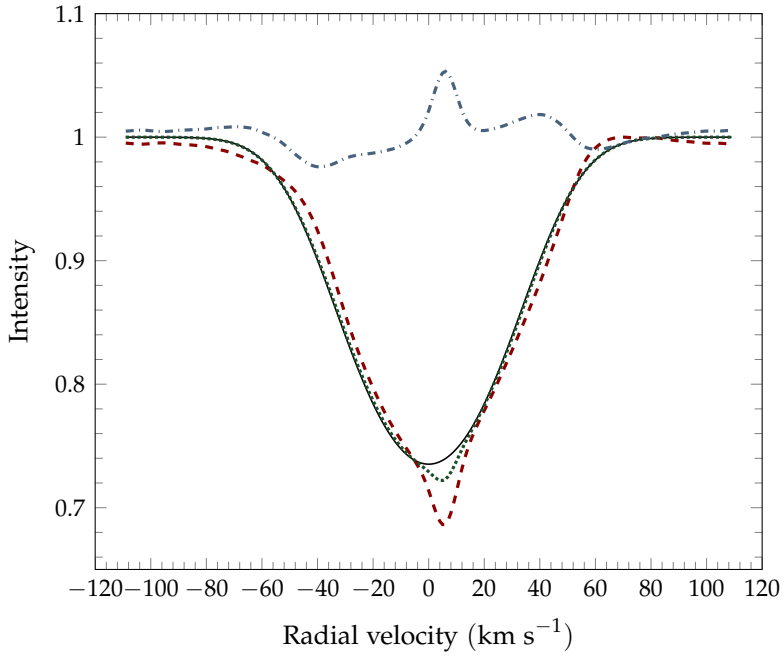

FIGURE 3.3: HD153580 after the first normalization pass. The dashed line indicates the pre-normalization mean line profile, the dash-dotted line is the scaling function, the dotted line is the normalized mean line profile, and the solid line is the synthetic line profile.

Scaling each line profile by this factor,

$$L_n = F \cdot O_n \quad \forall\, n \in \{1, \ldots, k\} \tag{3.3}$$

where L_n are the scaled line profiles. Now we have an iterative process that can be performed to normalize the mean line profile to that of a generated synthetic profile. Note that it is important to generate the synthetic zero-point profile S with a reasonably accurate $v \sin i$, equivalent width, intrinsic width, and radial velocity. Inaccurate values will change the shape of the mean line profile more than is necessary (or physical). Due to the shape of the distortions in HD153580, precise radial velocity determination is difficult. The most recent literature value of $v_r = 4.9$ km s^{-1} (Casagrande et al., 2011) has been used.

Figures 3.3 and 3.4 illustrate this process of line profile normalization. Using five passes of the algorithm removes any residual non-uniformities that still remain after the first pass.

It is a necessary investigation to ensure that the normalizations described above do not have a detrimental effect on our ability to perform mode identification. That is, we must ensure that the pixel-by-pixel pulsation amplitudes remain relatively unchanged.

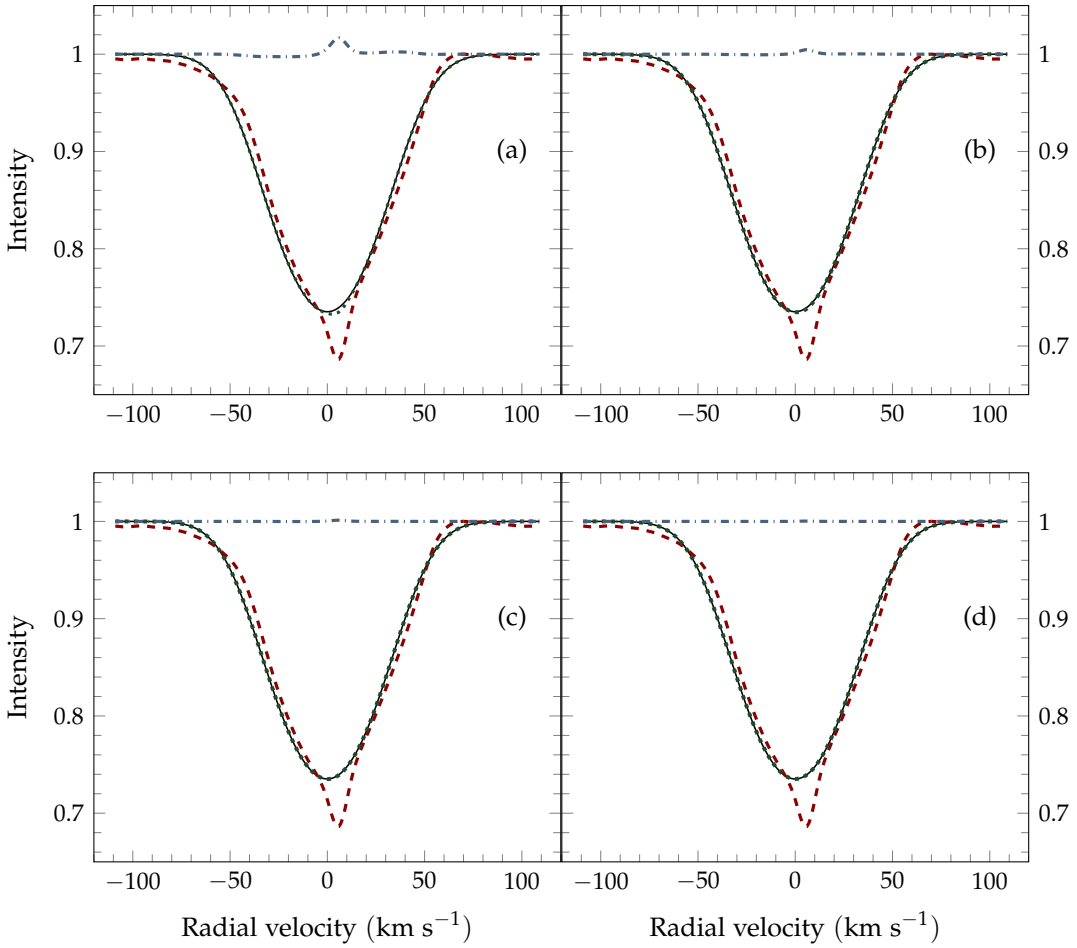

FIGURE 3.4: HD153580 normalization passes 2 through 5 (subfigures (a) through (d)). The dashed line indicates the pre-normalization mean line profile, the dash-dotted line is the scaling function, the dotted line is the normalized mean line profile, and the solid line is the synthetic line profile.

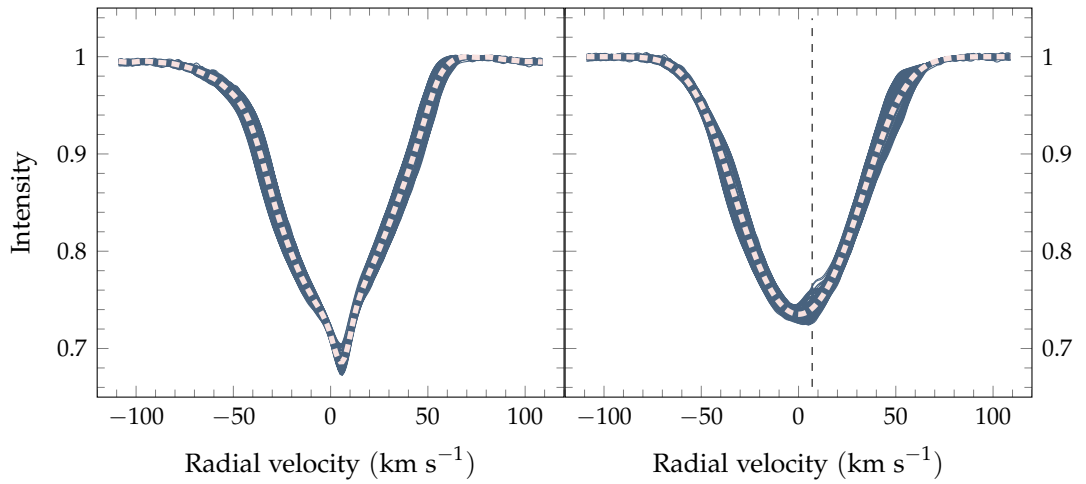

FIGURE 3.5: Radial velocity line profiles of HD153580, prior to (left) and after (right) normalization. Note the residual, excess variations that coincide with position of the spectral line due to the secondary component (as indicated by the dashed line at 7 km s^{-1}).

Figures 3.5 and 3.6 show the difference between the line profiles and their least-squares fits at $f_1 = 0.6589$ d^{-1}.

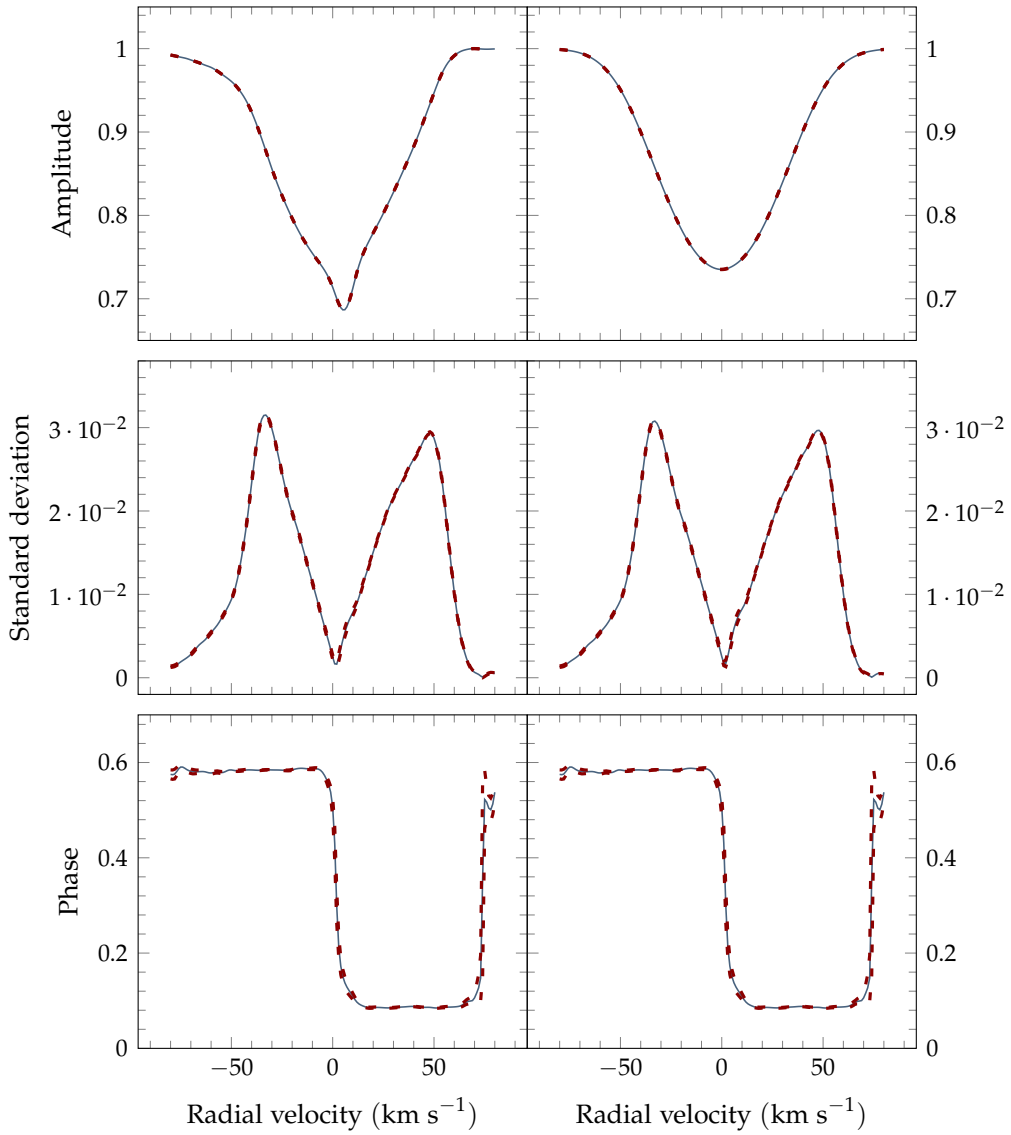

FIGURE 3.6: The least-squares fits of the uncorrected (left) and corrected (right) line profiles, at the pulsation frequency $f_1 = 0.6589$ d^{-1}. Note that although the mean line profile has changed shape considerably (top panels), the least-squares fitted standard deviation profiles (centre panels) are essentially untouched. The phase fits across the line profile (lower panels) are also not visibly affected. In these plots, the solid lines represent the calculated values and the dashed lines are the uncertainty boundaries.

3.3 FREQUENCY IDENTIFICATION

Both the spectroscopic data from MJUO and photometric data from HIPPARCOS (Perryman et al., 1997) were used in the frequency analysis. These two sets of data are analysed separately, and an optimal result would return the same frequencies from both the spectroscopic and photometric data.

3.3.1 *Spectroscopic frequency analysis*

Both SIGSPEC and the Fourier analysis tools in FAMIAS have been used to determine the frequencies of pulsations in the representative line profiles produced from the MJUO spectroscopic data. The -80 km s^{-1} to $+80$ km s^{-1} dispersion range is analysed, which encompasses the effective line profile width of the primary star. There are no significant periodic variations outside this range. The typical frequency range searched for pulsations is from 0 d^{-1} to 6 d^{-1}, which encompasses the expected frequency range for γ Doradus-type pulsations.

FAMIAS can compute a significance level value on a per-pixel basis.[2] This means that in the pixel-by-pixel, one-dimensional mean Fourier spectrum mode, the significance level cannot be assessed (some accuracy is lost when computing the Fourier periodogram using only the pixel with the highest variation at a chosen frequency). This is the reason why the significance levels are only shown for the moment calculations.

Figure 3.7 shows the spectral window of HD153580, indicating that there is a reasonably significant level of aliasing due to the concentrated temporal range of observations.

2 A 'pixel' is a discrete radial velocity bin in the line profiles.

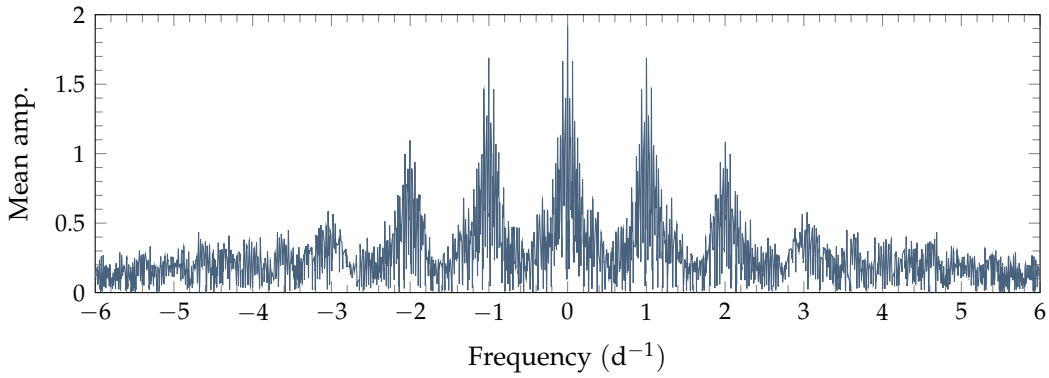

FIGURE 3.7: The spectral window of HD153580, from the MJUO spectroscopic data.

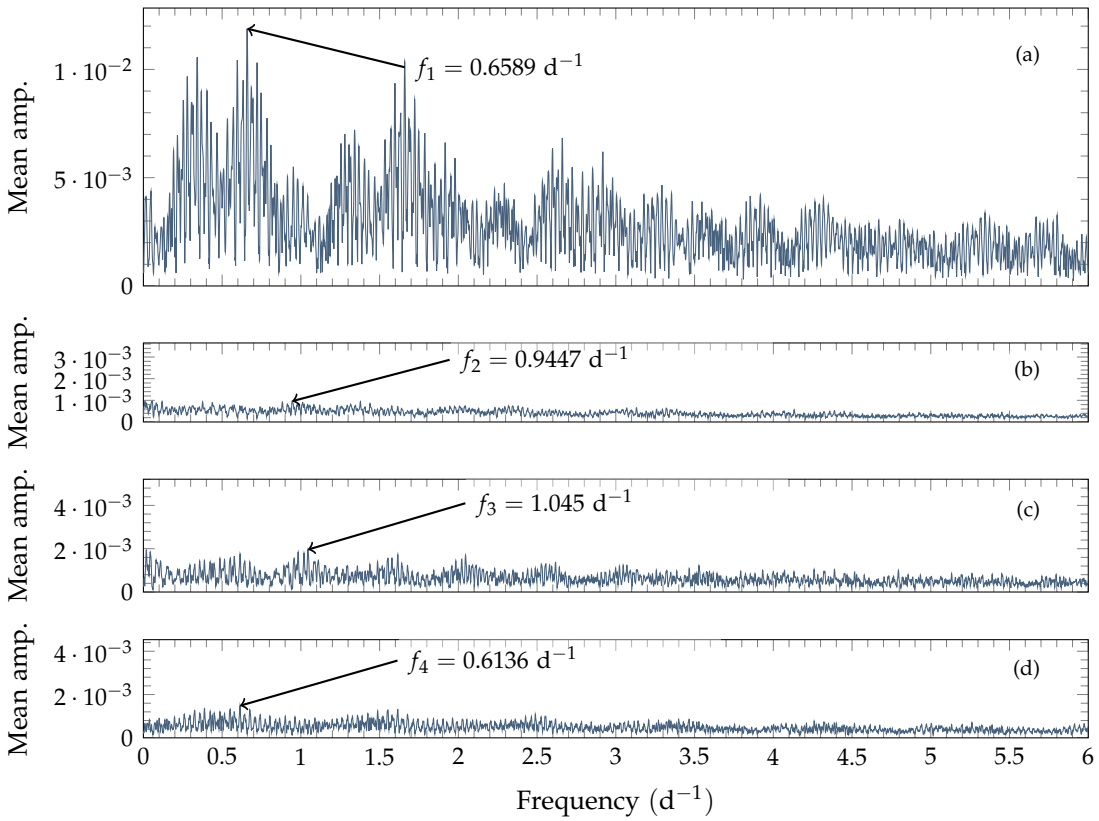

FIGURE 3.8: The Fourier spectrum frequency selection process for HD153580, showing the progressive prewhitening of highest-peak frequencies. Each panel is analysed following the removal (prewhitening) of the previous frequency. Panels (a) and (b) show the mean Fourier spectrograms across the entire line profile (-80 km s^{-1} to $+80$ km s^{-1}). Since no further frequencies of significance in HD153580 were found, the lower two panels, (c) and (d), are subsequent analyses performed only on a restricted dispersion range between -17 km s^{-1} and $+24$ km s^{-1}.

The Fourier spectrum frequency selection process, using the pixel-by-pixel method in FAMIAS, is illustrated in Figure 3.8. After removing the first two frequencies, including the only significant frequency found in the primary component, $f_1 = 0.6589$ d^{-1}, a restricted dispersion range of -17 km s^{-1} to $+24$ km s^{-1} is analysed in an attempt to isolate possible periodicities in the secondary component (lower two panels). Only the first frequency, f_1, appears to have a significant contribution above the noise floor of the Fourier spectra. $f_1 = 0.6589$ d^{-1} displays convincing line profile variations, however no further frequencies do.

Figure 3.9 shows a two-dimensional Fourier periodogram, where the distribution of frequency peaks is seen across each pixel of the line profile. This figure shows clearly that there are variations in this range likely attributable to the secondary component,

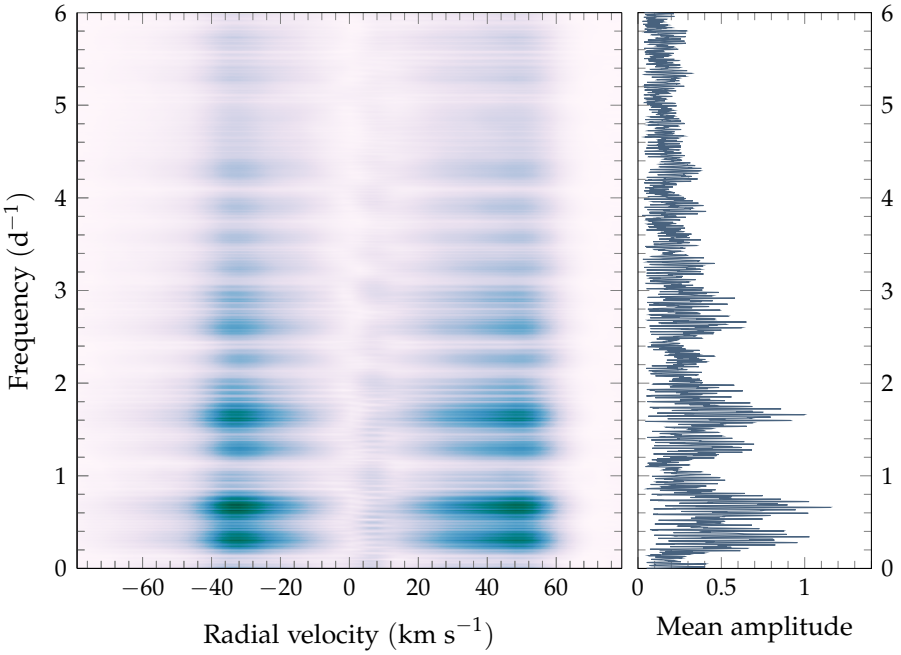

FIGURE 3.9: The two-dimensional Fourier periodogram of the MJUO spectroscopic data (left), with lighter colours on the colourmap representing frequency peaks. On the right is the mean Fourier periodogram across all pixels.

at a radial velocity of around 7 km s^{-1}. Even if frequencies could be identified in the secondary component, a successful mode identification is unlikely to be possible due to the very small resolution in radial velocity space. The primary frequency $f_1 = 0.6589$ d^{-1} (and its aliases) is the dominant pulsation across the line profile and is reasonably symmetric about its centre.

Figures 3.10 to 3.13 illustrate the process of frequency determination using FAMIAS from the zeroth to third moments respectively. The frequency $f_1 = 0.6589$ d^{-1} is present in the first and third moments and the frequency $f_8 = 0.34116$ d^{-1}, found in the second moment, is expected to be an alias frequency (likely $1 - f_1$). It has a very similar fit to the standard deviation profiles of $f_1 = 0.6589$ d^{-1} shown in Figure 3.18, yet as shown in Table 3.3, using SIGSPEC f_1 was found in the second moment but f_8 was not. For these reasons f_8 is considered an alias. The latter two frequencies f_9 and f_{10} are not significant above the noise floor and are not found elsewhere, so are expected to be peaks arising from noise. A similar line of reasoning can be applied to the frequencies found in the other moments (except f_1): their appearance is not duplicated elsewhere and the peaks are not significant in comparison to the noise floor. The significance level indicated in the figures is defined by Zima (2008b), where the significance level of a frequency is computed for a signal-to-noise ratio of 4 on a Fourier spectrum that has been pre-whitened by that same frequency.

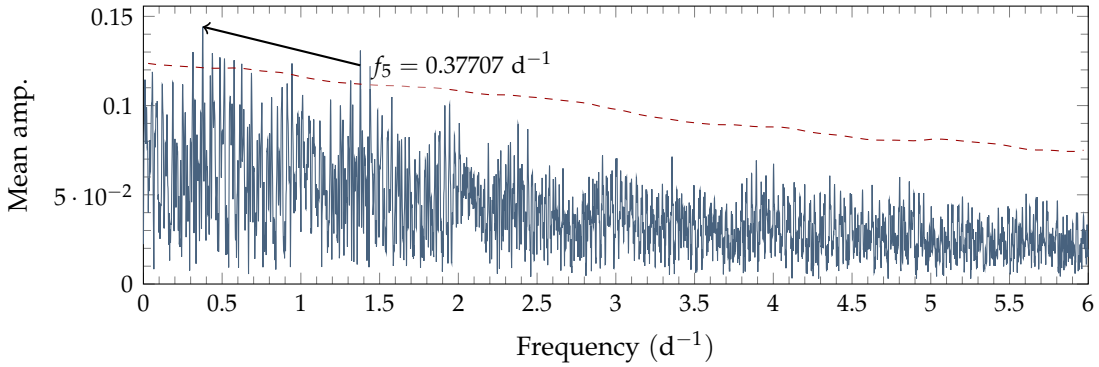

FIGURE 3.10: The Fourier spectrum frequency selection process for HD153580, computed using the zeroth moment of the moment method in FAMIAS. The dashed line represents the significance level at a signal-to-noise ratio of 4.

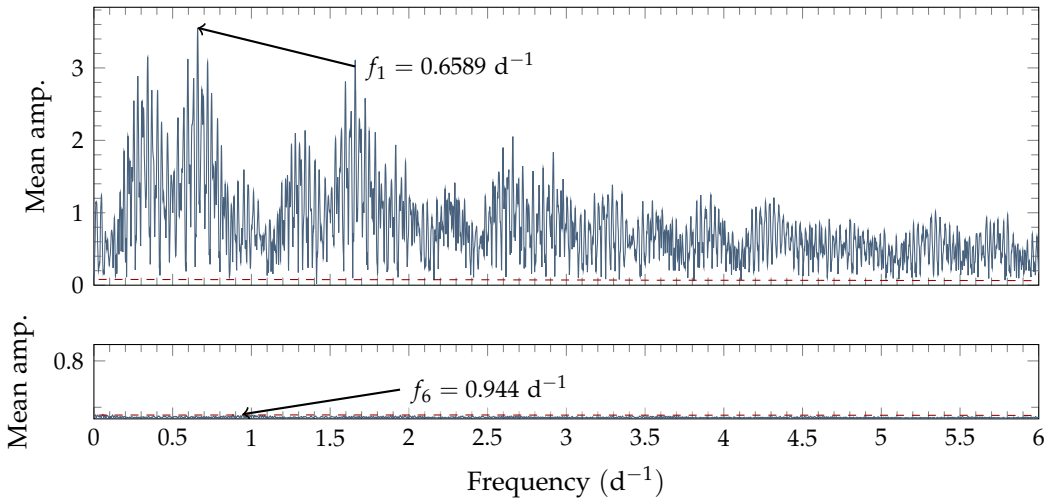

FIGURE 3.11: The Fourier spectrum frequency selection process for HD153580, computed using the first moment of the moment method in FAMIAS. The dashed line represents the significance level at a signal-to-noise ratio of 4.

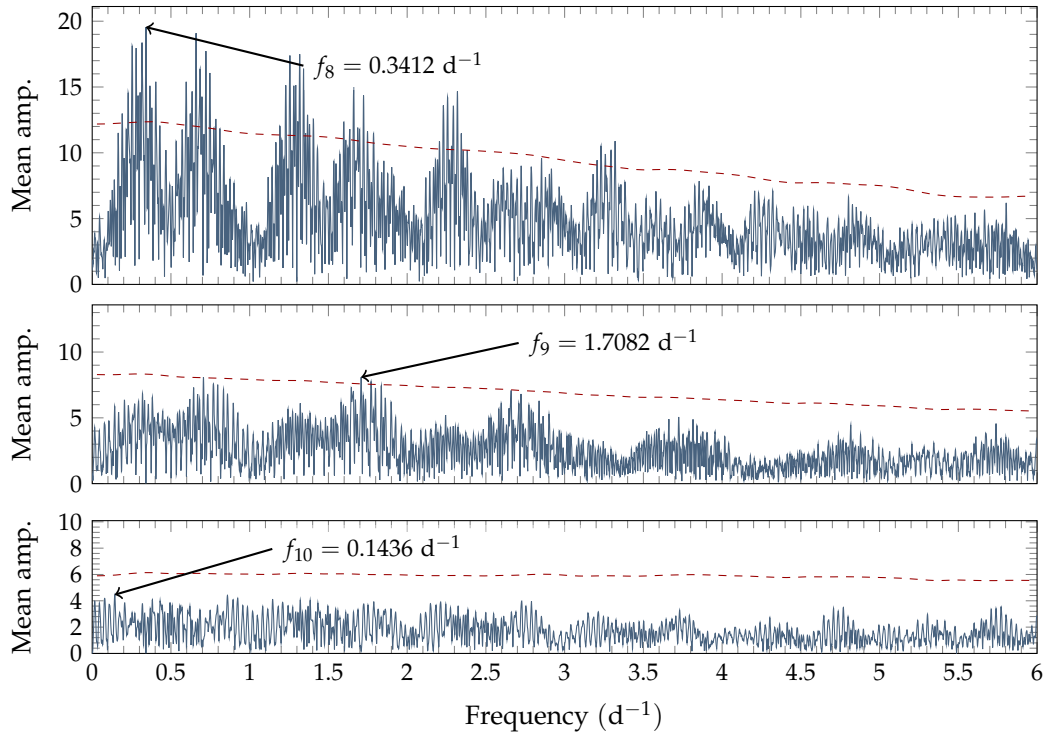

FIGURE 3.12: The Fourier spectrum frequency selection process for HD153580, computed using the second moment of the moment method in FAMIAS. The dashed line represents the significance level at a signal-to-noise ratio of 4.

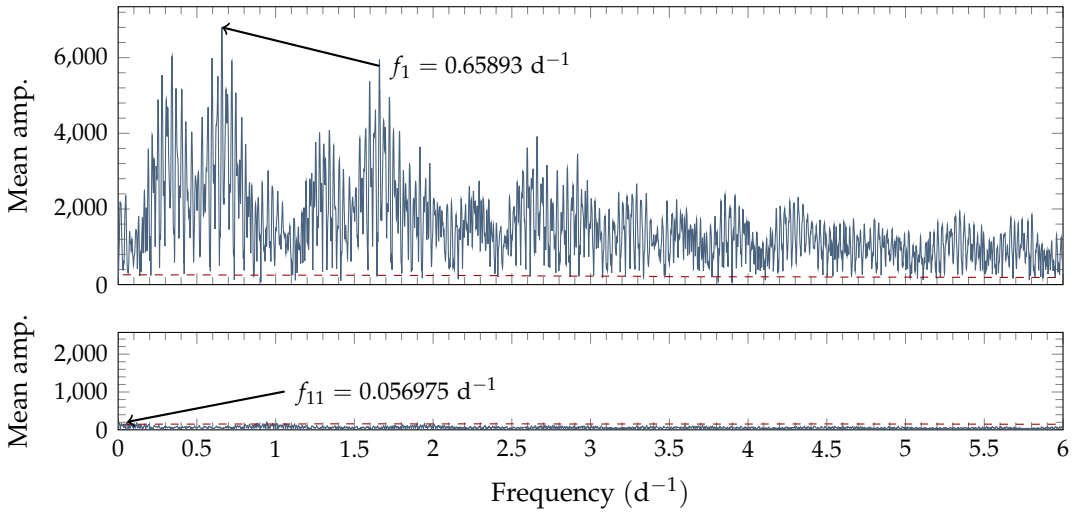

FIGURE 3.13: The Fourier spectrum frequency selection process for HD153580, computed using the third moment of the moment method in FAMIAS. The dashed line represents the significance level at a signal-to-noise ratio of 4.

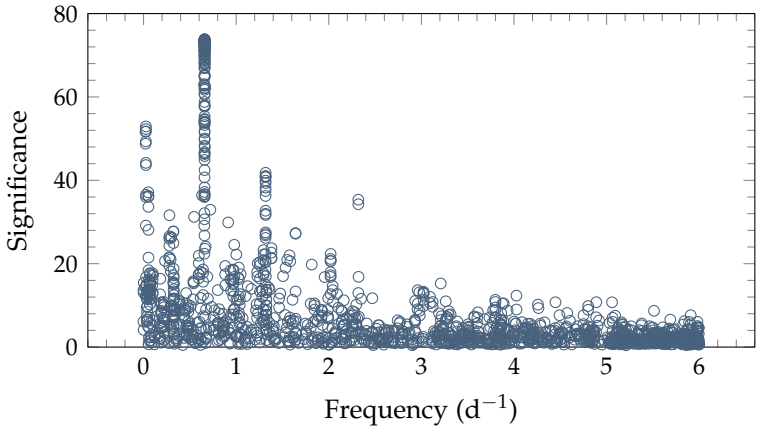

FIGURE 3.14: SIGSPEC significance values for all frequencies found through the analysed dispersion range of -80 km s^{-1} to $+80$ km s^{-1}.

Figures 3.14 to 3.16 illustrate the frequency results found using a pixel-by-pixel SIGSPEC analysis. The SIGSPEC results show a clearly significant peak around $f_1 = 0.6589$ d^{-1}. There are also some high-significance frequencies detected around 0.025 d^{-1} and 1.3177 d^{-1}. These frequencies likely correspond to f_{16} and f_{19}, found using SIGSPEC on the first and second moments respectively. However, they are found in relatively few pixels and do not appear in FAMIAS results so are not expected to be true frequencies. f_{16} does not show a significant pattern in the least-squares fitted standard deviation profiles, while f_{19} appears similar to f_1 and thus is expected to be an alias frequency. The pixel-by-pixel SIGSPEC results in Figure 3.15 show that, even when restricting the analysed dispersion range to that of the secondary component, there are no prominent frequencies detected besides $f_1 = 0.6589$ d^{-1}.

Table 3.3 summarizes these potential periodicities detected using both FAMIAS and SIGSPEC. The frequency $f_1 = 0.6589$ d^{-1} is observed in the pixel-by-pixel method as well as all moments except the zeroth moment. The zeroth moment represents equivalent width variations, so it is not expected that a non-radial pulsation is observable here.

Of the periods summarized in Table 3.3, only one frequency ($f_1 = 0.6589$ d^{-1}) has been identified as a true pulsation frequency. Another frequency, $f_5 = 0.37794$ d^{-1}, displays least-squares fit line profile variations very similar to those of f_1 illustrated in Figure 3.18. However its relatively low SIGSPEC significance of 26.9 (in comparison to f_1's significance of ≈ 72), in combination with the fact that it has only been detected in the zeroth moment, makes it a probable alias frequency. The only frequency which is consistently identified with both SIGSPEC and FAMIAS, using the moment and pixel-by-pixel methods, is $f_1 = 0.6589$ d^{-1}. This frequency accounts for 81.3% of variations throughout the line profile and the majority of the remaining variations are isolated to the radial velocity range occupied by the secondary component. Figure 3.23 shows

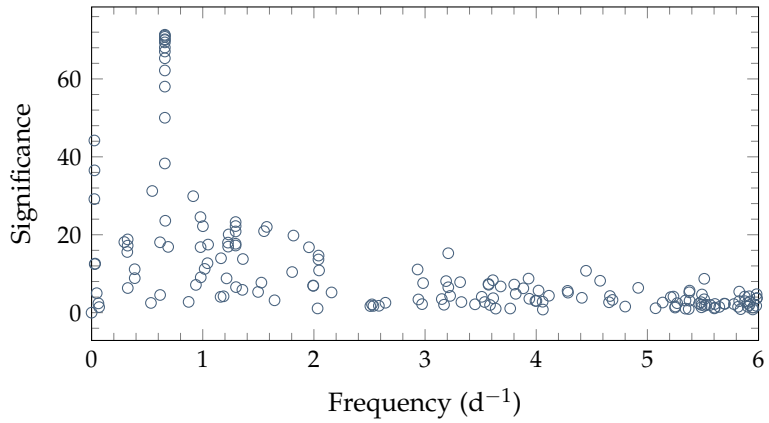

FIGURE 3.15: SIGSPEC frequency results found through a restricted dispersion range of -4 km s^{-1} to $+12$ km s^{-1}, encompassing the radial velocity range of the secondary component's line profiles.

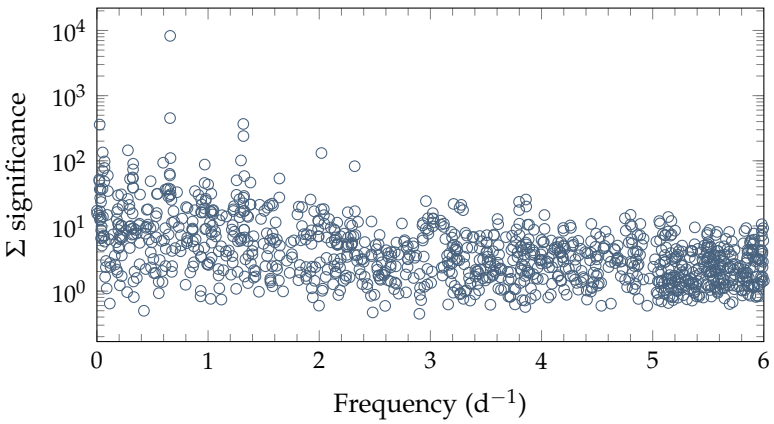

FIGURE 3.16: Cumulative SIGSPEC frequency results across the -80 km s^{-1} to $+80$ km s^{-1} dispersion range. The ordinate shows the sum of SIGSPEC significance values at each frequency across the dispersion range. At each radial velocity bin, SIGSPEC was set up to find the ten most significant periodicities. Before summing, detected frequencies have been binned to 1×10^{-3} d^{-1} intervals.

TABLE 3.2: The proportion of line profile variations (in terms of the mean standard deviation across the line profile, σ) detected frequencies.

Frequencies removed	σ	% of σ explained
—	0.009414	—
f_1	0.001763	81.3%
$f_1 + f_2$	0.001632	82.7%
$f_1 + f_2 + f_3$	0.001473	84.4%
$f_1 + f_2 + f_3 + f_4$	0.001366	85.5%

how the progressive pre-whitening of frequencies removes the observed line profile variations, and Table 3.2 displays the proportion of line profile standard deviations that are explained by the cumulative removal of frequencies.

Given that any remaining periodicities in the line profile of the primary component are too small to be reliably established, and that no further frequencies are consistently determined across different methods that can explain a further significant portion of line profile variations in the secondary component, $f_1 = 0.6589$ d^{-1} remains the sole identified pulsation frequency. In order to estimate the uncertainty in this frequency, there are three possible methods. Equations (2.2) and (2.3) provide error estimations for frequencies determined by FAMIAS and SIGSPEC, over an observation timebase T.

To estimate the effective timebase T (as per the limitations discussed in Section 2.5.2), we use the fact that most of the spectra for HD153580 were obtained in four concentrated runs from June 2012 to August 2012, resulting in 321 spectra over a total of 16 nights. We thus approximate the effective timebase as 16 days. For $f_1 = 0.6589$ d^{-1}, this returns an error upper limit on uncertainties in SIGSPEC frequencies of ± 0.007 d^{-1}. With an estimated signal-to-noise ratio of 200, in FAMIAS-determined frequencies we estimate an uncertainty on the order of 1×10^{-5} d^{-1}. In practice, the SIGSPEC uncertainty estimate is likely an over-estimate, and the FAMIAS determination is likely an under-estimate. Figure 3.17 provides an alternative method, where the uncertainty may be regarded as the spread of the observed per-pixel periods with significance $\gtrsim 70$. By encompassing this range of frequency determinations, perhaps a realistic frequency determination is $f_1 = 0.65890 \pm 0.00005$ d^{-1}.

Figures 3.18 to 3.21 show the least-squares fitted standard deviation profiles for frequencies found in the spectroscopic data. The fits in these figures were computed simultaneously with one another, as FAMIAS applies its least-squares fitting algorithm to fine tune the amplitude and phase fits across all fitted frequencies. With the exception of $f_1 = 0.6589$ d^{-1}, the plots of the phase variations are poor and it is likely that none of these are true pulsation frequencies. Furthermore, the lack of structure (indicative of phase transitions) in the phase plots is not indicative of a non-radial pulsation. Certainly, the peaks in the standard deviation curves occur at radial velocities that

TABLE 3.3: A summary of frequencies found using the progressive pre-whitening process of FAMIAS as well as the frequency analysis tool SIGSPEC. Frequencies above the significance limits of FAMIAS, or with a SIGSPEC significance > 6, have been reported.

	FAMIAS	SIGSPEC	
Label	Frequency (d^{-1})	Frequency (d^{-1})	Significance
Pixel-by-pixel			
f_1	0.65895	0.65890 ± 0.00005[a]	≈ 72
f_2	0.94482		
f_3	1.0447		
f_4	0.61362		
Zeroth moment			
f_5	0.37707	0.37794	26.9
f_{13}		0.32656	18.3
f_{14}		0.011901	12.4
f_{15}		2.9150	6.6
First moment			
f_1	0.65893	0.65891	72.2
f_6	0.94402		
f_7	0.09976		
f_{16}		0.026979	20.6
f_{17}		3.5752	7.4
f_{18}		3.2926	7.8
Second moment			
f_1		0.65913	50.1
f_8	0.34120		
f_9	1.7082		
f_{10}	0.14362		
f_{19}		1.2943	21.2
f_{20}		0.92485	9.7
Third moment			
f_1	0.65893	0.65890	72.1
f_{11}	0.056975		
f_{12}	1.1008		
f_{21}		0.027895	16.3

[a] This is the effective range of frequencies detected, as shown in Figure 3.17.

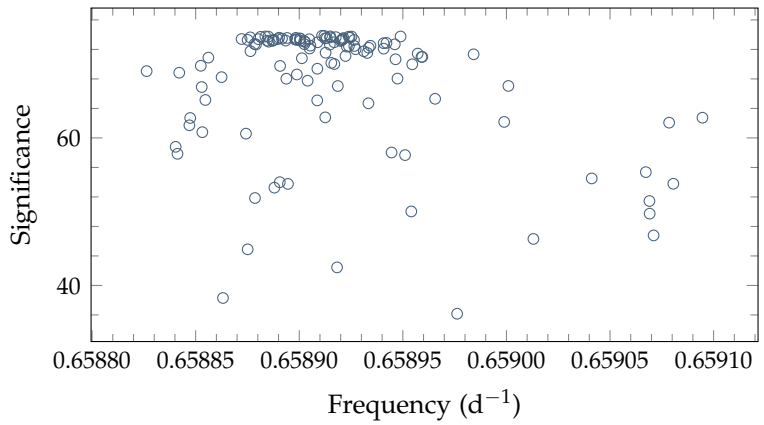

FIGURE 3.17: SIGSPEC significance values for all frequencies near $f_1 = 0.6589$ d^{-1} found through the analysed dispersion range of -80 km s^{-1} to $+80$ km s^{-1}. There are 122 data points displayed here, each found in one of the 161 radial velocity bins through the dispersion range.

coincide with the secondary component. Figure 3.22 shows that there is a relatively uneven phase coverage of f_1 with a trimodal distribution.

Figure 3.23 shows the pixel-by-pixel standard deviations across the line profile (that is, the total standard deviation as opposed to the frequency-dependent variations determined by FAMIAS). Detected frequencies are pre-whitened by FAMIAS in order to remove those variations from the line profile. After removing the first frequency, f_1, most deviations except those centred on the secondary component are removed. The cause of the small deviations seen at -40 km s^{-1} and 60 km s^{-1} is not clear, as they are not associated with, or affected by the removal of, any found frequencies. Removing the frequency $f_1 = 0.6589$ d^{-1} removes almost all variations in the line profile that are intrinsic to the primary star. The successive removal of further frequencies progressively reduces the secondary standard deviation bumps due to the secondary star (peaking at around 6 km s^{-1} to 7 km s^{-1}).

Figure 3.24 shows the line profile variations phased to $f_1 = 0.6589$ d^{-1}, while Figure 3.25 shows the same variations theoretically computed in FAMIAS, with the final mode identification parameters listed in 3.5. The match between the two is quite good; however, there is a slight phase shift in the fit.

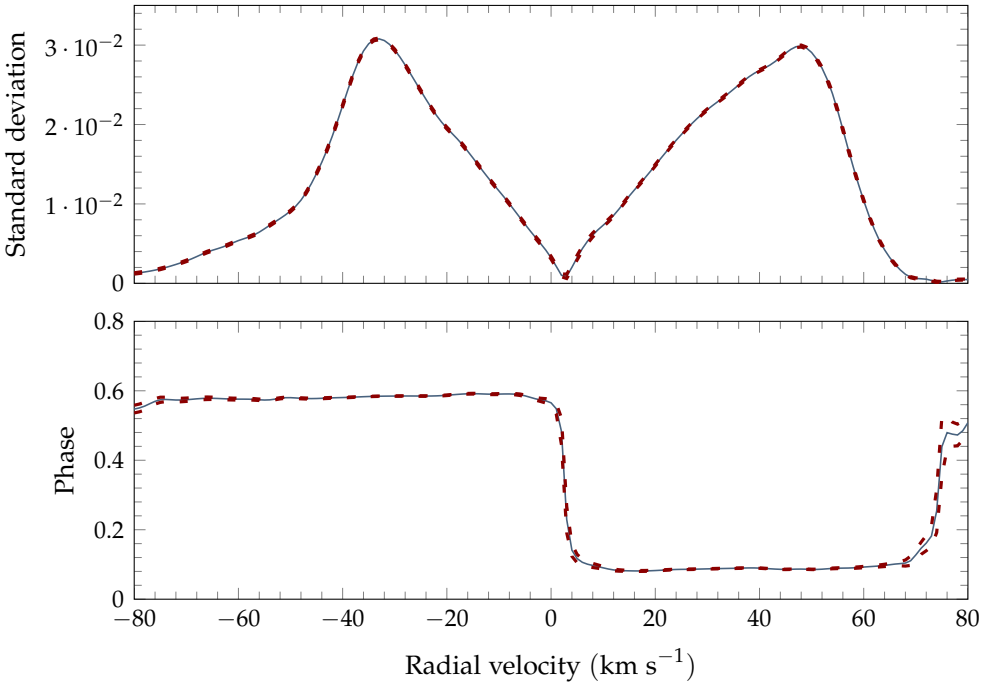

FIGURE 3.18: The least-squares fitted standard deviation profiles for $f_1 = 0.6589$ d^{-1} (top), and the phase fits (bottom). The outlines on either side of the central curve represent an error estimation.

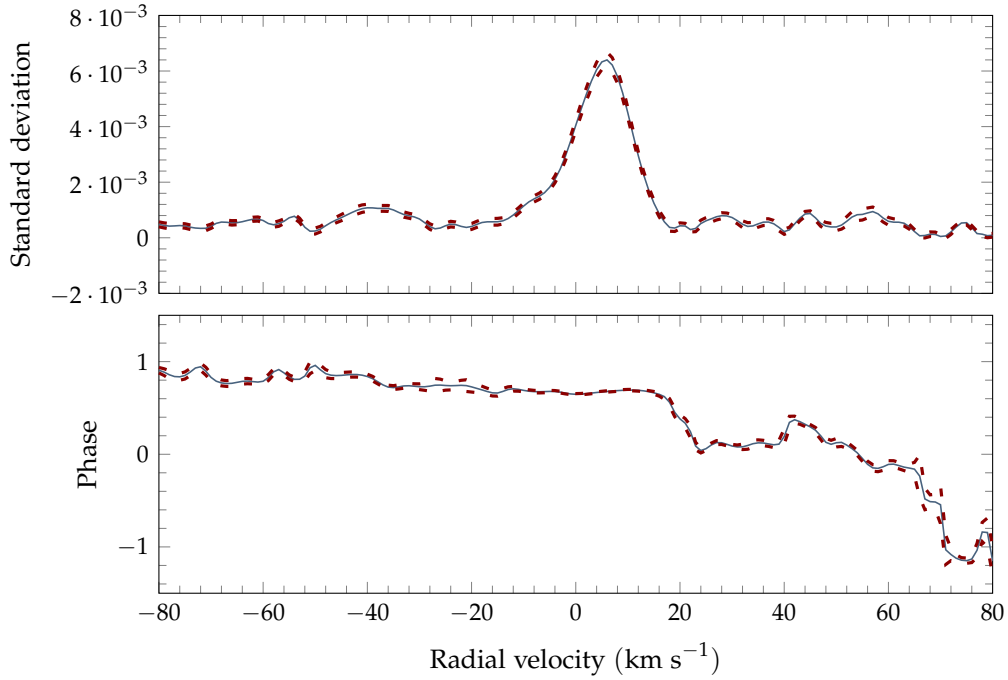

FIGURE 3.19: The least-squares fitted standard deviation profiles for $f_2 = 0.9447$ d^{-1} (top), and the phase fits (bottom). The outlines on either side of the central curve represent an error estimation.

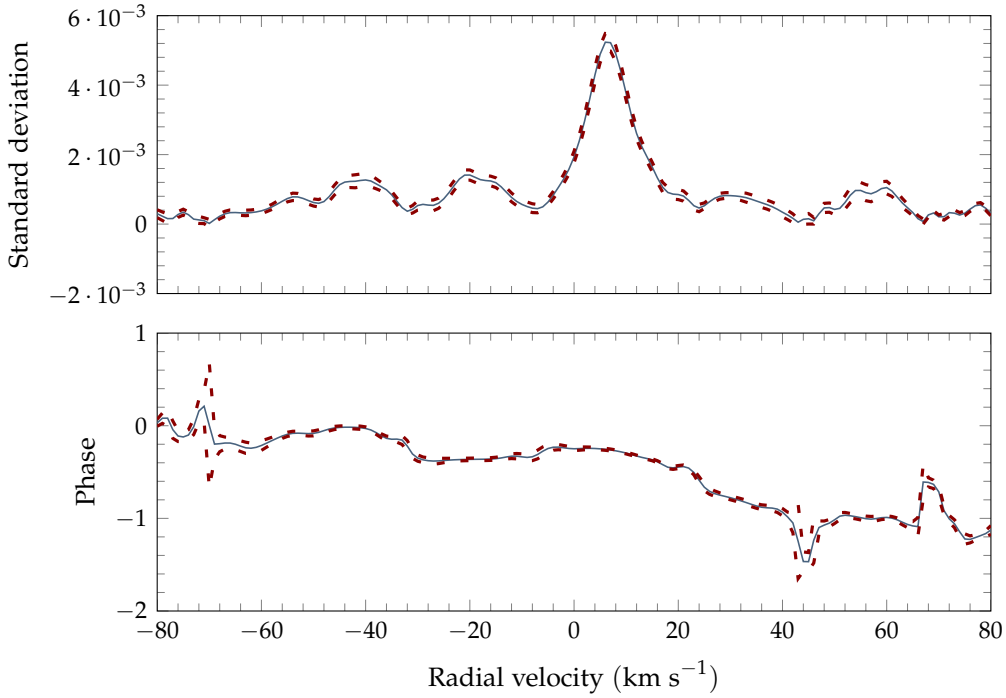

FIGURE 3.20: The least-squares fitted standard deviation profiles for $f_3 = 1.045$ d^{-1} (top), and the phase fits (bottom). The outlines on either side of the central curve represent an error estimation.

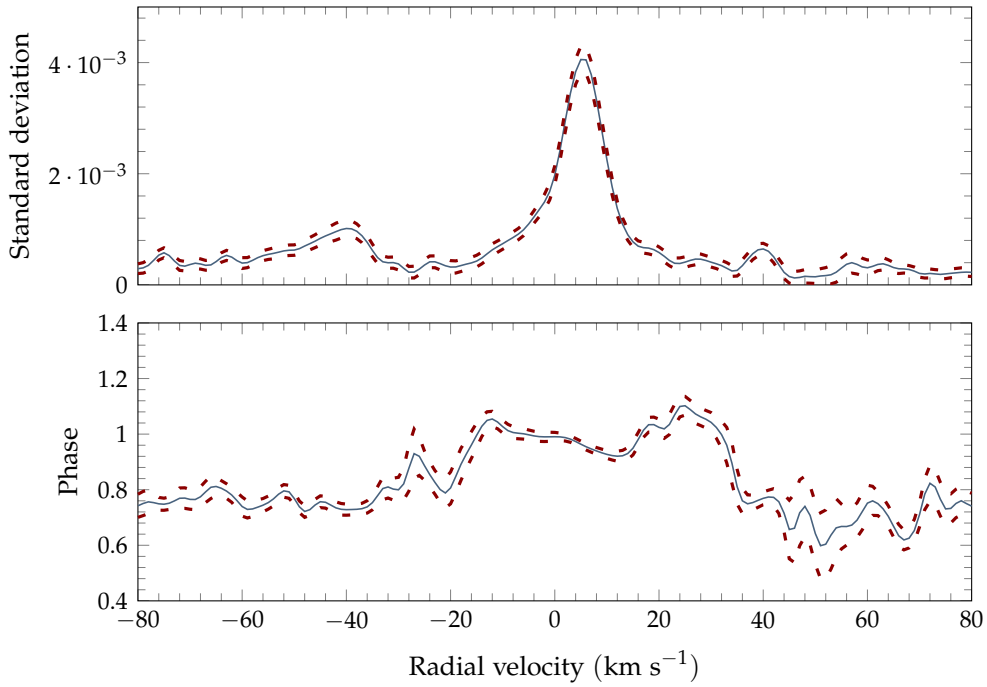

FIGURE 3.21: The least-squares fitted standard deviation profiles for $f_4 = 0.6136$ d^{-1} (top), and the phase fits (bottom). The outlines on either side of the central curve represent an error estimation.

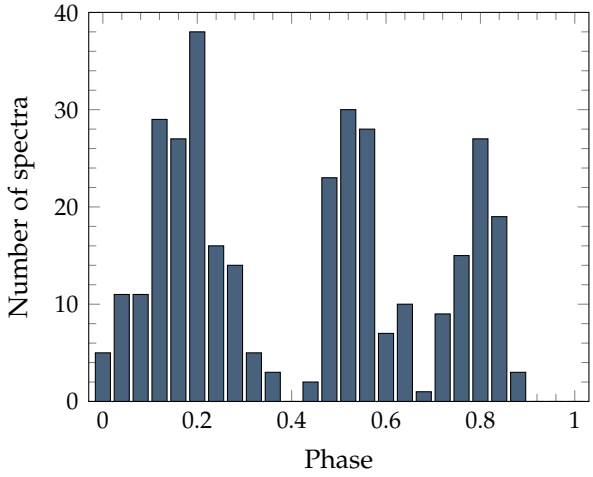

FIGURE 3.22: Phase coverage histogram of the MJUO spectroscopic data, for the frequency $f_1 = 0.6589$ d^{-1}.

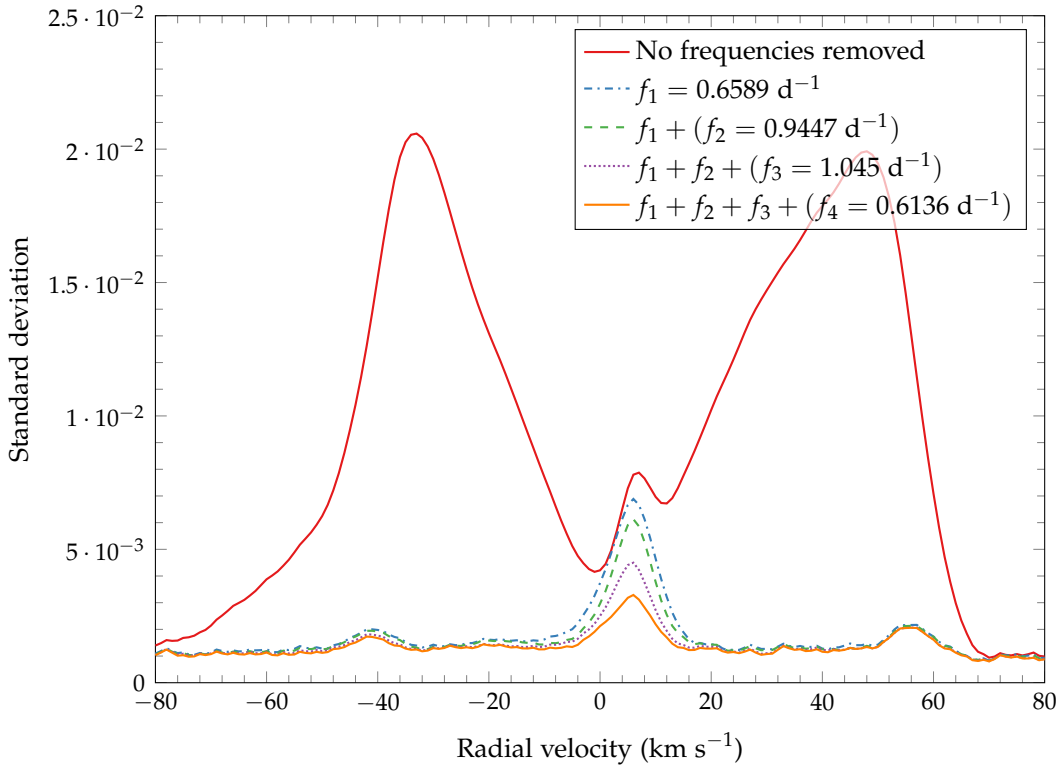

FIGURE 3.23: Per-pixel standard deviations across the line profile of HD153580, demonstrating the effects of progressive pre-whitening by the indicated frequencies.

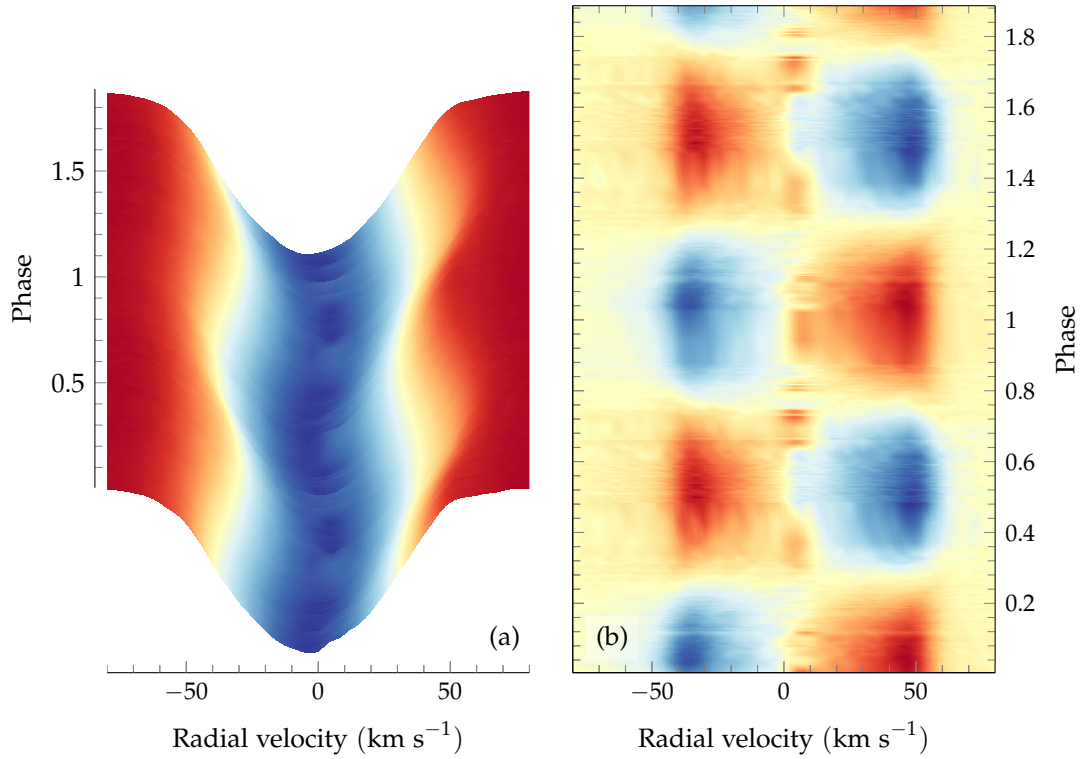

FIGURE 3.24: (a) A three-dimensional representation of the line profile variations of HD153580, phased to $f_1 = 0.6589$ d^{-1} and repeated over two cycles. The shading represents the intensity map of the line profile of each observation, and the observations are vertically stacked and interpolated. This shows how the shape of the line profile changes over time when the observations are phased to f_1. Panel (b) is the same data, except the mean line profile has been subtracted so that only the residual variations remain. The viewpoint has been changed such that this is a two-dimensional representation. Again, an interpolation shader is used to fill in the uneven phase coverage. The interpolation shader does not, however, perform a median filter: the remarkably smooth appearance of the variations is a testament to the accuracy and consistency of the data. The reason why the phase axis on both plots has a maximum value of 1.89 is that this is the limit of the phase coverage (as seen in Figure 3.22).

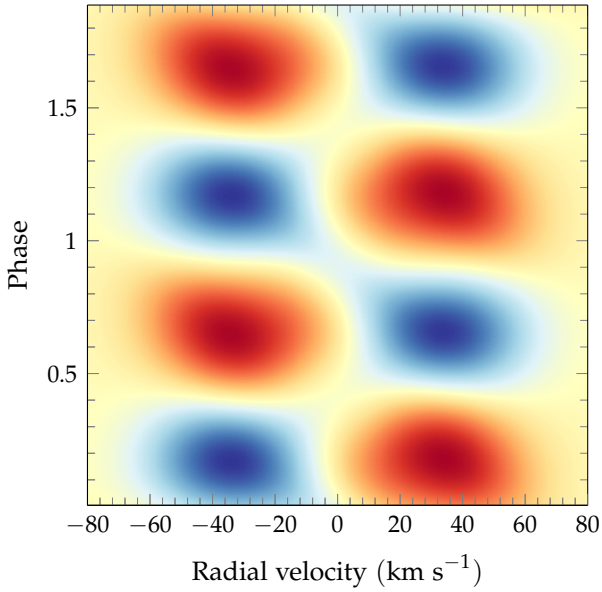

FIGURE 3.25: Synthetic line profile variations for HD153580, computed with FAMIAS using the same parameters as the final mode identification.

3.3.2 *Photometric frequency analysis*

The 77 photometric data points from the HIPPARCOS satellite (Perryman et al., 1997) were analysed using both FAMIAS and SIGSPEC. The spectral window shown in Figure 3.26 shows little significant aliasing owing to the good temporal spread of the observations. Using SIGSPEC, the most significant frequency found from was $f = 1.6562$ d^{-1}, at a significance of 4.8. In practice, this level of significance is not deemed to represent a true pulsation and this frequency was not duplicated in the spectroscopic data. In Figure 3.27 it can be seen that the highest frequency peaks found using FAMIAS appear to be peaks in the noise floor. As with the moment method periodograms computed from the spectroscopic data, the red line in Figure 3.27 represents the significance level at a signal-to-noise ratio of 4. Their subsequent removals do not appear to remove any periodicities in the Fourier periodograms, and none of these frequencies found in photometry match a corresponding spectroscopic frequency.

The standard deviation and phase plots of the photometric frequencies achieve similar results to that of f_2, f_3, and f_4 in Figures 3.19 to 3.21, as when fitted *in conjunction with* $f_1 = 0.6589$ d^{-1}, the spectroscopic variability of these frequencies is confined to the secondary component. It appears possible that the secondary component is a variable star, but either these variations are aperiodic or the star is simply too dim and the signal is too weak properly to determine their existence. *If* these frequencies are indeed attributable to the secondary star, it is a curious anomaly that the separation of the two components was resolved by HIPPARCOS (Perryman et al., 1997). This would

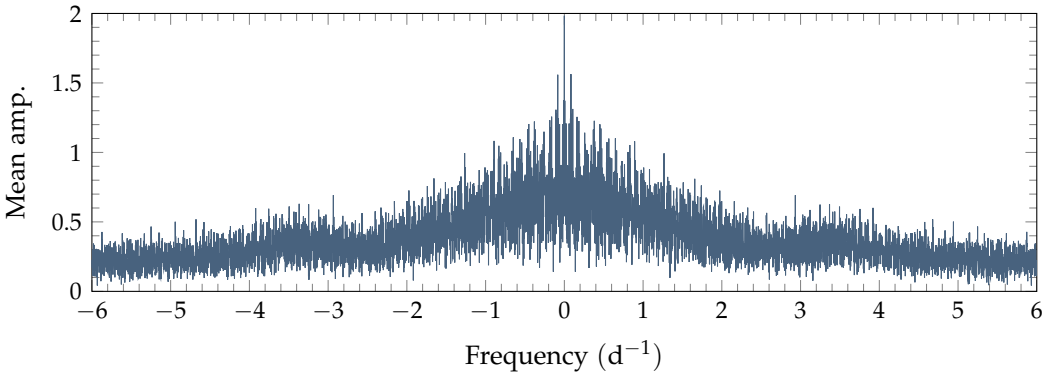

FIGURE 3.26: HD153580 spectral window from HIPPARCOS photometry. No significant aliasing is seen.

raise the question of how the HIPPARCOS photometry was 'contaminated', such that variabilities in the secondary component are visible in the photometry of the first. The second, and more likely possibility, is that the variations seen are due to atmospheric seeing. The telescope is guided to the primary component, not the secondary: thus, the amount of light gathered from the secondary component will vary as the seeing conditions fluctuate.

None of these frequencies observed photometrically appear to be significant, and their discovery has not been duplicated spectroscopically. Thus, no pulsation frequencies have been identified photometrically.

3.4 MODE IDENTIFICATION AND STELLAR PARAMETERS

With the frequency of $f_1 = 0.6589$ d^{-1} explaining the majority of observed line profile variations, the task remains to identify its mode of pulsation. Following the reported properties of HD153580 in the literature, the parameters $T_{\rm eff} = 6400$ K, $\log g = 4.1$, and [Fe/H] $= 0.15$ have been chosen as reasonable values for this analysis. Adopting the polynomial relationships empirically determined by Torres et al. (2010) and using the $T_{\rm eff}$, $\log g$, and [Fe/H] parameters from Table 3.4, the radius of HD153580 can be estimated as 1.62 R$_\odot$, where an observational standard deviation in radius of $\sigma = 3.2\%$ is reported by Torres et al. (2010). Allowing for unknown uncertainties in the adopted stellar parameters and the typical properties of γ Doradus stars, it can be reasonably estimated that the true radius is 1.6 R$_\odot \pm 0.1$ R$_\odot$. These initial stellar parameters required by FAMIAS prior to mode identification are listed in Table 3.4.

The mode identification process follows the FPF method described in Section 2.5.5. The first step is to compute the $v \sin i$, equivalent width, intrinsic width[3], and radial

3 The intrinsic width is the width of the Gaussian line profile that is not broadened by rotation and pulsation.

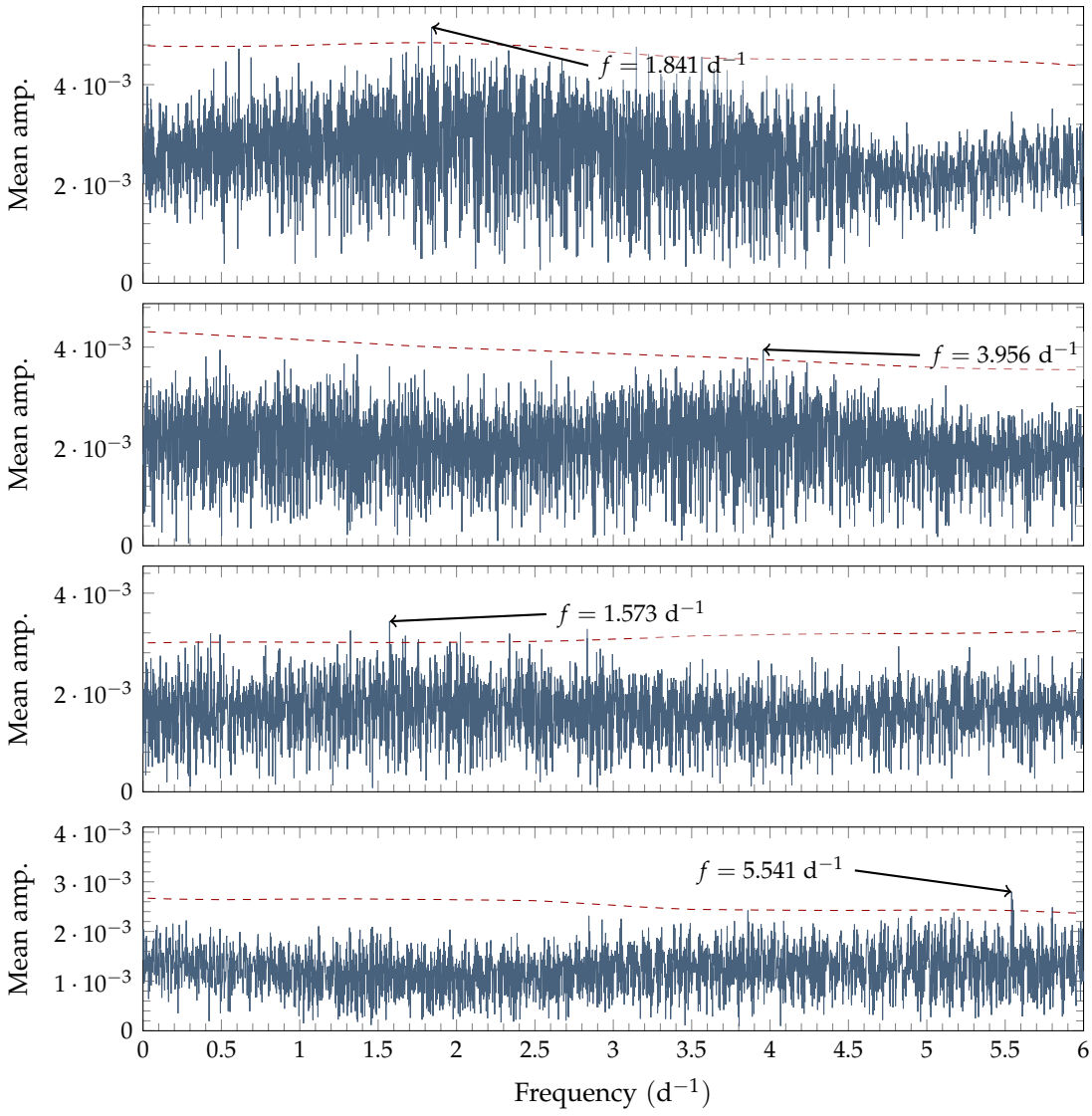

FIGURE 3.27: HD153580 HIPPARCOS photometry frequency selection process within FAMIAS. The dashed line represents the significance level at a signal-to-noise ratio of 4.

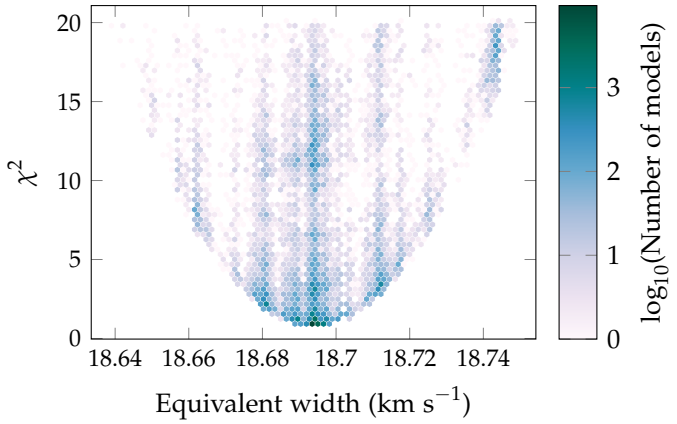

FIGURE 3.28: A hexagonally-binned histogram of modelled equivalent width values for the zero-point fit of HD153580.

velocity offset of the mean line profile – the so-called zero point fit (the fitted 'zero point' is the at-rest, non-distorted line profile). Owing to the normalization process done to these line profiles, FAMIAS was able to fit the zero-point with a reduced χ^2 of 0.922, giving an equivalent width of 18.69 km s^{-1}, intrinsic width of 15.87 km s^{-1}, velocity offset of -0.07875 km s^{-1}, and $v \sin i = 43.6$ km s^{-1}. Figures 3.28 illustrates the equivalent width values that have been explored. Only inclination, velocity amplitude, and phase have been allowed to vary for this fit: all other parameters remain fixed as in Table 3.4

Pursuant to Baade and Kjeldsen (1997), who report the appearance of γ Doradus-like pulsations line profile variations of azimuthal order between $8 \leq m \leq 14$, the parameter space has been widened further than usual during mode identification for this star. No γ Doradus-like pulsations with $\ell \geq 7$ have been confirmed in the past, and most have $\ell \leq 3$ (Brunsden, 2013). This would be an unusually high-order mode.

TABLE 3.4: The fundamental stellar parameters determined prior to the mode identification process. The $T_{\rm eff}$, $\log g$, mass, and [Fe/H] parameters have been interpolated by making a reasonable estimation based on the range of literature values reported in Table 3.1.

Parameter	Value
$T_{\rm eff}$	6400 K
$\log g$	4.1 (cm s^{-2})
Radius	1.6 $R_\odot$
Mass	1.4 $M_\odot$
[Fe/H]	0.15

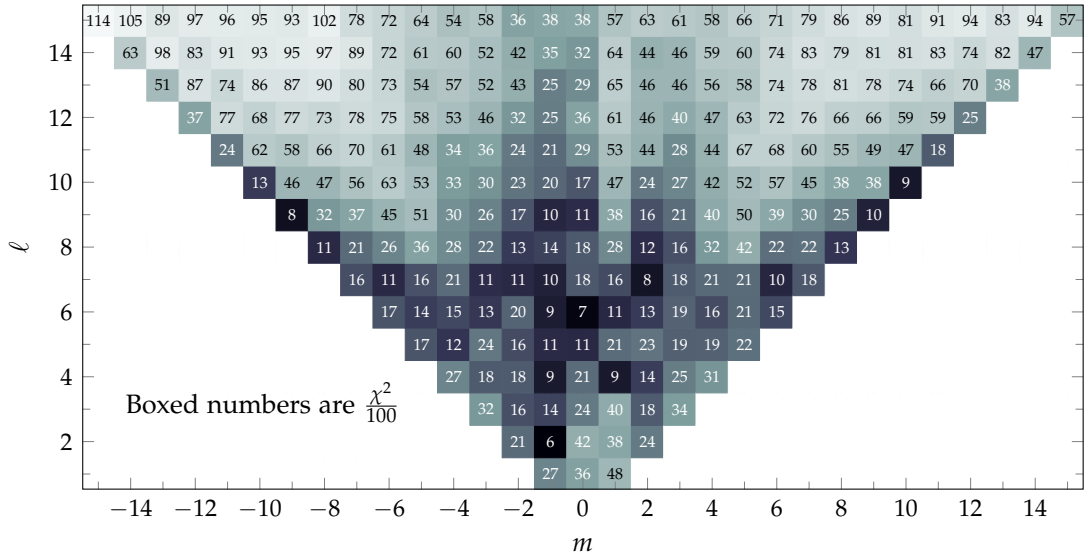

FIGURE 3.29: The lowest χ^2 values fitted for each ℓ and m combination found using FAMIAS. For clarity, the χ^2 values are colourmapped and divided by 100.

Because of the strongly bimodal shape of the standard deviation profiles for $f_1 = 0.6589$ d^{-1} in Figure 3.18, with one clearly visible phase transition about the centre of the line profile, it is expected that a best-fit mode will have $\ell - |m| = 1$.

Prior to further fitting, the velocity offset value was changed to 1.6 km s^{-1}: this change aided the fitting process as it is the location of the bottom of the central dip in the standard deviation profiles for $f_1 = 0.6589$ d^{-1}. It is also the central radial velocity value of the phase transition visible in that frequency. By adjusting for this radial velocity offset, where the central minimum of the standard deviation profiles does not quite match the centre of the zero-point profile, this asymmetry is then discounted from the fitting process. The dispersion range was restricted slightly further to ± 70 km s^{-1}, which excludes the sharp phase transition seen past $+70$ km s^{-1} in Figure 3.18. Since this transition occurs in the far wing of the line profile, is not mirrored at -70 km s^{-1}, and there is no significant change in the amplitude of the standard deviation profile, it is assumed to be an artefact. Therefore excluding this transition will improve the fitting.

Figures 3.29 illustrates the search for the best-fit degree ℓ and azimuthal order m modes. The radius, mass, and other stellar parameters were fixed as per Table 3.4, and inclination allowed to vary between 5° and 90° in increments of 0.1°. The 'Fit AP' mode within FAMIAS was used, which excludes the zero-point fit from the χ^2 optimization process and bases its computations on the standard deviation profiles, rather than the much more computationally expensive time-series modelling. A grid search was carried out that iteratively analyses each (ℓ, m) combination for the optimal fit.

TABLE 3.5: The ℓ and m combinations of HD153580 with $\chi^2 < 1000$. The best-fit parameters for each mode combination are described below.

(ℓ, m)	χ^2	Incl.($^\circ$)	Vel. Amp. (km s^{-1})	Phase
$(2, -1)$	628	66.7	0.772	0.585
$(4, -1)$	886	38.9	1.91	0.585
$(4, 1)$	876	72.4	0.001	0.582
$(6, -1)$	913	29.8	7.31	0.586
$(6, 0)$	671	54.3	1.16	0.590
$(7, -1)$	974	20.4	9.27	0.585
$(7, 2)$	823	33.6	3.85	0.585
$(9, -9)$	770	85.3	55.1	0.591
$(10, 10)$	856	88.0	44.1	0.583

Table 3.5 lists the most likely pulsation modes identified using the grid search technique. These fits of these modes are plotted in Figures 3.30 and 3.31, where it can be seen that some of the modes display a poor zero-point fit due to excessive pulsational broadening of the line profile. They would inevitably have a much higher χ^2 value were the zero-point values taken into account in its computation. The figures show that the $(\ell, m) = (2, -1)$ mode has the best visual fit when accounting for the zero-point, standard deviation, and phase fits, as well as having the lowest χ^2 by a factor of $\Delta\chi^2 = 43$. Some of the fits (particularly where $\ell \gtrsim 9$) also have unrealistically large velocity amplitudes and high inclination angles.

Figure 3.32 shows that the best-fit inclination is around 67° based on the $(\ell, m) = (2, -1)$ mode identification, while the other possible modes do diverge from this determination (see Table 3.5).

At a radius of $R = 1.6$ R$_\odot$, $v \sin i = 43.6$ km s^{-1}, and inclination $i = 67^\circ$, the rotational frequency of the star is calculated as 0.585 d^{-1}. This is the main source of doubt over the mode identification. Because the frequency of $f_1 = 0.6589$ d^{-1} is faster than the rotational frequency, this implies a prograde mode, as opposed to the retrograde $(\ell, m) = (2, -1)$ determination. A smaller radius or lower inclination could raise the rotational frequency above this threshold; for example, a radius of 1.5 R$_\odot$ and inclination of 60° results in $f_{\rm rot} = 0.663$ d^{-1}. The presence of the secondary component also renders some uncertainty over the $v \sin i$ value. Within any reasonable variation of the parameters, the rotation and pulsation frequencies remain quite close together. Despite this, the most likely mode is with $(\ell, m) = (2, -1)$, and $\chi^2 = 632$. The reason why the χ^2 values are unusually high is because the variations themselves are very strongly defined by the observations. Thus, the statistical significance of discrepancies between the model and the observations is greater. With only a single significant frequency,

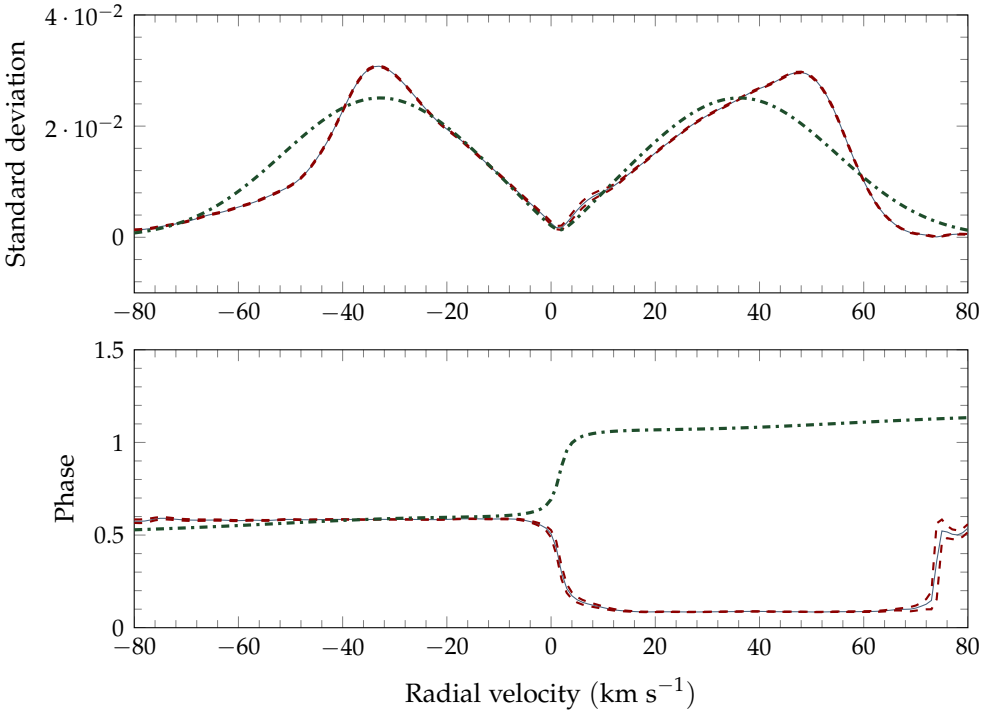

FIGURE 3.30: The mode identification for $f_1 = 0.6589$ d^{-1} (dash-dotted), laid over the least-squares fitted profiles (solid, with dashed uncertainties). The best-fitted mode by a significant margin is a $(\ell, m) = (2, -1)$ mode.

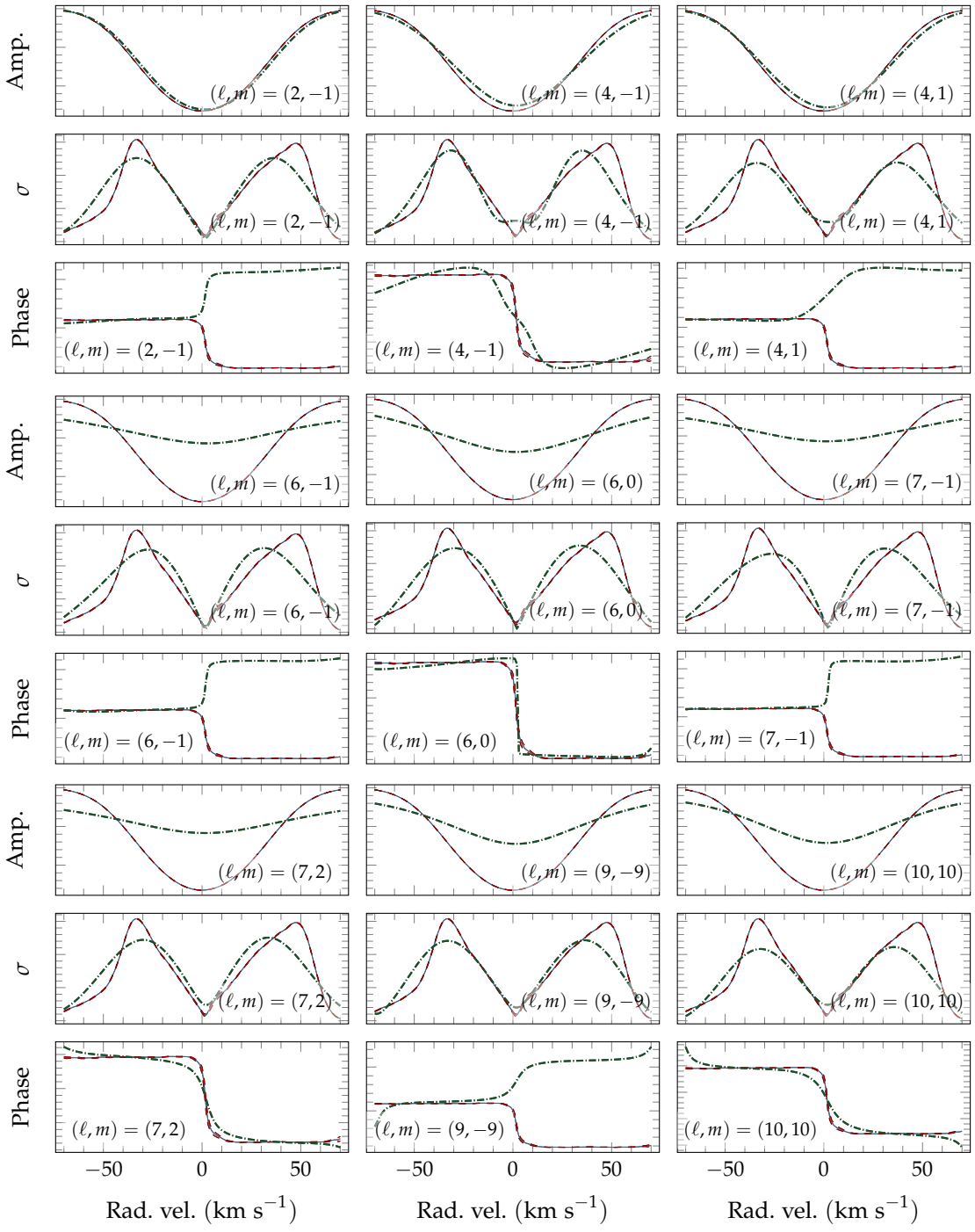

FIGURE 3.31: The best-fitted modes for $f_1 = 0.6589$ d^{-1}, corresponding to the parameters listed in Table 3.5. Plotted are the zero-point, pulsation amplitude, and phase fits for each of the indicated modes (dash-dotted lines), as well as the least-squares fitted profiles for $f_1 = 0.6589$ d^{-1} (solid, with dashed uncertainties).

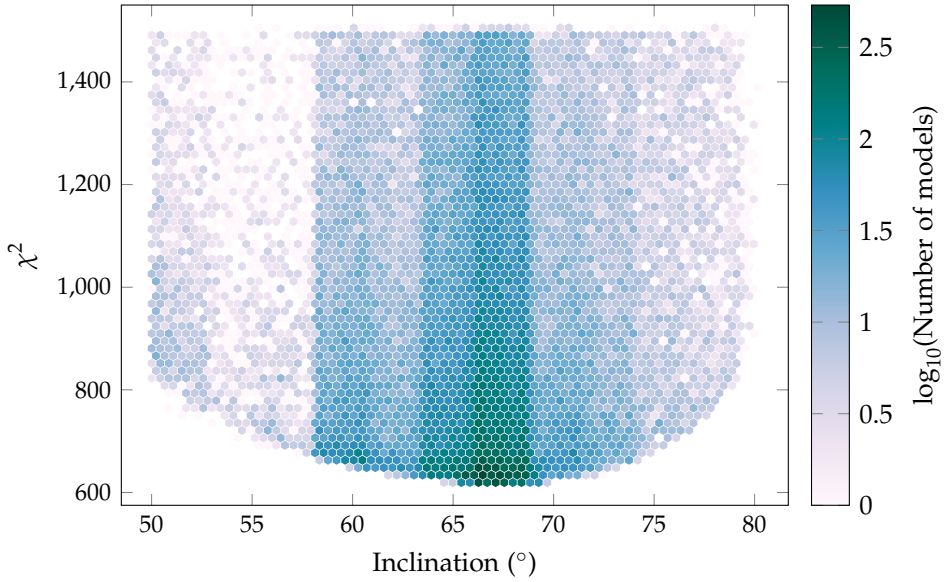

FIGURE 3.32: A hexagonally-binned histogram of modelled inclination values of HD153580, for $f_1 = 0.6589$ d^{-1} as an $(\ell, m) = (2, -1)$ mode.

determining the mass and radius during mode identification were unsuccessful, with no value having a significantly lower χ^2 over another.

3.5 DISCUSSION

The primary component has been observed to pulsate at $f_1 = 0.6589$ d^{-1}, as an $(\ell, m) = (2, -1)$ mode. This frequency accounts for 81.3% of all observed line profile variations, and most of the remaining variations are due to the secondary (binary) component. The suggestion by Baade and Kjeldsen (1997) that HD153580 could show γ Doradus-like line profile variations due to pulsational modes with high azimuthal orders between $8 \leq m \leq 14$ is not supported here.

No further pulsations have been found, making this a bona fide γ Doradus star. It is also a single-mode star, unless other modes exist with amplitudes of only a few per cent or less of the primary mode. The presence of the secondary component precludes any abundance analysis, as either sophisticated deconvolution or a space-based spectrograph would be required in order to disentangle the spectra. Given the inclination angle of 67° is well away from the IACC (as discussed in Section 1.2.4), it is unclear why this significantly strong pulsation is not strongly visible in HIPPARCOS photometry – it is most likely that the data are simply too sparse, but perhaps the frequencies of HD153580 are unstable and vary over timescales greater than our short observational campaign (although this is unlikely). A possible hypothesis is that this non-sectoral,

retrograde mode has had its photometric variability suppressed owing to the effects of its inclination and equatorial waveguide effects.

It is possible that the numerous frequencies identified in the secondary component are real. However, there is not sufficient resolution in the radial velocity space to identify the modes. The standard deviation plots show a single peak associated with the secondary component, which no non-radial pulsation can produce, though effective temperature variations could produce that shape. Another possibility is that there are truly multiple peaks, but these have not been resolved owing to the limited resolution of the spectrograph. Because none of the frequencies found have significantly reduced the variability of this peak, the frequency identification remains uncertain. The dimmer magnitude of the secondary star also presents problems: at a magnitude of $m_V = 8.65$, the facilities at MJUO simply will not be able to produce spectra with both an adequate signal-to-noise ratio and sufficient temporal resolution. Thus it remains a task for larger observatories to investigate the secondary component further.

The most likely explanation for the variations observed in the secondary star is simply that of the effects of atmospheric seeing. Slight errors in guiding and variations in seeing throughout the night will result in the secondary component having a variable, but non-periodic, influence in the resulting spectra.

It is curious that there is only one observed pulsation frequency that accounts for any significant variation in the primary component. What physical conditions could cause only one pulsation frequency to be observable? Guzik et al. (2000) note that the number of excited modes decreases as the convection zone depth increases. Thus it is theoretically probable that a cooler star, such as HD153580, will only have one g-mode. The cool effective temperature of HD153580 is also interesting. It is not a unique observation that HD153580 lies within the δ Scuti instability strip yet does not show any δ Scuti pulsations (Handler and Shobbrook, 2002), yet this star lends further credence to the idea that a γ Doradus star is *less likely* to show δ Scuti pulsations than a non-γ Doradus star in a similar location on the HR diagram (Handler and Shobbrook, 2002).

4

HD139095

HD139095 (otherwise known as NX Lup or HIP76485) is a bona fide (Handler and Shobbrook, 2002) γ Doradus star in the constellation Lupus, at coordinates 15 h 37 m 16.94 s, -32° 03′ 26.37″ (J2000 epoch, van Leeuwen, 2007). HIPPARCOS data places the star at a distance of 118 pc from the Sun (van Leeuwen, 2007), and it has a spectral type of A9/F0 V (Houk, 1982).

HD139095 was initially categorized by Handler (1999) using HIPPARCOS photometry, where there was some uncertainty between whether it belonged to the γ Doradus or δ Scuti class of variable stars. A single photometric period of 0.634 d was discovered from HIPPARCOS data. Handler and Shobbrook (2002) later found no evidence of δ Scuti-like photometric variability within a limit of 1.1 mmag, but did observe multi-periodic γ Doradus-like variability and classified HD139095 as a bona fide γ Doradus star. However, no further frequencies were confirmed.

4.1 OBSERVATIONS

The primary data set for this analysis is 278 spectra taken at MJUO. Figure 4.1 shows a small portion of the mean stellar spectrum and Figure 4.2 shows the resultant cross-correlated line profiles. Typical exposure times were 30 minutes through the 100 μm fibre, as the star is reasonably dim ($m_V = 7.9$) and it can be difficult to get a good signal-to-noise ratio. Supporting the spectroscopic data are 70 HIPPARCOS observations, and the first photometric frequency found (also discovered by Handler and Shobbrook, 2002) reinforces the identification of one of the spectroscopic frequencies.

TABLE 4.1: A summary of properties of HD139095 from the literature. Henry et al. (2011) cite Handler and Shobbrook (2002) as the source for these data, but it is not clear from Handler and Shobbrook where the colour index, luminosity, and radius data come from. The period listed is the dominant period found in photometric data.

V (mag)	$B-V$ (mag)	M_V (mag)	L ($L_\odot$)	R ($R_\odot$)	Period (d)	Reference
7.91	0.366	2.62	7.0	1.9	0.634	Handler and Shobbrook (2002)

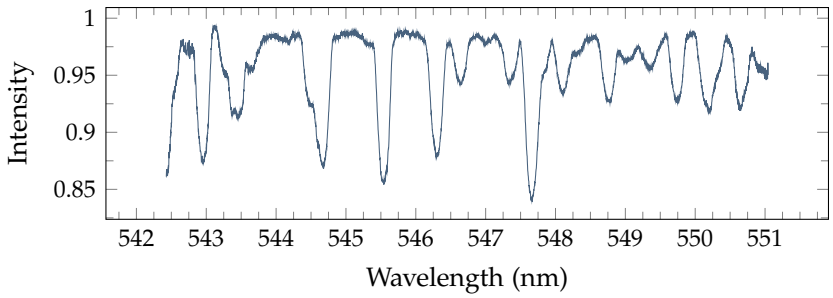

FIGURE 4.1: The mean spectrum of HD139095, across MJUO spectral order 104.

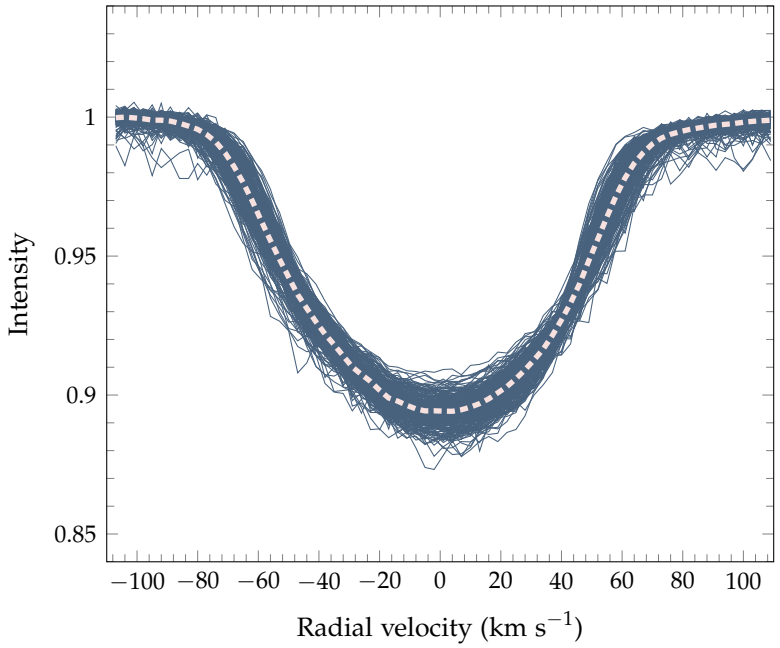

FIGURE 4.2: Radial velocity line profiles for HD139095, with the dashed line representing the mean line profile.

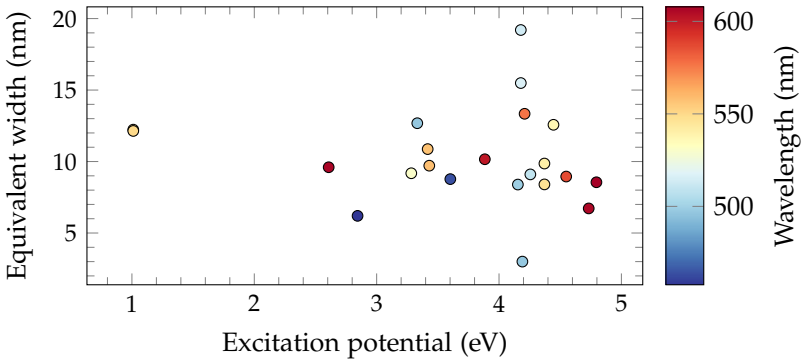

FIGURE 4.3: The excitation potential versus equivalent width for HD139095.

4.2 ABUNDANCE ANALYSIS AND STELLAR PARAMETER ESTIMATION

The abundance analysis methods described in Section 2.4 are used to determine the fundamental stellar parameters of HD139095. The number of usable spectral lines for the FUNDPAR method in the mean spectrum of HD139095 is relatively small as a result of line blending, and only 21 Fe I lines were chosen for analysis as too few Fe II lines were available.[1] Figure 4.3 shows that there is no correlation between the excitation potential and equivalent width of the spectral lines analysed using the equivalent width method. A lack of correlation is best in order to converge to a good solution. SPECTRE was used to measure the equivalent widths, and these measurements are tabulated in Table D.2.

The spectral synthesis method, using SME, was used in conjunction with a VALD linelist (Kupka et al., 2000) to derive the fundamental stellar parameters listed in Table 4.2. Accurate uncertainty measurements are difficult, but Valenti and Fischer (2005) find, in a survey of 1,040 cool stars using SME, a per-spectrum precision of 44 K in $T_{\rm eff}$, 0.03 dex in [M/H], and 0.06 dex in $\log g$. Certainly, the correlation between spectral synthesis and equivalent width analysis is less obvious than hoped. The effective temperatures match to a reasonable degree. However, the surface gravity result from SME is questionably small. SME also reports a macroturbulence value of 17.5 km s^{-1}.

It is not certain why SME returns a clearly unreasonable $\log g$ value. However, the $\log g = 3.99$ from FUNDPAR is reasonable to expect from a γ Doradus star. The most likely scenario is that the relatively high $v \sin i$ of HD139095 is preventing the stellar parameters from being constrained simultaneously. Both results do show that the star likely has a slightly higher microturbulence than a typical value of 2 km s^{-1}, and is slightly more metal rich than the Sun.

1 FUNDPAR requires at least one Fe II line in the linelist or the program will run in an infinite loop. The workaround is to include at least one Fe II line in the linelist (arbitrary numbers will suffice) and excluding Fe II lines from the χ^2 analysis.

TABLE 4.2: The abundance analysis results from both SME and FUNDPAR, showing a large discrepancy in $\log g$ values.

	$T_{\rm eff}$ (K)	$\log g$	$v \sin i$ (km s^{-1})	$v_{\rm mic}$ (km s^{-1})	$v_{\rm mac}$ (km s^{-1})	[M/H]	[Fe/H]
SME	7092	3.51	63.6	2.7	17.5	0.071	
FUNDPAR	6921	3.99		2.29			0.26

4.3 FREQUENCY ANALYSIS

Both the spectroscopic data from MJUO and photometric data from HIPPARCOS (Perryman et al., 1997) were used in order to determine the pulsation frequencies of HD139095. The *period* of 0.634 d found by Handler and Shobbrook (2002) by photometry has potentially been rediscovered spectroscopically as the *frequency* $f_{2b} = 1.5972$ d^{-1}; however, there is a small discrepancy between the photometric and spectroscopic frequencies. Four possible frequencies have been identified spectroscopically, using both the discrete Fourier transform methods in FAMIAS and the more sophisticated algorithms of SIGSPEC.

4.3.1 *Spectroscopic frequency analysis*

Figure 4.4 shows the spectral window, indicating that although there is some 1-day aliasing, the Fourier spectra do have a temporal spread that reasonably suppresses other degrees of aliasing. Figure 4.5 shows the pixel-by-pixel, two-dimensional Fourier periodogram computed by FAMIAS. Complementary to this is Figure 4.6, which summarizes the two-dimensional results computed using SIGSPEC rather than FAMIAS, and plotting the ten most significant frequencies found at each pixel in the line profile. The presence of several frequency peaks indicates that there is a rich range of frequencies to be analysed. Although the chosen radial velocity resolution in Figure 4.6 is 1 km s^{-1}, the data in the rest of this chapter have been processed at a radial velocity resolution of 3 km s^{-1}. The 1 km s^{-1} resolution allows a better visual distinction of the common pulsation frequencies in the SIGSPEC analysis, but in other cases the noise reduction by using coarser bins is advantageous. The results in Figure 4.6 are also presented in Table 4.3.

Figures 4.7 to 4.11 illustrate the iterative process of frequency discovery in FAMIAS, where the highest-detected frequency peaks are successively pre-whitened until further detections are not significantly distinguishable from the noise. The frequencies found using these methods are summarized in Table 4.3, which also includes the SIGSPEC results for the zeroth to third moments.

Table 4.3 lists the frequencies found that are of a reasonable level of significance, with either a SIGSPEC significance ≥ 10, or those that are detected clearly above the noise floor in FAMIAS. Four frequencies, $f_1 = 1.2263$ d^{-1}, $f_2 = 0.59460$ d^{-1}, $f_4 =$

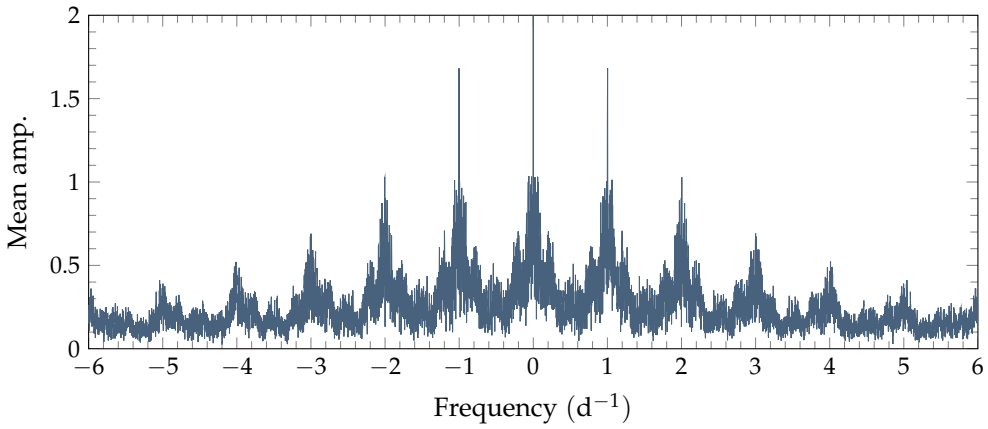

FIGURE 4.4: The spectral window of the MJUO observations.

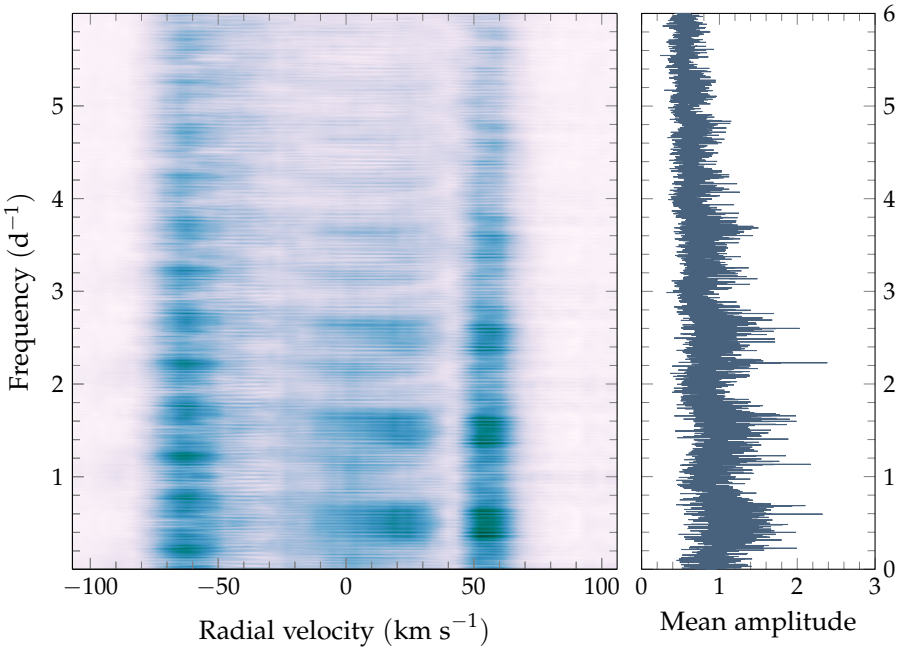

FIGURE 4.5: The two-dimensional Fourier periodogram of the MJUO spectroscopic data (left), with darker colours on the colourmap representing frequency peaks. On the right is the mean Fourier periodogram across all pixels.

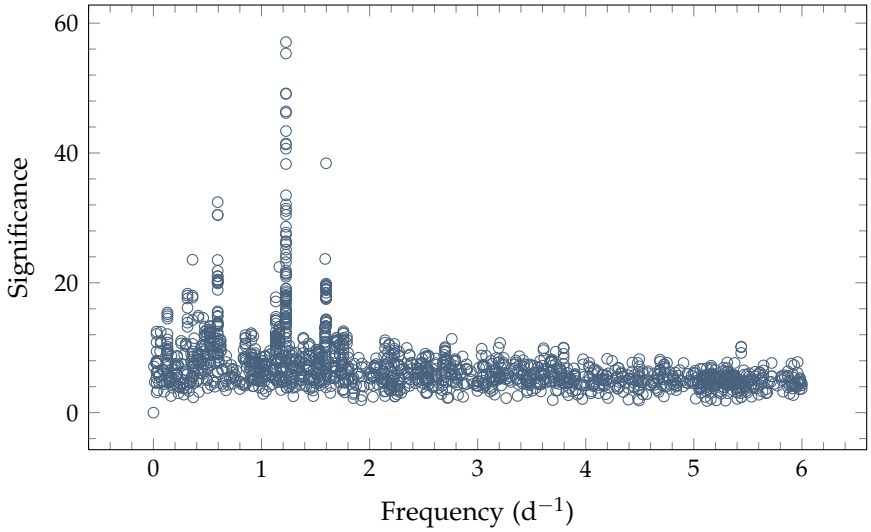

FIGURE 4.6: A visualization of the pixel-by-pixel SIGSPEC analysis for HD139095. For each radial velocity pixel of the line profile, SIGSPEC analyses the time series data and outputs the ten most prominent frequencies with their corresponding significance levels. Each frequency found in each radial velocity bin is plotted. In contrast to the rest of the analysis, a radial velocity resolution of 1 km s^{-1} was used here, as it visually enhances the number of frequency detections.

1.1323 d^{-1}, and $f_5 = 1.3871$ d^{-1} have been found with multiple detections. These are the frequencies chosen for further analysis, as no others have been identified with sufficient confidence. A cautionary note is that the distinction between $f_{2b} = 1.5972$ d^{-1} and $f_2 = 0.59460$ d^{-1} is not entirely clear: one is almost certainly an alias of the other; however, which is the true frequency is not certain at this stage of the analysis. The errors in these frequencies are estimated in Table 4.4. Based on Equation 2.3 and a signal-to-noise estimation of 100, the error in frequencies detected by FAMIAS can be estimated as 7×10^{-6} d^{-1}. This may be an under-estimate and so should be treated with caution.

4.3.2 *Photometric frequency analysis*

The HIPPARCOS data suffer from a poor number of observations, and as such no frequencies have been identified photometrically. The period previously reported in the literature of 0.634 d ($f = 1.58$ d^{-1}) is very close to $f_{2b} = 1.5972$ d^{-1}, so it is probable there is a dual detection and that uncertainties in the photometrically detected frequency are responsible for the discrepancy. The least-squares fitted line profile variations at the photometrically detected frequency $f_{p1} = 1.5780$ d^{-1}, as seen in Figure 4.14, do not show a significantly recognizable pattern. Figure 4.13 also shows a possi-

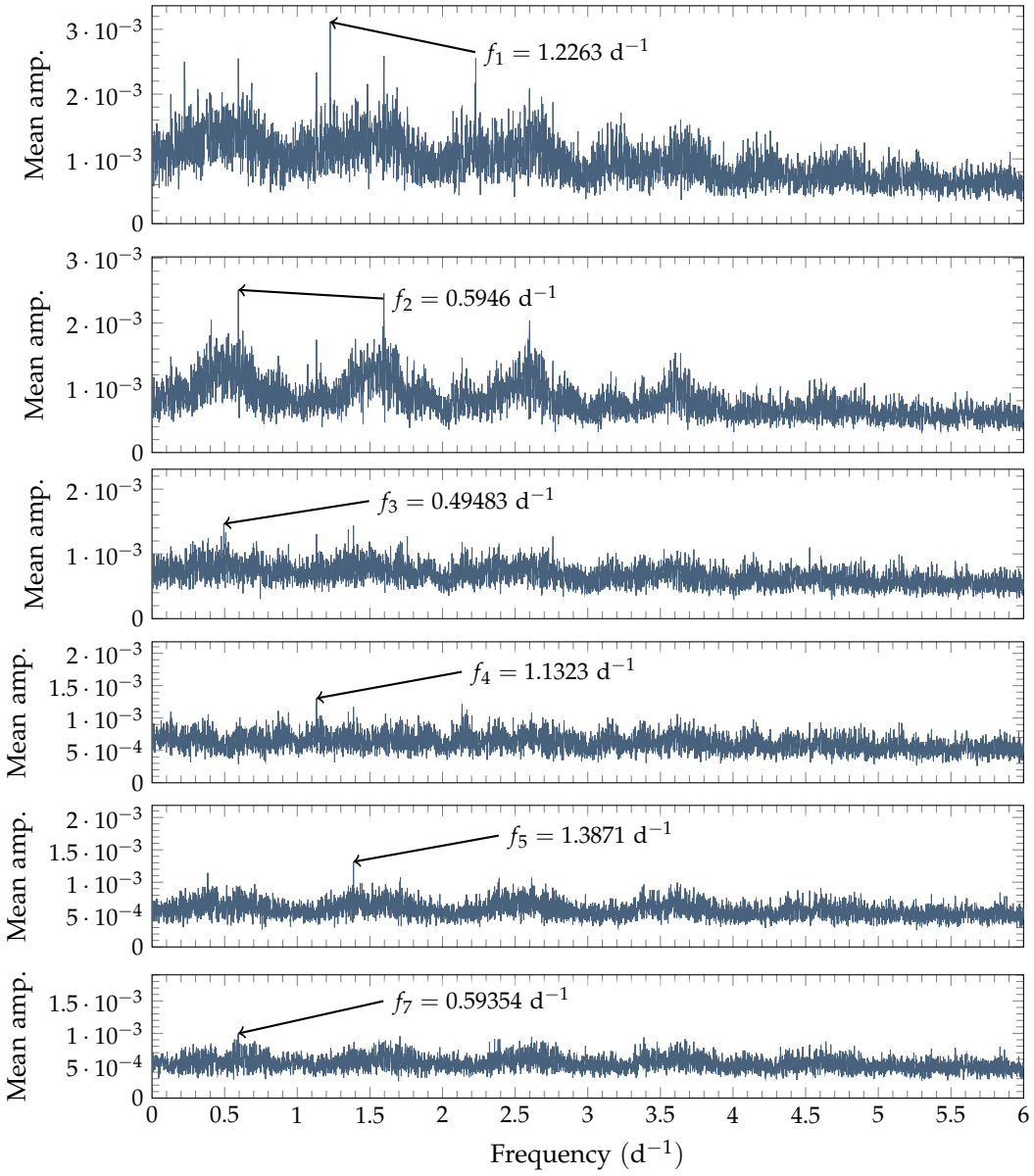

FIGURE 4.7: The pixel-by-pixel Fourier pre-whitening process, performed in FAMIAS.

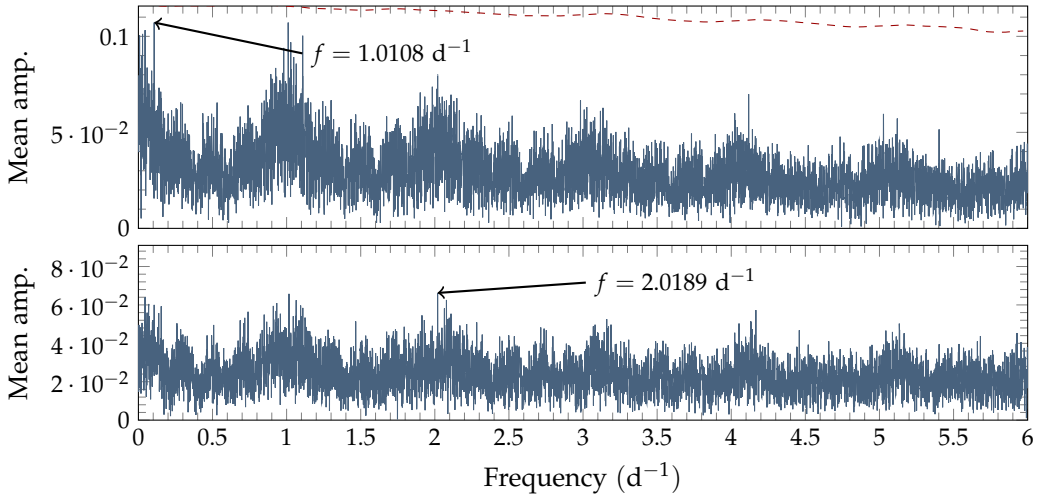

FIGURE 4.8: The Fourier spectrum frequency selection process for HD139095, computed using the zeroth moment of the moment method in FAMIAS. The dashed line represents the significance level at a signal-to-noise ratio of 4.

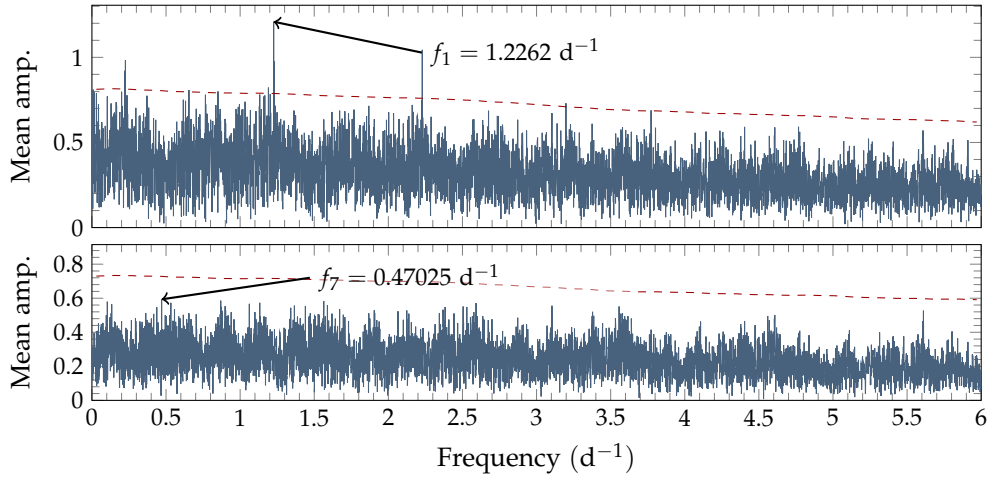

FIGURE 4.9: The Fourier spectrum frequency selection process for HD139095, computed using the first moment of the moment method in FAMIAS. The dashed line represents the significance level at a signal-to-noise ratio of 4.

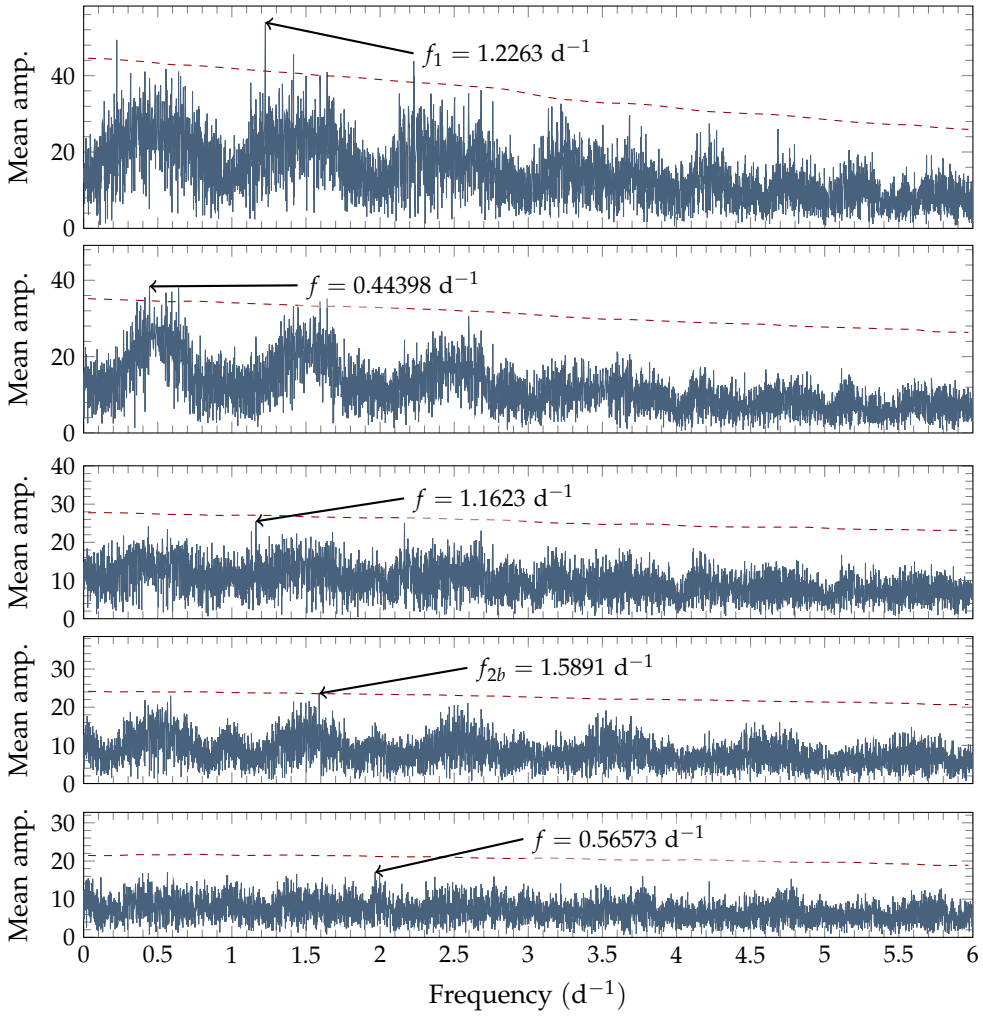

FIGURE 4.10: The Fourier spectrum frequency selection process for HD139095, computed using the second moment of the moment method in FAMIAS. The dashed line represents the significance level at a signal-to-noise ratio of 4.

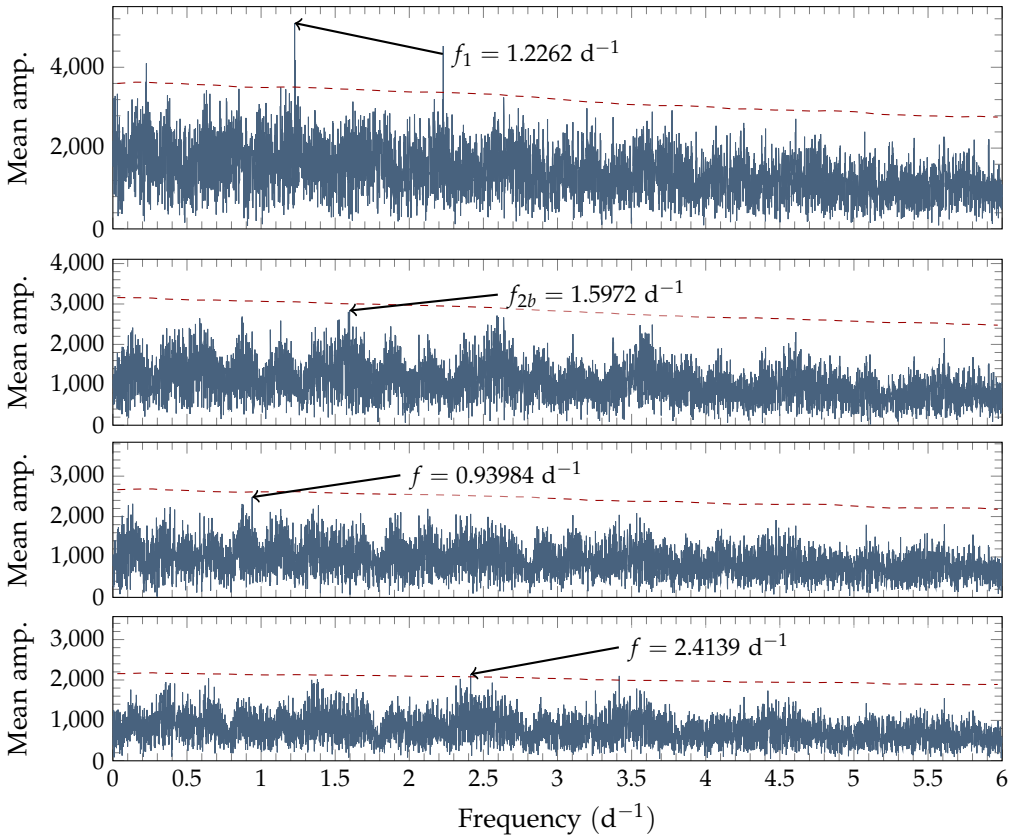

FIGURE 4.11: The Fourier spectrum frequency selection process for HD139095, computed using the third moment of the moment method in FAMIAS. The dashed line represents the significance level at a signal-to-noise ratio of 4.

TABLE 4.3: A summary of frequencies found using the progressive pre-whitening process of FAMIAS as well as the frequency analysis tool SIGSPEC. Frequencies reasonably above the significance limits of FAMIAS, or with a SIGSPEC significance $\gtrsim 10$, have been reported.

	FAMIAS	SIGSPEC	
Label	Frequency (d^{-1})	Frequency (d^{-1})	Significance
Pixel-by-pixel			
f_1	1.2262	1.2263	57
f_2	0.59460	0.59446	32
f_3	0.49483		
f_4	1.1324	1.1323	15
f_5	1.3871		
f_6	1.7073		
Zeroth moment			
None of significance			
First moment			
f_1	1.2262	1.2262	27
f_7	0.47025		
Second moment			
f_1	1.2263	1.2263	21
f_{2b} and f_2	1.5891	0.59460	13
f_5		1.3872	11
Third moment			
f_1	1.2262	1.2262	26
f_{2b}	1.5972	1.5973	12

TABLE 4.4: An estimation of the uncertainty in the observed frequencies, based upon Equation 2.2 and dependent on an observation timebase T and the spectral significance (sig) from SIGSPEC. The observation timebase used, of 69 days, is equal to the number of nights that spectra were taken on.

Frequency	sig	Error estimation (d^{-1})
$f_1 = 1.2263\ d^{-1}$	57	0.002
$f_2 = 0.59460\ d^{-1}$	32	0.003
$f_{2b} = 1.5972\ d^{-1}$	12	0.004
$f_4 = 1.1323\ d^{-1}$	15	0.004
$f_5 = 1.3871\ d^{-1}$	11	0.004

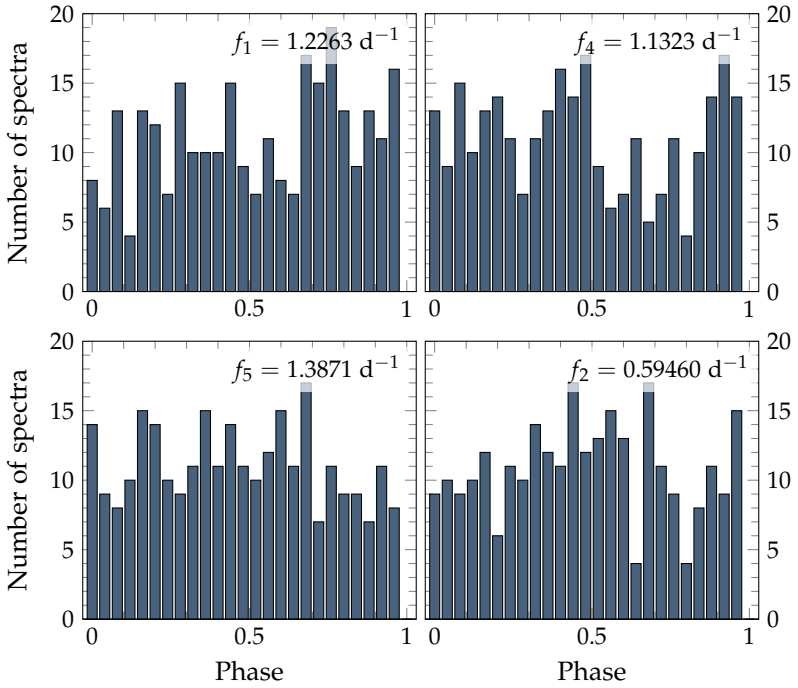

FIGURE 4.12: Phase coverage histograms for the indicated frequencies.

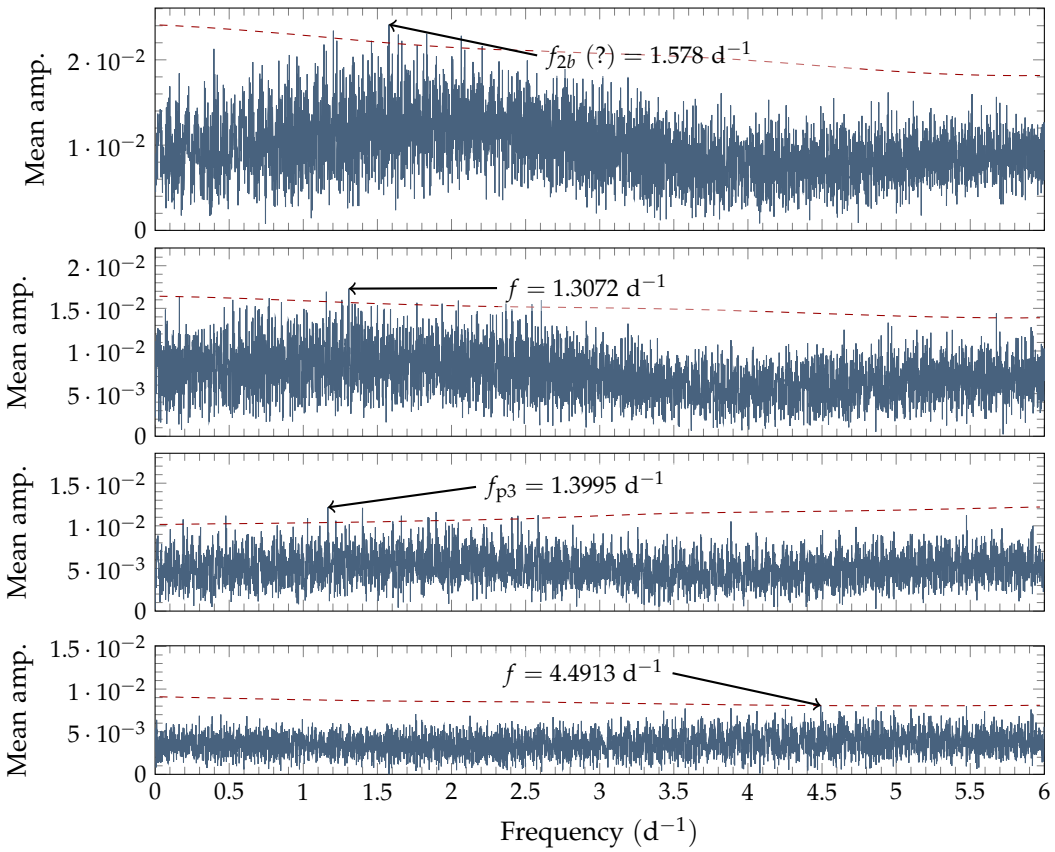

FIGURE 4.13: The Fourier spectrum frequency selection process for HD139095, using the photometric HIPPARCOS data. The dashed line represents the significance level at a signal-to-noise ratio of 4.

ble match between $f_5 = 1.3871$ d^{-1} and $f_{p3} = 1.3995$ d^{-1}. However, once again, the frequency peaks are barely above the noise level so the detection could be pure chance.

The pulsation frequencies $f_1 = 1.2263$ d^{-1}, $f_4 = 1.1323$ d^{-1}, $f_5 = 1.3871$ d^{-1}, and $f_2 = 0.59460$ d^{-1} have been chosen as candidates for mode identification, as they are the only frequencies that have been detected more than once, in the pixel-by-pixel and moment methods of both FAMIAS and SIGSPEC. It is apparent that HD139095 probably has many modes of pulsation, as nearly 75% of the line profile variations still remain after removal of these four frequencies. Although the relatively noisy data and somewhat low number of observations may contribute to this, it is still probable that several more modes remain undetected.

Figure 4.15 shows the residual variation of each frequency once the other frequencies have been removed, while Table 4.5 and Figure 4.17 describe the proportion of line profile variations that is explained by including each frequency. Figure B.1 shows the theoretical line profiles of HD139095 at each of the final frequencies, modelled with

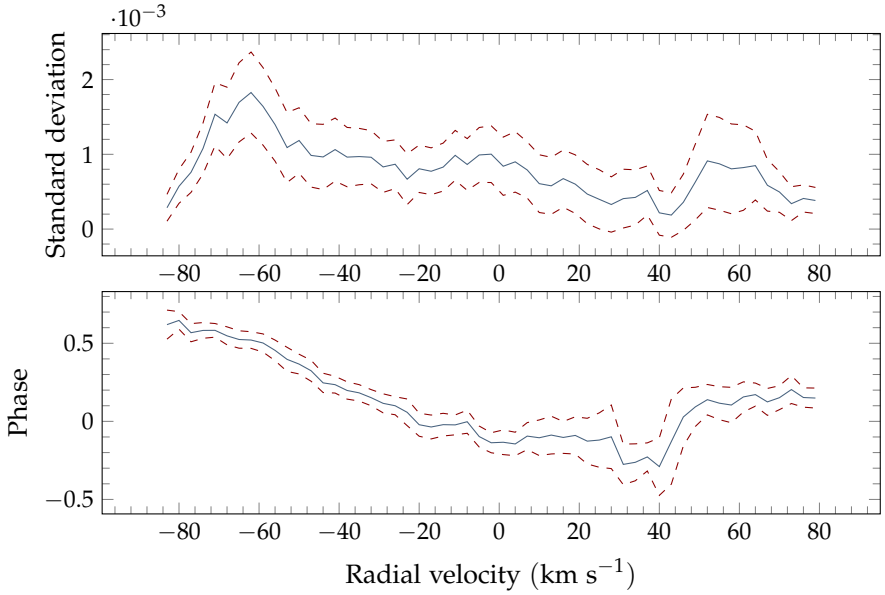

FIGURE 4.14: The least-squares fitted line profile variations of HD139095 at $f_{p1} = 1.5780$ d^{-1}.

the parameters shown in Table 4.7. The general shape of the pulsations is matched well. However, noise does impede the clarity of results. In order to try to resolve the uncertainty between $f_2 = 0.59460$ d^{-1} and $f_{2b} = 1.5972$ d^{-1}, the phased line profile variations are inspected for each frequency, as in Figure 4.16. The frequency $f_{2b} = 1.5972$ d^{-1} does appear to show cleaner variations. However, this frequency does not explain as great a proportion of the variations as $f_2 = 0.59460$ d^{-1} (see Table 4.5).

Another method of comparison between the two frequencies is to examine the least-squares fitted standard deviation profiles for $f_2 = 0.59460$ d^{-1} and $f_{2b} = 1.5972$ d^{-1}. In Figure 4.18, the profiles for these two frequencies are compared, and it can be seen that they have very similar standard deviation profiles, however $f_2 = 0.59460$ d^{-1} has a stronger indication of a fourth bump at around -40 km s^{-1}. Combined with the slightly smaller margins of error in the standard deviation amplitude plots, this is another point in favour of $f_2 = 0.59460$ d^{-1}; but $f_{2b} = 1.5972$ d^{-1} still cannot be ruled out.

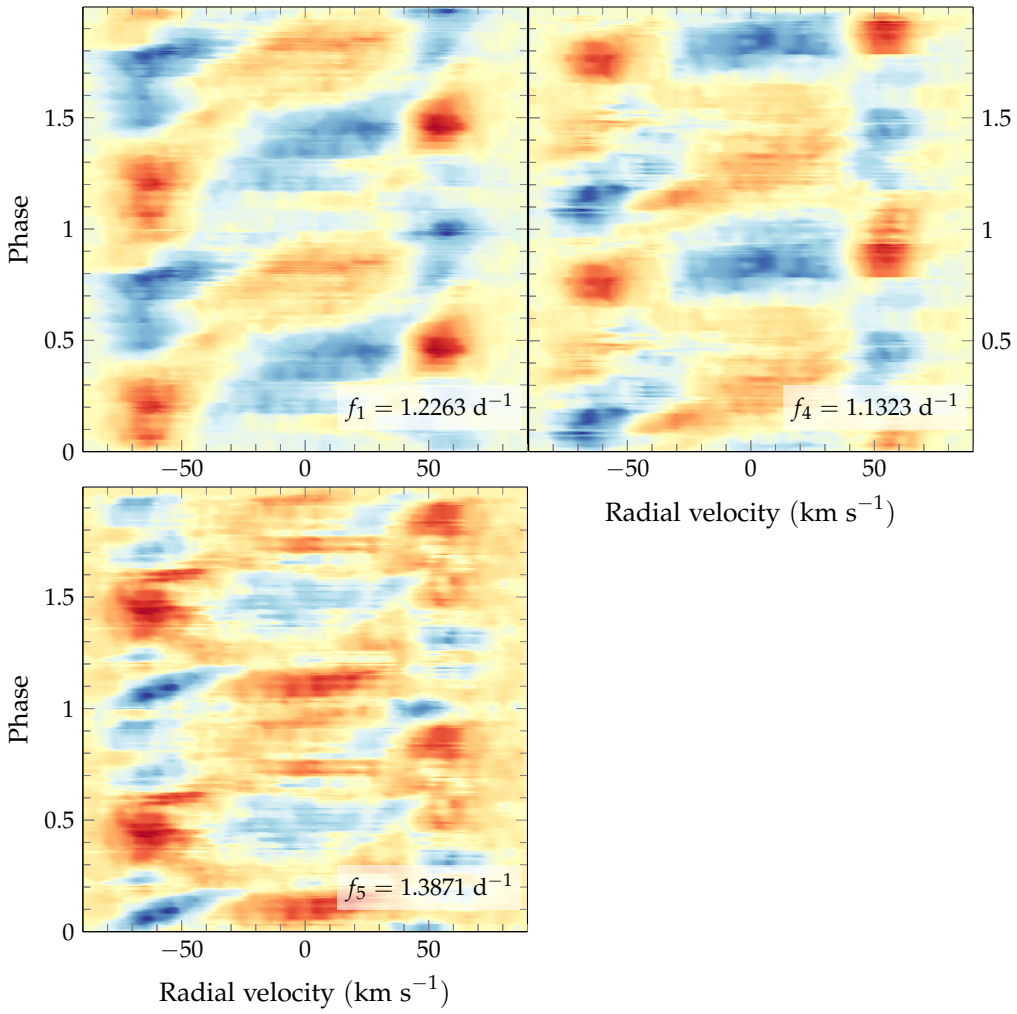

FIGURE 4.15: The residual (i.e. the after mean has been subtracted) line profile variations phased to each of the indicated frequencies that are the top candidates for mode identification. In each case, the observations have been pre-whitened by the other three frequencies. A median filter is used to smooth the appearance of the data.

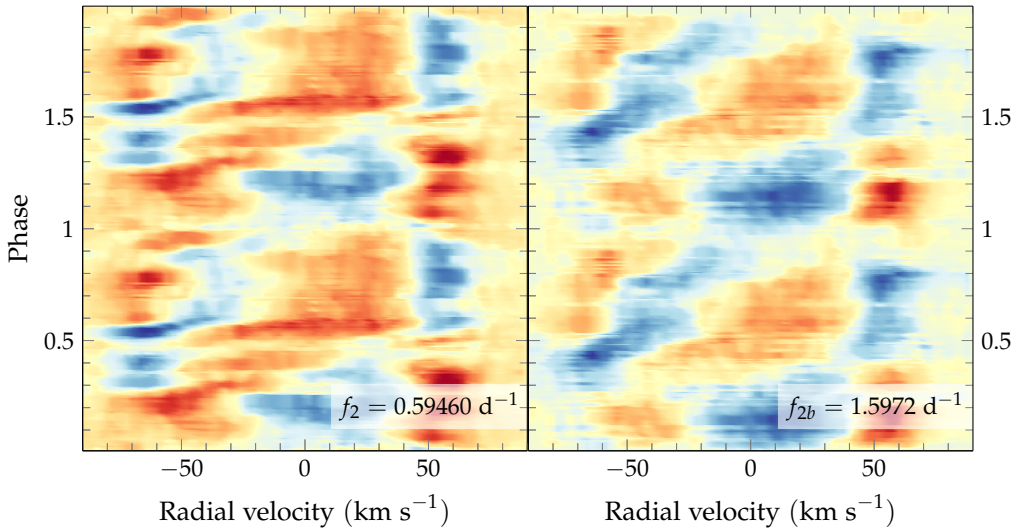

FIGURE 4.16: A comparison between the residual line profile variations of HD139095, phased to $f_2 = 0.59460$ d^{-1} and $f_{2b} = 1.5972$ d^{-1}. A median filter is used to smooth the appearance of the data.

TABLE 4.5: The proportion of line profile variations (in terms of the mean standard deviation across the line profile, σ) explained by the cumulative pre-whitening of detected frequencies. Note that $f_2 = 0.59460$ d^{-1} is able to explain a greater portion of the observed line profile variations than $f_{2b} = 1.5972$ d^{-1}.

Frequencies removed	σ	% of σ explained
—	0.009414	—
f_1	0.004328	12.26%
$f_1 + f_4$	0.004093	17.04%
$f_1 + f_4 + f_5$	0.003898	20.98%
$f_1 + f_4 + f_5 + f_{2b}$	0.003652	25.97%
$f_1 + f_4 + f_5 + f_2$	0.003519	28.67%

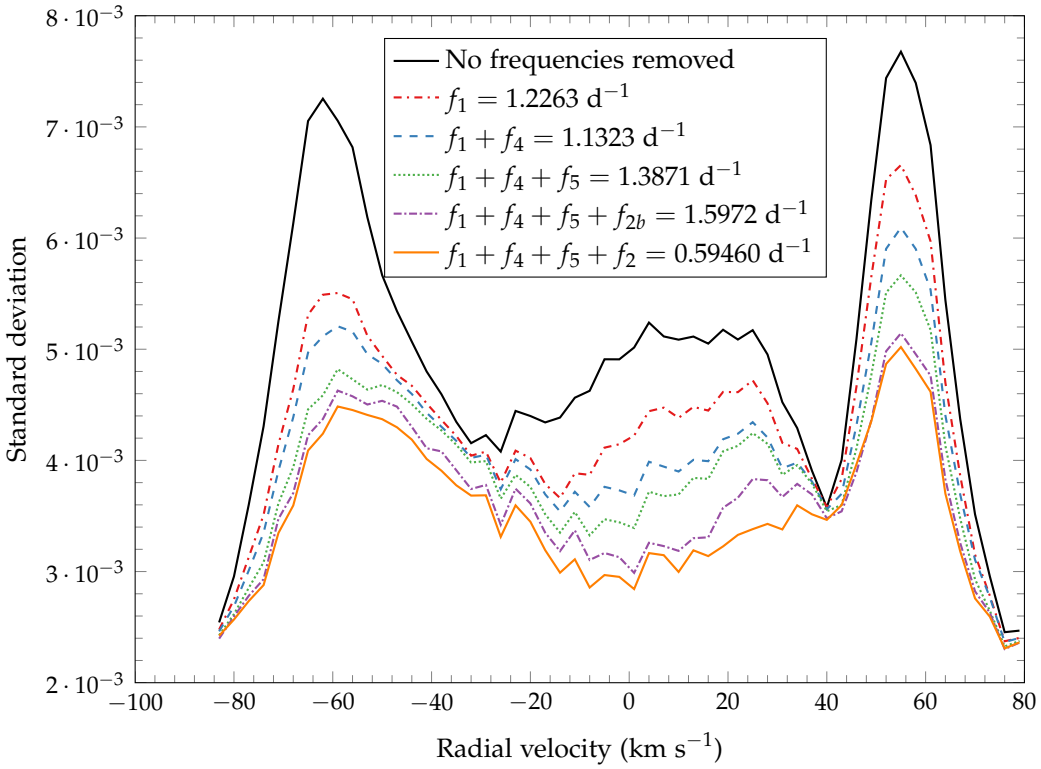

FIGURE 4.17: Per-pixel standard deviations across the line profile of HD139095, demonstrating the effects of progressive pre-whitening by the indicated frequencies.

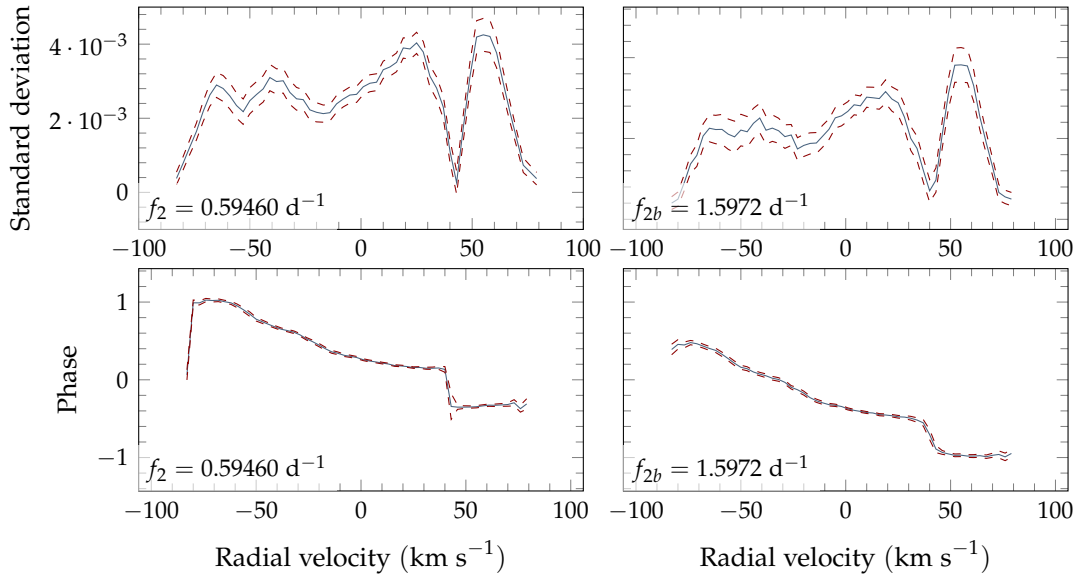

FIGURE 4.18: Plotted are the standard deviation and phase fits for $f_{2b} = 1.5972$ d^{-1} and $f_2 = 0.59460$ d^{-1}, with dashed uncertainties. The overall shape of these two frequencies is very similar, reinforcing the fact that one is merely an alias of the other.

4.4 MODE IDENTIFICATION

The initial parameters used for mode identification are derived from a combination of literature values and abundance analysis results. These parameters are summarized in Table 4.6. The radial velocity offset was set as a free parameter during these fits, in order best to compensate for any asymmetries in the pulsations.

Fitting the modes in a multi-mode fit configuration would result in inordinately large computation times. Coupled with the lack of a command-line batch mode in FAMIAS and its 32-bit memory limitations, multi-mode fits are generally not feasible with many free parameters, in particular ℓ and m. Instead, the process is to fit each mode individually within FAMIAS, and then try further to refine the parameter space – in particular, looking for mass and radius constraints – using the best-fit ℓ and m. All mode identifications were performed using the pixel-by-pixel method of FAMIAS, fitting only the amplitude and phase profiles to exclude the zero-point profile from the χ^2 values.

Figure 4.19 shows the minimum χ^2 values obtained for a grid of ℓ and m values, and Figures B.2 to B.6 show the results for the nine best-fit models at each frequency. Further parameters related to the best fits are summarized in Table 4.7.

The exploration of higher-order modes has not been shown because these invariably produce poor fits, for either of two reasons stemming from the fact that the higher order pulsations have more complex line profiles with more amplitude peaks and phase

TABLE 4.6: The fundamental stellar parameters determined prior to the mode identification process.

Property	Value	Reference
T_{eff}	7000 K	Table 4.2
$\log g$	4.0 (cm s^{-2})	Table 4.2
Radius	1.9 $R_\odot$	Handler and Shobbrook (2002) [a]
Mass	1.6 $M_\odot$	Polynomial relationships (Torres et al., 2010)
[Fe/H]	0.0 dex	Table 4.2 [b]
$v \sin i$	65.3 km s^{-1}	FAMIAS zero-point fit
Equivalent width	10.34 km s^{-1}	FAMIAS zero-point fit
Intrinsic width	11.75 km s^{-1}	FAMIAS zero-point fit

[a] The polynomial relationships by Torres et al. (2010) give $R = 2.1$ $R_\odot$, based on $\log g = 4.0$, [Fe/H] $= 0$, and $T_{\text{eff}} = 7000$. For the radius to drop to $R = 1.9$ $R_\odot$, the required parameters are $\log g = 4.08$, [Fe/H] $= 0.1$, and $T_{\text{eff}} = 7000$ K. In both cases, the mass is $M = 1.6$ $M_\odot$. These fundamental parameters are still rather uncertain, but fortunately they only weakly affect the shape of the line profile, so these reasonable estimates remain sufficient.

[b] Since the metallicity results are relatively uncertain, and that metallicity does not observably affect the modelled line profiles (Brunsden, 2013), [Fe/H] has been left at 0.0 dex.

transitions. First, if the zero-point is to be fitted adequately the pulsation amplitude must be low and consequently the resulting amplitude and phase fits will be poor. The second possibility is where, if the pulsation amplitude is higher, the line profile can be pulsationally broadened to a very high degree. This has the effect of broadening the amplitude and phase fits, such that not all of the amplitude peaks and phase transitions fit within the radial velocity range of the target star's line profiles. The central part of the model that remains within the observed radial velocity range may be fitted well. However, there are additional, hidden peaks that are pushed out of the plot by pulsational broadening. The tell-tale sign of this effect is that the zero-point fit of the line profile is extremely poor.

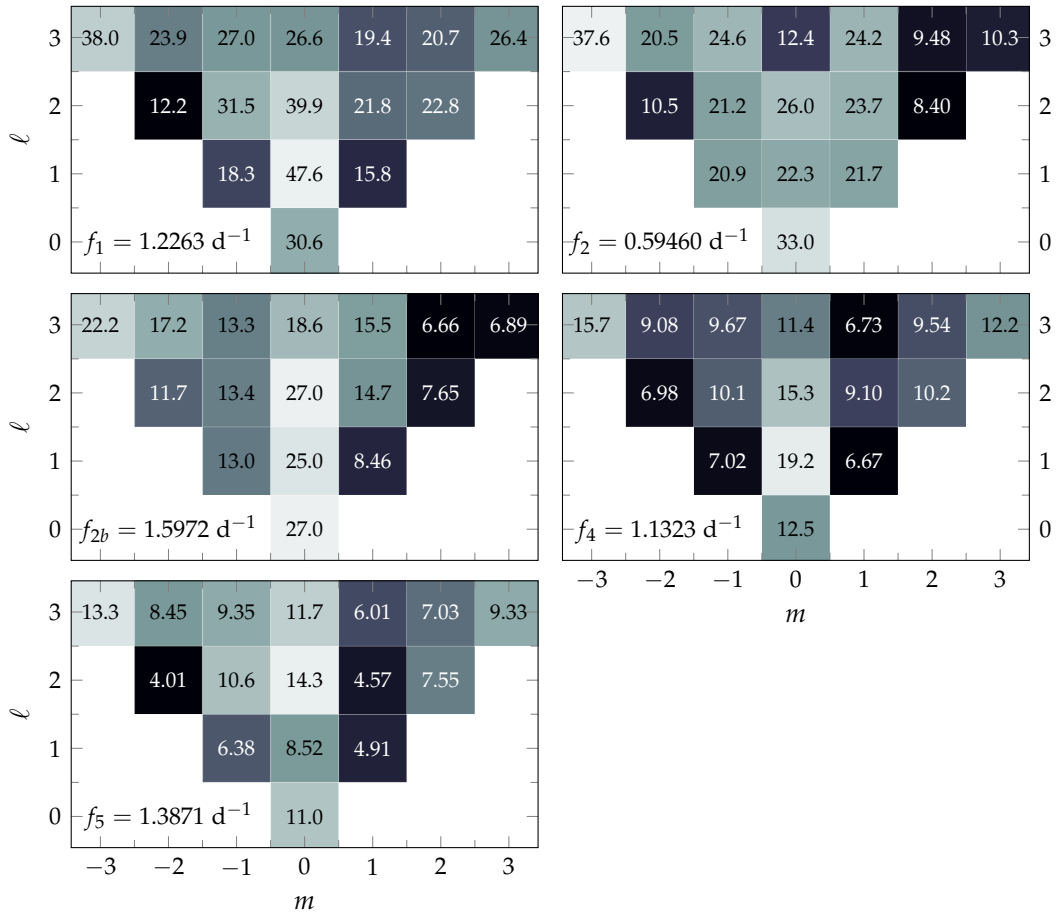

FIGURE 4.19: The χ^2 values for each indicated frequency, with $0 \leq \ell \leq 3$ and $-3 \leq m \leq 3$.

TABLE 4.7: The best-fit modes for each of the five analysed frequencies for HD139095. Where multiple values exist in the same row of a column, several non-unique models have been computed for that mode, which have the same minimum χ^2.

Mode	χ^2	Inclination	Vel. amp. (km s^{-1})	Phase
		$f_1 = 1.2263$ d^{-1}		
$(1,-1)$	18.3	11.6	19.8	0.593
$(1,1)$	15.8	7.62	20.0	0.102
$(2,-2)$	12.2	20.5	15.2, 15.2, 15.3	0.615
$(2,1)$	21.8	53.3	10.6	0.462
$(2,2)$	22.8	9.19, 10.3	15.8, 17.7	0.112, 0.141
$(3,-2)$	23.9	32.8	2.24	0.605
$(3,1)$	19.4	11.6, 56.4	11.6, 19.9	0.423, 0.564
$(3,2)$	20.7	9.24	15.2, 15.2, 15.2, 15.2, 15.2	0.137
$(3,3)$	26.4	13.4	19.7, 19.7	0.644
		$f_{2b} = 1.5972$ d^{-1}		
$(1,-1)$	13.0	5.17	3.89	0.354
$(1,1)$	8.46	68.4	0.430	0.898
$(2,-2)$	11.7	25.3	8.21	0.441
$(2,-1)$	13.4	5.00, 25.4	4.52, 9.62	0.347, 0.409
$(2,1)$	14.7	9.15	0.489	0.843
$(2,2)$	7.65	9.40	15.3	0.953
$(3,-1)$	13.3	5.00, 6.99	4.15, 4.18	0.347, 0.362
$(3,2)$	6.66	8.49	14.7	0.929
$(3,3)$	6.89	12.8	19.8	0.480
		$f_2 = 0.59460$ d^{-1}		
$(1,-1)$	20.9	5.79, 20.7, 22.2	3.23, 5.16, 12.9	0.00787, 0.0866, 0.984
$(1,1)$	21.7	6.41, 11.3	3.23, 5.16	0.488, 0.976
$(2,-2)$	10.5	18.3	13.6	0.0866
$(2,-1)$	21.2	11.4, 18.8	3.87, 18.1	0.126, 0.480
$(2,2)$	8.41	10.3	17.4	0.606
$(3,-2)$	20.6	22.3	3.23	0.0315
$(3,0)$	12.4	25.1	16.8	0.622
$(3,2)$	9.48	9.40	12.9	0.606
$(3,3)$	10.3	14.7	20.0	0.110

Continued on next page

Table 4.7 – continued from previous page

Mode	χ^2	Inclination	Vel. amp. (km s^{-1})	Phase
		$f_4 = 1.1323$ d^{-1}		
$(1,-1)$	7.02	11.0	12.6	0.347
$(1,1)$	6.67	7.66	19.9	0.846
$(2,-2)$	6.98	19.5	10.3	0.386
$(2,-1)$	10.1	5.00	4.11	0.315
$(2,1)$	9.10	62.3	19.6	0.213
$(3,-2)$	9.08	29.8	1.78	0.362
$(3,-1)$	9.67	5.42	3.89	0.323
$(3,1)$	6.73	44.3	0.567	0.433
$(3,2)$	9.54	9.53	10.1	0.843
		$f_5 = 1.3871$ d^{-1}		
$(1,-1)$	6.38	12.1	11.4	0.213
$(1,0)$	8.52	88.4	9.23	0.063
$(1,1)$	4.91	7.24	19.1	0.701
$(2,-2)$	4.01	21.7	8.58	0.213
$(2,1)$	4.57	44.2	11.3	0.614
$(2,2)$	7.55	10.2	14.5	0.732
$(3,-2)$	8.45	32.0	1.47	0.221
$(3,1)$	6.01	46.6	15.0	0.284
$(3,2)$	7.03	9.11	9.74	0.740

HD139095 must, of course, have the same modelled inclination value for each pulsation mode, as FAMIAS does not support modelling pulsations whose axes are offset from the rotational axis of the star. Thus, it is neither certain nor guaranteed that the axis of each pulsation frequency is aligned with the rotational axis of the star: it is merely assumed. By finding a set of mode identifications for each frequency that have similar inclination values, we can suppose that such a set of mode identifications is most likely to represent the true pulsation characteristics of the star.

The most important, and rigorous, constraint is that it is not possible for a prograde mode to exist where the pulsation period is longer than the rotation period of the star. This case, by definition, would mean that the pulsation travels across the stellar surface more slowly than the star rotates, making it a retrograde mode. Indeed many of the modes listed in Table 4.7 are likely impossible – with $v \sin i = 65.3$ km s^{-1} and $R = 1.9$ R$_\odot$, the most rapid frequency $f_{2b} = 1.5972$ d^{-1} still requires that $i \gtrsim 26^\circ$ for a prograde mode. The critical minimum inclination at this $v \sin i$ and radius is $i_{\text{crit}} = 9.4^\circ$, below which the photosphere is rotating at greater than the theoretical Keplerian break-up velocity.

TABLE 4.8: The final mode identification for HD139095.

Frequency	(ℓ, m)	Vel. Amp. (km s^{-1})	Phase
$f_1 = 1.2263$ d^{-1}	$(2, -2)$	17.1	0.614
$f_2 = 0.59460$ d^{-1}	$(2, -2)$	9.29	0.378
$f_4 = 1.1323$ d^{-1}	$(2, -2)$	11.3	0.228
$f_5 = 1.3871$ d^{-1}	$(2, -2)$	9.97	0.0945

The consistent pattern that emerges from Table 4.7 is that for each frequency the identified modes that both have the lowest χ^2, and are physically possible, are $(\ell, m) = (2, -2)$ modes (for all frequencies) with $i \approx 20°$. There is no other pattern of common inclinations detected among the frequencies, that suggests another possibility.

The strongest indication that $f_{2b} = 1.5972$ d^{-1} is an alias is that the $(\ell, m) = (2, -2)$ modelled with an inclination of $i = 25.3°$ is bordering on impossible. At a radius $R = 1.9$ R$_\odot$ the rotational frequency of the star, 1.589 d^{-1}, is slightly slower than the pulsation frequency. A decrease either in radius or inclination is required in order to make this mode possible.

The frequency $f_2 = 0.59460$ d^{-1} is once again favoured, and along with the other three frequencies a multi-frequency mode identification in FAMIAS has been performed. The radius and mass are allowed to vary as free parameters, along with inclination and radial velocity offset.

Table 4.8 summarizes the mode identifications for HD139095 by listing all parameters identified. As was the case for HD153580, identifying the mass and radius to a reasonable level of precision has not proven possible using the modelling techniques available within FAMIAS. It is quite precisely the fact that within reasonable bounds the models generated by FAMIAS are relatively insensitive to the mass and radius parameters (Brunsden, 2013) which means it is correspondingly difficult to identify these parameters, even when modelling four frequencies simultaneously. Figure 4.21 illustrates this lack of convergence. The χ^2 values for the inclination do converge reasonably well: it is most likely that the inclination of HD139095 is between 15° and 20°.

The final fitted velocity offset is -3.5 km s^{-1}, however this does not precisely correspond with the radial velocity of the star. The offset is modified in the optimization process to minimize the χ^2 values of the standard deviation and phase fits. The optimal velocity offset of the zero-point fit is -1.21 km s^{-1}, which is in addition to the wavelength-based correction for a radial velocity of -2.8 km s^{-1} (the star is receding) that was done before the cross-correlation stage. The minimum χ^2 for this multi-mode fit is $\chi^2 = 9.51$.

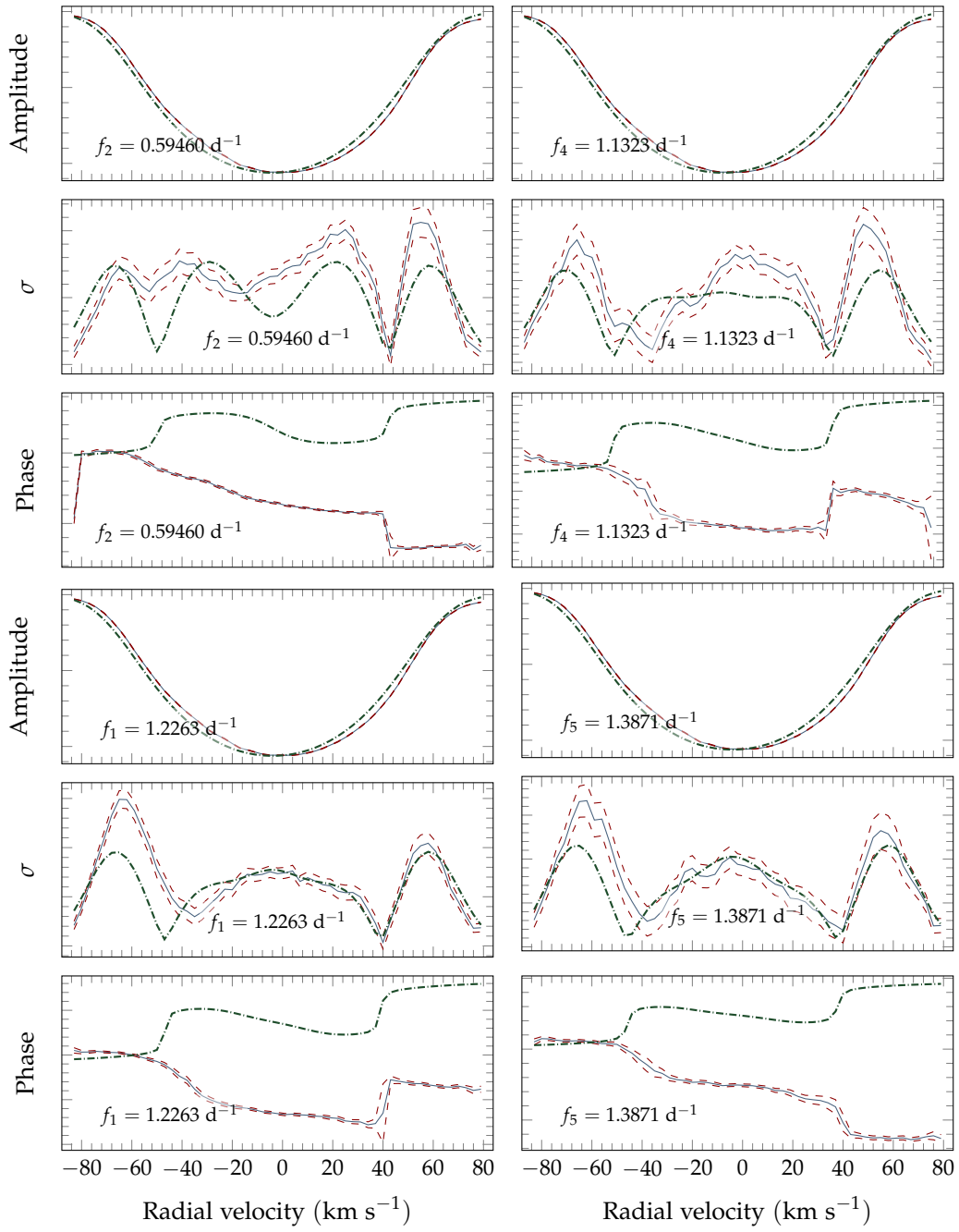

FIGURE 4.20: Plotted are the zero-point, amplitude, and phase fits for the best-fit models at each indicated frequency. They are all $(\ell, m) = (2, -2)$ modes. For each indicated frequency, the zero-point, pulsation amplitude, and phase fits (dash-dotted lines), as fitted by FAMIAS, are plotted. Additionally, the least-squares fitted profiles are plotted (solid, with dashed uncertainties).

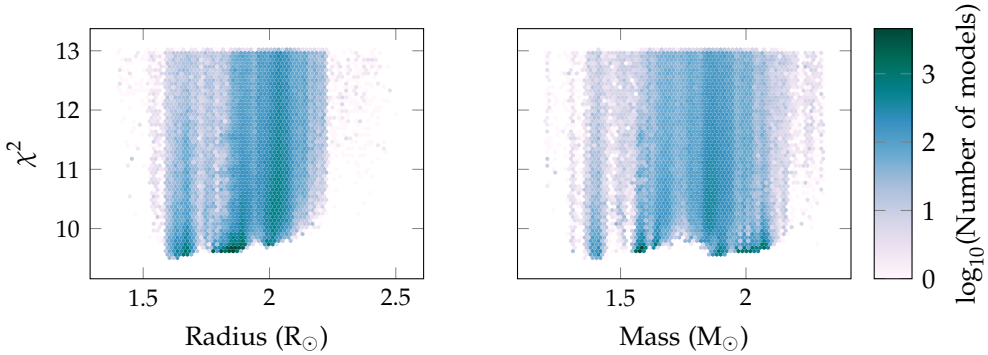

FIGURE 4.21: Modelled mass and radius values for the multi-mode fit of HD139095. No clear consensus of the true values can be reached using mode identification: the χ^2 values differ only trivially.

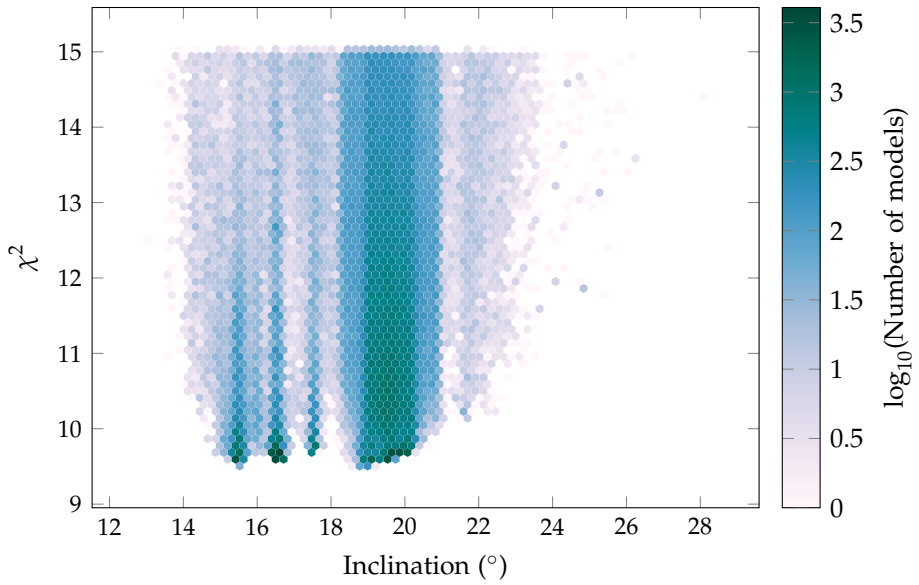

FIGURE 4.22: Modelled inclination values for the multi-mode fit of HD139095, showing a reasonable degree of convergence.

4.5 DISCUSSION

The Fourier analysis of HD139095 revealed four frequencies that have been identified reasonably confidently: $f_1 = 1.2263$ d^{-1}, $f_4 = 1.1323$ d^{-1}, $f_5 = 1.3871$ d^{-1}, and $f_2 = 0.59460$ d^{-1}. Although the former three are quite closely spaced, there is no suggestion that the frequencies are related. All four frequencies have been identified as $(\ell, m) = (2, -2)$ modes: the same identification for each is an interesting result. The frequencies account for only 28.7% of the variations across the line profile. If more observations were taken, ideally with a larger telescope and better signal-to-noise performance, it is highly likely that more pulsation frequencies would be found. Certainly, the variations due to currently known frequencies would become more precisely defined, allowing a more certain mode identification.

The results of this star have also shown that it is very difficult to obtain the stellar mass and radius with current methods. The abundance analysis results are not consistent enough to draw any substantial conclusions, but the parameters determined in Table 4.2 (with the exception of the SME $\log g$ result) correlate reasonably with the expected values.

The macroturbulence value of $v_{\rm mac} = 17.5$ km s^{-1} derived by SME is an interesting result. It certainly appears to be a feasible figure. Ideally it should be verified by comparing the Fourier spectrogram of the line profile with that of a theoretical line profile generated by a model that incorporates both rotational and macroturbulent broadening. It is likely that non-radial pulsations contribute to macroturbulent broadening and this has been studied in hot, high-mass O and B-type stars (Aerts et al., 2009; Simón-Díaz et al., 2010). A survey directed towards γ Doradus- and δ Scuti-type stars would be a welcome extension.

5

HD197541

HD197541 (HIP102435) is a candidate (Handler, 1999) γ Doradus star in the constellation of Microscopium, at the coordinates 20 h 45 m 23.85 s, -30° 28′ 41.56″ (J2000 epoch, Perryman et al., 1997). HIPPARCOS data place the star at a distance of (60 ± 2) pc from the Sun (van Leeuwen, 2007).

No previous photometric data beyond the 88 HIPPARCOS observations have been published. Two periods of 1.400 d and 1.093 d have been previously identified from this photometry (Handler, 1999). HD197541 is part of a double system, with an 11^{th} magnitude companion at a separation of 9.795 ± 0.015 arcsec (Sinachopoulos et al., 2007), named WDS J20454-3029B. The large separation and dim magnitude of the secondary component mean that it is of no significant concern during observation and analysis. The two components are quite visibly separated in the HERCULES guide camera, as shown in Figure 5.1.

5.1 OBSERVATIONS

The primary data set for this chapter consists of 339 spectra taken at MJUO. Figure 5.2 illustrates a small section of the mean spectrum, showing spectral lines that are uncommonly narrow for a γ Doradus star, indicative of either a low inclination or a low $v \sin i$. Typical exposure times for the star were 20 minutes through the 100 μm fibre. The particularly low levels of line broadening in this star contribute to the fact that the resultant cross-correlated line profiles show a very low level of noise. The cross-correlated line profiles are shown in Figure 5.3.

Figure 5.4 shows all the spectra of HD197541 taken in 2013, as a sequence of line profiles vertically displaced from one another in sequential order. Some observations show an extremely large amount of distortion due to pulsations. In particular, this can be seen in the fourth series from the bottom, in the left hand panel. The appearance of the large distortions is similar to that of a large 'bump' moving from left to right across the line profile, rendering the whole profile grossly non-Gaussian. The appearance of this is not regular enough to establish a periodicity. It is possible that these distortions are due to resonances between modes that occasionally become very constructive.

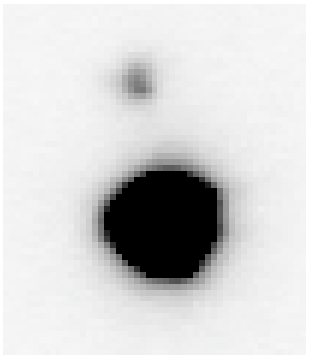

FIGURE 5.1: An inverted still image from the HERCULES guide camera, showing a very over-exposed HD197541 below its dimmer companion. The separation between the two stars is just under 10 arcseconds.

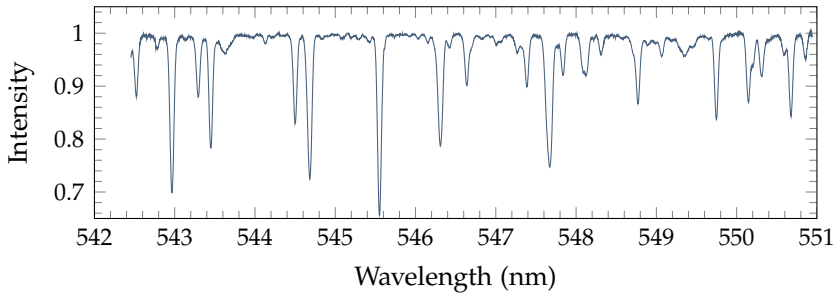

FIGURE 5.2: The mean spectrum of HD197541, for MJUO spectral order 104.

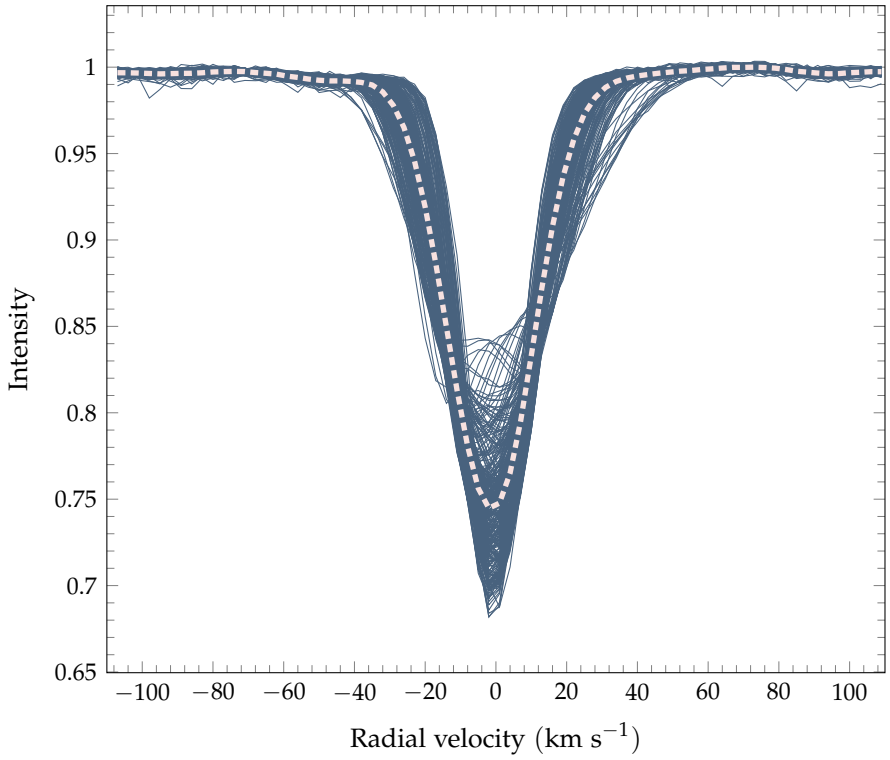

FIGURE 5.3: The cross-correlated line profiles of HD197541, with the bold dashed line representing the mean line profile.

TABLE 5.1: A summary of properties of HD197541, including the abundance analysis results returned by SME as described in Section 5.2.

V	$B-V$							Reference
6.78	0.333							Perryman et al. (1997)
$T_{\rm eff}$ (K)	$\log g$	[Fe/H]	[M/H]	Mass ($M_\odot$)	$v \sin i$ (km s^{-1})	$v_{\rm mic}$ (km s^{-1})	$v_{\rm mac}$ (km s^{-1})	Reference
6977		−0.11		1.45				Casagrande et al. (2011)
7228	3.89		0.063		15.9	2.3	16.2	SME results
7128	4.01	0.14				1.58		FUNDPAR results

Indeed, these variations seem suggestive of the Blazhko effect, where modulations in the light curve are seen of a periodicity of typically 100 times longer than the star's oscillation period. Over this Blazhko cycle, there is a considerable and relatively brief increase in maximum luminosity, while the minimum luminosity changes relatively little (Aerts et al., 2010). Balona et al. (2011) found a number of stars from Kepler photometry that show similar behaviour, with beating between two dominant and closely spaced frequencies. The spectroscopic line profile distortions are also of a similar shape to those found in RR Lyrae stars – see Kaye (2007); Preston (2011). A set of continuous, high-precision photometry data would be very useful to determine whether this is the case: it simply is not clear whether or not the large line profile distortions seen are periodic. Certainly, FAMIAS has some difficulty modelling them, which probably also interferes with its ability to model the three frequencies found in this thesis. Perhaps there are as-yet undiscovered links between the temporal stability of pulsation modes (the frequencies of HD197541 may not be stable) and these Blazhko-like variations.

5.2 ABUNDANCE ANALYSIS AND STELLAR PARAMETER ESTIMATION

Both the equivalent width and spectral synthesis methods were used for the abundance analysis for HD197541. The relatively narrow width of the cross-correlated line profiles does not appear consistent with the previously reported $v \sin i$ value of 29 km s^{-1} (Royer et al., 2007). The SME and FUNDPAR abundance analysis results, along with other relevant literature parameters, are presented in Table 5.1. The spectral synthesis results once again return a relatively large macroturbulence value around 15 km s^{-1}, which might be an emerging trend in γ Doradus stars. The $\log g$ of 3.89 is perhaps slightly low, as this returns a mass of 1.7 $M_\odot$ and radius of 2.3 $R_\odot$ when using a temperature of 7000 K and [Fe/H] = 0 with the polynomial relationships of Torres et al. (2010). That is a large, but not unheard of, radius for a γ Doradus star. The relatively low $v \sin i$ of this star did, however, aid in the measurement of equivalent widths: many more spectral lines of HD197541 could be measured than for HD139095.

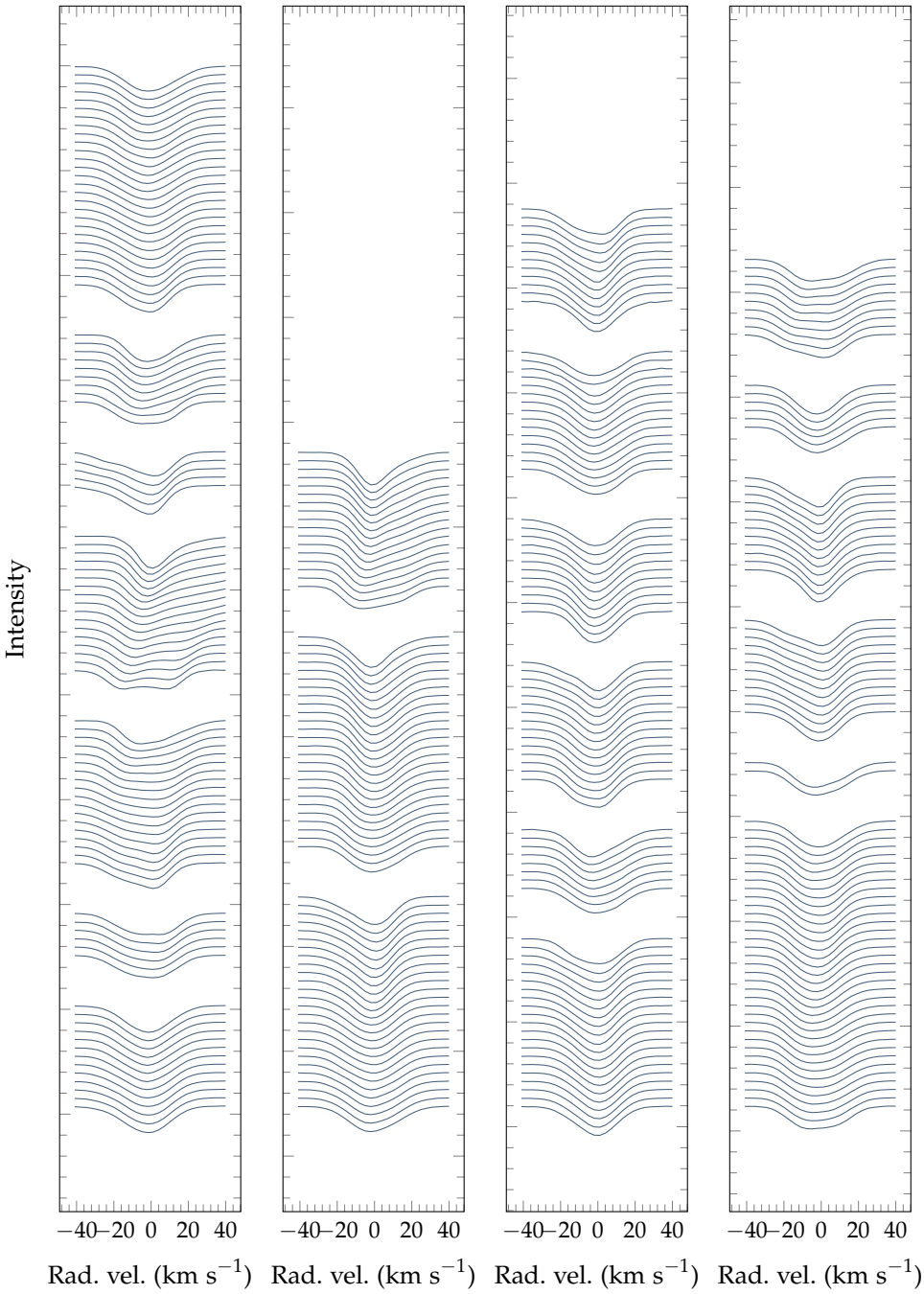

FIGURE 5.4: The 324 line profiles of HD197541, processed from spectra taken during 2013, from June to October, in time order (from the bottom up, and left to right). A large gap in the intensity axis represents a time gap of at least 6 hours between observations.

The equivalent widths were measured using SPECTRE, and these measurements are tabulated in Table D.1.

5.3 FREQUENCY SELECTION AND ANAYLSIS

Both the spectroscopic and photometric data are useful for finding frequencies in the data. Figure 5.5 shows the two-dimensional, pixel-by-pixel Fourier periodogram for the spectroscopic data. There is a reasonable amount of aliasing in the data as shown in Figure 5.6, due to the compressed time period of the observations: certainly enough to urge caution in the frequency analysis. Some slight asymmetry in the amplitudes across the radial velocity axis is apparent, which, in comparison with Figure 5.3, suggests that the pulsations are not centred about the middle of the line profile. Figures 5.7 to 5.11 show the frequency pre-whitening process for the spectroscopic data, for the first four moments and pixel-by-pixel data. Figure 5.12 shows the same periodogram series for the 80 reliable photometric data points[1] obtained by HIPPARCOS. The pixel-by-pixel SIGSPEC results are displayed in Figure 5.13, where several prominent peaks of detection, including some probable aliasing, are visible. The frequency results of these Fourier analyses are summarized in Table 5.2.

The detection of two reasonably strong frequencies in the equivalent width (zeroth) moment is suggestive of some temperature variations across the stellar surface. Strong frequencies in the first (radial velocity) and third (skewness) moments are also seen, and the most strongly detected frequency, $f_1 = 0.71344\ \mathrm{d}^{-1}$, has also been detected in the HIPPARCOS photometry. The HIPPARCOS frequency of $0.91468\ \mathrm{d}^{-1}$, first reported by (Handler, 1999), does not show convincing line profile variations, so it is likely that it is just an anomalous peak in the noise (perhaps it is a weak alias of the spectroscopic detection at $f_4 = 1.1158\ \mathrm{d}^{-1}$, specifically $2 - f_4$, but the spectroscopic detection does not show convincing variations either).

As Table 5.2 shows, it is likely that f_4 is manifested either at the frequency $f_4 \approx 1.1158\ \mathrm{d}^{-1}$, or at $f_4 \approx 0.10710\ \mathrm{d}^{-1}$. There is also some potential confusion between f_2 and f_4, as the addition or subtraction of one frequency will significantly affect the line profile variations of the other. Certainly the frequencies are defined poorly enough such that there is some confusion between the two. However, whether or not there are one or two frequencies is not clear. The spectra were gathered over a relatively short time scale, which probably contributes to this uncertainty. The frequency $f_2 = 1.0181\ \mathrm{d}^{-1}$ has been chosen instead of the other options around $\approx 1.04\ \mathrm{d}^{-1}$, as the latter do not appear to be independent from $f_1 = 0.71344\ \mathrm{d}^{-1}$ and can affect the shape of that frequency's pulsations. Additionally, if the Fourier spectra are compared by pre-whitening by $f_1 = 0.71344\ \mathrm{d}^{-1}$ and then either $f_2 = 1.0181\ \mathrm{d}^{-1}$ or $1.0394\ \mathrm{d}^{-1}$, the latter frequency leaves a noticeable peak at $f_1 = 0.71344\ \mathrm{d}^{-1}$. Pre-whitening by

1 Eight points (out of 88 total) were marked as unreliable and excluded from the analysis

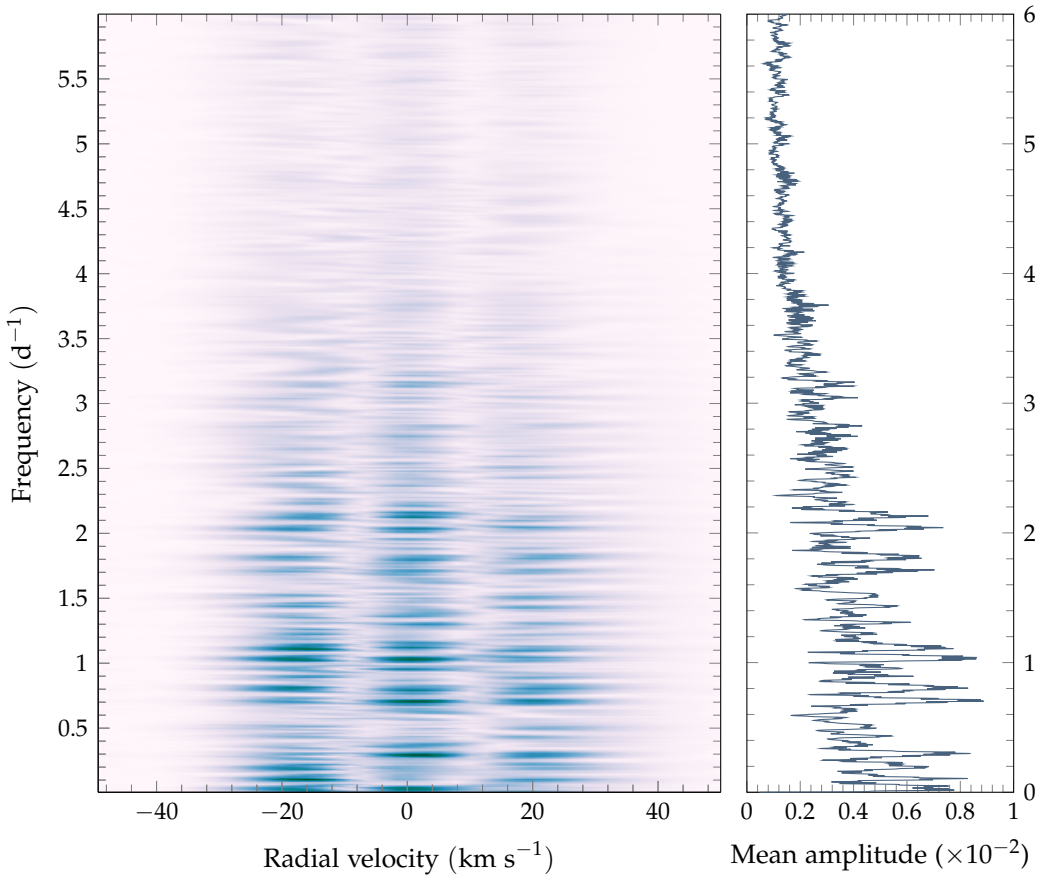

FIGURE 5.5: The two-dimensional, pixel-by-pixel Fourier periodogram computed by FAMIAS, before any frequencies are pre-whitened.

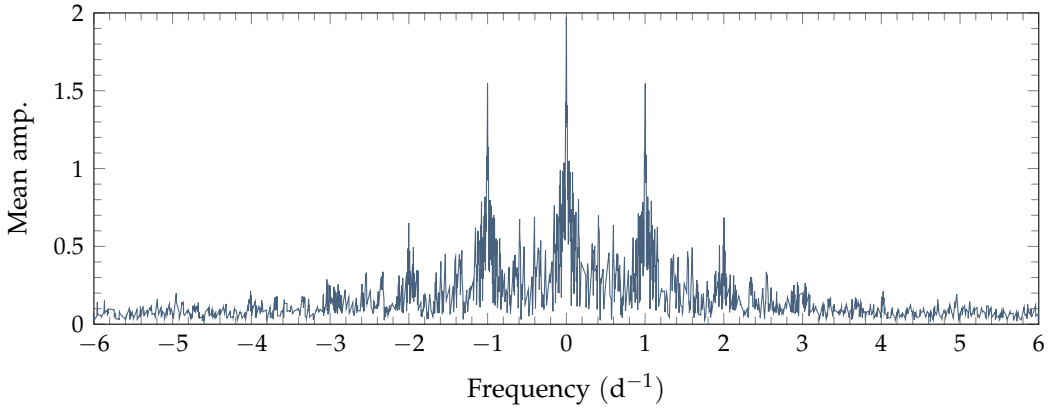

FIGURE 5.6: The spectral window of HD197541 spectra, as computed by FAMIAS.

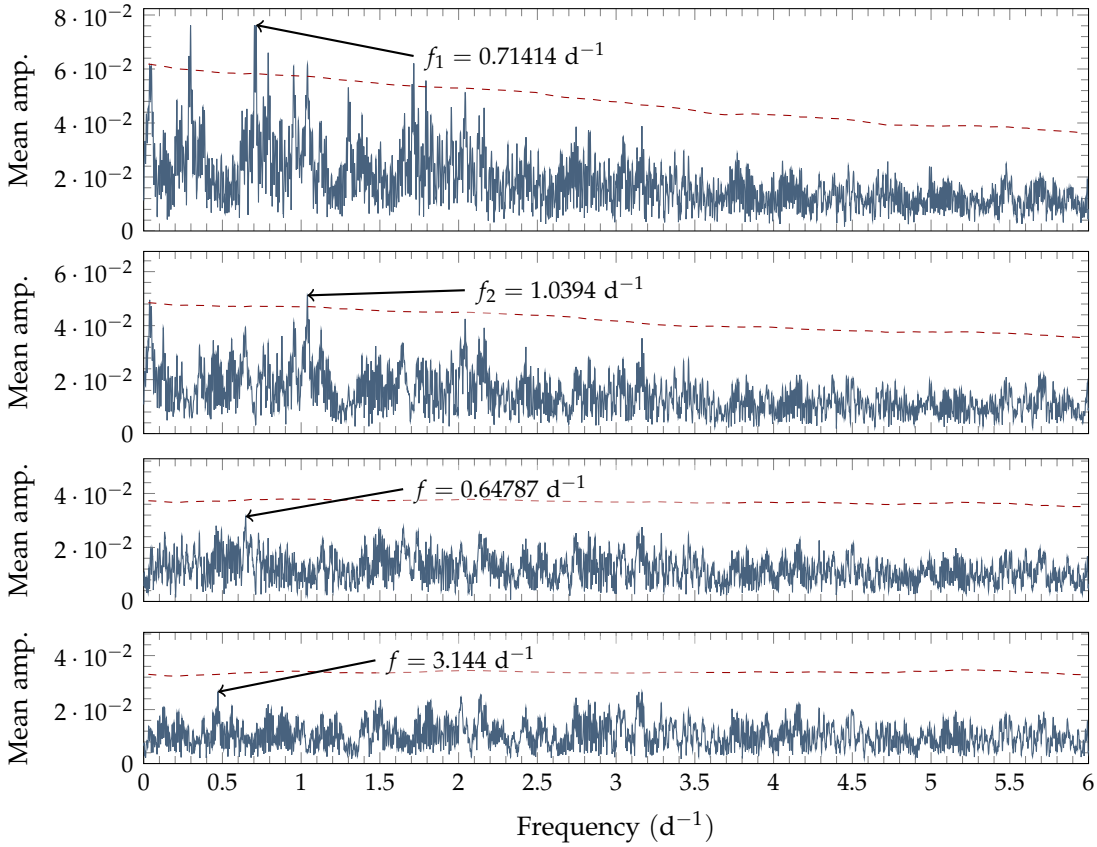

FIGURE 5.7: The Fourier spectrum frequency selection process for HD197541, computed using the zeroth moment of the moment method in FAMIAS. The dashed line represents the significance level at a signal-to-noise ratio of 4.

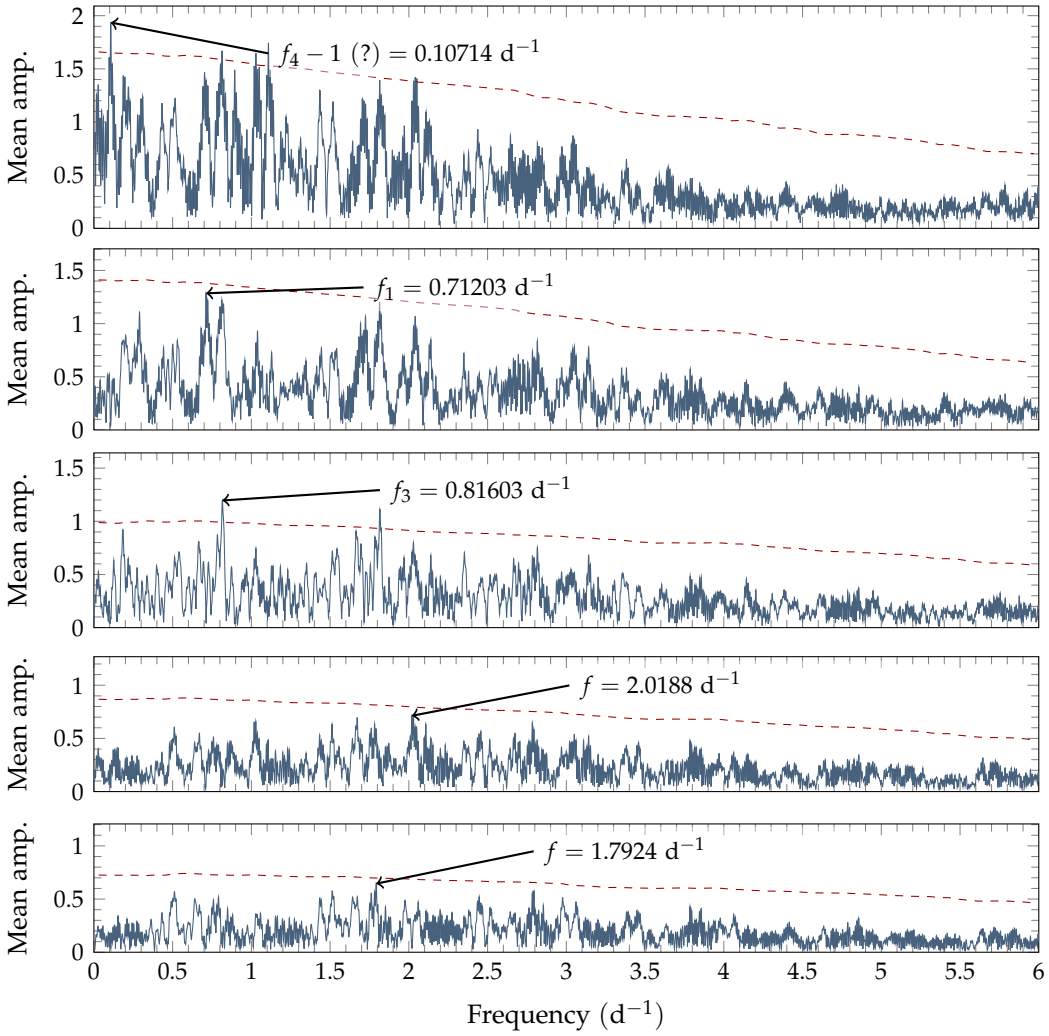

FIGURE 5.8: The Fourier spectrum frequency selection process for HD197541, computed using the first moment of the moment method in FAMIAS. The dashed line represents the significance level at a signal-to-noise ratio of 4.

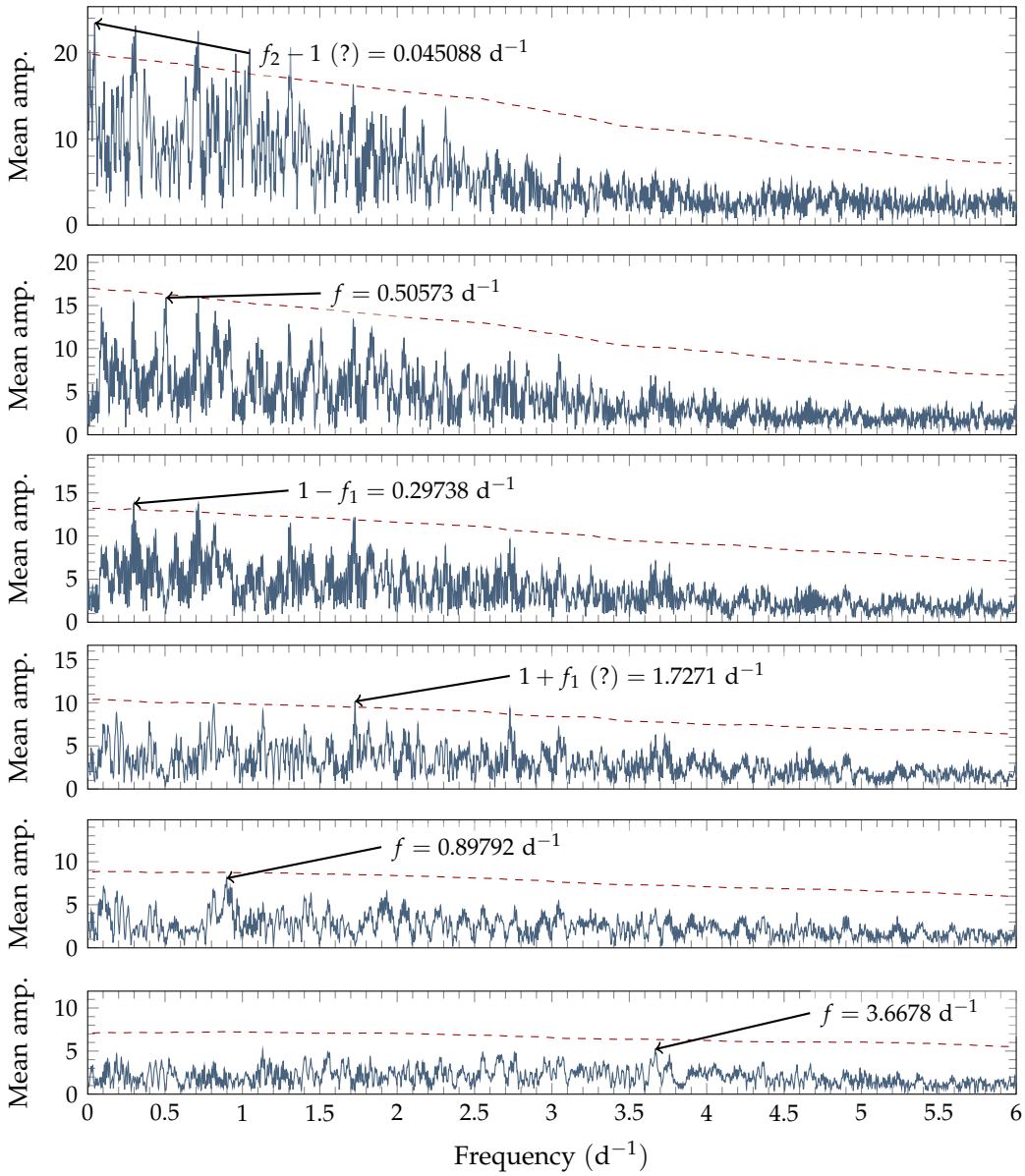

FIGURE 5.9: The Fourier spectrum frequency selection process for HD197541, computed using the second moment of the moment method in FAMIAS. The dashed line represents the significance level at a signal-to-noise ratio of 4.

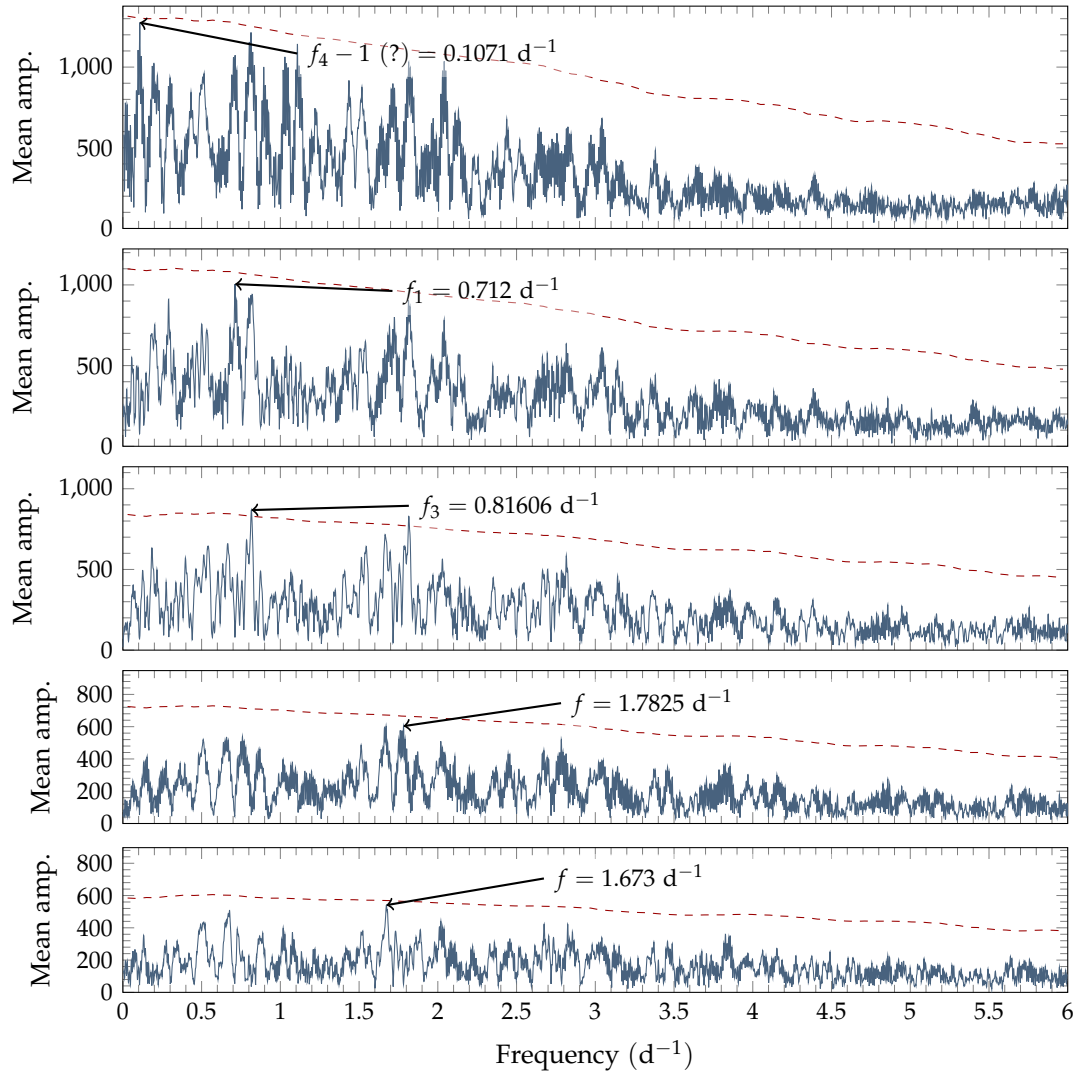

FIGURE 5.10: The Fourier spectrum frequency selection process for HD197541, computed using the third moment of the moment method in FAMIAS. The dashed line represents the significance level at a signal-to-noise ratio of 4.

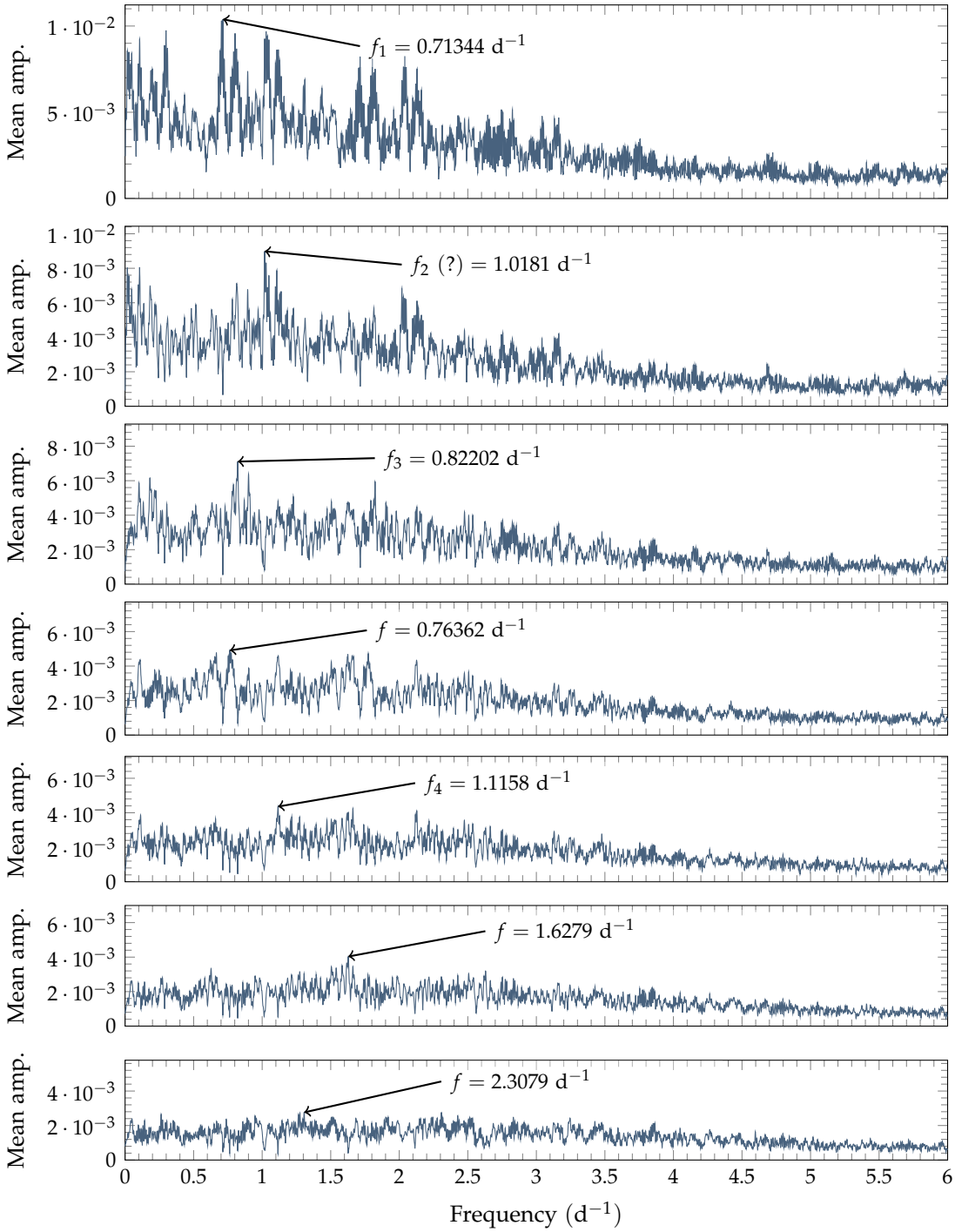

FIGURE 5.11: The Fourier spectrum frequency selection process for HD197541, computed using the pixel-by-pixel method in FAMIAS.

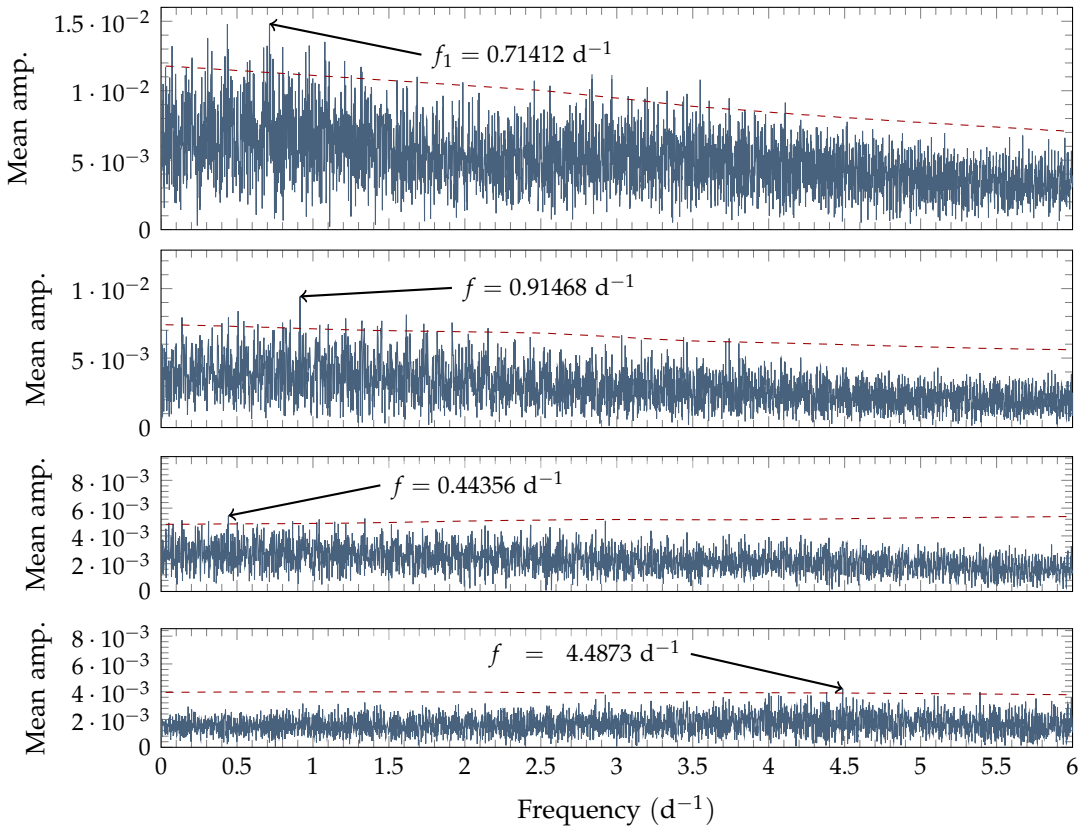

FIGURE 5.12: The Fourier spectrum frequency selection process for HD197541, computed in FAMIAS from the HIPPARCOS photometric data. The dashed line represents the significance level at a signal-to-noise ratio of 4.

TABLE 5.2: A summary of frequencies found using the progressive pre-whitening process of FAMIAS as well as the frequency analysis tool SIGSPEC. Frequencies above the significance limits of FAMIAS, or that show reasonabe line profile variations, have been reported. Identifications marked with a question mark are not certain.

	FAMIAS	SIGSPEC	
Label	Frequency (d^{-1})	Frequency (d^{-1})	Highest significance
Pixel-by-pixel			
f_1	0.71344	0.7141	31
f_2 (?)	1.0181	1.04	25
f_3	0.82202	0.8016	30
f_4	1.1158		
Zeroth moment			
f_1	0.71414	0.71555	17
f_2	1.0394	0.047212	27
First moment			
$f_4 - 1$ (?)	0.10714	0.10710	24
f_1	0.71203	0.72342	23
f_3	0.81603	1.8137	14
f_2		1.0382	16
Second moment			
$f_2 - 1$ (?)	0.045088	0.047140	36
$1 - f_1$	0.29738	0.71554	34
Third moment			
$f_4 - 1$ (?)	0.10710	1.1084	26
f_1	0.71200	0.70683	22
f_3	0.81606	0.81310	21
f_2		1.0391	23
Photometry			
f_1	0.71412	0.71413	8.6

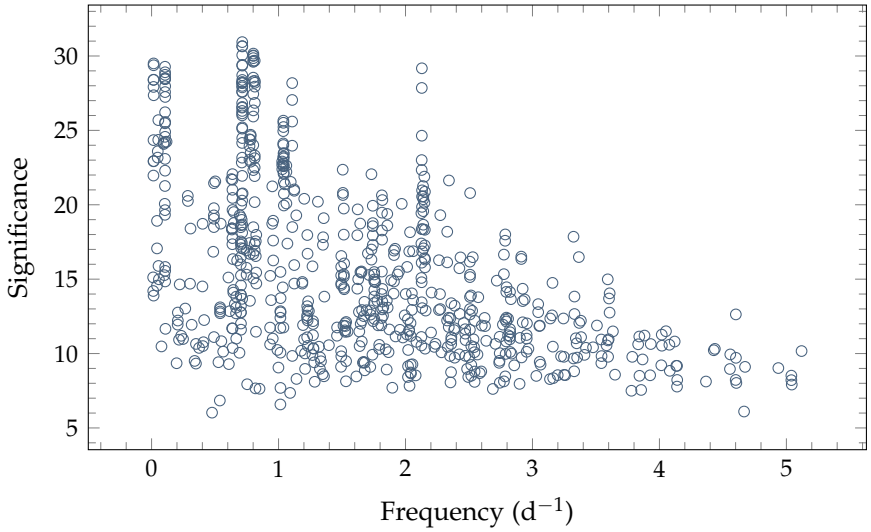

FIGURE 5.13: The two-dimensional, pixel-by-pixel SIGSPEC results. The top ten frequencies for each radial velocity bin between -35 km s^{-1} and $+35$ km s^{-1} (at a resolution of 1 km s^{-1}) are shown.

$f_1 = 0.71344$ d^{-1}, however, removes the peak at 1.0394 d^{-1}. Thus, $f_2 = 1.0181$ d^{-1} is the better candidate frequency.

The phase coverage for all three analysed frequencies ($f_1 = 0.71344$ d^{-1}, $f_2 = 1.0181$ d^{-1}, and $f_3 = 0.82202$ d^{-1}), shown in Figure 5.14, is reasonably even. A possible explanation for the uncertainty in frequencies is that the frequencies may be temporally unstable: a rough analysis (Figure 5.15) displays the Fourier periodograms while sequentially adding more spectra taken at later and later dates. We might expect to see some instability here, but the hypothesis is not satisfactorily resolved as there are no significant variations seen once enough spectra had been gathered. Several months of continuous, millimag-accuracy photometric observations would be needed in order truly to test the stability of these frequencies, which is data that ground-based facilities generally cannot provide. Such instability in g-modes has been observed before, such as in the very rapidly rotating ($v \sin i \approx 239$ km s^{-1}) star Rasalhague, but it is suspected that these frequency instabilities are caused by the very rapid rotation rate (Monnier et al., 2010).

Figure 5.16 shows the phased, residual variations due to the three most likely frequencies, $f_1 = 0.71344$ d^{-1}, $f_2 = 1.0181$ d^{-1}, and $f_3 = 0.82202$ d^{-1}. There is a noticeable "three bump profile" for each of these frequencies, strongly indicative of non-radial pulsations. For comparison, Figure C.1 shows the theoretical line profiles produced by FAMIAS, with the same parameters as the final mode identifications in Table 5.6. The general shape of the variations is well matched. Figure 5.17 and Table 5.3 accompany Figure 5.16, showing that each of the three frequencies has a roughly equal contribu-

TABLE 5.3: The proportion of line profile variations (in terms of the mean standard deviation across the line profile, σ) explained by the cumulative pre-whitening of detected frequencies. Note that $f_2 = 0.59460$ d^{-1} is able to explain a greater portion of the observed line profile variations than $f_{2b} = 1.5972$ d^{-1}.

Frequencies removed	σ	% of σ explained
f_1	0.01299	14.3%
$f_1 + f_2$	0.01134	25.1%
$f_1 + f_2 + f_3$	0.009854	35.0%

TABLE 5.4: An estimation of the uncertainty in the observed frequencies. The observation timebase used, of 28 days, is equal to the number of nights during which spectra were taken.

Frequency	sig	SIGSPEC Error estimation (d^{-1})
$f_1 = 0.71344$ d^{-1}	31	0.006
$f_2 = 1.0181$ d^{-1}	17	0.009
$f_3 = 0.82202$ d^{-1}	30	0.007

tion to the observed line profile variations. The patchiness of the phased line profile variations, combined with the fact that around two thirds of the originally observed line profile variations still remain after subtraction of the first three frequencies, show that there is likely to be a rich spectrum of pulsation frequencies to be uncovered. Perhaps higher resolution spectra will reveal more detail across the line profile, and more observations would of course be helpful in resolving further frequencies. Another interesting feature is that the overall shape of the standard deviations is suggests that a single type of mode probably dominates the variations. It is possible that a collection of similar modes with a relatively close frequency spacing is responsible for the observed line profile variations and also the occasionally very strong line profile distortions seen in Figure 5.4.

Table 5.4 shows the estimated errors in the three identified frequencies, based on a timebase T of 28 days and Equation (2.2).

5.4 MODE IDENTIFICATION

The zero-point line profile for HD197541 has proven somewhat difficult to model, particularly in light of the discrepancies between the $v \sin i$ of 16.1 km s^{-1} determined by SME and the literature value of 29 km s^{-1}. It was decided to leave the zero-point parameters free, while performing a grid search to identify each of the three frequencies individually. Owing to the uncertain determination of stellar parameters, the $T_{\rm eff}$, $\log g$,

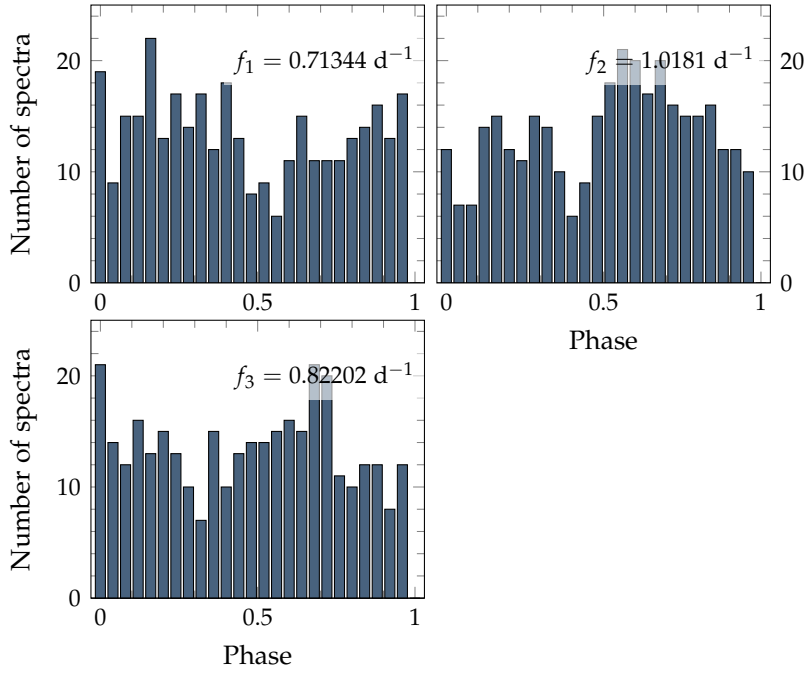

FIGURE 5.14: Phase coverage histograms for the indicated frequencies.

and [M/H] were left at typical values of 7000 K, 4.0, and 0 respectively, with a mass of 1.5 $M_\odot$ and radius 1.8 $R_\odot$. These parameters only weakly affect the modelled line profiles, so only estimating the atmospheric parameters is not a significant limitation.

Figure 5.18 shows that all three frequencies have been modelled with good certainty as $(\ell, m) = (1, 1)$ modes. However, on initial inspection, $f_1 = 0.71344$ d^{-1} could also be a $(\ell, m) = (3, 1)$ mode. The $(\ell, m) = (3, 1)$ mode for $f_1 = 0.71344$ d^{-1} has a modelled inclination of 5°, which renders this model impossible. Figures C.2 to C.4 show the best-fitted line profiles for the results that are summarized in Table 5.4. The low inclination (and its subsequent implications for the rotational velocity) mean that the fitted mode *must* be a retrograde mode.

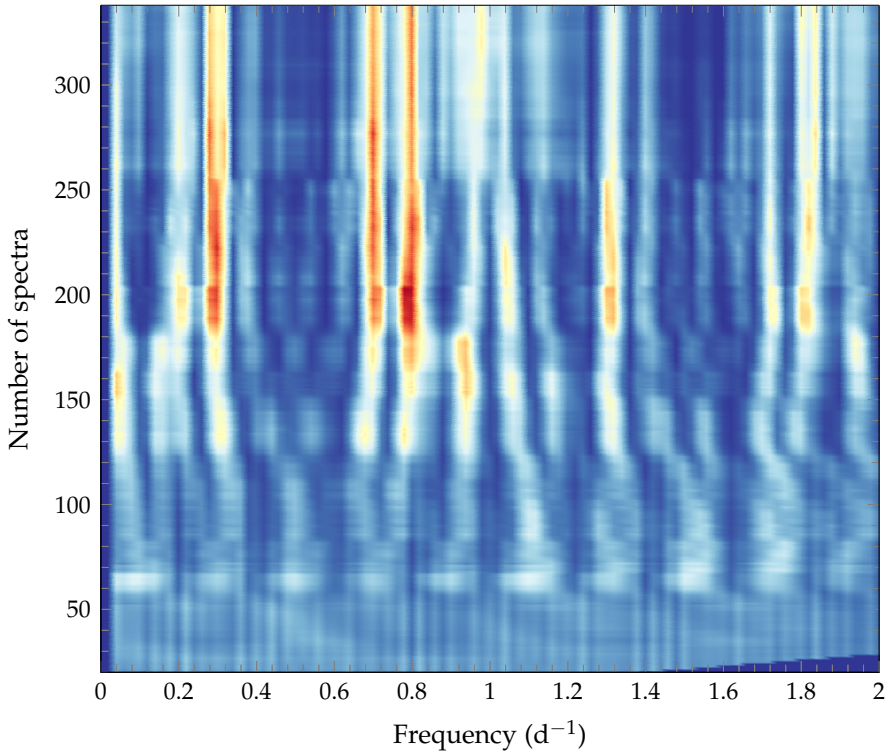

FIGURE 5.15: The frequency stability of HD197541 over time. For each individual pixel of the line profile, the Fourier periodograms were calculated while sequentially adding one additional spectrum with each iteration. The result is then presented as the mean of the pixel-by-pixel results. Thus, each 'row' of the plot shows the mean Fourier periodogram for the first n spectra obtained at MJUO. The data have been smoothed in the frequency domain. The individual Lomb-Scargle periodograms were calculated using Dmitry Savransky's MATLAB script `lomb.m`, available on the MATLAB File Exchange. As evidenced by the pre-whitening cascades in Figures 5.7 and 5.11, the strong peak seen at 0.29 d^{-1} is an alias $(1 - f_1)$ of $f_1 = 0.71344$ d^{-1}.

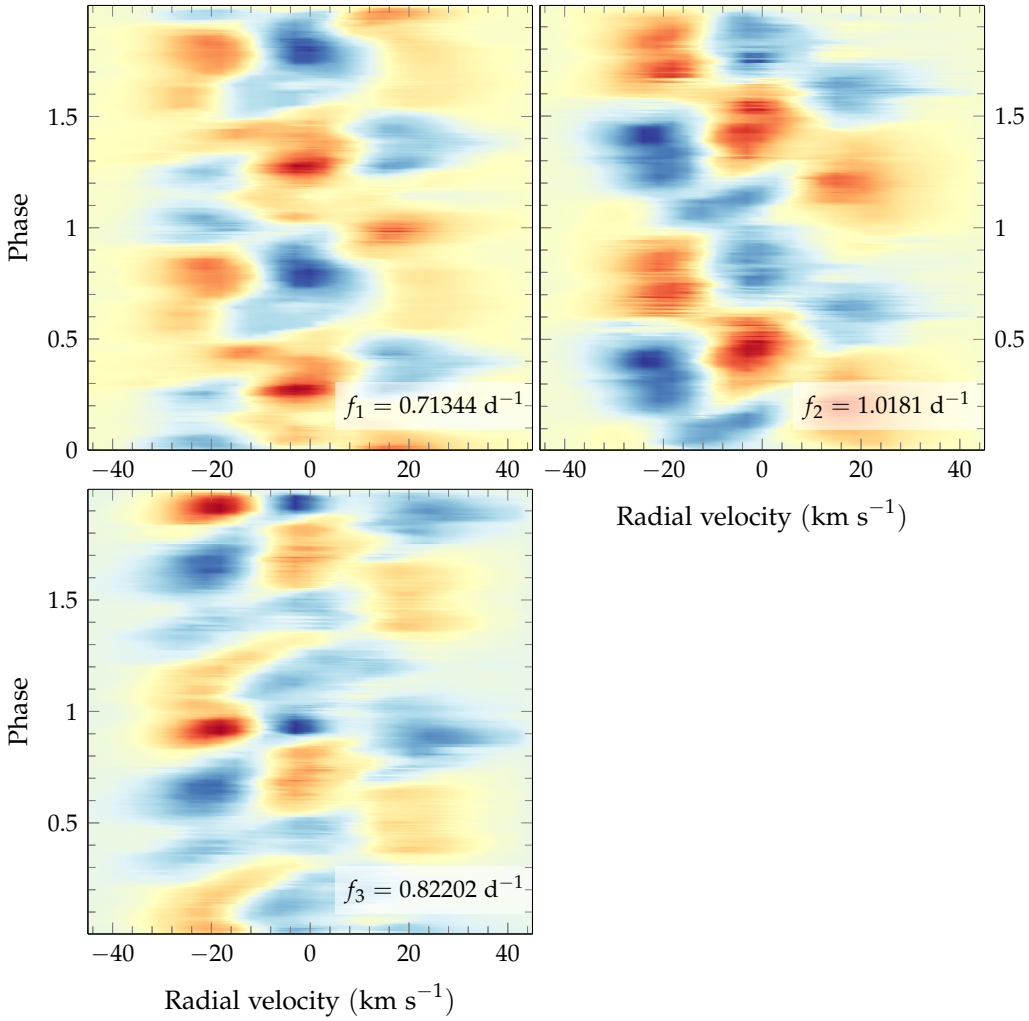

FIGURE 5.16: The residual (i.e. the mean has been subtracted) line profile variations phased to each of the indicated frequencies that are the top candidates for mode identification. In each case, the observations have been pre-whitened by the other two frequencies. A median filter is used to smooth the appearance of the data.

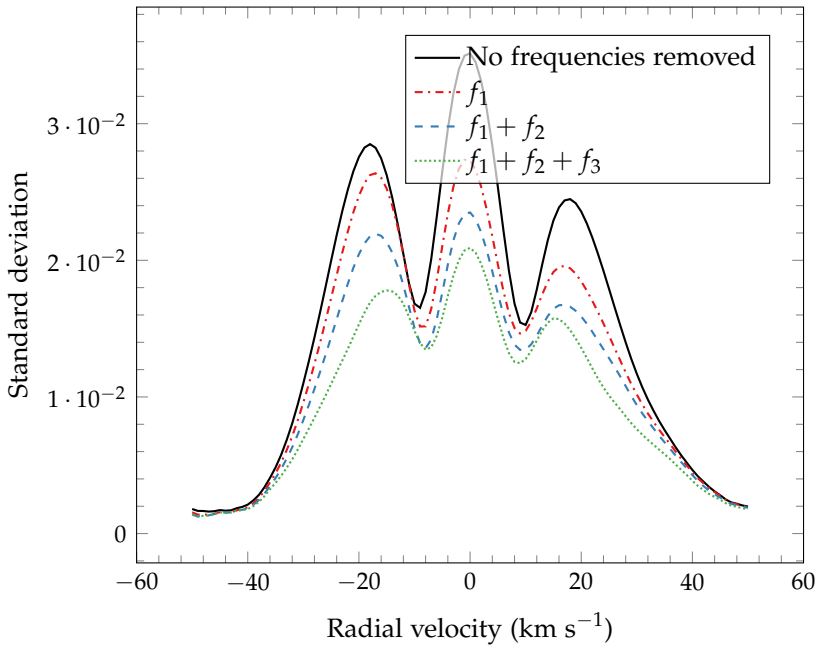

FIGURE 5.17: The per-pixel standard deviations across the line profile. By pre-whitening by each of the three chosen frequencies, the residual variations decrease.

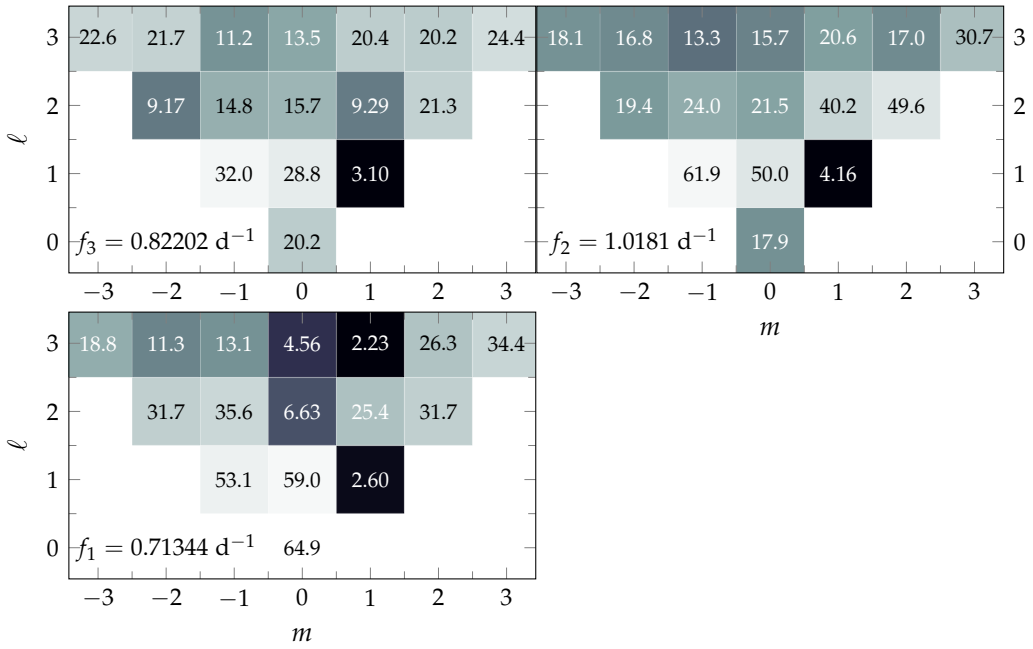

FIGURE 5.18: The χ^2 values for the best-fit modes of each of the three candidate frequencies.

TABLE 5.5: The best-fit modes for each of the three analysed frequencies for HD197541. Where multiple values exist in the same row of a column, several non-unique models have been computed for that mode, which have the same minimum χ^2.

(ℓ, m)	χ^2	Incl. (°)	$v \sin i$ (km s^{-1})	Eq. wid. (km s^{-1})	Intrins. wid. (km s^{-1})	Vel. Amp. (km s^{-1})	Phase
			$f_1 = 0.71344$ d^{-1}				
(1, 1)	2.599	54	20	7.29	7.88	0.219	0.528
(2, 0)	6.629	60	12.4	5	7.29	1.58	0.535
(2, 1)	25.42	81	17.4	14.5, 14.6	5	7.16	0.535
(3, −3)	18.76	45	12	20	12.5	0.43	0.0472
(3, −2)	11.27	28	18	19.7	8.88	0.391	0.0315
(3, −1)	13.14	23, 64, 90	14.5, 19.6, 23.5	7.35, 16.6, 20	7.82, 9.59, 10.2	0.141, 0.18, 0.594	0.0315, 0.528, 0.535
(3, 0)	4.563	40	10.2	12.9	8.53	0.813	0.528
(3, 1)	2.235	5	14.6	9.18	8.35	0.688	0.528
(3, 2)	26.27	20	24.6	13.6	5	4.05	0.0394
			$f_2 = 1.0181$ d^{-1}				
(0, 0)	17.88	48, 49, 54	16.8, 21, 22.9	6.29, 7.76	6.24, 10.1, 10.3	0.538, 0.626, 0.723	0.37, 0.378
		78, 90	24.4, 26.5	9.24, 11.4, 12.8	10.8, 12	0.85, 4.57	0.874, 0.882
(1, 1)	4.161	28	19.1	8.65	8.29	0.528	0.378
(2, −2)	19.42	41	14.8	19.1	8.76	0.626	0.874
(3, −3)	18.09	51, 89	10, 26.5	12.5, 18.1	6.24, 13.2	0.538, 4.64	0.874, 0.882
(3, −2)	16.78	49	15.6, 21.7	9.88, 16.4	10.4, 12.1	0.332, 0.587	0.37, 0.874
(3, −1)	13.27	90	22.9	15.3	10.1	0.401	0.378
(3, 0)	15.65	46, 79	19.4, 21.7	10.1, 20	10.7, 11.1	0.362, 0.831	0.378
(3, 1)	20.56	5	18.4	8.24	10.3	0.704	0.386
(3, 2)	17	18, 45	19.9, 27.6	19.1, 20	5.06, 11.1	0.342, 4.89	0.378, 0.858

Continued on next page

Table 5.5 – continued from previous page

(ℓ, m)	χ^2	Incl. (°)	$v \sin i$ (km s^{-1})	Eq. wid. (km s^{-1})	Intrins. wid. (km s^{-1})	Vel. Amp. (km s^{-1})	Phase
			$f_3 = 0.82202$ d^{-1}				
$(0, 0)$	20.17	89	28.4	9.06, 9.12	9.47, 9.53	5.69, 5.7, 5.74	0.78
$(1, 1)$	3.096	38	22.9	8	8	0.244	0.276
$(2, -2)$	9.167	25	12.1	20	9.94	1.19	0.78
$(2, -1)$	14.81	65, 87	24.3, 27.1	5.88, 16.2	5, 7.29	1.29, 5.54	0.78
$(2, 0)$	15.68	43, 56	10, 18.6	8, 9.76	5, 5.18	16.7, 18.3	0.591, 0.756
$(2, 1)$	9.289	85	15.1	11.4	5	14.3	0.276
$(3, -1)$	11.22	65	29.8	7.53	5.59	6.19	0.772
$(3, 0)$	13.49	43, 65	18.6, 25	7.35, 9.59	5, 6.53	5.39, 16.7	0.591, 0.764
$(3, 2)$	20.22	23, 69, 70	23.5, 28.3	9.06, 9.35, 9.76	5.53, 9.06, 9.35, 9.47	1.09, 5.2, 5.29, 5.32, 5.34	0.78, 0.795
		76, 89	28.4, 28.7	9.82, 9.94	9.53, 9.59, 9.76	5.37, 5.71, 5.74, 5.86	

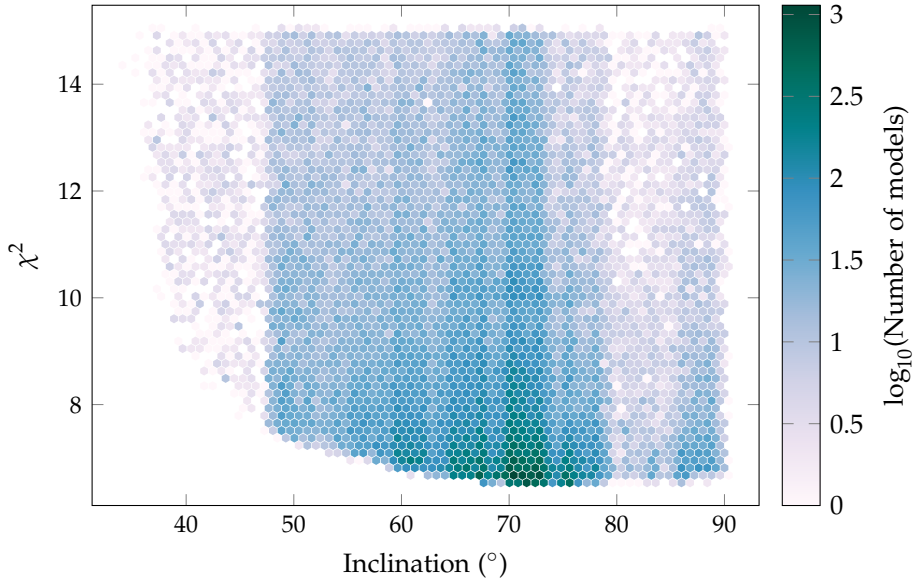

FIGURE 5.19: Modelled inclination values for the multi-mode fit of HD197541.

The conclusion is that all three frequencies are described by $(\ell, m) = (1, 1)$ modes. The amplitude and phase fits, especially for $f_1 = 0.71344$ d^{-1} and $f_2 = 1.0181$ d^{-1}, are very good. The zero-point fits are also reasonably close, though it should be noted that the radial velocity offset has been left as a free parameter and the zero-point is excluded from the χ^2 minimization. Each of the individual models appear relatively insensitive to inclination, so it falls to a multi-mode fit to try to constrain the parameters further.

Figure 5.19 shows the convergence of the inclination values for the multi-mode fit, where the three frequencies are modelled together. The inclination of HD197541 appears relatively high at $\gtrsim 60°$, which is interesting especially given its fairly low $v \sin i$. The best-fit $v \sin i$ is 20.8 km s^{-1}, and the spread of the models is shown in Figure 5.20. Table 5.6 summarizes the final parameters for HD197541, and these models are plotted in Figure 5.21. As found in the other stars, it has not been possible reasonably to converge to a particular value for the mass and radius of the star: the pulsation profiles are simply too insensitive to these parameters to get anything more accurate than a basic isochrone estimate. The final best-fit parameters for each frequency are described in Table 5.6.

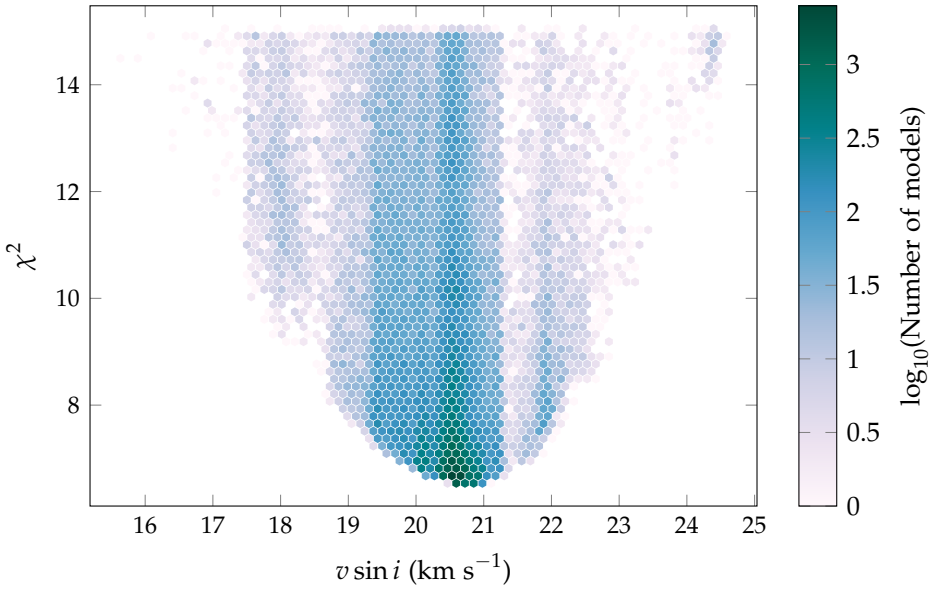

FIGURE 5.20: Modelled $v \sin i$ values for the multi-mode fit of HD197541.

TABLE 5.6: The final mode identification for HD197541. The final zero-point parameters are $v \sin i$ = 20.8 km s^{-1}, equivalent width = 5.58 km s^{-1}, intrinsic width = 7.54 km s^{-1}, and velocity offset = 0.20 km s^{-1}.

Frequency	(ℓ, m)	Vel. Amp. (km s^{-1})	Phase
$f_1 = 0.71344$ d^{-1}	$(1, 1)$	0.268	0.528
$f_2 = 1.0181$ d^{-1}	$(1, 1)$	0.583	0.378
$f_3 = 0.82202$ d^{-1}	$(1, 1)$	0.286	0.276

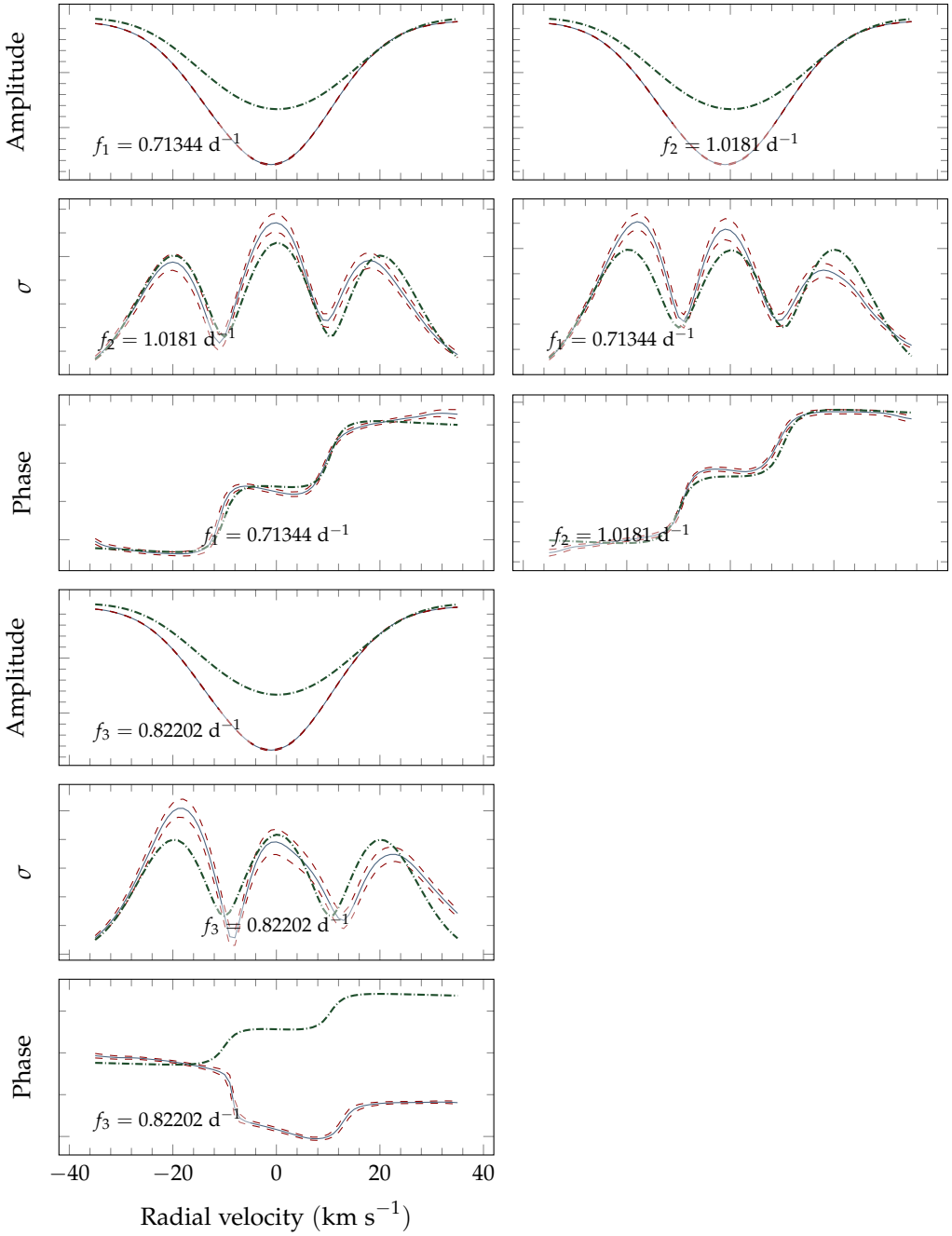

FIGURE 5.21: Plotted are the zero-point, amplitude, and phase fits for the best-fit models at each indicated frequency. They are all $(\ell, m) = (1, 1)$ modes. It is possible that resonances between the frequencies are distorting the mean line profile and impeding the fit. For each indicated frequency, the zero-point, pulsation amplitude, and phase fits (dash-dotted lines), as fitted by FAMIAS, are plotted. Additionally, the least-squares fitted profiles are plotted (solid, with dashed uncertainties).

5.5 DISCUSSION

The three analysed frequencies, $f_1 = 0.71344\,\mathrm{d}^{-1}$, $f_2 = 1.0181\,\mathrm{d}^{-1}$, and $f_3 = 0.82202\,\mathrm{d}^{-1}$, have all been identified as $(\ell, m) = (1, 1)$ modes. Since these three frequencies only account for a third of the observed line profile variations, it appears very likely that there are several more modes to be discovered. Because the shape of the overall variations is similar to the three identified frequencies, and the large distortions occasionally observed, it seems possible that there are several $(\ell, m) = (1, 1)$ frequencies which occasionally beat in phase together to produce very large distortions in the line profile.

These very large distortions are reminiscent of the Blazhko effect, however good photometric data would be needed to compare the lightcurves of HD197541 with known Blazhko stars, as well as the lightcurves of other γ Doradus stars from Kepler photometry (Balona et al., 2011) that might show similar variations. If a successful proposal were put forward, satellite photometry from MOST may prove very useful.

The zero-point of the final multi-mode fit is not as well fitted as the individual fits, as the multi-mode fit has converged to smaller equivalent width and intrinsic width values. Nevertheless, the ℓ and m values at $(\ell, m) = (1, 1)$ are the best fits by a significant margin, so there is a high degree of confidence that they are the true modes of pulsation in the star. Owing to the fact that there is still some residual uncertainty in the accuracy of the frequency determinations, further observations would be especially welcome to confirm the frequencies and perhaps detect lower amplitude pulsations that were not reliably found in this analysis.

6

CONCLUSIONS

Three stars were analysed in this thesis: HD139095, HD153580, and HD197541. HD139095 was already confirmed as a bona fide γ Doradus variable by Handler and Shobbrook (2002), but the latter two were previously only candidates for the class. In this thesis, all three stars are confirmed as bona fide γ Doradus stars through the spectroscopic observation of one or more frequencies characteristic of γ Doradus stars. The spectroscopic mode identifications are the most important results presented in the previous chapters in this thesis, as no mode identifications for these stars previously existed. Table 6.1 summarizes the mode identifications for the three stars, and Table 6.2 summarizes the fundamental stellar parameters determined.

The low-degree modes identified in each star are typical of γ Doradus type stars, and the velocity amplitudes of the three frequencies of HD197541 and the one frequency of HD153580 are reasonably low. The best-fit velocity amplitudes for the four HD139095 modes (see Table 6.1) are anomalously high for a γ Doradus star, in comparison to many previous observational results that show amplitudes on the order of 1 km s^{-1} in radial velocity (Brunsden, 2013; Davie, 2013; Mathias et al., 2004). This could be due to a misidentification of the stellar inclination. The data for HD139095 are the lowest quality out of the three stars here: although the temporal sampling is good, the data still suffer from noise (an unavoidable consequence of the star's dim $m_V = 7.9$). All the frequencies found are within the expected range, although there is still some uncertainty over the identity of $f_2 = 0.59460$ d^{-1}, as it is possible this is an alias of another frequency.

One problem that remains unsolved is that of the unusually strong line profile variations sometimes seen in HD197541 (see Figure 5.4). It is simply unclear whether these are due to a resonance (of unknown periodicity) between a group of $(\ell, m) = (1, 1)$ modes, or some other unidentified phenomenon. This feature alone makes HD197541 a very interesting object, certainly worthy of further study.

The analysis of HD153580 is reasonably conclusive: the variations are extremely well defined by our current observations. The limiting factor here, most definitely, is our ability to model the shape of these variations. The large χ^2 values of the fits are a manifestation of this, and are inflated because the models do not conform well to within the error limits of these strongly defined variations. Obtaining more spectra may only be

TABLE 6.1: The final mode identification for HD197541, HD139095, and HD153580

Star	Frequency	(ℓ, m)	Vel. Amp. (km s^{-1})	Phase
HD197541	$f_1 = 0.71344$ d^{-1}	$(1, 1)$	0.268	0.528
HD197541	$f_2 = 1.0181$ d^{-1}	$(1, 1)$	0.583	0.378
HD197541	$f_3 = 0.82202$ d^{-1}	$(1, 1)$	0.286	0.276
HD139095	$f_1 = 1.2263$ d^{-1}	$(2, -2)$	17.1	0.614
HD139095	$f_2 = 0.59460$ d^{-1}	$(2, -2)$	9.29	0.378
HD139095	$f_4 = 1.1323$ d^{-1}	$(2, -2)$	11.3	0.228
HD139095	$f_5 = 1.3871$ d^{-1}	$(2, -2)$	9.97	0.0945
HD153580	$f_1 = 0.6589$ d^{-1}	$(2, -1)$	0.772	0.585

a useful exercise if done from a space-based spectroscopic observatory, where the light from the dimmer companion could be excluded (thus making a spectroscopic abundance analysis much easier), or if the mechanisms producing the line profile variations are better modelled in an analysis with more data.

Both HD139095 and HD197541 may be good targets for re-analysis if more spectra were obtained. A significant proportion of their line profile variations remains unexplained by the currently determined frequencies, and perhaps with many more spectra and some photometric observations, a rich spectrum of frequencies may be uncovered in each star. This prospect differs significantly from HD153580, where only one frequency has been found and it is unlikely any other significant frequencies exist. This is probably a manifestation of the fact that cooler γ Doradus-type stars are theoretically expected to have fewer modes of pulsation (Guzik et al., 2000).

The testing of two methods of spectroscopic abundance analysis (spectrum synthesis and the equivalent width method) has given reasonable (but not conclusive) results. Both methods produce feasible values of $T_{\rm eff}$, $\log g$, and metallicity, but small discrepancies remain between the values obtained via each method. Both are apparently viable methods of obtaining reasonable abundance analysis results, but it is not clear which method is truly more reliable.

SME is the more easily automated of the two, and with detailed care and plenty of computation time it may produce the abundances of many elements. The equivalent width method using FUNDPAR is (computationally) comparatively quick to execute, but it remains a time-consuming task manually to measure equivalent widths. The automatic equivalent-width finding method (using ARES) may be useful for very high signal-to-noise spectra if a routine were implemented to remove anomalous measurements, but for measuring the lines of one element in a few stars, manual measurements are easily feasible.

TABLE 6.2: The final stellar parameters for HD197541, HD139095, and HD153580, that have been determined from the analyses in this thesis. The mass and radius values are estimated from the FUNDPAR results. An abundance analysis was not carried out on HD153580 owing to its binarity.

Property	HD139095	HD153580	HD197541	Source
Mass ($M_\odot$)	1.6		1.7	Polynomials (Torres et al., 2010)
Radius ($R_\odot$)	2.1		2.1	Polynomials (Torres et al., 2010)
$T_{\rm eff}$ (K)	7092		7228	SME
	6921		7128	FUNDPAR
$\log g$	3.51		3.89	SME
	3.99		4.01	FUNDPAR
[M/H]	0.071		0.063	SME
[Fe/H]	0.26		0.14	FUNDPAR
$v \sin i$ (km s^{-1})	65.3	43.6	20.8	FAMIAS
	63.6		15.9	SME
$v_{\rm mic}$ (km s^{-1})	2.7		2.3	SME
	2.29		1.58	FUNDPAR
$v_{\rm mac}$ (km s^{-1})	17.5		16.2	SME
Inclination	$15-20^\circ$	$64-71^\circ$	$60-90^\circ$	FAMIAS

6.1 FUTURE WORK

The work in this thesis has identified some interesting problems that should be investigated further. A comparison between abundance analysis techniques using many more stars would be welcome, as currently it is difficult to ascertain which method is the more reliable. Abundance analysis is a significant challenge for higher $v \sin i$ stars such as HD139095, as a significant amount of line blending can make it almost impossible adequately to resolve a good number of spectral lines. Not only does this complicate equivalent width measurements, but (especially with a somewhat noisy spectrum) it also makes the spectrum synthesis much more difficult. $T_{\rm eff}$, $\log g$, and [Fe/H] become very difficult to constrain for these faster rotators.

Another area to investigate further is the macroturbulence of these stars. It is possible to compute macroturbulence by finding the zeros of the Fourier transform of the line profile (see, for example, Gray, 1988) and matching them to a synthetically generated line profile. This is what SME does to compute macroturbulence using the radial-tangential model. It would be a useful extension to apply this same analysis to the cross-correlated line profile. A MATLAB routine exists already (Wright, 2008) for finding the $v \sin i$ in this manner, but it is necessary to apply disk-integration techniques when combining multiple forms of line broadening. One cannot convolve a rotationally-broadened line profile with a macroturbulent-broadening kernel and obtain a line profile that is correctly broadened.

Spectroscopic survey data do exist for γ Doradus stars, for example Mathias et al. (2004) present a survey of 59 northern γ Doradus stars, and De Cat et al. (2006) analyse 37 southern γ Doradus stars. No abundance results for the former have been published. However, a follow-up to the latter paper (Bruntt et al., 2008) finds that γ Doradus stars have similar $T_{\rm eff}$, $\log g$, and abundance properties to non-pulsating stars of the same spectral type. Neither study makes any report on the subject of macroturbulence: these existing spectroscopic data are ripe for the picking. It would be a useful exercise to perform Fourier analysis on the cross-correlated mean line profiles of these stars to see if there are any trends to be uncovered.

Useful information will probably be gained from more observations of HD139095 and HD197541. More observations would allow for the frequencies and their associated line profile variations to be better defined, and it is expected that several more frequencies would be found in each star. A more comprehensive mode identification of each star may provide very valuable observational data with regards to how γ Doradus modes are excited. More observations of HD197541 would be especially welcome, as they might shed some more light onto the potentially Blazhko-like variations seen. A long run of continuous satellite photometry data would be particularly useful.

High-priority targets for future observations are HD109799 and HD103257. We already have 59 and 53 MJUO spectra of each star respectively, and these stars are prioritized targets for observing runs during the first half of 2014. A preliminary reduction

of these stars' line profiles shows strong variations that are likely to result in a good mode identification. HD17310 is a bona fide γ Doradus star (Henry et al., 2007) in a SB1 spectroscopic binary system (no detectable companion), with 81 existing MJUO spectra. The list of targets that is internal to the MUSICIAN group is in great need of an update: the targets that are suitable for analysis are simply approaching exhaustion. Perhaps the results emerging from Kepler (for Northern collaborators) and CoRoT will identify some useful targets.

Further advances in the sophistication of mode identification software will also be very welcome. Development of the FAMIAS software is unfortunately stagnating at the current time, so either further development efforts of FAMIAS, or a replacement program, are needed to keep pace with theoretical developments. Command-line and 64-bit implementations of FAMIAS will be especially welcome, as memory limitations and the requirement manually to operate the GUI can slow down the exploration of a large parameter space. For an example of theory that should be implemented, recent developments about the effects of the Coriolis force (Bouabid et al., 2013) should be implemented in our modelling. Another possibility worth investigating is whether it is possible for the rotation and pulsation axes can be misaligned: this could help resolve some of the asymmetries commonly observed in the line profiles of γ Doradus stars that we cannot currently model accurately.

6.2 FINAL WORDS

The frequency and mode identification results generally agree well with those found in past literature for γ Doradus stars. The three stars in this thesis are complicit with the increasing trend that γ Doradus pulsation modes are of low degree and azimuthal order, with frequencies on the order of 1 d^{-1}, as detailed in the most recent compilation of γ Doradus mode identifications by Brunsden (2013). HD153580 is an interesting case, as it almost certainly pulsates with a single mode (that we can still only poorly model). The odd line profile variations seen in HD197541 are reminiscent of the Blazhko effect, which has not previously been observed spectroscopically in γ Doradus stars (but has been suggested by photometric observations, such as Henry et al., 2007). With the caveat that abundance analysis results in fast rotators ($v \sin i \gtrsim 50$ km s^{-1}) may not converge properly (Bruntt et al., 2008), the results obtained are still well within expected values. As the number of γ Doradus mode identifications continues to grow, theoretical modelling work must continue in earnest, in order better to explain our observations.

ACKNOWLEDGMENTS

Firstly I would like to thank my supervisors, Associate Professor Karen Pollard and Professor Peter Cottrell, for their valuable support and input throughout the period of this research. Their consistently high expectations, in-depth feedback, and veritably encyclopaedic knowledge have kept me on my toes. I am grateful for the year-long financial support of the Department of Physics and Astronomy, as well as the Marsden fund which allowed me to attend the annual RASNZ conference in Invercargill in May.

My thanks also go to my office mates for their company and conversation – both for useful discussions about computer coding and not-so-useful discussions about cake and the meaning of life.

Emily Brunsden, Florian Maisonneuve, Matt Davie, and Pam Kilmartin have all spent time observing stars at MJUO whose spectra were used in this thesis, and for that I am also grateful: I could not have gathered enough by myself.

I also have significant gratitude for the assistance of The Internet, mostly with regards to the typesetting of this thesis. The many developers of LaTeX 2ε, Till Tantau who wrote the *fantastic* PGF/Ti*k*Z packages, Christian Feuersänger who wrote the PGFPLOTS package, Nico Schlömer who wrote MATLAB2Ti*k*Z, André Miede who wrote the `classicthesis` style for LaTeX 2ε, and the many users of TeX.StackExchange whose repository of questions and answers provided many useful nuggets. I owe the presentation of this thesis to these wonderful folk.

Finally, my friends and family – thank you for your support and frequent (much needed) distractions.

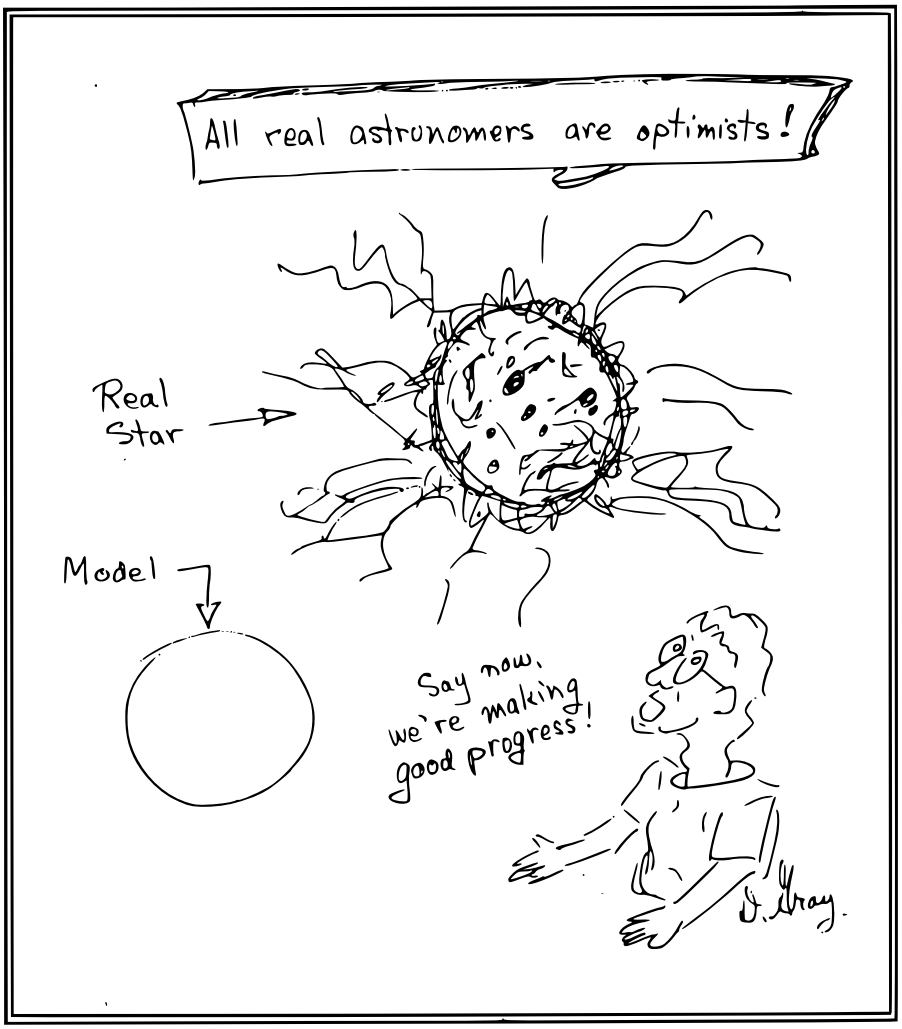

One of the many cartoons in David Gray's 1988 book *Lectures on spectral-line analysis: F, G, and K stars*.

A

FITS SPECTRUM EXAMPLES

The following two figures are examples of spectra taken by the HERCULES spectrograph at MJUO on October 9, 2013.

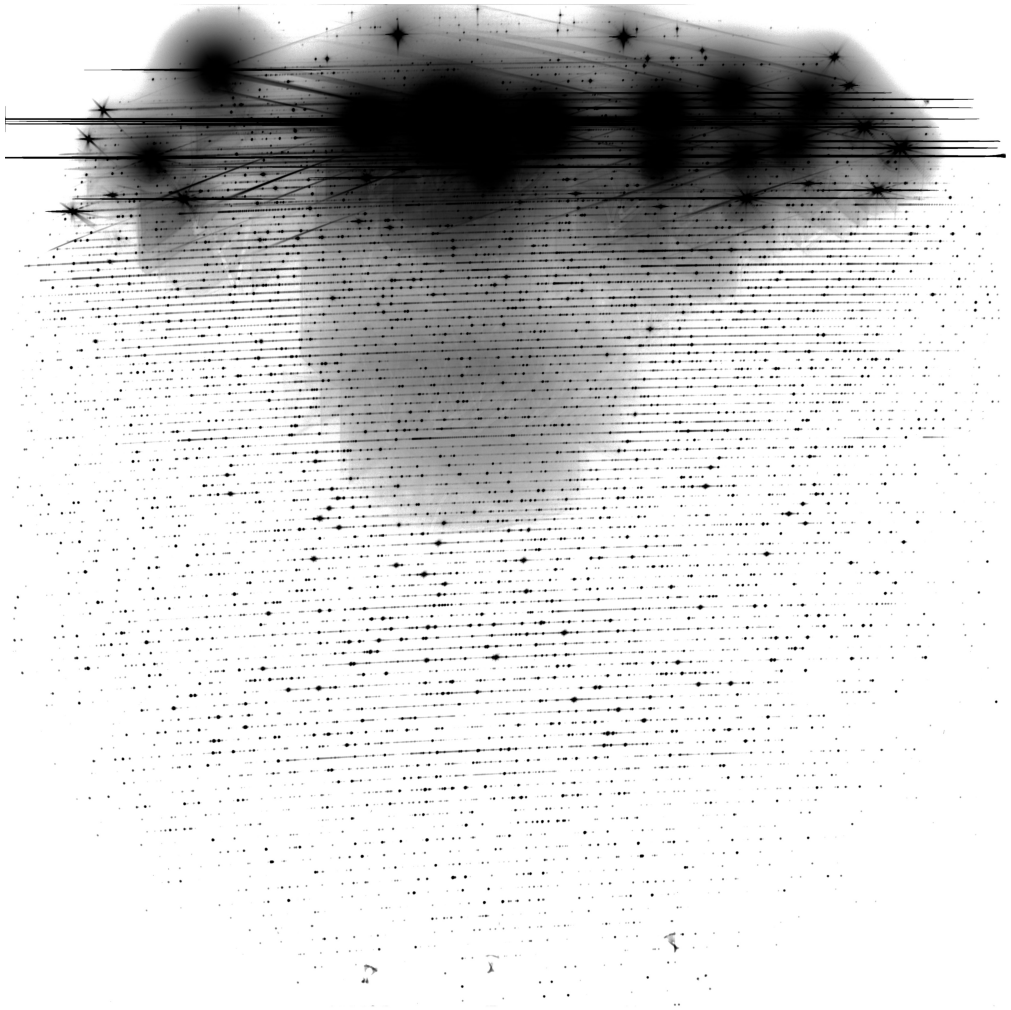

FIGURE A.1: A thorium-argon lamp image taken with the HERCULES spectrograph. The wavelength range is approximately 380 nm to 880 nm, and the bottom of the image corresponds to the blue end of the spectrum. The intensity data have been scaled by the program SAOImage DS9, and then inverted, to improve visibility of details. The overexposed regions of the chip are not relied upon for wavelength calibration. The HERCULES flux meter recorded 4.8 million total counts, and the exposure time was 12 seconds.

FIGURE A.2: An image of HD14940 taken with the HERCULES spectrograph. The intensity data have been scaled by the program SAOImage DS9, then inverted, to improve visibility of details. Some strong stellar absorption lines, as well as telluric (atmospheric absorption) regions, are visible. The HERCULES flux meter recorded 3.2 million total counts, and the exposure time was 20 minutes.

B

ADDITIONAL PLOTS OF HD139095

Figure B.1 shows the synthetic line profile variations of the final four frequencies, computed using FAMIAS with the same parameters as the final mode identification in Table 4.8. Figures B.2 to B.6 display a range of best-fit modes for HD139095 at each of the analysed frequencies.

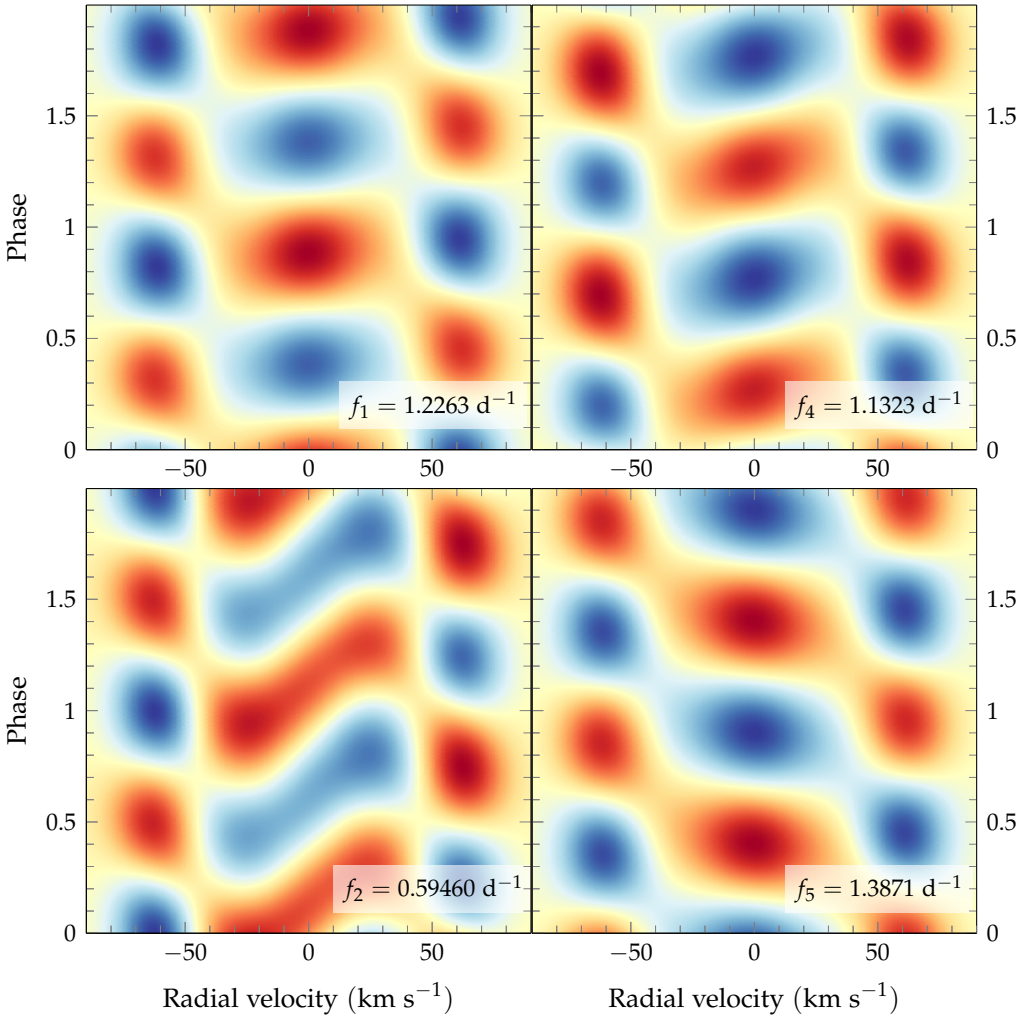

FIGURE B.1: Synthetic line profile variations for each of the identified frequencies of HD139095, computed with FAMIAS using the same parameters as the final mode identifications. All of these synthetic variations appear to be out of phase with the true observations by a factor of π, so the colourmap has been inverted (in comparison to Figures 4.15 and 4.16).

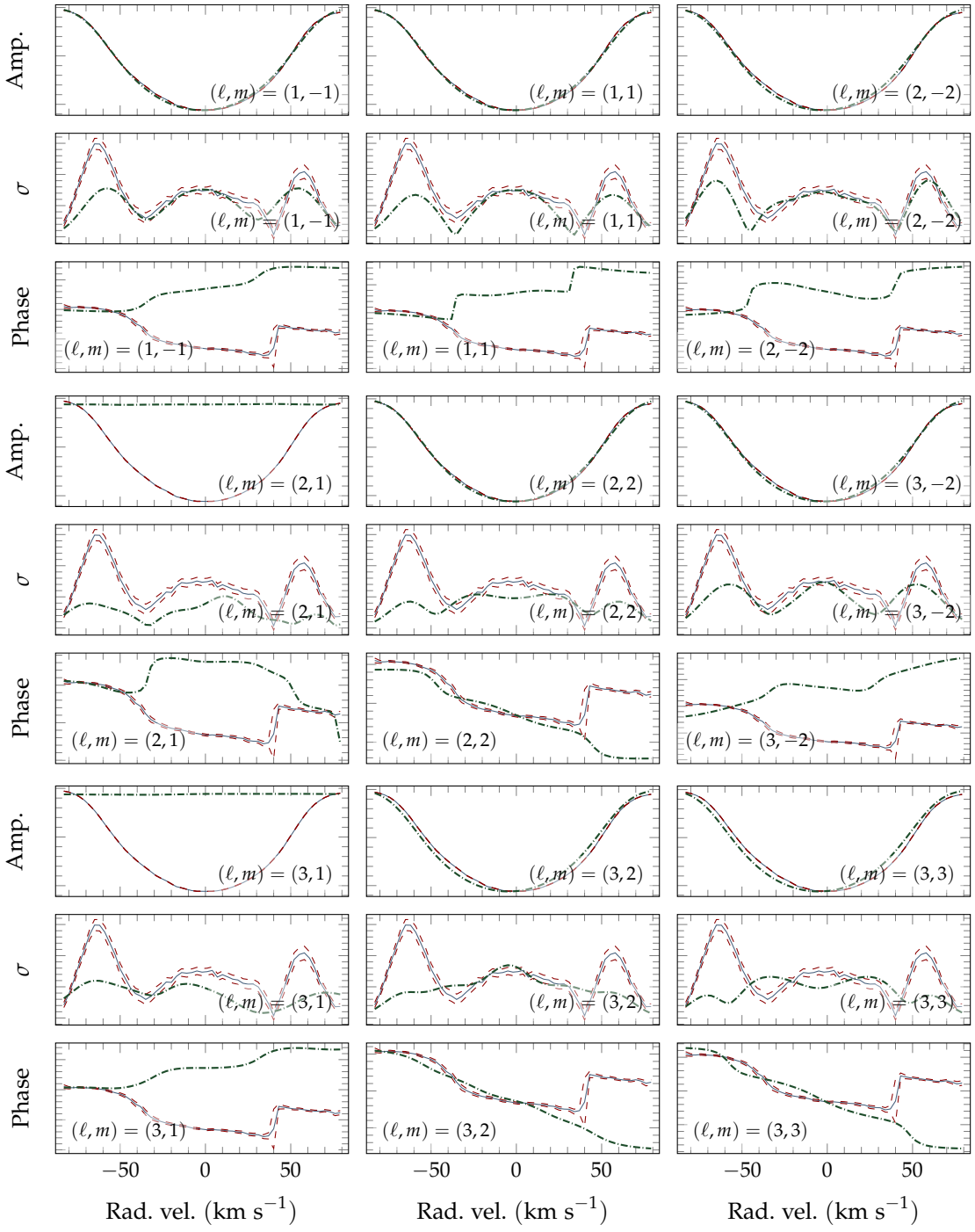

FIGURE B.2: The best-fit modes for HD139095 at $f_1 = 1.2263$ d^{-1}. For each indicated (ℓ, m) combination, the zero-point, pulsation amplitude, and phase fits for each of the indicated modes (dash-dotted lines), as fitted by FAMIAS, are plotted. Additionally, the least-squares fitted profiles are plotted (solid, with dashed uncertainties).

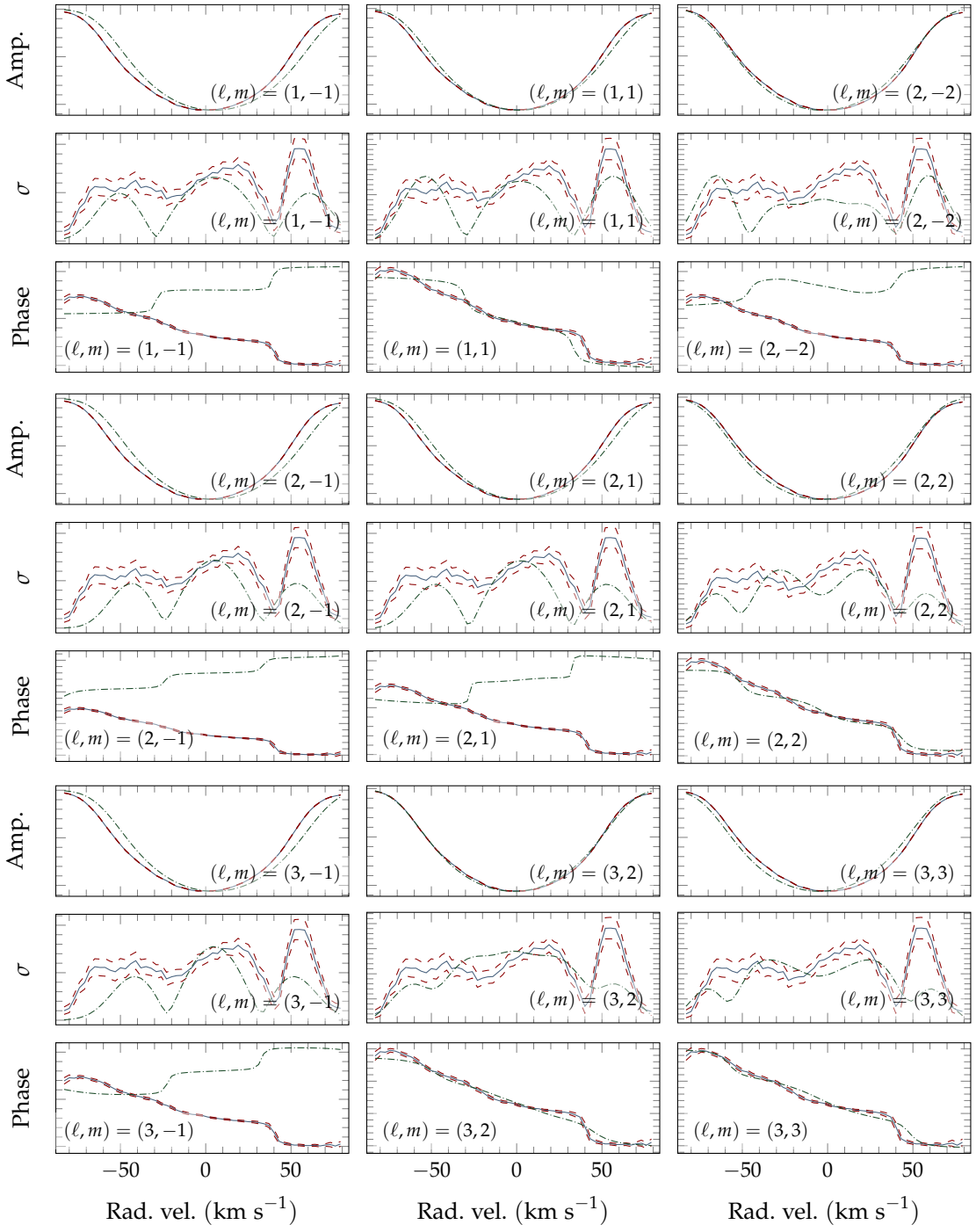

FIGURE B.3: The best-fit modes for HD139095 at $f_{2b} = 1.5972$ d^{-1}. For each indicated (ℓ, m) combination, the zero-point, pulsation amplitude, and phase fits for each of the indicated modes (dash-dotted lines), as fitted by FAMIAS, are plotted. Additionally, the least-squares fitted profiles are plotted (solid, with dashed uncertainties).

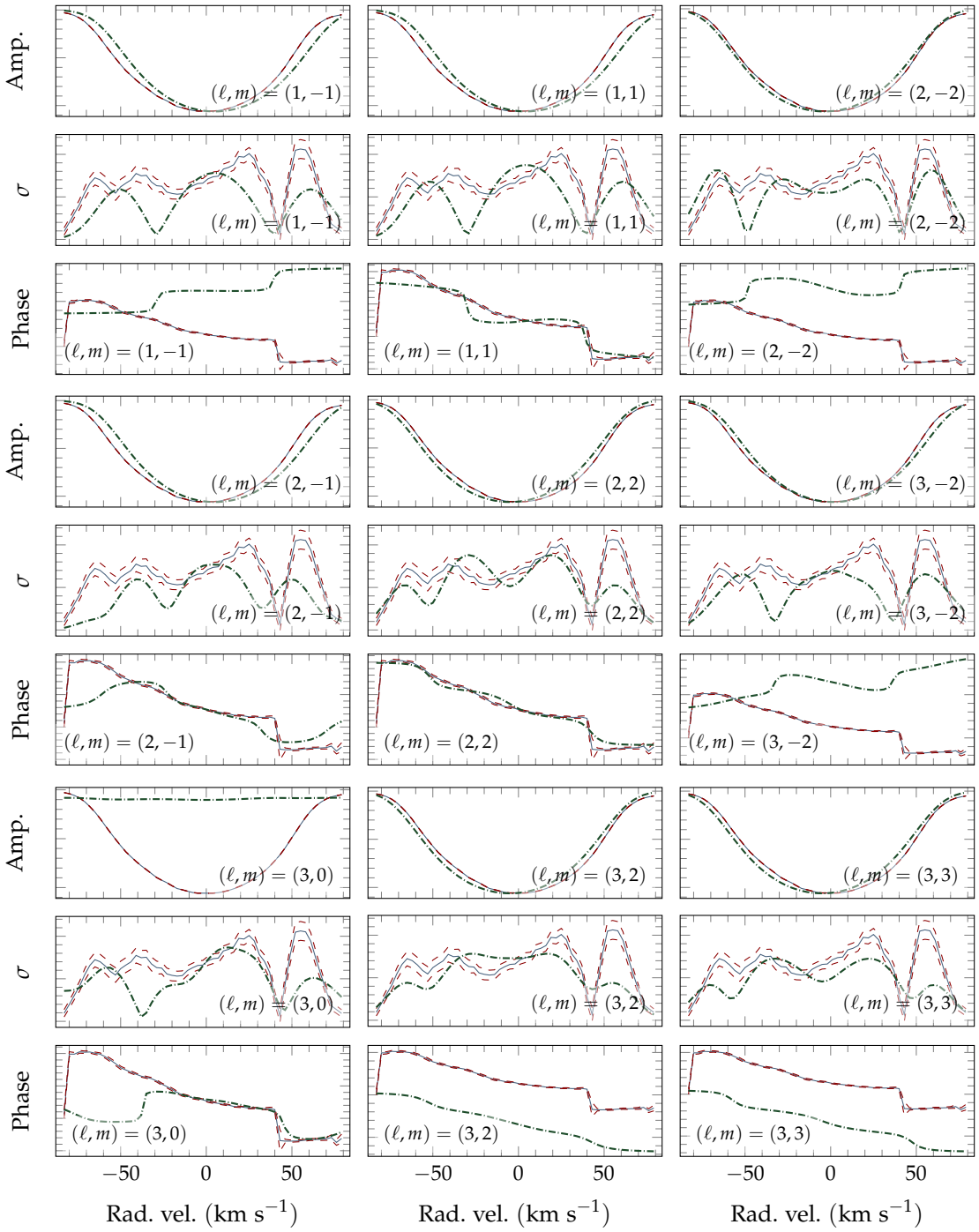

FIGURE B.4: The best-fit modes for HD139095 at $f_2 = 0.59460$ d^{-1}. For each indicated (ℓ, m) combination, the zero-point, pulsation amplitude, and phase fits for each of the indicated modes (dash-dotted lines), as fitted by FAMIAS, are plotted. Additionally, the least-squares fitted profiles are plotted (solid, with dashed uncertainties).

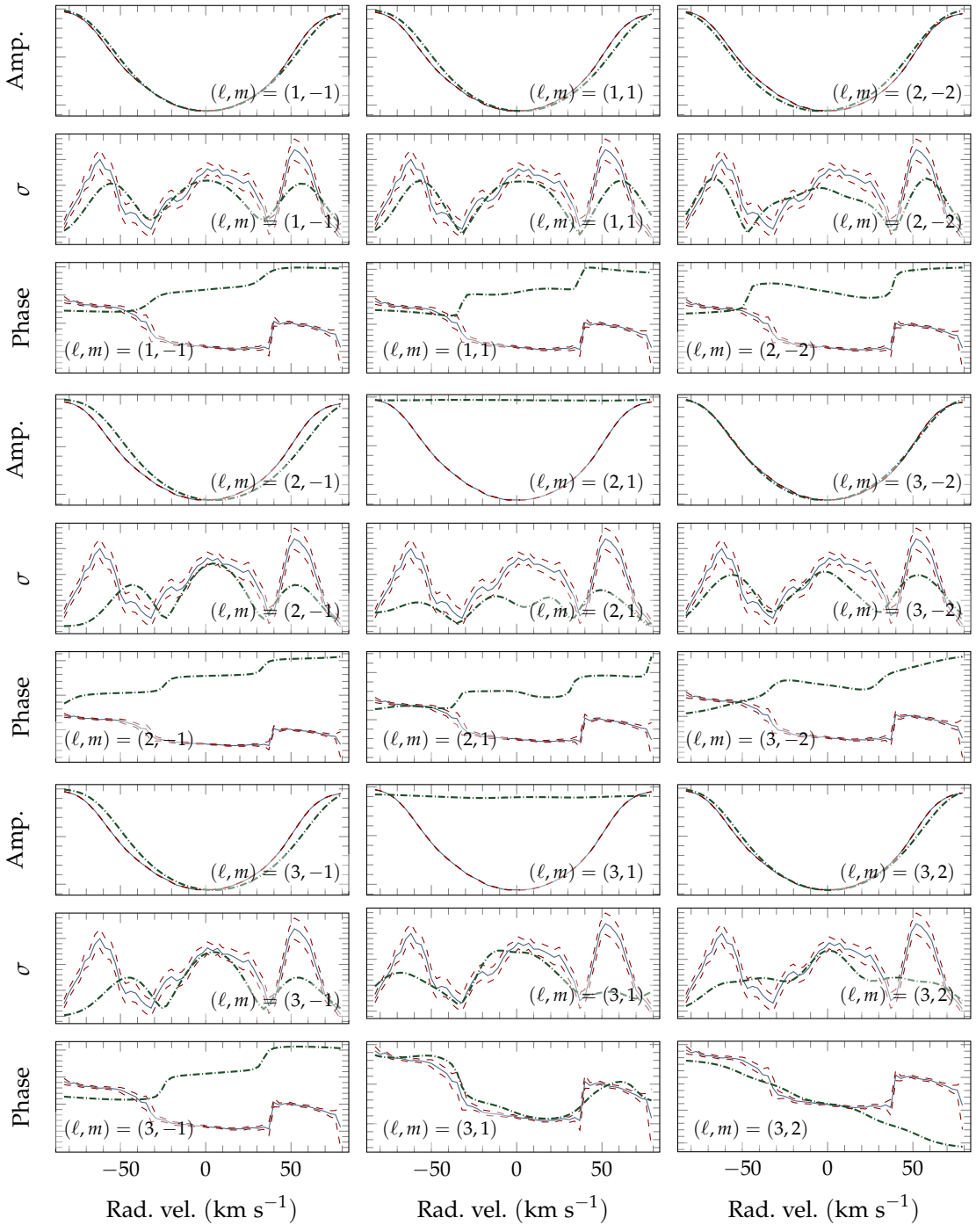

FIGURE B.5: The best-fit modes for HD139095 at $f_4 = 1.1323$ d^{-1}. For each indicated (ℓ, m) combination, the zero-point, pulsation amplitude, and phase fits for each of the indicated modes (dash-dotted lines), as fitted by FAMIAS, are plotted. Additionally, the least-squares fitted profiles are plotted (solid, with dashed uncertainties).

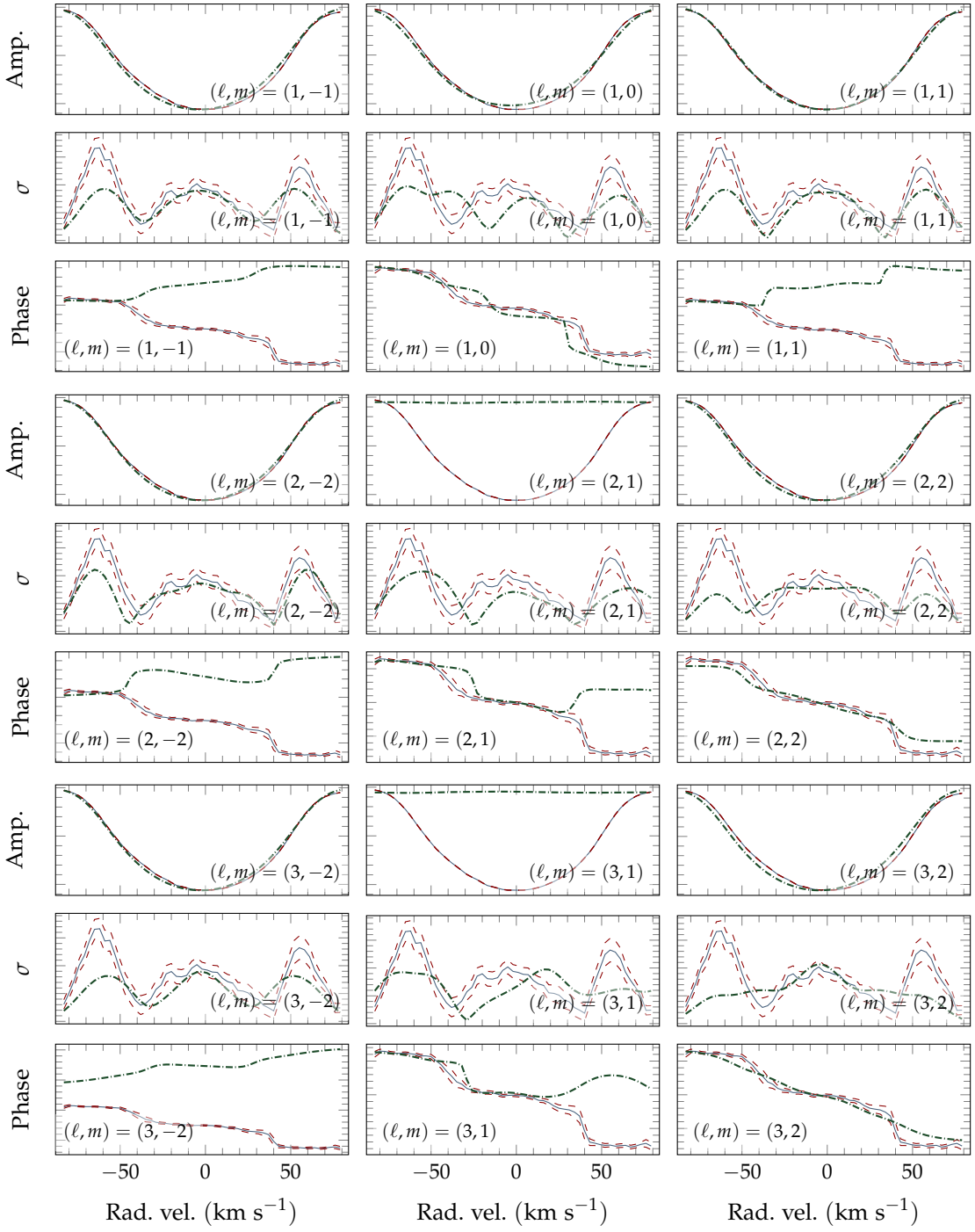

FIGURE B.6: The best-fit modes for HD139095 at $f_5 = 1.3871$ d^{-1}. For each indicated (ℓ, m) combination, the zero-point, pulsation amplitude, and phase fits for each of the indicated modes (dash-dotted lines), as fitted by FAMIAS, are plotted. Additionally, the least-squares fitted profiles are plotted (solid, with dashed uncertainties).

C

ADDITIONAL PLOTS OF HD197541

Figure C.1 shows the synthetic line profile variations of HD197541 computed at each frequency by FAMIAS, using the final mode identification parameters for each frequency identified in Table 5.6. Figures C.2 to C.4 display a range of best-fit modes for HD197541 at each of the analysed frequencies. In cases where the zero-point fits are extremely poor, this is because in these situations the modelled pulsation amplitude is extremely high. Thus, there is a large degree of pulsational broadening. These fits are not reliable.

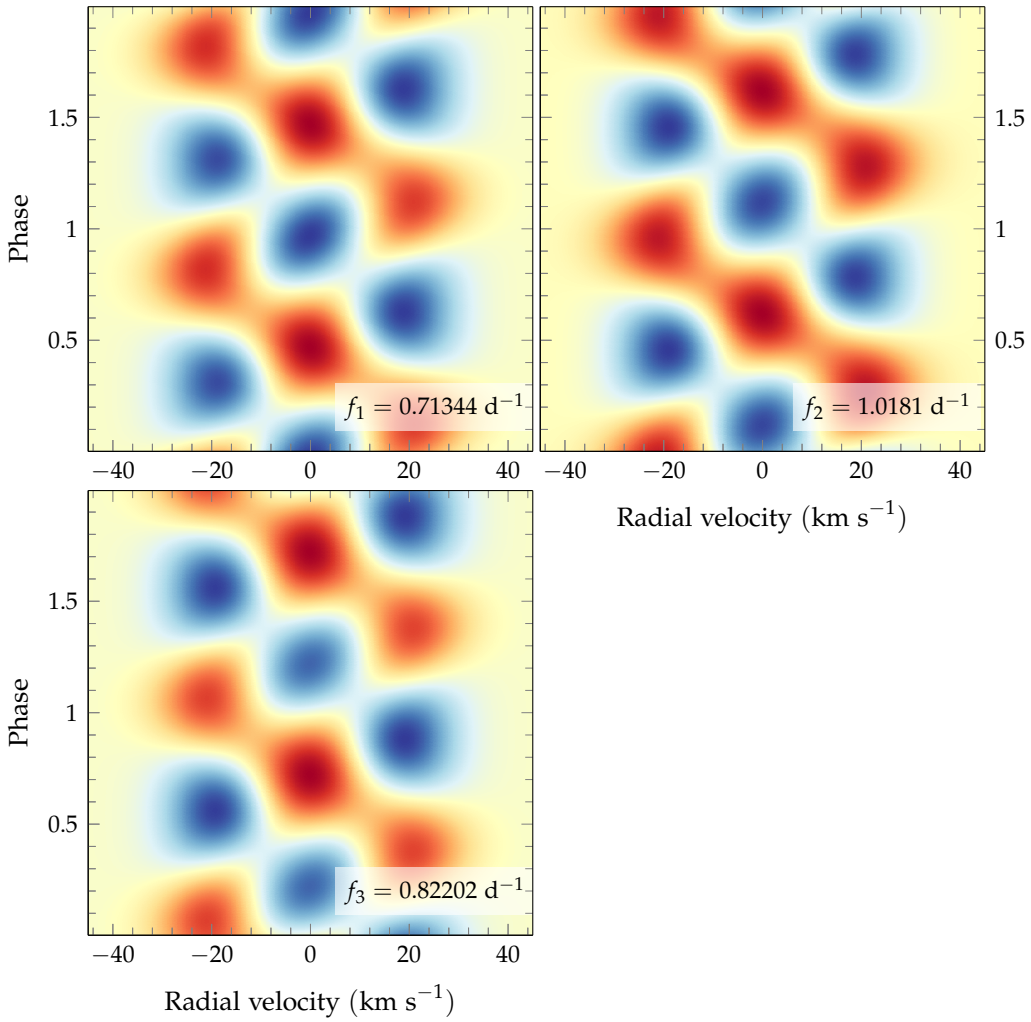

FIGURE C.1: Synthetic line profile variations for each of the identified frequencies of HD197541, computed with FAMIAS using the same parameters as the final mode identifications. All of these synthetic variations appear to be out of phase with the true observations by a factor of π, so the colourmap has been inverted (in comparison to Figure 5.16).

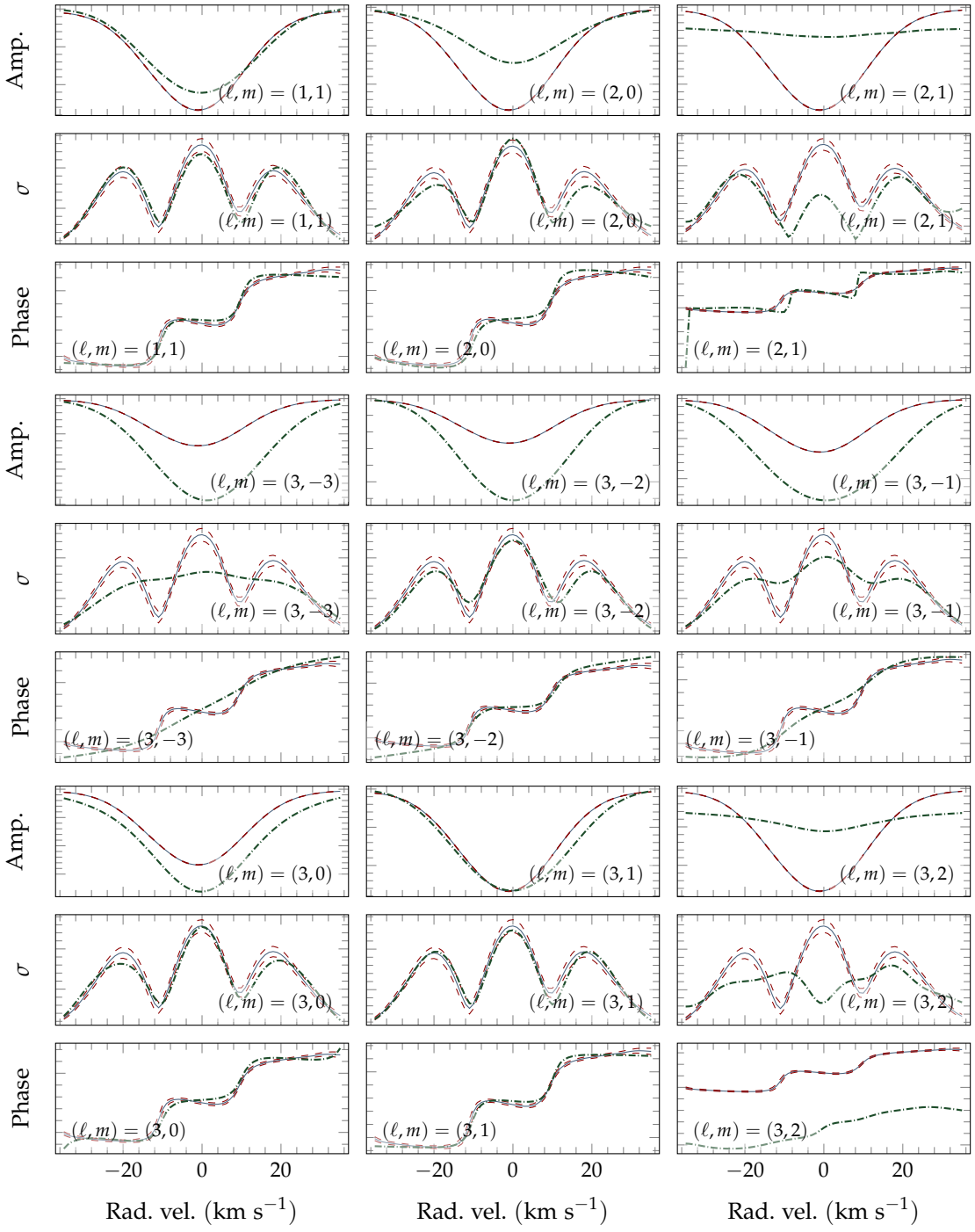

FIGURE C.2: The best-fit modes for HD197541 at $f_1 = 0.71344$ d^{-1}. For each indicated (ℓ, m) combination, the zero-point, pulsation amplitude, and phase fits for each of the indicated modes (dash-dotted lines), as fitted by FAMIAS, are plotted. Additionally, the least-squares fitted profiles are plotted (solid, with dashed uncertainties).

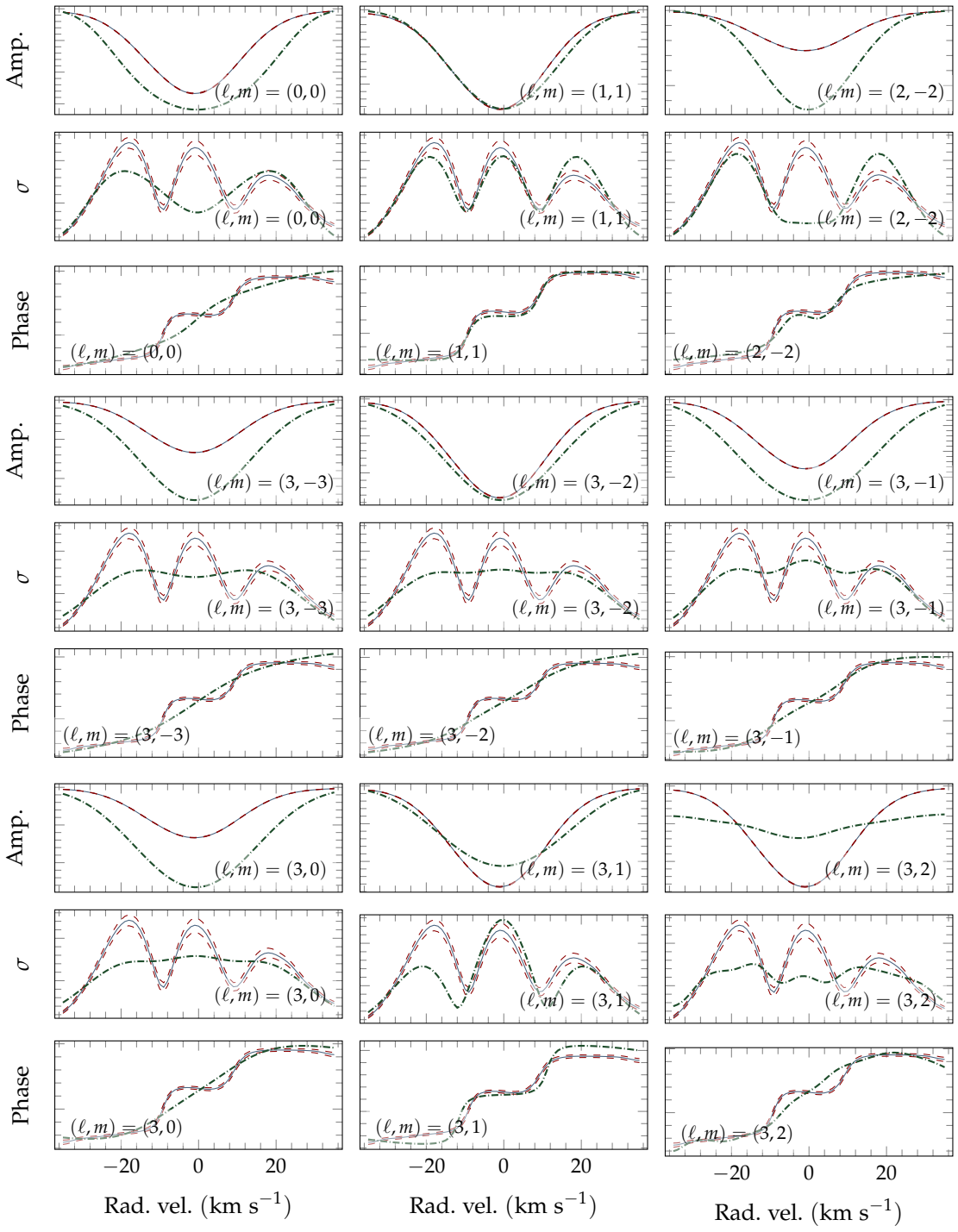

FIGURE C.3: The best-fit modes for HD197541 at $f_2 = 1.0181$ d^{-1}. For each indicated (ℓ, m) combination, the zero-point, pulsation amplitude, and phase fits for each of the indicated modes (dash-dotted lines), as fitted by FAMIAS, are plotted. Additionally, the least-squares fitted profiles are plotted (solid, with dashed uncertainties).

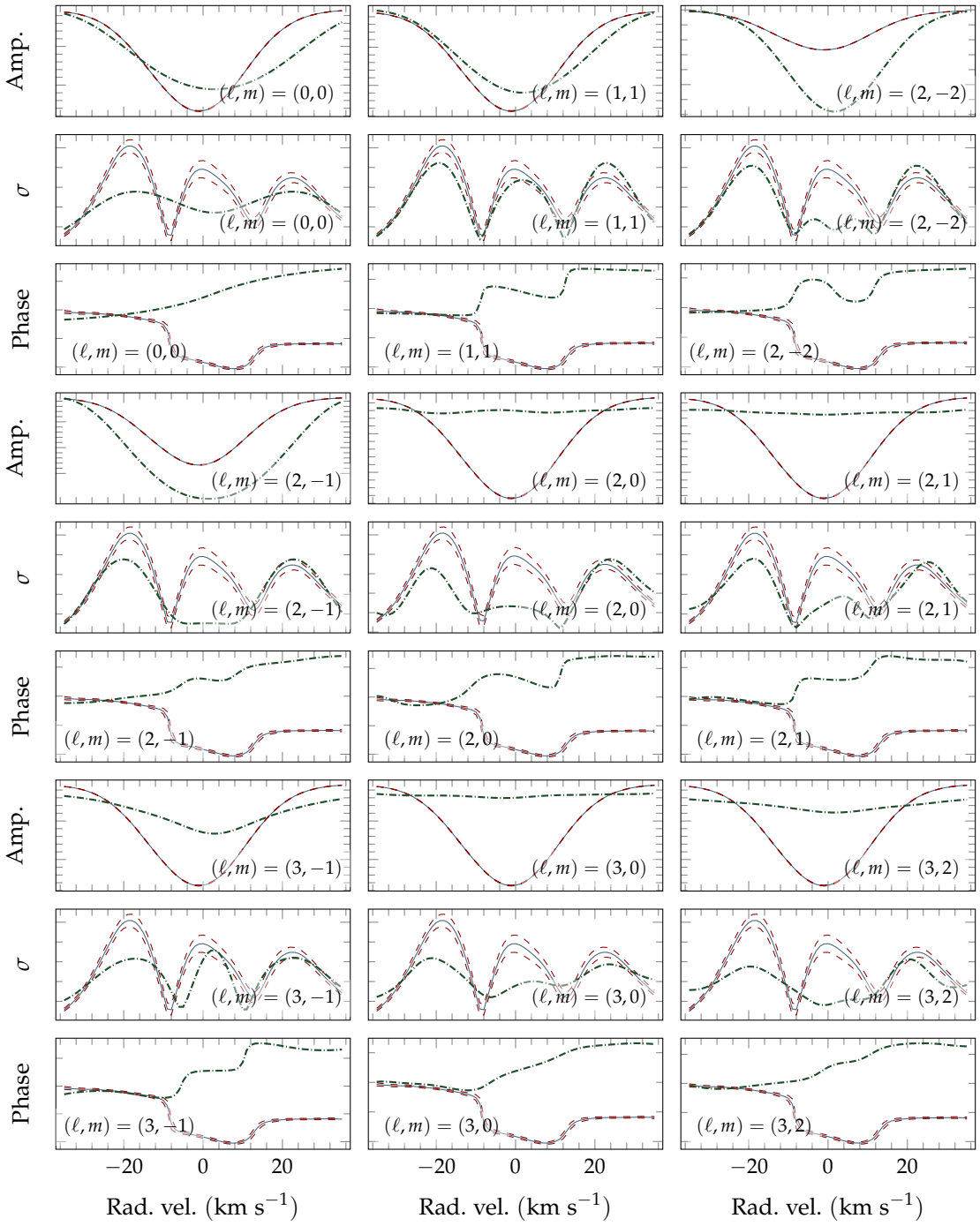

FIGURE C.4: The best-fit modes for HD197541 at $f_3 = 0.82202$ d^{-1}. For each indicated (ℓ, m) combination, the zero-point, pulsation amplitude, and phase fits for each of the indicated modes (dash-dotted lines), as fitted by FAMIAS, are plotted. Additionally, the least-squares fitted profiles are plotted (solid, with dashed uncertainties).

D

LINE-LISTS USED FOR ABUNDANCE ANALYSIS

The following tables present the equivalent width measurements made using SPECTRE, for HD139095 and HD197541. They are presented in monospaced font, so that in the electronic version of this thesis, the table may be directly copied from a PDF reader to create a FUNDPAR-compatible input file. The underscore characters (which have been inserted to ensure compatibility) must be replaced with spaces. The columns are wavelength (Å), species, excitation potential (eV), $\log(gf)$, and equivalent width (mÅ). The linelist used was that of Davie (2013).

TABLE D.1: The equivalent-width measurements for HD197541.

HD197541		7000	4.0	-0.10	2.00
4602.941	26.0	1.485	-2.209		83.7
4607.646	26.0	3.266	-1.467		65.9
4613.203	26.0	3.292	-1.670		65.0
4625.045	26.0	3.241	-1.340		54.4
4632.911	26.0	1.608	-2.913		50.6
4638.010	26.0	3.602	-1.119		57.7
4733.591	26.0	1.485	-2.988		47.9
4735.843	26.0	4.076	-1.325		31.2
4736.773	26.0	3.211	-0.752		102.1
4745.800	26.0	3.654	-1.270		39.7
4802.880	26.0	3.642	-1.514		31.0
4942.459	26.0	4.22	-1.409		34.4
4946.387	26.0	3.368	-1.170		63.9
4966.088	26.0	3.332	-0.871		85.5
4967.897	26.0	4.191	-0.487		58.0
4969.917	26.0	4.217	-0.710		51.9
4973.102	26.0	3.96	-0.950		59.4
4988.950	26.0	4.154	-0.890		63.2
4994.130	26.0	0.915	-3.080		83.2
5014.942	26.0	3.943	-0.303		89.8
5027.123	26.0	4.154	-0.534		95.0
5029.618	26.0	3.415	-2.050		18.4
5067.150	26.0	4.22	-0.970		37.9
5074.748	26.0	4.22	-0.200		93.5
5076.264	26.0	4.301	-0.809		45.4
5121.639	26.0	4.283	-0.810		48.6
5123.720	26.0	1.011	-3.068		58.0
5131.468	26.0	2.223	-2.515		47.5
5133.688	26.0	4.178	0.140		116.0
5141.739	26.0	2.424	-1.964		44.1
5150.839	26.0	0.99	-3.003		62.1
5151.911	26.0	1.011	-3.322		40.7
5159.058	26.0	4.283	-0.820		39.8
5162.273	26.0	4.178	0.020		118.1
5194.941	26.0	1.557	-2.090		102.4
5198.711	26.0	2.223	-2.135		58.7
5250.646	26.0	2.198	-2.181		67.9

__5302.300_____26.0_____3.283____-0.720_____________________93.4
__5315.070_____26.0_____4.371____-1.550_____________________11.2
__5341.024_____26.0_____1.608____-1.953_____________________109.2
__5361.625_____26.0_____4.415____-1.430_____________________18.1
__5373.709_____26.0_____4.473____-0.860_____________________35.7
__5389.479_____26.0_____4.415____-0.410_____________________61.7
__5391.459_____26.0_____4.154____-0.782_____________________46.4
__5393.167_____26.0_____3.241____-0.715_____________________91.6
__5398.279_____26.0_____4.445____-0.670_____________________44.8
__5400.501_____26.0_____4.371____-0.160_____________________81.5
__5405.775_____26.0_____0.99____-1.844_____________________143.0
__5410.910_____26.0_____4.473_____0.398_____________________106.9
__5415.199_____26.0_____4.386_____0.642_____________________127.7
__5424.068_____26.0_____4.32_____0.520_____________________145.2
__5434.524_____26.0_____1.011____-2.122_____________________113.6
__5445.042_____26.0_____4.386____-0.020_____________________89.2
__5473.901_____26.0_____4.154____-0.760_____________________55.4
__5483.099_____26.0_____4.154____-1.407_____________________20.0
__5497.516_____26.0_____1.011____-2.849_____________________87.2
__5506.779_____26.0_____0.99____-2.797_____________________85.3
__5543.147_____26.0_____3.695____-1.570_____________________34.7
__5563.600_____26.0_____4.191____-0.990_____________________45.3
__5569.618_____26.0_____3.417____-0.486_____________________94.0
__5576.089_____26.0_____3.43____-1.000_____________________75.4
__5586.756_____26.0_____3.368____-0.120_____________________131.4
__5633.946_____26.0_____4.991____-0.270_____________________42.6
__5717.833_____26.0_____4.284____-1.130_____________________30.6
__5752.032_____26.0_____4.549____-1.177_____________________23.9
__5762.992_____26.0_____4.209____-0.450_____________________84.4
__5816.373_____26.0_____4.548____-0.601_____________________39.9
__5859.586_____26.0_____4.549____-0.419_____________________42.2
__5862.357_____26.0_____4.549____-0.127_____________________58.2
__5934.655_____26.0_____3.928____-1.170_____________________34.7
__5987.065_____26.0_____4.796____-0.429_____________________41.6
__6003.011_____26.0_____3.881____-1.120_____________________44.1
__6020.169_____26.0_____4.607____-0.270_____________________79.2
__6024.058_____26.0_____4.548____-0.120_____________________81.0
__6027.051_____26.0_____4.076____-1.089_____________________34.7
__6065.482_____26.0_____2.608____-1.530_____________________77.7
__6213.430_____26.0_____2.223____-2.482_____________________33.8
__6219.281_____26.0_____2.198____-2.433_____________________45.5

__6230.722______26.0_____2.559____-1.281_____________________100.1
__6232.640______26.0_____3.654____-1.223_____________________41.6
__6252.555______26.0_____2.404____-1.687_____________________75.0
__6265.132______26.0_____2.176____-2.550_____________________36.8
__6335.330______26.0_____2.198____-2.177_____________________51.0
__6336.823______26.0_____3.686____-0.856_____________________63.1
__6380.743______26.0_____4.186____-1.376_____________________20.2
__6421.350______26.0_____2.279____-2.027_____________________64.8
__4620.521______26.1_____2.828____-3.315_____________________73.9
__5256.938______26.1_____2.891____-4.182_____________________27.6
__5362.869______26.1_____3.199____-2.616_____________________121.7
__6084.111______26.1_____3.199____-3.881_____________________30.1
__6147.741______26.1_____3.889____-2.827_____________________68.4
__6149.258______26.1_____3.889____-2.841_____________________59.3
__6238.392______26.1_____3.889____-2.754_____________________61.4
__6247.557______26.1_____3.892____-2.435_____________________94.8
__6416.919______26.1_____3.892____-2.877_____________________60.6
__6432.680______26.1_____2.891____-3.687_____________________59.2

TABLE D.2: The equivalent-width measurements for HD139095.

```
HD139095_________________7000_____4.0_____0.00_____2.00
__4638.010______26.0_____3.602____-1.119_____________________87.7
__4966.088______26.0_____3.332____-0.871_____________________126.8
__4967.897______26.0_____4.191____-0.487_____________________30.0
__4988.950______26.0_____4.154____-0.890_____________________83.9
__5090.773______26.0_____4.256____-0.400_____________________91.0
__5133.688______26.0_____4.178_____0.140_____________________192.0
__5162.273______26.0_____4.178_____0.020_____________________154.9
__5302.300______26.0_____3.283____-0.720_____________________91.8
__5364.871______26.0_____4.445_____0.228_____________________125.7
__5400.501______26.0_____4.371____-0.160_____________________98.6
__5466.396______26.0_____4.371____-0.630_____________________84.0
__5497.516______26.0_____1.011____-2.849_____________________122.3
__5497.516______26.0_____1.011____-2.849_____________________121.4
__5569.618______26.0_____3.417____-0.486_____________________108.7
__5576.089______26.0_____3.430____-1.000_____________________97.1
__5762.992______26.0_____4.209____-0.450_____________________133.4
__5862.357______26.0_____4.549____-0.127_____________________89.5
__6008.556______26.0_____3.884____-0.986_____________________101.6
__6056.005______26.0_____4.733____-0.460_____________________67.2
__6065.482______26.0_____2.608____-1.530_____________________96.0
__6078.491______26.0_____4.796____-0.321_____________________85.5
__4576.340______26.1_____2.844____-2.976_____________________62.0
```

BIBLIOGRAPHY

Aerts, C. (1996). Mode identification of pulsating stars from line-profile variations with the moment method: a more accurate discriminant. *Astronomy and Astrophysics*, 314:115–122. (Cited on pages xix, 35, and 41.)

Aerts, C., Christensen-Dalsgaard, J., and Kurtz, D. W. (2010). Asteroseismology. *Asteroseismology*. (Cited on pages 3, 5, 6, 9, 11, 20, 40, and 110.)

Aerts, C., de Pauw, M., and Waelkens, C. (1992). Mode identification of pulsating stars from line profile variations with the moment method. an example - The Beta Cephei star Delta Ceti. *Astronomy and Astrophysics*, 266:294–306. (Cited on pages 9 and 41.)

Aerts, C., Puls, J., Godart, M., and Dupret, M. A. (2009). Collective pulsational velocity broadening due to gravity modes as a physical explanation for macroturbulence in hot massive stars. *Astronomy and Astrophysics*, 508(1):409–419. (Cited on page 106.)

Aerts, C. and Waelkens, C. (1993). Line Profile Variations of Rotating Pulsating Stars. *Astronomy and Astrophysics*, 273:135. (Cited on page 41.)

Ammler-von Eiff, M. and Reiners, A. (2012). New measurements of rotation and differential rotation in A-F stars: are there two populations of differentially rotating stars? *Astronomy and Astrophysics*, 542:116. (Cited on pages 46 and 47.)

Antonello, E. and Mantegazza, L. (1984). CO AUR and the double mode Cepheids. *Astronomy and Astrophysics (ISSN 0004-6361)*, 133:52–56. (Cited on page 5.)

Aston, F. W. (1920). The Constitution of the Elements. *Nature*, 106(2):468. (Cited on page 1.)

Baade, D. and Kjeldsen, H. (1997). A spectroscopic search for high azimuthal-order pulsation in broad-lined late F- and early G-stars. *Astronomy and Astrophysics*, 323:429–441. (Cited on pages 45, 46, 73, and 78.)

Balona, L. A. (1986). Mode identification from line profile variations. *Monthly Notices of the Royal Astronomical Society*, 219:111–129. (Cited on pages xix and 36.)

Balona, L. A., Guzik, J. A., Uytterhoeven, K., Smith, J. C., Tenenbaum, P., and Twicken, J. D. (2011). The Kepler view of γ Doradus stars. *Monthly Notices of the Royal Astronomical Society*, 415(4):3531–3538. (Cited on pages 110 and 132.)

Balona, L. A., Krisciunas, K., and Cousins, A. W. J. (1994). Gamma-Doradus - Evidence for a New Class of Pulsating Star. *Monthly Notices of the Royal Astronomical Society*, 270:905. (Cited on page 19.)

Barnes, S. I. (2004). *The design and performance of high resolution échelle spectrographs in astronomy*. PhD thesis, University of Canterbury. (Cited on page 25.)

Bouabid, M. P., Dupret, M. A., Salmon, S., Montalbán, J., Miglio, A., and Noels, A. (2013). Effects of the Coriolis force on high-order g modes in γ Doradus stars. *Monthly Notices of the Royal Astronomical Society*, 429(3):2500–2514. (Cited on pages 9, 11, and 137.)

Bouabid, M. P., Montalbán, J., Miglio, A., Dupret, M. A., Grigahcène, A., and Noels, A. (2009). Hybrid γ Doradus/δ Scuti Stars: Comparison Between Observations and Theory. In *Stellar Pulsation: Challenges for Theory and Observation: Proceedings of the International Conference. AIP Conference Proceedings*, volume 1170, pages 477–479. UMR 6525 H. Fizeau, UNS, CNRS, OCA, Campus Valrose, 06108 Nice Cedex 2, France; Institut d'Astrophysique et de Géophysique de l'Université de Liège, Allée du 6 Août, 17 4000 Liège, Belgium. (Cited on page 23.)

Bouabid, M. P., Montalbán, J., Miglio, A., Dupret, M. A., Grigahcène, A., and Noels, A. (2010). Theoretical study of γ Doradus pulsations in pre-main sequence stars. *Astronomische Nachrichten*, 331(9-10):1044–1048. (Cited on page 20.)

Briquet, M. and Aerts, C. (2003). A new version of the moment method, optimized for mode identification in multiperiodic stars. *Astronomy and Astrophysics*, 398(2):687–696. (Cited on pages xix and 36.)

Brunsden, E. (2013). *The Music of the Stars*. PhD thesis, University of Canterbury. (Cited on pages 23, 30, 40, 73, 99, 103, 133, and 137.)

Bruntt, H., De Cat, P., and Aerts, C. (2008). A spectroscopic study of southern (candidate) γ Doradus stars. II. Detailed abundance analysis and fundamental parameters. *Astronomy and Astrophysics*, 478(2):487–496. (Cited on pages 33, 136, and 137.)

Casagrande, L., Schoenrich, R., Asplund, M., Cassisi, S., Ramirez, I., Melendez, J., Bensby, T., and Feltzing, S. (2011). Geneva-Copenhagen survey re-analysis (Casagrande+, 2011). *VizieR Online Data Catalog*, 353:09138. (Cited on pages 47, 48, 50, and 110.)

Castelli, F. and Kurucz, R. L. (2004). New Grids of ATLAS9 Model Atmospheres. *Proceedings of the International Astronomical Union*, page 5087. (Cited on page 34.)

Chapellier, E., Mathias, P., Weiss, W. W., Le Contel, D., and Debosscher, J. (2012). Strong interactions between g- and p-modes in the hybrid γ Doradus-δ Scuti CoRoT star ID 105733033. *Astronomy and Astrophysics*, 540:117. (Cited on page 11.)

Cowling, T. G. and Newing, R. A. (1949). The Oscillations of a Rotating Star. *Astrophysical Journal*, 109:149. (Cited on page 9.)

Daszyńska-Daszkiewicz, J., Dziembowski, W. A., and Pamyatnykh, A. A. (2005). Constraints on parameters of B-type pulsators from combined multicolour photometry and radial velocity data. I. β Cephei stars. *Astronomy and Astrophysics*, 441(2):641–651. (Cited on page 23.)

Davie, M. (2013). *Spectroscopic Mode Identifications of Three γ Doradus Stars*. PhD thesis, University of Canterbury. (Cited on pages 33, 133, and 159.)

De Cat, P., Eyer, L., Cuypers, J., Aerts, C., Vandenbussche, B., Uytterhoeven, K., Reyniers, K., Kolenberg, K., Groenewegen, M., Raskin, G., Maas, T., and Jankov, S. (2006). A spectroscopic study of southern (candidate) γ Doradus stars. I. Time series analysis. *Astronomy and Astrophysics*, 449(1):281–292. (Cited on page 136.)

Dupret, M. A., Grigahcène, A., Garrido, R., Gabriel, M., and Scuflaire, R. (2004). Theoretical instability strips for δ Scuti and γ Doradus stars. *Astronomy and Astrophysics*, 414:L17–L20. (Cited on pages 2 and 4.)

Dupret, M. A., Grigahcène, A., Garrido, R., Gabriel, M., and Scuflaire, R. (2005). Convection-pulsation coupling. II. Excitation and stabilization mechanisms in δ Sct and γ Dor stars. *Astronomy and Astrophysics*, 435(3):927–939. (Cited on pages 22 and 23.)

Dupret, M. A., Miglio, A., Grigahcène, A., and Montalbán, J. (2007). Theoretical aspects of g-mode pulsations in γ Doradus stars. *Communications in Asteroseismology*, 150:98. (Cited on page 22.)

Eddington, A. S. (1917). The pulsation theory of Cepheid variables. *The Observatory*, 40:290–293. (Cited on page 5.)

Eddington, A. S. (1920). The internal constitution of the stars. *The Observatory*, 43:341–358. (Cited on page 1.)

Feast, M. W. and Catchpole, R. M. (1997). The Cepheid period-luminosity zero-point from HIPPARCOS trigonometrical parallaxes. *Monthly Notices of the Royal Astronomical Society*, 286(1):L1–L5. (Cited on page 17.)

Félix, S., Audit, E., and Dintrans, B. (2013). Towards 3D simulations of Cepheids stars. In *SF2A-2013: Proceedings of the Annual meeting of the French Society of Astronomy and Astrophysics. Eds.: L. Cambresy*, pages 223–226. (Cited on page 17.)

Fitzpatrick, M. J. and Sneden, C. (1987). A Software Package for Microcomputer Reductions of Spectroscopic Data. *Bulletin of the American Astronomical Society*, 19:1129. (Cited on pages xix and 33.)

Garrido, R. (2000). Photometric Modal Discrimination in δ Scuti and γ Doradus Stars. *Delta Scuti and Related Stars*, 210:67. (Cited on page 16.)

Gontcharov, G. A. (2006). Pulkovo Compilation of Radial Velocities for 35 495 Hipparcos stars in a common system. *Astronomy Letters*, 32(11):759–771. (Cited on page 47.)

Gough, D. O. (1996). Astereoasteroseismology. *The Observatory*, 116:313–315. (Cited on page 1.)

Gray, D. F. (1975). Atmospheric turbulence measured in stars above the main sequence. *The Astrophysical Journal*, 202:148. (Cited on page 15.)

Gray, D. F. (1988). *Lectures on spectral-line analysis: F, G, and K stars*. The Publisher: Arva, Ontario. (Cited on pages 14, 15, 16, and 136.)

Gray, D. F. (2005). *The Observation And Analysis Of Stellar Photospheres*. Cambridge University Press, 3rd edition edition. (Cited on pages 14, 15, and 32.)

Gray, R. O., Corbally, C. J., Garrison, R. F., McFadden, M. T., Bubar, E. J., McGahee, C. E., O'Donoghue, A. A., and Knox, E. R. (2006). Contributions to the Nearby Stars (NStars) Project: Spectroscopy of Stars Earlier than Mo within 40 pc–The Southern Sample. *The Astronomical Journal*, 132(1):161–170. (Cited on page 47.)

Guzik, J. A., Kaye, A. B., Bradley, P. A., Cox, A. N., and Neuforge, C. (2000). Driving the Gravity-Mode Pulsations in γ Doradus Variables. *The Astrophysical Journal*, 542(1):L57–L60. (Cited on pages 5, 20, 22, 79, and 134.)

Handler, G. (1999). The domain of γ Doradus variables in the Hertzsprung-Russell diagram. *Monthly Notices of the Royal Astronomical Society*, 309(2):L19–L23. (Cited on pages 20, 81, 107, and 112.)

Handler, G. and Shobbrook, R. R. (2002). On the relationship between the δ Scuti and γ Doradus pulsators. *Monthly Notices of the Royal Astronomical Society*, 333(2):251–262. (Cited on pages 22, 79, 81, 84, 99, and 133.)

Hareter, M. (2012). Preliminary results on γ Dor and δ Sct-γ Dor hybrid s in the CoRoT exo-field of LRa01. *Astronomische Nachrichten*, 333(1):1048. (Cited on page 22.)

Hareter, M., Reegen, P., Miglio, A., Montalbán, J., Kaiser, A., Dekany, I., Guenther, E., Poretti, E., Mathias, P., and Weiss, W. (2010). Gamma Dor and Gamma Dor - Delta Sct Hybrid Stars In The CoRoT LRa01. *arXiv.org*. (Cited on page 22.)

Hearnshaw, J. (2009). Astronomical Spectrographs and their History. *Astronomical Spectrographs and their History*. (Cited on page 25.)

Hearnshaw, J. B., Barnes, S. I., Kershaw, G. M., Frost, N., Graham, G., Ritchie, R., and Nankivell, G. R. (2002). The Hercules Échelle Spectrograph at Mt. John. *Experimental Astronomy*, 13(2):59–76. (Cited on pages xvii and 25.)

Henry, G. W., Fekel, F. C., and Henry, S. M. (2007). Photometry and Spectroscopy of 11 γ Doradus Stars. *The Astronomical Journal*, 133(4):1421–1440. (Cited on page 137.)

Henry, G. W., Fekel, F. C., and Henry, S. M. (2011). A Volume-limited Photometric Survey of 114 γ Doradus Candidates. *The Astronomical Journal*, 142(2):39. (Cited on pages 20, 22, 46, and 81.)

Hoffleit, D. and Warren, W. H. J. (1995). Bright Star Catalogue, 5th Revised Ed. (Hoffleit+, 1991). *VizieR Online Data Catalog*, 5050:0. (Cited on page 46.)

Holmberg, J., Nordström, B., and Andersen, J. (2009). The Geneva-Copenhagen survey of the solar neighbourhood. *Astronomy and Astrophysics*, 501(3):941–947. (Cited on page 47.)

Houk, N. (1982). Michigan Catalogue of Two-dimensional Spectral Types for the HD stars. Volume 3. Declinations -40 to -26. -1. (Cited on page 81.)

Hubeny, I. and Lanz, T. (2011). Synspec: General Spectrum Synthesis Program. *Astrophysics Source Code Library*. (Cited on page 30.)

Jeffery, C. S. (2008). The impact of asteroseismology on the theory of stellar evolution. *Communications in Asteroseismology*, 157:240–248. (Cited on page 19.)

Kallinger, T., Reegen, P., and Weiss, W. W. (2008). A heuristic derivation of the uncertainty for frequency determination in time series data. *Astronomy and Astrophysics*, 481(2):571–574. (Cited on page 36.)

Kaye, A. B. (2007). Asteroseismology of γ Doradus Variables: Past, Present, and Future. *Communications in Asteroseismology*, 150:91. (Cited on pages 19 and 110.)

Kaye, A. B., Handler, G., Krisciunas, K., Poretti, E., and Zerbi, F. M. (1999). Gamma Doradus Stars: Defining a New Class of Pulsating Variables. *The Publications of the Astronomical Society of the Pacific*, 111(7):840–844. (Cited on page 20.)

King, H., Matthews, J. M., Row, J. F., Cameron, C., Kuschnig, R., Guenther, D. B., Moffat, A. F. J., Rucinski, S. M., Sasselov, D., Walker, G. A. H., and Weiss, W. W. (2006). HD 114839 - An Am star showing both δ Scuti and γ Dor pulsations discovered through MOST photometry. *Communications in Asteroseismology*, 148:28–33. (Cited on page 22.)

Kippenhahn, R., Weigert, A., and Weiss, A. (2013). Stellar Structure and Evolution. *Stellar Structure and Evolution:*. (Cited on page 7.)

Krisciunas, K. (1993). A new class of pulsating stars. *American Astronomical Society*, 183:1422. (Cited on page 19.)

Kupka, F. G., Ryabchikova, T. A., Piskunov, N. E., Stempels, H. C., and Weiss, W. W. (2000). VALD-2 – The New Vienna Atomic Line Database. *Baltic Astronomy*, 9:590–594. (Cited on pages xix, 35, and 83.)

Kurucz, R. (1993). ATLAS9 Stellar Atmosphere Programs and 2 km/s grid. *ATLAS9 Stellar Atmosphere Programs and 2 km/s grid. Kurucz CD-ROM No. 13. Cambridge, Mass.: Smithsonian Astrophysical Observatory, 1993.*, 13. (Cited on page xvii.)

Mantegazza, L. (2000). Mode Detection from Line-Profile Variations. *IAU Colloq. 193: Variable Stars in the Local Group*, 210:138. (Cited on page 40.)

Martens, L. and Smeyers, P. (1982). On the linear adiabatic oscillations of a uniformly and synchronously rotating component of a binary. *Astronomy and Astrophysics*, 106:317–326. (Cited on page 41.)

Mathias, P., Le Contel, J. M., Chapellier, E., Jankov, S., Sareyan, J. P., Poretti, E., Garrido, R., Rodríguez, E., Arellano Ferro, A., Alvarez, M., Parrao, L., Peña, J., Eyer, L., Aerts, C., De Cat, P., Weiss, W. W., and Zhou, A. (2004). Multi-site, multi-technique survey of γ Doradus candidates. I. Spectroscopic results for 59 stars. *Astronomy and Astrophysics*, 417:189–199. (Cited on pages 133 and 136.)

Monnier, J. D., Townsend, R. H. D., Che, X., Zhao, M., Kallinger, T., Matthews, J., and Moffat, A. F. J. (2010). Rotationally Modulated g-modes in the Rapidly Rotating δ Scuti Star Rasalhague (α Ophiuchi). *The Astrophysical Journal*, 725(1):1192–1201. (Cited on page 121.)

Montgomery, M. H. and Odonoghue, D. (1999). A derivation of the errors for least squares fitting to time series data. *Delta Scuti Star Newsletter*, 13:28. (Cited on page 37.)

Perryman, M. A. C., Lindegren, L., Kovalevsky, J., Hoeg, E., Bastian, U., Bernacca, P. L., Crézé, M., Donati, F., Grenon, M., Grewing, M., van Leeuwen, F., van der Marel, H., Mignard, F., Murray, C. A., Le Poole, R. S., Schrijver, H., Turon, C., Arenou, F., Froeschlé, M., and Petersen, C. S. (1997). The HIPPARCOS Catalogue. *Astronomy and Astrophysics*, 323:L49–L52. (Cited on pages 27, 45, 46, 54, 70, 84, 107, and 110.)

Pesnell, W. D. (1987). A new driving mechanism for stellar pulsations. *The Astrophysical Journal*, 314:598–604. (Cited on page 22.)

Pollard, K. R. (2009). A Review Of γ Doradus Variables. In *Stellar Pulsation: Challenges for Theory and Observation: Proceedings of the International Conference. AIP Conference Proceedings*, pages 455–466. Department of Physics and Astronomy, University of Canterbury, Private Bag 4800, Christchurch, New Zealand. (Cited on page 19.)

Preston, G. W. (2011). RR Lyrae Atmospherics: Wrinkles Old and New. A Preview. *The Astronomical Journal*, 141(1):6. (Cited on page 110.)

Reegen, P. (2011). SigSpec User's Manual. *Communications in Asteroseismology*, 163:3. (Cited on page 35.)

Reese, D., Lignières, F., and Rieutord, M. (2006). Acoustic oscillations of rapidly rotating polytropic stars. II. Effects of the Coriolis and centrifugal accelerations. *Astronomy and Astrophysics*, 455(2):621–637. (Cited on page 11.)

Royer, F., Zorec, J., and Gómez, A. E. (2007). Rotational velocities of A-type stars. III. Velocity distributions. *Astronomy and Astrophysics*, 463(2):671–682. (Cited on page 110.)

Saffe, C. (2011). FUNDPAR: A program for Deriving Fundamental Parameters from Equivalent Widths. *Revista Mexicana de Astronomía y Astrofísica Vol. 47*, 47:3–14. (Cited on pages xvii and 34.)

Sandage, A. and Tammann, G. A. (1969). The Double Cepheid CE Cassiopeiae in NGC 7790: Tests of the Theory of the Instability Strip and the Calibration of the Period-Luminosity Relation. *Astrophysical Journal*, 157:683. (Cited on page 17.)

Sbordone, L., Bonifacio, P., Castelli, F., and Kurucz, R. L. (2004). ATLAS and SYNTHE under Linux. *Memorie della Società Astronomica Italiana Supplement*, 5:93. (Cited on pages xvii and 34.)

Schrijvers, C., Telting, J. H., Aerts, C., Ruymaekers, E., and Henrichs, H. F. (1997). Line-profile variations due to adiabatic non-radial pulsations in rotating stars. I. Observable characteristics of spheroidal modes. *Astronomy and Astrophysics Supplement Series*, 121:343–368. (Cited on pages 12 and 41.)

Schröder, C., Reiners, A., and Schmitt, J. H. M. M. (2009). Ca II HK emission in rapidly rotating stars. *Astronomy and Astrophysics*, 493(3):1099–1107. (Cited on page 47.)

Simón-Díaz, S., Herrero, A., Uytterhoeven, K., Castro, N., Aerts, C., and Puls, J. (2010). Observational Evidence for a Correlation Between Macroturbulent Broadening and Line-profile Variations in OB Supergiants. *The Astrophysical Journal Letters*, 720(2):L174–L178. (Cited on pages 16 and 106.)

Sinachopoulos, D., Gavras, P., Dionatos, O., Ducourant, C., and Medupe, T. (2007). CCD astrometry and components instrumental magnitude difference of 432 Hipparcos wide visual double stars. *Astronomy and Astrophysics*, 472(3):1055–1057. (Cited on page 107.)

Skuljan, J. (2004). HRSP - A dedicated echelle reduction software package for Hercules. *IAU Colloq. 193: Variable Stars in the Local Group*, 310:575. (Cited on pages 28 and 30.)

Sneden, C. (1973). The nitrogen abundance of the very metal-poor star HD 122563. *The Astrophysical Journal*, 184:839–849. (Cited on pages xviii and 34.)

Sousa, S. G., Santos, N. C., Israelian, G., Mayor, M., and Monteiro, M. J. P. F. G. (2007). A new code for automatic determination of equivalent widths: Automatic Routine for line Equivalent widths in stellar Spectra (ARES). *Astronomy and Astrophysics*, 469(2):783–791. (Cited on pages xvii and 33.)

Stokes, N. R. (1972). Four-colour and Hbeta photometry of some bright southern stars. *Monthly Notices of the Royal Astronomical Society*, 159:165–177. (Cited on page 45.)

Tkachenko, A., Aerts, C., Yakushechkin, A., Debosscher, J., Degroote, P., Bloemen, S., Pápics, P. I., de Vries, B. L., Lombaert, R., Hrudkova, M., Frémat, Y., Raskin, G., and Van Winckel, H. (2013). Detection of a large sample of γ Doradus stars from Kepler space photometry and high-resolution ground-based spectroscopy. *Astronomy and Astrophysics*, 556:52. (Cited on pages 20, 21, and 22.)

Tokovinin, A., Mason, B. D., and Hartkopf, W. I. (2010). Speckle Interferometry at the Blanco and SOAR Telescopes in 2008 and 2009. *The Astronomical Journal*, 139(2):743–756. (Cited on page 45.)

Torres, G., Andersen, J., and Gimenez, A. (2010). Accurate masses and radii of normal stars: modern results and applications. *The Astronomy and Astrophysics Review*, 18(1):67–126. (Cited on pages 20, 71, 99, 110, and 135.)

Townsend, R. H. D. (2003a). A semi-analytical formula for the light variations due to low-frequency g modes in rotating stars. *Monthly Notices of the Royal Astronomical Society*, 343(1):125–136. (Cited on pages 11, 12, and 13.)

Townsend, R. H. D. (2003b). Asymptotic expressions for the angular dependence of low-frequency pulsation modes in rotating stars. *Monthly Notices of the Royal Astronomical Society*, 340(3):1020–1030. (Cited on page 12.)

Twarog, B. A. and Anthony-Twarog, B. J. (1995). CA II H and K Filter Photometry on the UVBY System. II. The Catalog of Observations. *The Astronomical Journal*, 109:2828. (Cited on page 45.)

Valenti, J. A. and Fischer, D. A. (2005). Spectroscopic Properties of Cool Stars (SPOCS). I. 1040 F, G, and K Dwarfs from Keck, Lick, and AAT Planet Search Programs. *The Astrophysical Journal Supplement Series*, 159(1):141–166. (Cited on pages 16, 35, and 83.)

Valenti, J. A. and Piskunov, N. (1996). Spectroscopy made easy: A new tool for fitting observations with synthetic spectra. *Astronomy and Astrophysics Supplement Series*, 118:595–603. (Cited on pages xviii and 35.)

van Leeuwen, F. (2007). Validation of the new Hipparcos reduction. *Astronomy and Astrophysics*, 474(2):653–664. (Cited on pages 45, 81, and 107.)

Warner, P. B., Kaye, A. B., and Guzik, J. A. (2003). A Theoretical γ Doradus Instability Strip. *The Astrophysical Journal*, 593(2):1049–1055. (Cited on pages 2, 4, 20, and 46.)

Wells, D. C., Greisen, E. W., and Harten, R. H. (1981). FITS - a Flexible Image Transport System. *Astronomy and Astrophysics Supplement Series*, 44:363. (Cited on page xvii.)

Worley, C. E. and Douglass, G. G. (1997). The Washington Double Star Catalog (WDS, 1996.0). *Astronomy and Astrophysics Supplement Series*, 125:523–523. (Cited on page 45.)

Wright, D. J. (2008). *Spectroscopic Mode Identification in a Sample of Non-radially Pulsating Stars*. PhD thesis, University of Canterbury. (Cited on pages 30, 32, 40, and 136.)

Zboril, M. (1996). Version of CCP7 SYNSPEC Code. *IAU Colloq. 193: Variable Stars in the Local Group*, 108:193. (Cited on pages xix and 30.)

Zima, W. (2006). A new method for the spectroscopic identification of stellar non-radial pulsation modes. I. The method and numerical tests. *Astronomy and Astrophysics*, 455(1):227–234. (Cited on pages xvii and 40.)

Zima, W. (2008a). FAMIAS - A userfriendly new software tool for the mode identification of photometric and spectroscopic times series. *Communications in Asteroseismology*, 157:387. (Cited on pages 17 and 35.)

Zima, W. (2008b). FAMIAS User Manual. *Communications in Asteroseismology*, 155:17–121. (Cited on pages 6, 8, 12, 17, 37, 41, and 56.)

Zima, W., Wright, D., Bentley, J., Cottrell, P. L., Heiter, U., Mathias, P., Poretti, E., Lehmann, H., Montemayor, T. J., and Breger, M. (2006). A new method for the spectroscopic identification of stellar non-radial pulsation modes. II. Mode identification of the δ Scuti star FG Virginis. *Astronomy and Astrophysics*, 455(1):235–246. (Cited on page xvii.)